Fakultät für Physik der Technischen Universität München
Physik-Department E12

Simulation and Real-Time Analysis of Pulse Shapes from segmented HPGe-Detectors

Michael Christian Schlarb

Vollständiger Abdruck der von der Fakultät für Physik der Technischen Universität München zur Erlangung des akademischen Grades eines

Doktors der Naturwissenschaften (Dr. rer. nat.)

genehmigten Dissertation.

Vorsitzender:	Univ.-Prof. Dr. Harald Friedrich
Prüfer der Dissertation:	
	1. Univ.-Prof. Dr. Reiner Krücken
	2. Univ.-Prof. Dr. Stephan Paul

Die Dissertation wurde am 02.11.2009 bei der Technischen Universität München eingereicht und durch die Fakultät für Physik am 17.11.2009 angenommen.

Abstract

The capabilities of future HPGe arrays consisting of highly segmented detectors, like AGATA will depend heavily on the performance of γ-ray tracking. The most crucial component in the whole concept is the pulse shape analysis (PSA). The working principle of PSA is to compare the experimental signal shape with signals available from a basis set with known interaction locations. The efficiency of the tracking algorithm hinges on the ability of the PSA to reconstruct the interaction locations accurately, especially for multiple γ-interactions. Given the size of the arrays the PSA algorithm must be run in a real-time environment.

A prerequisite to a successful PSA is an accurate knowledge of the detectors response. Making a full coincidence scan of a single AGATA detector, however takes between two and three months, which is too long to produce an experimental signal basis for all detector elements. A straight forward possibility is to use a precise simulation of the detector and to provide a basis of simulated signals. For this purpose the ***J**ava **A**gata **S**ignal **S**imulation* (JASS) was developed in the course of this thesis. The geometry of the detector is given with numerical precision and models describing the anisotropic mobilities of the charge carriers in germanium were taken from the literature. The pulse shapes of the transient and net-charge signals are calculated using weighting potentials on a finite grid. Special care was taken that the interpolation routine not only reproduces the weighting potentials precisely in the highly varying areas of the segment boundaries but also that its performance is independent of the location within the detector. Finally data from a coincidence scan and a pencil beam experiment were used to verify JASS. The experimental signals are reproduced accurately by the simulation.

Pulse Shape Analysis (PSA) reconstructs the positions of the individual interactions and the corresponding energy deposits within the detector. This is accomplished by searching the simulated signal basis for the best agreement with the experimental signal. The particular challenge lies in the binomial growth of the search space making an intelligent search algorithm compulsory. In order to reduce the search space, the starting time t_0 for the pulse shapes can be determined independently by a neural network algorithm, developed in the scope of this work. The precision of $2-5ns$(FWHM), which is far beyond the sampling time of the digitizers, directly influences the attainable position resolution. For the search of the positions the so-called „Fully Informed Particle Swarm“ (FIPS) was developed, implemented and has proofed to be very efficient. Depending on the number of interactions an accurate reconstruction of the positions is accomplished within several μs to a few ms.

Data from a simulated (d,p) reaction in inverse kinematics, using a ^{48}Ti beam at an energy of 100 MeV, impinging on a deuterated titanium target were used to

test the capabilities of the developed PSA algorithms in a realistic setting. In the ideal case of an extensive PSA an energy resolution of $2.8\,keV$ ($FWHM$) for the $1382\,keV$ line of ^{49}Ti results but this approach works only on the limited amount of data in which only a single segment has been hit. Selecting the same events the FIPS-PSA Algorithm achieves $3.3\,keV$ with an average computation time of $\sim$ $0.9\,ms$. The extensive grid search, by comparison takes $27\,ms$. Including events with multiple hit segments increases the statistics roughly twofold and the resolution of FIPS-PSA does not deteriorate significantly at an average computing time of $2.2\,ms$.

Zusammenfassung

Die Leistungsfähigkeit zukünftiger HPGe Arrays aus hochsegmentierten Detektoren, wie z.B. AGATA hängt stark von der Güte des γ-Strahlen-Trackings ab. Der wichtigste Baustein im gesamten Konzept ist die Pulseform Analyse (PSA). Die Grundidee der PSA ist dabei, das experimentelle Signal mit einem Satz vorhandener Signale mit bekannter Wechselwirkunsposition zu vergleichen. Die Effizienz des γ-Tracking-Algorithmus ist begrenzt durch die Genauigkeit der Ortsrekonstruktion des verwendeten PSA Verfahrens, insbesondere im Fall von Mehrfachwechselwirkungen. In Anbetracht der großen Anzahl an Detektoren in einer Array muss der PSA Algorithmus in Echtzeit laufen.

Eine Grundvoraussetzung für eine erfolgreiche PSA ist eine präzise Kenntnis der Antwortfunktion der unterschiedlichen Detektoren. Der komplette Koinzidenz-Scan eines einzelnen AGATA Kristalls benötigt zwischen zwei und drei Monaten. Dieser Zeitraum ist viel zu lange um eine experimentelle Datenbasis fr jedes einzelne Detektorelement zu erstellen. Die einzig verbleibende Möglichkeit ist daher eine akkurate Simulation der Pulsformen zur Erzeugung einer Datenbasis zu verwenden. Zu diesem Zweck wurde die ***J**ava **A**gata **S**ignal **S**imulation* (JASS) im Rahmen dieser Arbeit entwickelt. Eine numerisch präzise Beschreibung der Detektorgeometrie wurde implementiert und die Modelle zur Beschreibung der anisotropen Beweglichkeiten der Ladungsträger in Germanium wurden der Fachliteratur entnommen. Die Pulsformen der einzelnen Segmente werden mit Hilfe sogenannter Weighting Potentiale, welche nur auf einem Gitter fester Größe gegeben sind berechnet. Besonderes Augenmerk wurde darauf gelegt, dass die Interpolationsroutine sowohl im Bereich der stark veränderlichen Weighting Potentiale am Rande der Segmente eine hohe Genauigkeit aufweist als auch, dass ihre Leistung nicht von der Orientierung innerhalb des Detektors abhängig ist. Schließlich wurde JASS mit Hilfe von Daten eines Koinzidenz-Scans verifiziert.

Die Pulsform Analyse (PSA) rekonstruiert die Orte der einzelnen Wechselwirkungen und bestimmt deren Energiedeposit im Detektor. Hierzu wird die simulierte Datenbasis nach der besten Übereinstimmung mit dem experimentellen Signal durchsucht. Die besondere Herausforderung hierbei, liegt im binomialen Anwachsen des Suchraumes. Ein intelligenter Suchalgorithmus ist somit zwingend erforderlich. Die Aufgabe des Suchalgorithmus kann jedoch vereinfacht werden in dem man die Startzeit t_0 der Pulsformen im Voraus bestimmt. Die Genauigkeit mit der diese bekannt ist hat direkten Einfluss auf die erreichbare Ortsauflösung. Mit Hilfe der im Rahmen dieser Arbeit entwickelten neuronalen Netze kann die Startzeit mit ausreichender Präzision bestimmt werden. Zur Suche der Wechselwirkungsorte wurde der sog. „Fully Informed Particle Swarm“ (FIPS) implementiert und hat sich als besonders effizient erwiesen. Der Algorithmus imitiert das Verhalten eines Vogelschwarms auf Futtersuche. In Abhängigkeit von der Anzahl

der Wechselwirkungen sind deren Positionen innerhalb einiger hundert μs bis weniger ms mit guter Präzision rekonstruiert.

Um Rückschlüsse auf die wahre Leistungsfähigkeit der entwickelten PSA Algorithmen zu ermöglichen wurden simulierte Daten einer $^{48}Ti(d,p)^{49}Ti$ Reaktion, bei 100 MeV in inverser Kinematik verwendet. Im Falle einer extensiven PSA ber die gesamte Datenbasis ergibt sich eine Auflösung von $2.8\,keV$ $(FWHM)$ für die $1382\,keV$ Linie von ^{49}Ti. Dieser Ansatz ist nur möglich unter der vereinfachenden Annahme einer einzigen Wechselwirkung pro getroffenen Segment und geht mit einem signifikanten Verlust an Statistik einher. Bei gleicher Eventselektion erreicht der FIPS-PSA Algorithmus eine Auflösung von $3,3\,keV$ (FWHM) nach durchschnittlich $0.9\,ms$. Die durchschnittliche Suchdauer der extensiven Suche betrug $27\,ms$. Verwendet man zusätzlich noch Daten mit mehreren getroffenen Segmenten erreicht man mit Hilfe des FIPS Algorithmus ungefähr die doppelte Statistik jedoch ohne signifikanten Verlust an Energieauflösung mit einer durchschnittlichen Berechnungszeit von 2.2ms.

Contents

Chapter 1

Introduction

The nucleus is a strongly-interacting many body system. In its simplest case of hydrogen it consists of a single proton only but it can contain up to a few hundred nucleons , e.g. ^{254}No. Several diverse models from the Liquid Drop model to the fully quantum mechanical Shell and Collective model exist though none can be applied to all existing nuclei and describe the observed phenomena. Naturally, this acts as a driving force in the quest to understand nuclear structure in more detail and give more predictive power to the model calculation. Especially nuclei with an extreme proton to neutron ratio will provide insight to the different components of the so-called residual interactions. The full nuclear landscape cannot be accessed using current experimental techniques especially very exotic nuclei with large isospin.

1.1 Introduction to γ-ray Spectroscopy

Historically γ-ray spectroscopy is one of the most important means to learn about nuclear structure. γ-rays emitted in the depopulation of excited states provide access to some of the most important observables needed for comparison with nuclear structure models. The transition probability can be deduced from life-time measurements, the angular distribution or correlation of the γ-rays gives information about the spin of the states, the linear polarization about the parity and the γ-ray energy about the states' excitation energy. Given the manifold of different research directions in nuclear structure only two select cases together with the basic experimental approaches will be presented here. A feature common to both approaches is that the excited nucleus emits the γ-ray(s) in flight and the recorded γ-ray energy E_γ is therefore shifted away from its initial energy E_0 due to the Doppler-Effect according to the following equation:

$$E_\gamma \;=\; E_0 \cdot (1 + \beta \cdot \cos(\theta)) \,. \tag{1.1}$$

with β the nucleus' velocity in units of c and θ the angle between the directions of the γ-ray and the nucleus. Consequently, the excitation energy is not resolved

with the detectors intrinsic resolution but has a broadened line width proportional to the detectors' solid angle coverage and requires some corrections to be performed (see sec. 1.2).

The shell model of nuclear structure was developed in analogy to the atomic shell model. The nucleons are situated in bound states of a central potential, e.g. a Woods-Saxon potential, obeying the Pauli principle. In addition the nucleons combine to pairs of opposite spin minimizing the total energy. Analogously closed shells or sub-shells for either the proton number Z or neutron number N lead to the so-called magic numbers $2, 8, 20, 28, 50, ...$ characterized by a larger energy gap to the next state and an increased energy of the first excited state.

Similarly to the chemically inert noble gases, nuclei with magic N or Z exhibit a greater stability, especially true for *doubly-magic* nuclei with magic N and Z. The shell models predictions are accurate for stable nuclei but the evolution of shell structure for unstable, especially neutron-rich nuclei shows deviations. Such nuclei are investigated by means of so-called *Radioactive Ion Beams* (RIB) which are produced using for example secondary fragmentation reactions or the *ISOL* technique. The typically rather low production cross sections, however, lead to equally low beam intensities. A high background radiation is common in these experimental conditions. In systematic investigations of the energy of the first

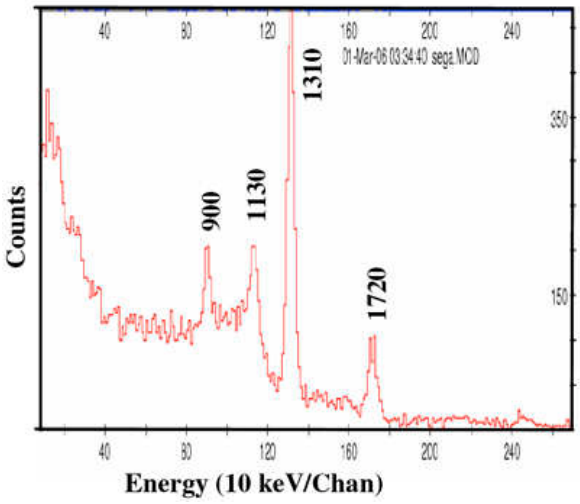

Figure 1.1: γ-ray spectrum of ^{28}Ne as reported by (Fallon et al., 2006). The transition energies are given in keV and the $900, 1720$ and $1310\,keV$ γ-rays were assigned to the $4^+ \rightarrow 2^+ \rightarrow 0^+$ cascade with the initial state of the $900\,keV$ line being unassigned. The line at $1130\ keV$ is not in coincidence with the ground state band.

excited state as a function of neutron number as well as for isotones shell or sub-shell closures should show up as a clear increase in the states energy. Conversely, the reduced transition probability $B(^E_M L)$[1] should decrease for nuclei with closed shells. Additionally, the transition rate of the first excited 2^+ to a 0^+ ground state (see fig. 1.1) provides information on the shell structure via $B(E2)$ through its dependence on the transition matrix element involving the wave function of the initial and final state. Another example is the ratio of the 4^+ to the 2^+

[1] E and M indicate whether it is an electric or magnetic transition and L is its multipolarity.

energy $R_{4/2}$ in even-even nuclei which gives an indication whether the nuclei are rotational ($R_{4/2} = 3.33$) or vibrational ($R_{4/2} = 2$).

Another interesting question concerns the changes to nuclear structure at high angular momenta. In a simple picture the total angular momentum of a nucleus can be thought of as a composition of the angular momenta of the individual nucleons and collective vibrational and rotational excitations of the whole nucleus. At very high spin the rotational forces as well as the Coriolis force try to break up the pairing correlations and transfer angular momentum from the collective modes to energetically more favorable individual particle modes. This behavior

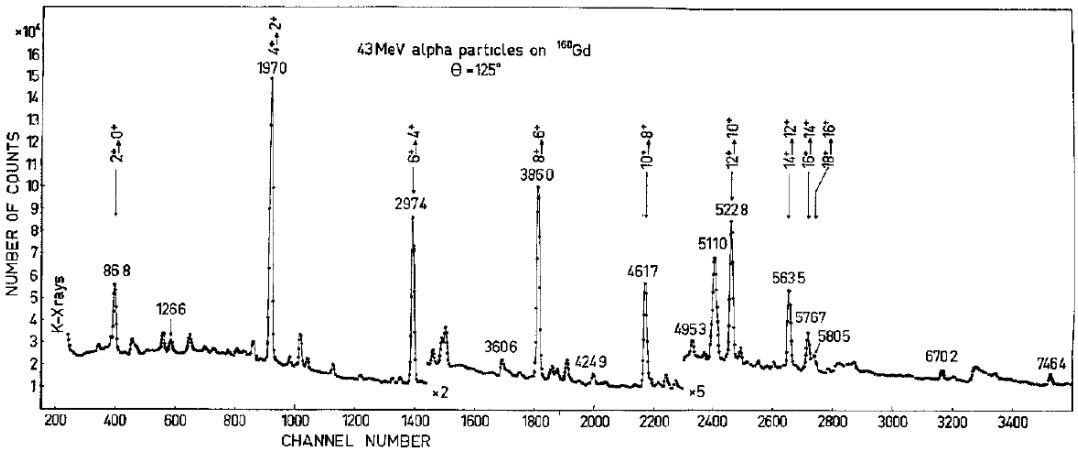

Figure 1.2: γ-ray spectrum of ^{160}Dy at high spins. The spectrum was recorded at an angle of $\theta = 125°$ relative to the beam line after a $(\alpha, 4n)$ reaction with the peaks belonging to ^{160}Dy being indicated. This figure was taken from (Johnson et al., 1972).

manifests itself in the emergence of rotational bands next to the ground state band showing up as an additional band structure in the γ-ray spectra. One of the earliest experimental evidences for this behavior was reported by (Johnson et al., 1972) for ^{160}Dy and showed a deviation from the regular ground-state rotational band for the $18^+ \rightarrow 16^+$ and $16^+ \rightarrow 14^+$ transitions. Besides these additional bands also shape changes can be induced up to super-deformed (2:1 frequency ratio along semi-major axis) or even hyper-deformed shapes (3:1 ratio). These experiments are conducted with high intensity beams of stable isotopes and allow conclusions on the collectivity of nuclear structure. The rather high overall event rate does not facilitate the detection of the low intensity γ-ray cascades. However, the level of background in the spectra can be reduced by placing gates on one or more line energies of a cascade removing any γ-rays not emitted in coincidence with these lines.

1.2 Existing Arrays

Since a complete recount of all γ-arrays used in γ-spectroscopy is beyond the scope of this thesis the further discussion will concentrate on the 4π-arrays *GAMMASPHERE* and *EUROBALL* and the *MINIBALL* array of sixfold segmented HPGe detectors. For an excellent review of the historical development of germanium detectors in the context of nuclear structure physics the reader is referred to (Eberth & Simpson, 2008). Before the properties of existing arrays are discussed it is best to explain some of the used terms in detail.

- **Full Energy Peak Efficiency** (ε): the efficiency of the complete array to detect the full energy of the γ-ray, also called *photo peak efficiency*.
- **Peak-to-Total ratio** (P/T): is defined for a monoenergetic γ-ray as the ratio of counts in the full energy peak to the total counts.
- **Isolated Hit Probability**: the probability to detect individual γ-rays, e.g. from a cascade, in different detectors.

Each of these depends in one way or the other on the setup of the detector array. The P/T can be increased by surrounding the HPGe detectors with other detectors of high Z material, e.g. bismuth germanate ($Bi_4Ge_3O_{12}$,BGO) crystals. These are the so-called *Anti-Compton-* or *Compton-Suppression-Shields* which give a veto signal to the data acquisition system if a γ-ray scatters out of the germanium detector, i.e. not depositing its full energy, and into the BGO crystals. These events are thus removed from the spectra as they would only contribute to the background. The ε on the other hand is limited by the efficiency of the individual germanium detectors and their solid angle coverage, which in turn is limited to $\sim 50\%$ if Anti-Compton shields are used. The maximal efficiencies are $10 - 12\%$ at an energy of $1.3\,MeV$ (Eberth & Simpson, 2008). The isolated hit probability depends on the granularity, i.e. number of detectors in the array. Two γ-rays interacting within the same detector cannot be distinguished by current arrays and thus contribute to the background only. The probability of a full energy deposit of both γ-rays is small. Another important aspect of an array is its energy resolution which, as was already pointed out in the previous section, is typically not that of the used detector but suffers from Doppler-line broadening. The contribution of the Doppler effect to the line width is given by:

$$\Delta E_\gamma \;=\; E_0 \cdot \beta \cdot \sin(\theta)\, d\theta, \tag{1.2}$$

with $d\theta$ the polar opening angle of the detector, i.e. its angular resolution.

The concept of *resolving power* (RP) has proven beneficial in combining these various aspects of an array into a single number and enables a fair comparison of arrays with very different setups. The RP is a measure for the weakest intensity of a line which can be distinguished from the background. A line is considered

to be resolved if it stands out from the background, has N counts in the peak and a peak-to-background ratio N/N_0 of one. The description given here follows that by (Deleplanque et al., 1999) though other definitions exist as well. In a typical experiment with higher γ-ray multiplicity M_γ the γ-rays are emitted in a cascade with an average spacing in line energy SE. In order to improve the peak-to-background ratio coincidence gates can be placed on one or more line energies and for each gate the ratio improves by a factor of

$$R = 0.76 \cdot \frac{SE}{\Delta E_\gamma} \cdot P/T. \tag{1.3}$$

This takes into consideration that around 76% of the line are included in the FWHM ΔE, i.e. the width of the gate, and that the peak only represents the fraction P/T of the total γ-ray intensity. For a gate fold $f-1$ and a branch of intensity α the peak-to-background ratio is thus αR^f.

The number of counts N in the peak on the other hand is given by the full-energy efficiency ε of the array and amounts to $N = \alpha N_0 \varepsilon^f$, where N_0 is the total number of events. The criteria outlined above for a branch of minimum intensity α_0 to be resolved then define the resolving power RP as $1/\alpha_0 = R^F$ with F the maximal fold for which the criteria are just met. Eliminating F using the equations for α_0 and N an expression for RP is obtained depending on R and ε:

$$RP = \exp\{\log(N_0/N) / (1 - \log(\varepsilon)/\log(R))\}. \tag{1.4}$$

In the following discussion $N = 100$, $N_0 = 2.88 \cdot 10^{10}$, corresponding to a reaction rate of $10^5/s$ for 80 h, and $SE = 60\,keV$ are assumed.

1.2.1 GAMMASPHERE

GAMMASPHERE (Deleplanque & Diamond, 1987) is the first dedicated 4π-array that was built in the United States. It started operating in 1993 at Lawrence Berkeley National Laboratory and was moved to Argonne National Laboratory at the end of 1997. GAMMASPHERE uses the technique of Compton-suppression and consists of 110 modules[2] which was a compromise between achieving a high granularity for a small Doppler broadening as well as a high isolated hit probability and keeping the cost within a reasonable range on the other side. The individual modules have hexagonally shaped BGO shields with an entrance window for the γ-rays and coaxial n-type HPGe detectors in the middle (see fig. 1.3), these were of the largest size producible at the time. Around 70 of the 110 germanium detectors were longitudinally segmented forming two D-shaped halves. This feature improved the energy resolution ΔE from $5.5\,keV$ to $3.9\,keV$ at recoil velocities of $\beta = 0.02$. In order to be able to also suppress forward-scattering γ-rays leaving the germanium detectors at the rear end a sophisticated

[2]One possible geodesic tiling of the sphere is 110 hexagons with 12 pentagons (see fig. 1.8).

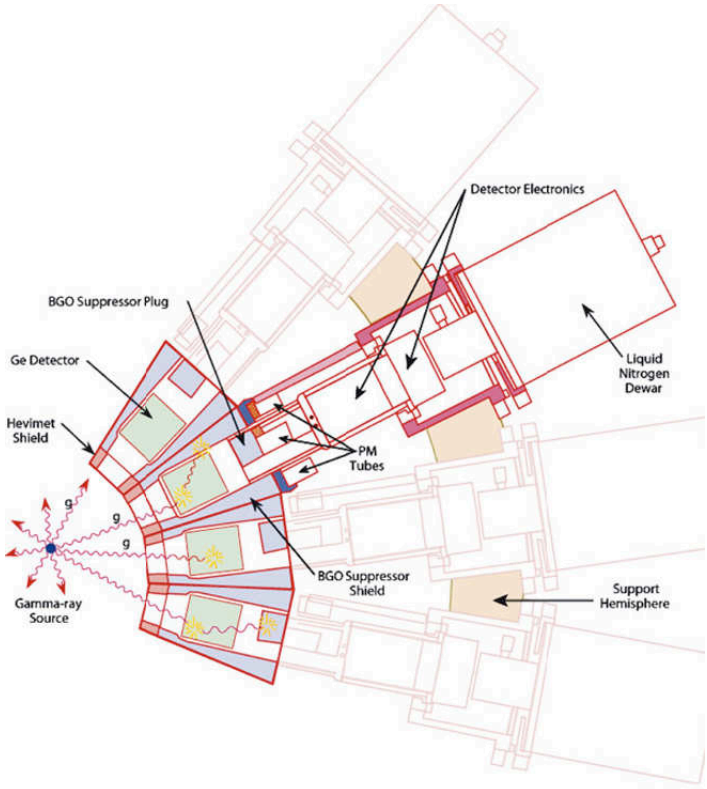

Figure 1.3: Schematic view of GAMMASPHERE. This figure was taken from (Eberth & Simpson, 2008).

solution was found. The cryostat's cold finger was mounted off center allowing the mounting of another BGO crystal behind the germanium detectors. All in all the relative efficiency of a single GAMMASPHERE detector is 70% and a P/T of $46 - 68\%$ is achieved. A total of 95% of the 4π solid angle are covered by the complete array with 46% being covered by the germanium detectors. The data analysis is facilitated by the fact that all detectors have the same shape and are arranged in a highly symmetric manner. GAMMASPHERE's efficiency is $\varepsilon = 0.09$ and thus the resolving power, as given by equation 1.4, is in the range of $3000 - 7000$. An example of this high resolving power is the discovery of the 'linking transitions' between superdeformed states and normally deformed states in some nuclei around mass 190 (Khoo et al., 1996). These transitions are very weak having around 1% of the intensity of the superdeformed bands which in turn also have only an intensity of about 1% of the total cross section.

1.2.2 EUROBALL

The development of the EUROBALL array took place in several stages and with different configurations. Only the next to last one, called EUROBALL-III (see fig. 1.4) will be covered here. EUROBALL-IV only added an inner ball of BGO crystals as ancillary detector. Besides the standard coaxial n-type germanium detectors EUROBALL contained two new detector technologies developed in the course of the project. The first one was the clover detector (Duchêne et al., 1999) developed by CRN-Strasbourg and Intertechnique (now Canberra Eurisys). It consists of four closed-packed coaxial n-type germanium detectors with a diameter of $50\,mm$ and a front-face tapered into a rectangular shape. The clover detector increases the relative efficiency by about a factor of two over standard coaxial detectors due to its 30% larger volume and by adding back the energy deposits in the four detectors into the full energy peak. Additionally, it increases the granularity by a factor of four. The four detectors are housed in a single common cryostat of rectangular shape, a geometry not suitable to cover a full sphere but better suited for a positioning of the detectors at 90° to the beam axis. The full-energy peak efficiency of the clover detectors grouped with 30 single element detectors was 8.1% at $1.3\,MeV$.

The second major development of EUROBALL was the so-called cluster detector housing seven hexagonal n-type germanium detectors in a single cryostat. The surrounding BGO Compton-suppression shields also had a hexagonal shape of the size that 60 units would cover a full sphere minus the pentagonal elements (see fig. 1.8). The first step was to show that it was possible to produce the tapered hexagonal germanium detectors without loss in energy resolution and timing properties (Eberth et al., 1992). However there was still doubt about the possibility and feasibility of grouping seven closed packed detectors in a common cryostat. The development of hermetically encapsulated germanium detectors (Eberth et al., 1996), a technology also used by AGATA, by the University of

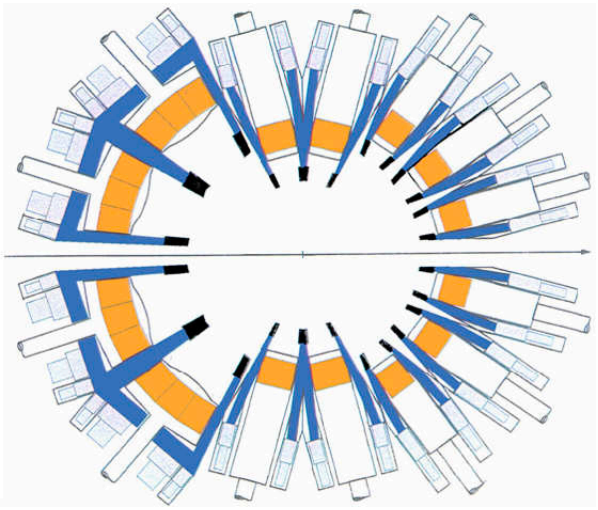

Figure 1.4: Schematic drawing of the EUROBALL-III array. The beam direction is from left to right and the 15 cluster detectors are set up at backward angles, the 26 clover modules around 90° and 30 individual Compton-suppressed germanium detectors at forward angles. The germanium crystals are drawn in orange and the BGO Compton-suppression shields are drawn in blue. This figure was taken from (Eberth & Simpson, 2008).

Cologne, Eurisys Mesure and KFA Jülich proved to solve the problems. The vacuum in the capsules is independent of the vacuum in the cryostat and the encapsulation allows to anneal the detectors to remove any neutron damage in an ordinary oven at 105° and also prevents a contamination of the detector surface if the cryostat's vacuum is broken. Similarly to GAMMASPHERE, BGO back plugs were mounted behind the germanium crystals in the cryostat. The intrinsic P/T of the cluster detector without Compton-suppression is already a high 39% and increases to 50% by using the BGO back plugs. Despite its completely different setup EUROBALL has the same full energy efficiency of $\varepsilon = 0.09$ and a comparable resolving power to GAMMASPHERE with $RP \approx 4800$. A compilation of the achievements with EUROBALL can be found in (Korten & Lunardi, 2003).

1.2.3 MINIBALL

The MINIBALL array (Eberth et al., 2001; Habs et al., 1997) was built by a Belgian-German collaboration for experiments at the REX-ISOLDE facility at CERN. It uses the same encapsulation technology and detector shape as developed for the cluster detector of EUROBALL (see sec. 1.2.2) but does not include the BGO back plugs for Compton-suppression. Another difference is the symmetric 6-fold longitudinal segmentation (through the center of each side of the

hexagon) of the germanium crystals. In the final design MINIBALL would consist of 40 detectors, 24 are currently available and arranged in 8 cryostats with 3 detectors. Figure 1.5 shows a picture of MINIBALL set up at REX-ISOLDE

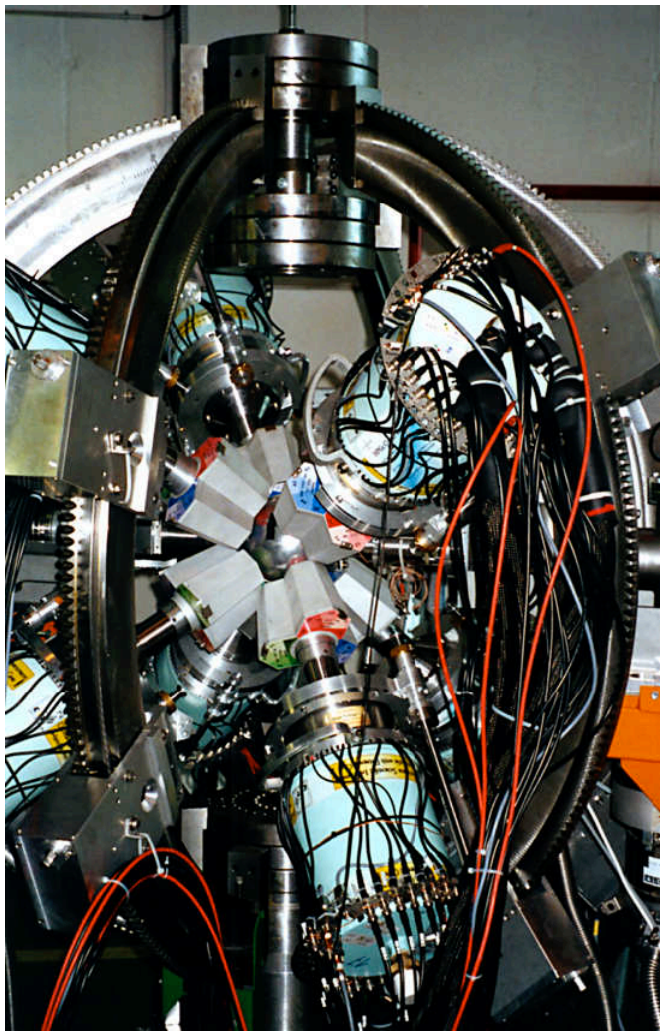

Figure 1.5: Picture of the MINIBALL array at REX-ISOLDE, CERN. This figure was taken from (Eberth & Simpson, 2008).

though it has been used at other laboratories as well. MINIBALL was also the first Ge array to use a digital processing of the preamplifier signals allowing for a simplified real time pulse shape analysis (PSA) to recover the interaction location(s) of the γ-ray. In the data analysis the energy deposits in a cluster are added back together and the assumption is made that the detector segment where the most energy was deposited contains the first interaction point along the scattering path of the γ-ray. This position is then used to correct the Doppler-shifted energy. In order to deduce the effective granularity of MINIBALL one detector

was scanned with a collimated ^{137}Cs source and the source position was reconstructed by the simplified PSA. It was shown that 16 different collimator positions could be distinguished (Eberth & Simpson, 2008) bringing the effective granularity of the full 40 detector MINIBALL setup to 4000 compared to the $170 - 240$ of GAMMASPHERE and EUROBALL. These values are confirmed by the experimentally achieved energy resolutions after Doppler correction (Eberth et al., 2001). The flexibility of the overall setup allows MINIBALL to be positioned optimally for many different experimental conditions and leads to a resolving power comparable to EUROBALL and GAMMASPHERE but without the use of Compton-suppression shields. A nice result obtained with MINIBALL at GSI is the confirmation that shell-model calculations predicting a new shell closure in ^{54}Ca correctly describe the single-particle structure in the neighboring nucleus ^{55}Ti (Maierbeck et al., 2009).

1.3 AGATA - A 4π-γ-ray Tracking Array

In order to make full use of the possibilities offered by new experimental facilities, e.g. *FAIR* and *SPIRAL2*, and also to answer open questions regarding the structure of the nucleus (see sec. 1.1) it is necessary to build a detector array with a significantly higher resolving power than the existing arrays (see sec. 1.2). As the discussion in the previous section showed such an improvement requires the simultaneous improvement of P/T, ε and ΔE_γ. The full-energy peak efficiency ε can be improved by increasing the solid angle covered by the germanium detectors. This is only possible if the Compton-suppression shields are either replaced by germanium detectors or removed and the existing detectors are moved closer to the target with the goal of obtaining a near full shell of HPGe detectors[3]. The back adding of the energies of a γ-ray Compton-scattered to adjacent detectors would also increase ε but such an event could not be distinguished from an event in which two γ-rays were detected in two adjacent detectors. The only solution to this problem found in the early stages of GAMMASPHERE and EUROBALL was to use around 1000 individual germanium detectors which was ruled out due to the associated high costs (Eberth & Simpson, 2008). Ultimately (Deleplanque et al., 1999) showed that these problems could be remedied using the concept of γ-ray tracking.

The basic idea of tracking is to reconstruct the most likely scattering path of the γ-ray within the detector using the underlying interaction processes namely the Compton scattering, pair production and the photoelectric effect. As can be seen from figure 1.6(a) the probability of each interaction type to occur is strongly dependent on the γ-ray energy and the distribution of interaction points are characteristic for each type (see fig. 1.6(b)). These characteristics are exploited

[3]The efficiency of an ideal Ge-shell ($r_1 = 12cm, r_2 = 21cm$) is $\varepsilon = 70\%$ and $P/T = 78\%$ for $M_\gamma = 1$ (Schmid et al., 1999).

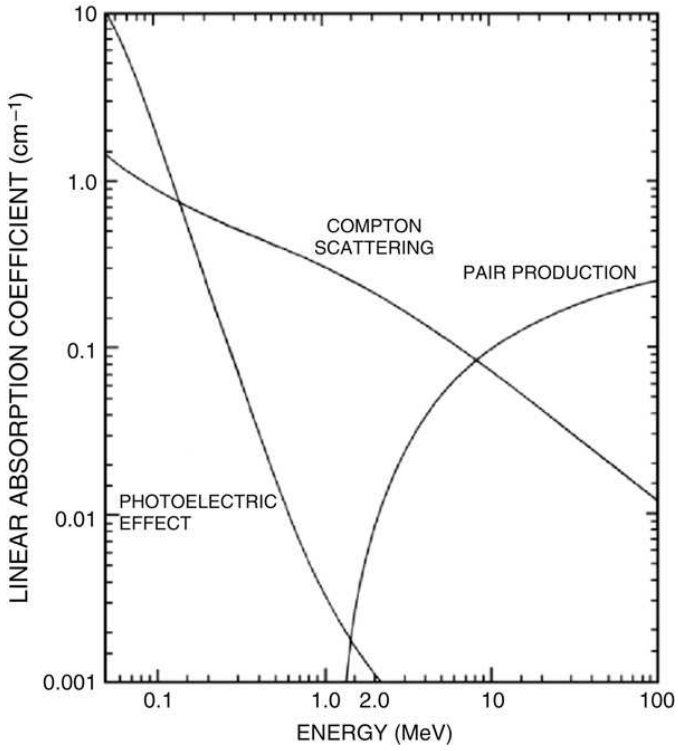

(a) Linear attenuation coefficients of the three main γ-ray interactions with germanium.

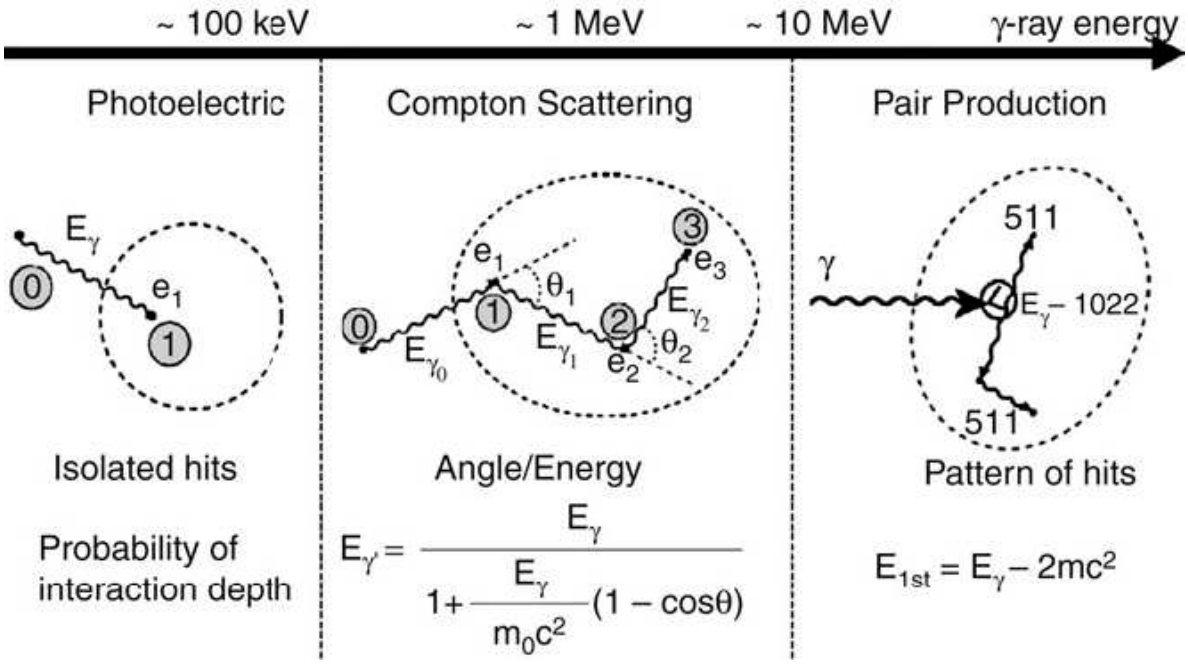

(b) The three main γ-ray interactions used for tracking.

Figure 1.6: (a)Linear attenuation coefficients of the three main γ-ray interactions with germanium and (b) a sample distribution of interactions points for each type. The tracking algorithm reconstructs the most likely scattering path of the γ-ray based on the underlying physical processes. These figures were taken from (Eberth & Simpson, 2008).

by tracking, to which there currently two distinctively different approaches. The back-tracking algorithm starts out by picking the most likely end point of the γ-ray track utilizing the fact that the most probable energy deposit of the final photoelectric interaction is in the energy range from $\sim$ $100\,keV$ to $250\,keV$. This feature was shown to be independent of the initial energy of the γ-ray (van der Marel & Cederwall, 1999). The upper limit is extended to $600\,keV$ for AGATA since close lying interaction points are packed together. Step by step further points are added to the track and checked for concordance with the event kinematics. The algorithm stops if the total probability for the scattering path reaches a certain threshold or a maximum of 5 interaction points are combined into a path. The first step of the forward-tracking algorithm (Schmid et al.,

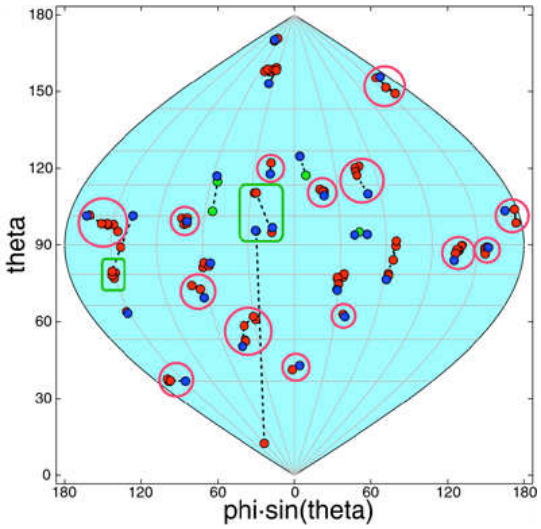

Figure 1.7: The so-called 'world map' view, used in the forward tracking, of a simulated event with 30 simultaneously emitted γ-rays of $E_\gamma = 1\,MeV$. The correctly identified clusters belonging to a single γ-ray are encircled and those wrongly combined are marked by green rectangles. This figure is taken from (Gerl & Korten, 2001).

1997) is to calculate the angular coordinates (θ, ϕ) and the angular separation of all points (see fig.1.7). These points are then assigned to several clusters, with no cluster containing more than six points and the maximum allowed angular separation being varied in steps. As the Compton scattering cross section peaks in forward direction and the mean free path of photons decreases with decreasing energy, the clusterisation procedure is justified. The initial energy of the γ-ray is taken to be the sum of all energy deposits belonging to the clustered interaction points. For all permutations of the contained points a *figure of merit* (FOM), given by the kinematics, is calculated and the ordering having the best FOM is chosen. A comparison of both approaches for AGATA showed forward tracking to be more efficient (Lopez-Martens et al., 2004). A prerequisite for both algorithms is the determination of the location, energy and time of each individual interaction point.

The precise reconstruction of these parameters is achieved by means of *Pulse Shape Analysis* (PSA) and is one major topic of this thesis (see chap. 4). The accuracy of the tracking algorithms naturally depends on the precision of PSA. Time differences between individual interaction points are only used to suppress

random background and define correlated interactions but cannot be used by the tracking algorithm. Based on simulations of such arrays the position resolution should be $< 5\,mm$ and the energy resolution $< 3\,keV$ (Schmid et al., 1999; Lopez-Martens et al., 2004). However, the performance of tracking is more dependent on the former than on the latter (Schmid et al., 1999). Since neither of the previously used detectors are capable of such a high position resolution and planar detectors having been ruled out due to an unfavorable ratio of active-to-dead material a new type of detector, the *Highly Segmented Ge detector* had to be developed. Several groups (e.g. (Vetter et al., 2000b; Vetter et al., 2000a; Kröll & Bazzacco, 2001)) contributed to the development and showed that in principle position resolutions in the range of $2 - 4\,mm$ can be obtained. Yet, a prerequisite for this is a proper understanding and simulation of the detectors response, the second major topic of this thesis (see 3). The current consensus is that 36-fold segmented closed-end coaxial n-type high purity germanium (HPGe) detectors represent the best choice for realizing a tracking array. Additionally, a tracking array has to be able to sustain high count rates since the most likely experimental conditions will feature either a high background from the radioactive ion beams or a stable beam with high luminosity, i.e. a high event rate, to also populate the weakest channels in the examined reactions.

Given the expected high costs of such an array and the highly demanding research and development to be carried out a European collaboration with the name of *Advanced GAmma Tracking Array* (AGATA) was established and the initial memorandum of understanding was signed by 10 countries in 2003. Similar developments in the USA lead to the establishment of the GRETA (*Gamma Ray Energy Tracking Array*) collaboration. The first topic to be addressed had to be the number of detectors to be used as this has a significant influence on the data rate and thus the real time requirements of the PSA and tracking algorithms. The stated goal is to cover as much of the 4π solid angle as possible with active material already ruling out cylindrical detector shapes. The question of the geodesic tiling of a sphere, i.e. with regular polygons, has already been addressed by Archimedes and the solution contains 12 pentagons and in the simplest case 20 hexagons. There are various numbers of hexagons possible and based on the results of several simulations suggesting between 100-200 detectors needed for a tracking array (Eberth & Simpson, 2008) the decision was taken that AGATA will use 180 detectors with three different hexagonal shapes (see sec. 2.1.1). These detectors will be housed in 60 identical triple clusters (3 crystals per cryostat) and the pentagonal elements will be left free for the beam line and the support structure. The inner radius of the sphere will be $23.5\,cm$ and 82% of the solid angle will be covered by the $363\,kg$ of germanium. GRETA will use 120 detectors with two different shapes housed in 30 clusters of 4 detectors each. The inner diameter of GRETA will be smaller than AGATA's leaving less space for ancillary detectors. Both collaborations will start with sub-arrays to deliver the proof of principle showing that tracking is in fact feasible. AGATA will start with the so-

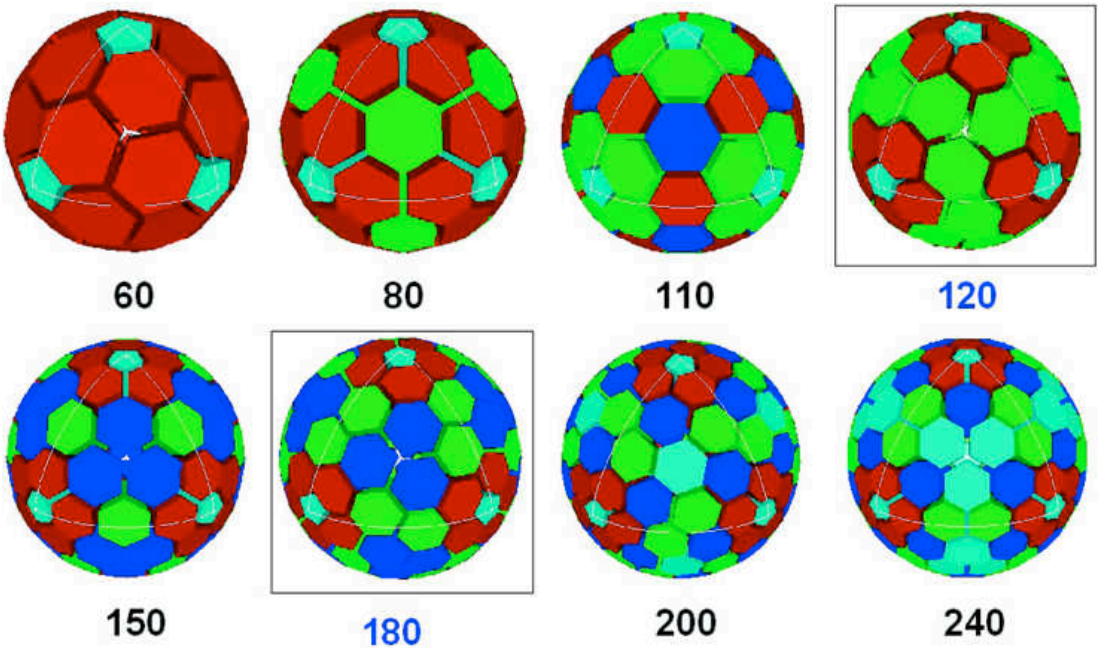

Figure 1.8: Possible geodesic tilings of the sphere. The number of pentagons remains constant at 12. This figure was taken from (Eberth & Simpson, 2008).

Array	No. Crystals	Total Granularity	$\epsilon_{FE}\,[P/T]\,(\%)$
EUROBALL III	239	239	9 [56]
GAMMASPHERE	110	∼170	9 [63]
AGATA Demonstrator	15	540	7 [7]
AGATA 4π	180	6480	43 [58]
GRETA 4π	120	4320	40 [53]

Table 1.1: A summary of the performance of current and future detector arrays for a γ-ray of $1\,MeV$ and a multilpicity of $M_\gamma = 1$.

called Demonstrator (see next chapter) consisting of 15 Ge detectors and GRETA will start with a sub-array of 30 detectors called GRETINA (*Gamma Ray Energy Tracking In beam Nuclear Array*). Table 1.1 compares the properties of AGATA

M_γ	1	10	20	30
$\varepsilon\,[\%]$	43.3	33.9	30.5	28.1
$P/T\,[\%]$	58.2	52.9	50.9	49.1
RP	$1.3 \cdot 10^6$	$3.7 \cdot 10^5$	$2.2 \cdot 10^5$	$1.5 \cdot 10^5$

Table 1.2: Summary of the predicted performance of AGATA for $1\,MeV$ γ-rays. A realistic energy resolution of $\Delta E = 3\,keV$ was assumed in the calculation of the resolving power RP.

with those of GRETA and the existing 4π arrays for $1\,MeV$ γ-rays. The AGATA demonstrator will already have a higher granularity than either EUROBALL or GAMMASPHERE and a photo peak efficiency of 7% which is close to the 9% of the existing arrays. The expected increase in ε and P/T of the tracking arrays is considerable and table 1.2 shows the resulting improvement in resolving power RP for various γ-ray multiplicities M_γ again for energies of $1\,MeV$. In these calculations a conservative energy resolution of $3\,keV$ was assumed but the remarkable point is that this resolution will be possible with velocities up to 50% the speed of light compared to the 3.95keV of GAMMASPHERE at a velocity of $0.02 \cdot c$. At $M_\gamma = 1$ the increase in resolving power is around a factor of 430 over GAMMASPHERE/EUROBALL while (Schmid et al., 1999) give an optimistic factor of around 600 for GRETA. At $M_\gamma = 30$ the resolving power will still be around 50 times higher.

1.4 Thesis Overview

The main goal of this thesis was to develop a real time pulse shape analysis (PSA) with AGATA, a basic requirement to run a tracking array. The properties and the design of the AGATA spectrometer are described in detail in chapter 2, together with the full data acquisition chain.

In order for PSA to succeed a detailed understanding of the detectors response is mandatory. While it is possible to provide an experimental signal basis through a coincidence scan of a detector, the time needed to complete such a scan, even with a rather coarse position resolution is too long. This is especially true if one considers, that all 180 detectors of AGATA would need to be scanned. For this reason a simulation of AGATA pulse shapes was developed with *JASS* (see chap. 3). After delineating the theoretical as well as the practical aspects of this task JASS is successfully checked for self-consistency (secs. 3.1-3.3.3). JASS was verified with data from a coincidence scan, with known interaction locations, of the S002 detector (sec. 3.6).

An introduction to the second main topic of this thesis, real-time pulse shape analysis is presented in chapter 4. This challenging task is split into the following two sequential parts:

- Determination of the starting time t_0 of the recorded pulse shapes.
- Reconstruction of the positions and energy deposits of the individual interactions.

The starting time t_0 can be identified independently of the position reconstruction and moreover, a predetermined t_0 facilitates the remaining PSA task considerably. Feedforward neural networks, which are introduced in section 4.2 are used for the identification of t_0, as they do not only require little computation time but also offer a predictable performance, a fact that is very important in a real-time setting as with AGATA. In order to achieve a precise position reconstruction in real-time, evolutionary algorithms offer the most promise. One such algorithm, the so called „Particle Swarm Optimization “ (PSO, sec. 4.3) provides a framework that is well suited to the problem at hand. The above presented approach is first applied to model problems in chapter 5. In chapter 6 data from a GEANT simulation of a $^{48}Ti(d,p)^{49}Ti$ reaction at $100\,MeV$ under inverse kinematics is used to assess its capabilities under realistic conditions.

Chapter 2

The Advanced Gamma Ray Tracking Array

The design of AGATA encompasses two main goals. First AGATA had to meet the requirements for a γ-tracking array (see sec. 1.3) and secondly its layout should be highly modular to allow for a stepwise completion of the array. The full 4π array will consist of 180 36-fold segmented HPGe detectors with optimized geometries (see sec. 2.1). Three of these detectors are combined into identical triple cluster detector units and run independently. One such triple cluster has 114 output channels, about equal in number to those of existing 4π arrays like Gammasphere. The complete AGATA array will hence have a total of 6840 channels, posing a considerably challenge for the data acquisition (DAQ). In order to be able to store the experimental data the DAQ has to reduce the data to usable sizes in real-time (see sec. 2.2).

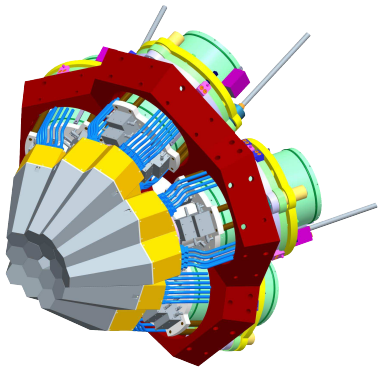

Figure 2.1: Schematic drawing of the AGATA Demonstrator. The five triple clusters are arranged in such a way that they leave a pentagonal hole for the beam line in the middle. The holding structure, shown in red, is easily expandable to allow adding further clusters once they are available. This figure was taken from (Simpson et al., 2008).

The AGATA array is being developed in several key phases:

- The AGATA demonstrator (see fig. 2.1), consisting of 5 triple clusters is currently stationed at INFN Legnaro for use with the PRISMA spectrometer (Gadea et al., 2005). After the end of the commissioning phase, and

the accompanying successful *proof of principle*, the physics campaign will commence later in 2009, using stable ion beams.

- New triple clusters will be added to the demonstrator in successive steps, once they are fully assembled and tested. It is currently planned that this evolving array will be moved to GSI/FAIR in Germany 2011/12. There AGATA will be used at the focal plane of the fragment recoil separator (FRS) to study exotic nuclei produced following high energy fragmentation. GANIL in France is a likely future host laboratory. The host laboratories offer a large variety of conditions under which AGATA will be tested, allowing one to properly assess its performance and capabilities.

- Development of the demonstrator into a 1π array, consisting of 15 triple clusters, followed by a continuous expansion to $4/3\pi$ and finally the full 4π AGATA array.

In the following the design of the AGATA components and the data acquisition system will be described in detail.

2.1 The Design of AGATA

The chosen design of AGATA aims on the one hand to fulfill the requirement of a tracking array (see sec. 1.3) while at the same time to have a setup, which features a high modularity and symmetry in terms of an arbitrary exchangeability of individual components. The full 4π AGATA array will consist of 180 electronically segmented, tapered, encapsulated n-type HPGe detectors. There are three different asymmetric hexagonal shaped geometries for the detectors which are housed in one of 60 identical triple cryostats. Each cryostat contains one detector of each shape. The resulting germanium shell is $9\,cm$ thick and has a solid angle coverage of up to 82%. The inner radius of the shell is $23.5\,cm$ providing enough space for most ancillary detectors to be mounted inside the shell.

2.1.1 The AGATA crystals

All 36-fold segmented detectors are manufactured out of coaxial HPGe crystals. Each crystal is $90 \pm 1\,mm$ long and has a diameter of $80^{+0.7}_{-0.1}\,mm$. In order for the detectors to be able to form a close packed shell with maximal solid angle coverage they have to be tapered at the front into a hexagonal shape with a tapering angle of 8°. The three different geometries used for the AGATA crystals differ only in the shape of the hexagonal front face (see fig. 2.3). Each geometry is assigned a letter and a color: A/red, B/green and C/blue. The symmetric prototype used in the R&D phase of AGATA is labeled S/yellow. The longitudinal segmentation creates segment rings of 8, 13, 15 , 18 , 18 and 18 mm width (see fig. 2.2(a)) and

the core contact has a specified diameter of 10 mm and extends up to 13 mm from the front face (see fig. 2.2(c)). The segmentation in depth has been chosen

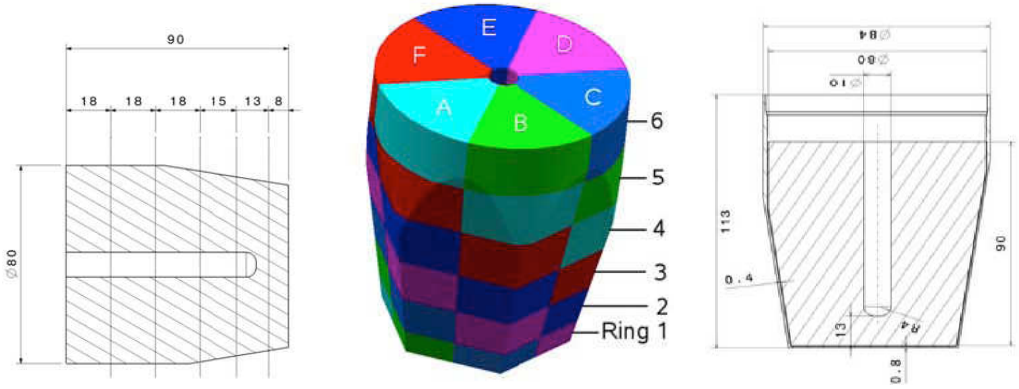

(a) The longitudinal segmentation of AGATA.

(b) The labeling scheme.

(c) Specifications for the encapsulation.

Figure 2.2: (a)The longitudinal segmentation creates six segment rings of different widths. For a nearly constant interaction probability of a γ-ray within each of the rings the width has to increase with depth. (b)The picture in the middle illustrates the labeling scheme used for the AGATA segments. (c)The AGATA crystals are encapsulated in tight fitting Al capsules, leaving only a space of 0.4 to 0.8 mm between the crystal the capsules. The core contact has a specified diameter of 10 mm and a distance of 13 mm to the front face. These figures ware taken from (Simpson et al., 2008).

to optimize pulse-shape sensitivity and to have an almost uniform distribution of the interactions (Simpson et al., 2008). The angular segmentation always goes through the middle of each flat hexagonal side (see fig. 2.3). However the segment sizes differ considerably due to the different geometries. Looking at the hexagonal front face from behind, the labeling scheme assigns each AGATA segment a letter from A through F in counter-clockwise fashion starting from the sector containing the positive x-axis and a ring number from 1 through 6 starting from the front (see figs. 2.2(b) and 2.3(a)).

Each crystal is made out of n-type HPGe material with a specified impurity concentration, or equivalently space charge concentration, between 0.4 and $1.8 \cdot 10^{10}\, cm^{-3}$. The crystals are grown in such a way that the z-axis, e.g. the middle of the core contact, is aligned with one of the three equivalent $\langle 100 \rangle$ axis. The surface of a bare germanium detector, as shown in figure 2.4(a), is very delicate. In order to facilitate the handling of these detectors they are encapsulated in a tight fitting aluminum capsule. The distance between crystal side faces and capsule walls is between $0.4 - 0.8\, mm$ (see fig. 2.2(c)). The connector feed throughs for the segments outer contacts are grouped by sectors (see fig. 2.4(b)). The core contact, used for applying the high voltage and to read out the core

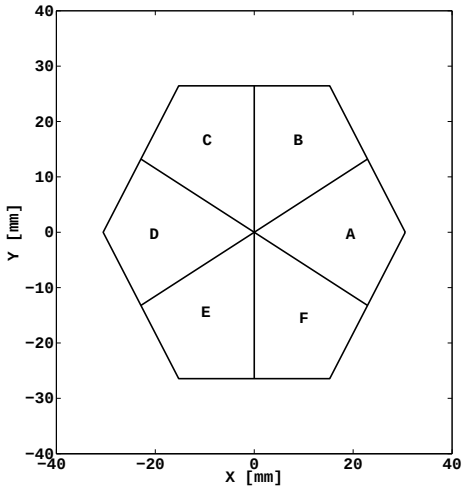

(a) Angular segmentation of the symmetric prototype.

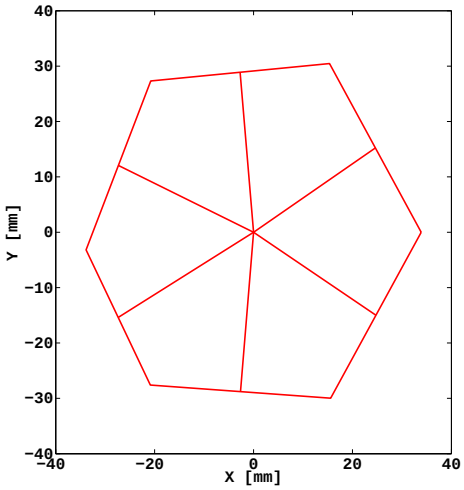

(b) Angular segmentation of the red/A type crystal

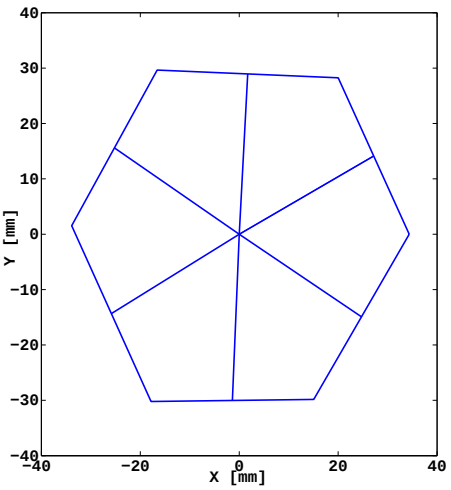

(c) Angular segmentation of the blue/C type crystal

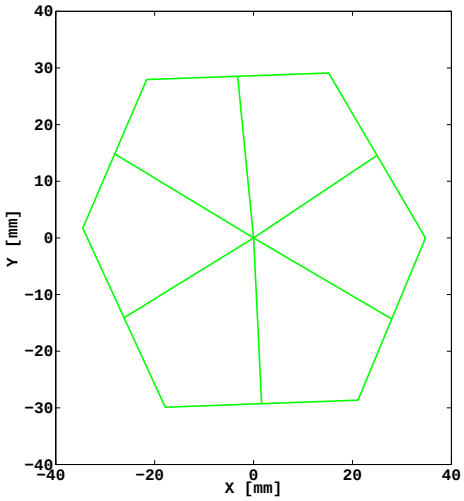

(d) Angular segmentation of the green/B type crystal

Figure 2.3: The angular segmentation schemes of all existing AGATA crystals. All segmentation lines go through the middle of each hexagons flat side faces. In order for the array to cover the largest possible solid angle three different asymmetric hexagonal front faces were necessary with the red type being the most and the blue type the least asymmetric.

(a) unsegmented AGATA crystal (b) encapsulated AGATA crystal

Figure 2.4: Picture (a) shows a still unsegmented bare AGATA crystal while in picture (b) an already encapsulated crystal, viewed from behind, is shown. The feed through for the core contact is situated in the middle and slightly elevated with respect to the six feed throughs for each segment column on the outside of the capsules back side. These figures were taken from (Simpson et al., 2008).

signal, sits in the middle of the capsules back side and is isolated by ceramics. Besides the geometrical characteristics an AGATA crystal also needs to fulfill stringent requirements in term of energy resolution (see tab. 2.1) before it is accepted by the collaboration.

Energy	Core Contact	Segment	Mean of Segments
$1.3\,MeV$	$\leq 2.35\,keV$	$\leq 2.30\,keV$	$\leq 2.10\,keV$
$122\,keV$	$\leq 1.35\,keV$	-	-
$60\,keV$	-	$\leq 1.30\,keV$	$\leq 1.20\,keV$

Table 2.1: The specifications for the energy resolutions (FWHM) of the AGATA crystals. For the segments the specifications define an upper limit for each segment individually and also for the mean resolution of all segments.

2.1.2 The AGATA cryostats

The cryostats do not only house the three AGATA crystals but also the cold and warm part of the preamplifiers (see sec. F.1), which have to be mounted close to the detectors in order to minimize noise contributions. The cold parts of the preamplifiers are operated at a temperature around 130 K where their

noise contribution is minimal, while the germanium crystals are cooled down to 90 K to prevent thermal excitations due to the small band gap of germanium (see sec. 3.1). The electric connection to the warm part of the preamplifiers, which contribute considerably less to the noise, is made using several hundred thin wires with low thermal conductivity. An electronic shielding between the various input stages ensures a small crosstalk contribution below 1‰ (see sec. 3.5.2). The detectors are thermally isolated by a vacuum with pressures less than $5 \cdot 10^{-6}\,mbar$ and the temperatures are monitored using platinum resistance thermometers (type PT100). Figure 2.5(b) shows the positioning of the three

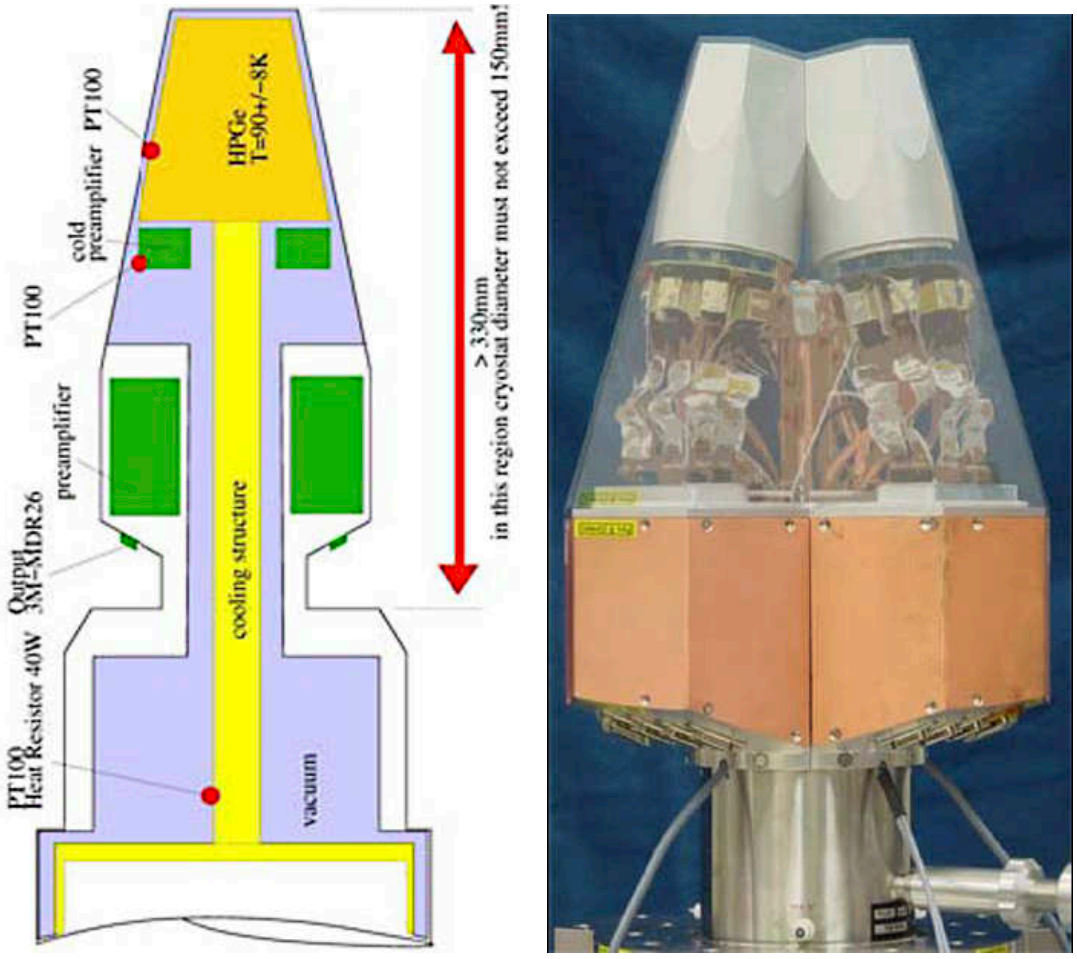

(a) Schematic drawing of the cryostat

(b) Transparent view of fully equipped asymmetric triple cluster.

Figure 2.5: (a) The positioning of the cold and warm preamplifier parts as well as of the temperature sensors is illustrated in this schematic drawing of an AGATA cryostat. (b) Transparent view of fully equipped asymmetric triple cluster. The distance between the detector capsules and the end cap of the cryostat is only $0.5\,mm$. The figures were taken from (Simpson et al., 2008).

detectors relative to the end cap, which has been rendered semi-transparent. The warm part of the preamplifiers is hidden under the copper plates. Current 4π spectrometers operated today have a total of 100 to 200 channels to be read out, comparable to the 114 channels of a single triple cryostat for AGATA.

A triple cluster unit weighs $38\,kg$ without the germanium crystals and has a length of $92\,cm$ demanding rather rigid holding structures since the clusters have to be positioned with high precision in the array. First of all because thermal conductivity between the end caps, there is a narrow 0.5mm wide spacing between adjacent end caps, has to be prevented and even more importantly to ensure an accurate tracking (see sec. 1.3). There are very low tolerances required for the manufacturing of the end caps as well, which have to stay within specifications even when bending under vacuum.

2.2 The AGATA Data Acquisition

The AGATA data acquisition (DAQ) system consists of two basic building blocks, one is hardware based comprising the detectors, preamplifiers, digitizers and the front-end electronics, and the second is software based running on PC server farms. In addition to processing and transporting the data, the DAQ is also responsible for controlling and monitoring the complete DAQ system, including all the algorithms running on the servers. This second task as well as the data handling on the server farms is carried out by the *Nouvelle Acquisition temp Réel Avec Linux*, (Grave et al., 2005), or NARVAL system. In the following the data flow, as depicted in figure 2.6, will be described and each component explained in separate sections.

The signals from the detectors are read out by charge-sensitive preamplifiers and then continuously digitized by sampling 14 bit Analog-to-Digital converters (ADC) at a rate of 100 MHz. The data rate out of each digitizer channel is 200 MBytes/sec, independent of the detectors event counting rate as 100% of the incoming signals are digitized. The front-end electronics assigns an event time and number, determines the energy depositions using the *Moving Window Deconvolution* (Georgiev et al., 1994) and extracts the useful parts, also called the leading edges, of the traces. These parts are about $6\,\mu s$ long and contain parts of the baseline, the complete rise time of the signal and parts of the exponentially decaying charge signal, recorded once all charge carriers created by the γ-ray interaction are collected. The latter takes up the most part of the extracted traces and is used by the MWD algorithm. This data package is reduced to $600\,ns$ and then sent to the PSA algorithm with data rates of up to 370 MBytes/sec. From this point on, marked by using red borders in figure 2.6, all the data is being handled on the servers. The interaction positions are then reconstructed by the PSA and the event builder merges all corresponding locations, and optionally data from an ancillary detector to form a single event. The tracking algorithm

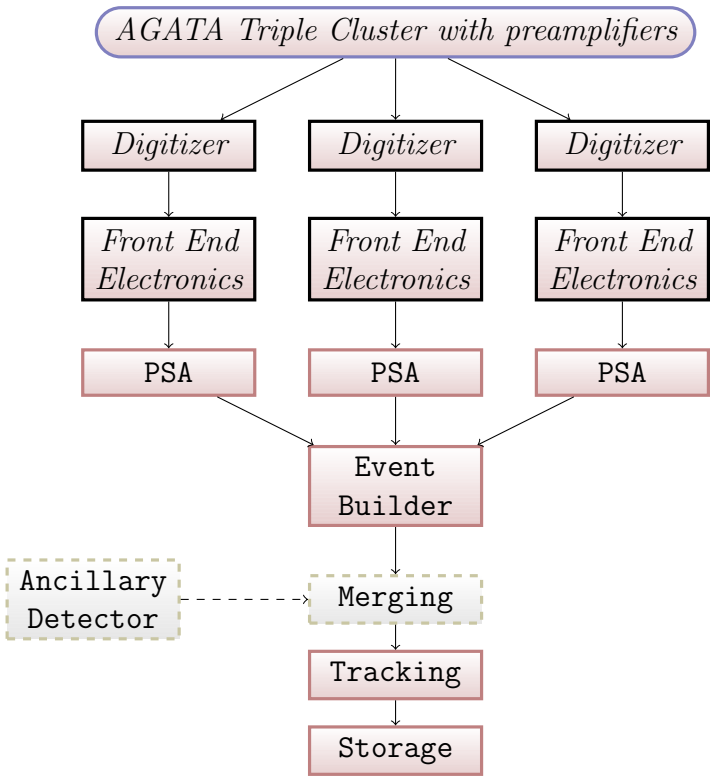

Figure 2.6: The AGATA Data Flow for one triple cluster. The preamplifiers for the signals are housed in the cryostat, together with the encapsulated crystals. The pulse shapes are then digitized and moved to the front end electronics using optical fibers. All the data is then sent to the PSA farms. The reconstructed positions in the three crystals are combined in the event builder. At this stage the data can optionally be merged with data from an ancillary detector. Finally tracking reconstructs the scattering path(s) of the γ-ray(s) and the data is stored onto mass storage devices.

then uses this information to reconstruct the most likely scattering path of the γ-ray(s). Finally the data will be stored onto a local file server before being eventually sent to a Grid Tier 1 computing center. For a more detailed description of the individual electronic components of the DAQ chain the interested reader is referred to appendix F.

Chapter 3

JASS - Simulating Agata Pulse Shapes

The basic approach to real-time pulse shape analysis (PSA) for AGATA is to search a basis set of available pulse shapes, with known interaction locations, for agreement with the experimnetal signal (see chap. 4). Hence it is imperative to have a precise knowledge of the detectors response as this directly influences the precision of the PSA. While a conventional coincidence scan can, in principle provide such a basis (Boston et al., 2007), it still takes about two months to complete for 2000 points out of the roughly 300000 needed for a basis on a 3-D grid with 1 mm steps. This is a far too long time frame considering that AGATA will consist of 180 detectors, with each one needing to be scanned. Additionally, as will be shown in section 3.6.1, the uncertainties of the scanning setup are too large to allow the production of a finely sized basis set. Therefore, an accurate simulation of the pulse shapes had to be developed. In the course of this work it became clear that the previous approach, using the *Multi Geometry Simulation* (Medina et al., 2004) suffered from inconsistencies especially at the segment boundaries. This prompted the development of JASS, the ***J****ava* ***A****gata* ***S****ignal* ***S****imulation*, in the frame work of this thesis.

In section 3.1 an introduction into the field of simulating pulse shapes is given. The peculiarities regarding germanium and the novel methods employed by JASS are discussed in sections 3.2 and 3.3. The electronic response functions and the detector specific influence on the signal shape due to crosstalk, needed before any comparison with experimental signals can take place, are presented in section 3.5. Finally, in section 3.6 the JASS calculations are verified using experimental data from a simple pencil beam as well as data from a coincidence scan with known interaction locations. The chapter closes with an outlook and discussion in section 3.7.

3.1 Simulation of HPGe Pulse Shapes

Given an interaction at position $P(x, y, z)$ within the germanium crystal a certain number of electron-hole pairs are created. However, these pairs are not created directly by the γ-ray but by the asociated Compton-/photo electron, or from e^+e^- pair production, which has a mean free path length of about $1\,mm$ at $1\,MeV$. While the band gap of germanium is $0.74\,eV$ at $90\,K$ it takes on average $2.96\,eV$ to create an electron hole pair due to the competing process of exciting lattice vibrations. Hence for a $1\ MeV$ interaction around $3.4 \cdot 10^5$ electron-hole pairs are created. In contrast to the charge clouds of electrons and holes in reality, a simulation assumes point-like charge carriers. This is justified, as in large volume detectors the expansion of the charge clouds, due to space charge, is negligible (Medina, 2006). For n-type germanium, like the AGATA crystals the holes (h) are drifting to the outer electrodes while the electrons (e^-) are collected at the central core contact (Knoll, 1999). The only observables of this event are the charge signals $Q_i(t)$ induced by the moving charge carriers $q_{e/h}$ on the electrodes i. This raises the two following questions:

- How do the charge carriers $q_{e/h}$ move through the crystal?
- What signals $Q_i(\overrightarrow{r_{e/h}}(t))$ are induced at the electrodes i?

Each part of the problem can be treated separately by using a quasi steady-state approximation. First, the assumption is made that the momentary electric fields are in electrostatic equilibrium, which is justified as the speed of the charge carriers $\sim 10^7 cm/s$ is small compared to the speed of light in germanium $c_{Ge} = 750{\cdot}10^7 cm/s$. Additionally, it is assumed that the perturbation to the electric field $\vec{E}$ inside the crystal, caused by the presence of the charges $q_{e/h}$ has a negligible influence on the charge carriers movement.

The trajectories of the charge carriers therefore are solely influenced by $\vec{E}$ and the crystal structure (see sec. 3.2), reducing the problem to electrostatics. The calculation of the electric field is a problem of mostly practical nature and is delineated in section 3.2.2. The effect of the crystal orientation on the charge carriers trajectories, however does take some theoretical understanding. It is owing to the band structure of germanium, resulting in an anisotropy of the drift times. Moreover this anisotropy is different for electrons and holes. The models describing this behavior can be found in the literature and are summarized in sections 3.2.3 and 3.2.4. As pointed out in detail in section 3.2.1, a precise description of the detectors geometry is also vital for a successful simulation.

Since the electric fields are considered to be in equilibrium the charge signals at time t are dependent on the momentary position of the charge carriers $\vec{r}(t)$ only. Under this assumption the calculation of the pulse shapes (see sec. 3.3) can be greatly simplified as the Shockley-Ramo theorem, described in section 3.3.1 is applicable. But the multitude of electrodes in a highly-segmented detector

brings about a high variability in the pulse shapes. Thus the limited precision of a numerical solver must be enhanced by a precise interpolation method (see sec. 3.3.3).

3.2 Calculating the Trajectories

In order to calculate the trajectories of the charge carriers the velocity vector of their motion through the crystal must be determined. The general relation between the drift velocity $\overrightarrow{v_d}$ and the electric field $\vec{E}$ is quite simple and given by:

$$\overrightarrow{v_d} = \pm\mu(|\vec{E}|) \cdot \vec{E} \tag{3.1}$$

with the mobility μ, which is influenced by the crystal structure. The minus sign is used for electrons to make them flow in the opposite direction of the applied electric field.

It is therefore necessary to understand how the crystal structure of germanium is affecting the mobilities of the charge carriers. The scalar behavior of the mobility in equation 3.1 only holds at low fields though. Once the fields become too strong the mobility is turning into a tensor $\boldsymbol{\mu}(|\vec{E}|)$. Only then it is influenced by the band structure of germanium. This influence is best described using the reciprocal lattice vectors $\vec{k}$. In semiconductors the charge carriers occupy the optima or band edge of the respective band structure. In the simple case of a non-degenerate band structure and the band edge being at the center of the Brillouin zone a strictly parabolic relationship between the energy ϵ and the wave vector $\vec{k}$ results (see (Conwell, 1967) p.49)

$$\epsilon(\vec{k}) = \frac{\hbar^2 k^2}{2m}, \tag{3.2}$$

with m the *effective mass* of the charge carrier, typically differing from the free electron mass m_0. In this case one observes an isotropic distribution of drift times as the drift velocity of a single charge carrier is related to $\epsilon(\vec{k})$ through the following equation:

$$\vec{v}(\vec{k}) = \frac{1}{\hbar}\overrightarrow{\nabla_k}\epsilon(\vec{k}). \tag{3.3}$$

It should be noted that the isotropy of the drift velocities is independent of the distribution of $\vec{k}$-states for all charge carriers. Germanium, by contrast to this simple picture, has a so-called many valley band structure with the charge carriers either occupying many equivalent valleys in the case of electrons or a twofold degenerate band in the case of holes. One resulting feature is that the current need not be parallel to the applied electric field. First experimental evidence of this was reported by (Sasaki & Shibuya, 1956). As presented later, the observed anisotropies of the drift velocities can all be understood in terms of deviations of

the $\epsilon - k$ relationship from eqn. 3.2. Since these deviations are different for the conduction and the valence band one needs distinct models for both cases.

As pointed out earlier, the internal crystal fields are neglected and all anisotropies are covered by the mobility model. So all it takes to calculate the electric field is to solve the Poisson equation. In order to be able to represent the boundary conditions of the Poisson equation accurately an equally accurate description of the crystals geometry is needed and for reasons detailed in section 3.2.1 it is advantageous not to drop this precise information after the Poisson equation has been solved.

3.2.1 Description of the Geometry

An easy way to describe an extended object for a computer program is to use a regular grid of points and each one being labeled as either outside or inside the object. For a given interaction location in the crystal point-like charge carriers are drifted according to the electric field and equation 3.1. Yet, as the electric field and the detector boundaries are only available in the precision of the finite grid it is likely that the charge carriers would drift into unphysical regions and not stop at the correct boundary. Also, chances are that the hit segment for an interaction location will be wrongly identified if the end point of the trajectory is in close vicinity of the unresolved segment boundaries. A fine enough grid to prevent this would most certainly need excessive computing resources.

JASS takes another approach to define the geometry and explicitly uses the equations used for manufacturing the crystals and an adequate model for the core contact. The shape of the latter is modeled as a cylinder with a spherical end and its tip being 13 cm from the front face of the crystal. It's characteristic radius is $R_{core} = 5.5\,mm$. A 2D cut of the crystal definition is shown in figure 3.4.

The surface of each AGATA crystal, however, has a rather irregular shape. The front part of a crystal is hexagonal while the back part is coaxial with an intermediate stage in between. Despite this irregularity a description with numerical precision is rather easily achieved. The coaxial contribution is modeled as a cylinder with radius $R_c = 40\,mm$ and depth $d_c = 90\,mm$. The hexagonal part is defined by the intersection of six planes, which are tilted away from the z-axis. Each plane is given by two pairs of points defining the straights of intersection with its neighboring planes. The surface of the crystal defines a set of points either on one plane or the cylinder, whichever is closest to the z-axis. The transition area from the hexagonal to the coaxial structure is defined by the conic sections of the planes with the cylinder. As an example the resulting shape for the symmetric AGATA prototype is shown in figure 3.1.

To enable the simulation to stop the charge carrier at the correct boundary a criterion must be formulated to determine, with numerical precision, whether a point $P(x, y, z)$ is inside or outside the crystal. So it has to be shown that P is

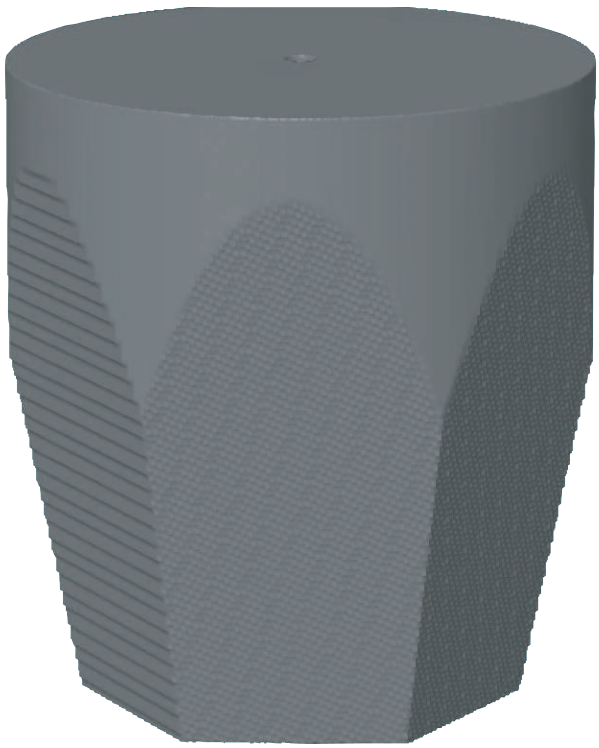

Figure 3.1: This figure shows the surface of the symmetric AGATA prototype crystal as it is reproduced by JASS. One can clearly see that the front part is hexagonal while the back areas are coaxial. The line of intersection for any of the six planes with the cylinder, defining also the transition from the hexagonal to the coaxial geometry is a conic section with hyperbolic shape.

inside the cylinder and at the same time on the same side of each plane as the origin point $P(0,0,0)$. In the case of the cylinder this is trivial as only the radial position of P and $0\,mm < z < 90\,mm$ has to be checked . Concerning the planes it is best to write the plane equations in Hesse's Normal Form (see app. C) as then the distance δ of the point P from the plane is calculated by:

$$\delta = x\cos\alpha + y\cos\beta + z\cos\gamma - p. \tag{3.4}$$

The angles α, β and γ define the direction of the plane's normal vector and p is it's distance to the origin. For a negative δ the point is on the same side of the plane as the origin (see e.g. (Bronstein, 2000), pp. 221). A test charge therefore reaches the boundaries of the crystals active volume if it either reaches the core contact or the outside, as described above. Hence the point $P(x,y,z)$ is inside the active volume of the crystal as long as the following conditions are met:

$$\begin{aligned}
\delta &< 0 \;\forall \text{ planes} \\
\sqrt{x^2+y^2} &< R_c \\
0 \le z &\le d_c \\
\sqrt{x^2+y^2} &\ge R_{core} \text{ for } z > 18.5 \\
\sqrt{x^2+y^2+(z-18.5)^2} &\ge R_{core} \text{ for } 13.0 \le z \le 18.5
\end{aligned} \tag{3.5}$$

Using this model the test charges are stopped within less than 10 μm of the true

boundary [1] enabling the simulation to correctly identify the hit segment within the accuracy of the trajectory.

3.2.2 Calculation of the Electric Field

As pointed out in the introduction the most important component necessary to calculate the trajectories of the electrons and holes is the electric Field $\vec{E}(\vec{r})$. The electric field can be obtained by solving the Poisson equation for the potential $\Phi(\vec{r})$ under adherence to the boundary conditions, precisely defined at the location of the electrical contacts:

$$\nabla^2\Phi(\vec{r}) = -\frac{\rho(\vec{r})}{\varepsilon_0\,\varepsilon_r} \tag{3.6}$$

with parameters space charge distribution $\rho(\vec{r})$ and the dielectric constant of germanium $\varepsilon_r = 16$. The electric field is simply given by the gradient of $\Phi(\vec{r})$.

Due to the complex geometry, however, there is no analytical solution to the Poisson equation for the AGATA crystals, leaving numerical methods as the only option. Hence the problem is discretized on a regular rectangular grid with a grid size still to be determined. This choice of grid type is related to the choice for an iterative finite difference algorithm (see app. D) to solve the equation. This class of algorithms uses the finite difference quotient (see app. D.1) to approximate the left hand side of equation 3.6 and solves the resulting equation for the potential $\Phi(\vec{r})$. The time for the algorithm to converge is not a constraint on the algorithm as the electric field has to be calculated only once per crystal. While there are faster converging methods available, JASS employs the Red-Black Gauß-Seidel algorithm (see (Trottenberg et al., 2000), p. 31 and app. D.2.1) for its ease of use and memory efficiency. Before the algorithm starts the grid is split into odd and even indexes[2] since only the values from the even indexes are needed to update the odd indexes and vice versa. This is evident by using central difference approximation to the to the left hand side of equation 3.6 and solving for $\Phi(x, y, z)$ (see app. D for details):

$$\begin{aligned} \Phi^{i+1}(x,y,z) &= \frac{\varepsilon_0\,\varepsilon_r(\Sigma\Phi^i_x + \Sigma\Phi^i_y + \Sigma\Phi^i_z) + \rho_{x,y,z}\,\Delta r^2}{6\,\varepsilon_0\,\varepsilon_r} \\ \text{with } \Sigma\Phi^i_x &= \Phi^i(x+1,y,z) + \Phi^i(x-1,y,z) \text{ and accordingly for y,z} \end{aligned} \tag{3.7}$$

and the grid size Δr.

At every iteration i the odd indexes are being updated first so that their values from iteration $i+1$ can be used to update the values of the even indexes. Without this ordering of grid points two copies of the grid would have to be kept in

[1] The precision naturally depends on the time step Δt used in the discretization of the trajectory calculation. JASS uses time steps of $0.1\,ns$ (see sec. 3.4).

[2] These are called the red and black points in reference to the two colors on a roulette wheel.

memory, one for the current values from iteration i and one to store the new values of iteration $i+1$. The solver has converged once the changes from one iteration to the next are below a given threshold for every grid point.

At this point the size of grid steps necessary to solve the Poisson equation with a certain accuracy has to be determined. In order to achieve this task a test case with a known analytical solution is required. The core weighting potential (see sec. 3.3.1 for details) of a true coaxial detector is such a test case which also offers a geometry that is at least in parts similar to the AGATA detectors. The potential is given by

$$\psi_0(\vec{r}) \;=\; 1 - \ln\left(\frac{r}{r_{min}}\right) / \ln\left(\frac{r_{max}}{r_{min}}\right) \tag{3.8}$$

While it is clearly advantageous to use a cylindrical grid for a true coaxial detector, as the potential has only a radial dependency the situation is different for the AGATA crystals. Their shape is dominated by the hexagonal structure defined by the six planes (see fig. 3.1) making a rectangular grid better suited to the problem. The core contact is placed in the center of the grid for both cases. A grid spacing of $0.5\,mm$ suffices to have a relative error smaller than 1% in the test case, confirming previous reports for the MINIBALL spectrometer (Bruyneel et al., 2006a).

Due to the absence of space charge in the test case, it is easier to calculate within a certain margin of error. Yet, in reality the electric potential is strongly influenced by the impurity concentrations in the germanium crystal making an appropriate model of their distribution a necessity. Figure 3.2 shows the average space charge densities as a function of depth within the detector, as provided by the manufacturer. According to current knowledge only the values at the boundaries at $z = 0\,mm$ and $90\,mm$ are measured and the intermediate values are interpolated linearly, explaining the observed perfect linearity. However, positive and negative slopes for the different crystals are observed. This is associated with the fact that the higher the space charge density the higher the electric field necessary for a full depletion of the detector. In the case of higher average impurity concentrations only a decrease with depth can ensure full depletion at the nominal core voltage of $5\,kV$ since the highest fields can only be found in the front part of the detector, especially at the tip of the core contact. Assuming reasonably that the impurity concentration at $r = 0$ also varies linearly with depth, coupled with the assumption of cylindrical symmetry as in (Bruyneel et al., 2006b) the distribution is fully characterized by four numbers. For the S002 symmetric prototype detector these are the following (in $10^{10} \cdot cm^{-3}$):

$$\begin{aligned} \rho(r=0, z=0) &= 2.0 \qquad & \bar{\rho}(z=0) &= 1.8 \\ \rho(r=0, z=90) &= 1.0 \qquad & \bar{\rho}(z=90) &= 0.51 \end{aligned} \tag{3.9}$$

There are two noteworthy points about the resulting distribution, displayed in figure 3.3 at $x = 0$. First of all the highest local space charge densities are all

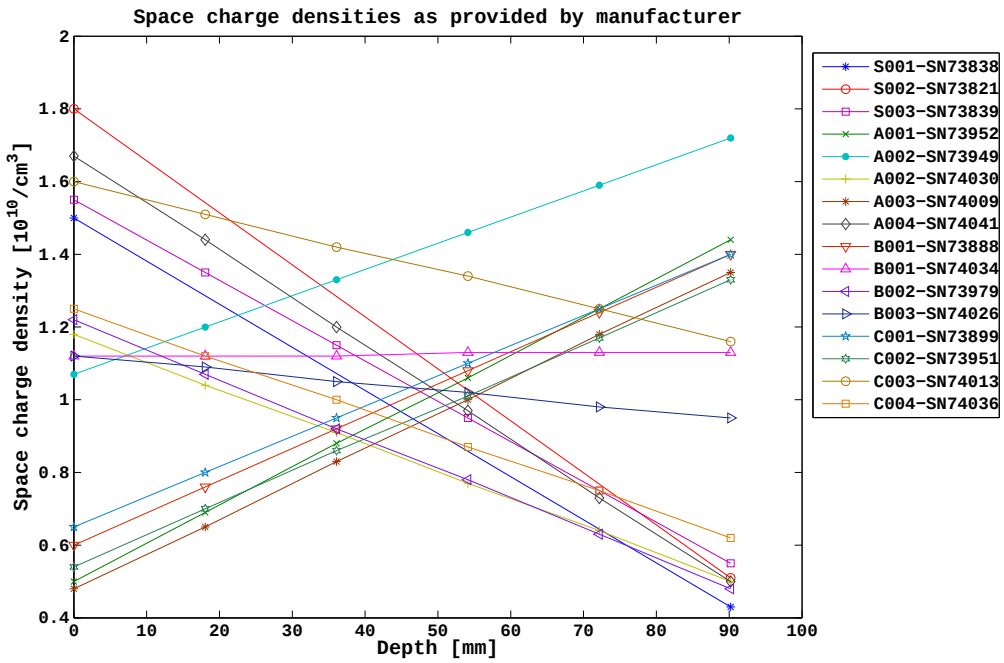

Figure 3.2: The impurity concentrations for several AGATA crystals, as provided by the manufacturer are plotted as a function of depth (z-direction) within the detector. The concentrations either increase or decrease linearly with depth.

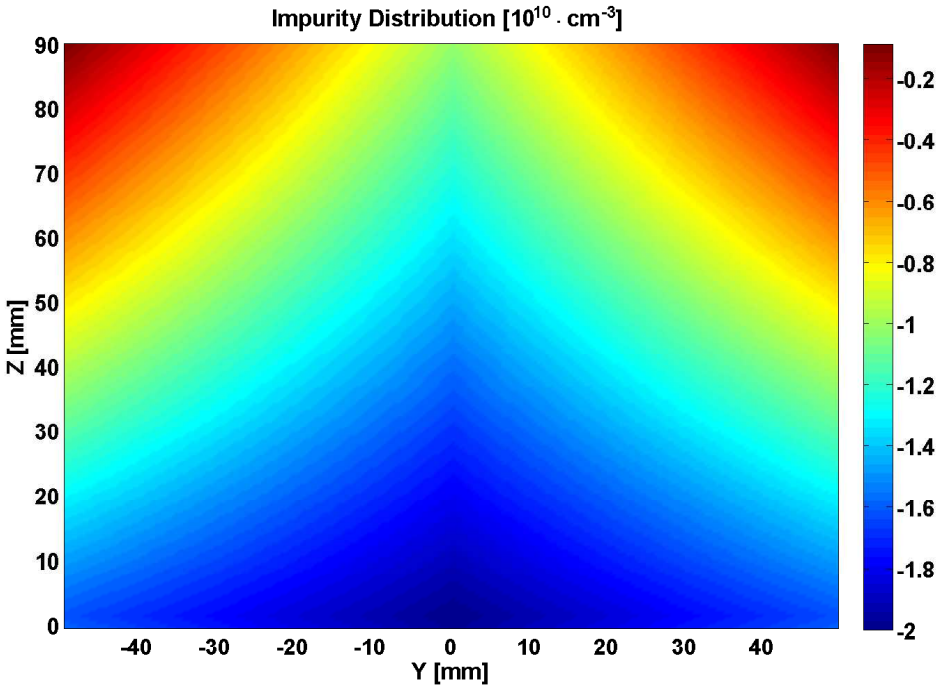

Figure 3.3: The distribution of space charge density for the S002 prototype detector at $x = 0$. Even though the distribution has only a linear dependency on the depth and the radius, the lines of equal impurity concentration show a clear curvature. This can be traced back to the fact that also the slope of the radial distribution changes linearly with depth.

located in the center of the crystal, being either in front or just next to the core contact tantamount to a negative slope for the radial dependency. Secondly the lines of equal density are not straight but show a curvature due to the 2D linear change.

The only remaining issue is the question of correct boundary conditions. The segmentation lines have widths of the order of $\sim 100\,\mu m$ and are therefore neglected in the further discussion. Thus there are just two different types of boundaries of the detector namely the surfaces of the segment and core electrodes as well as the passivated layer at the back. According to (Mihailescu, 2000) the latter can ideally be considered as an electrostatic mirror, so homogeneous von-Neumann boundary conditions are applicable:

$$\nabla\Phi(\vec{r}) \cdot \overrightarrow{n(\vec{r})} = 0 \quad \forall\, \vec{r} \in \partial\Omega_{back} \tag{3.10}$$

with the normal vector $\overrightarrow{n(\vec{r})}$ and the surface area of the passivated layer $\partial\Omega_{back}$. Equation 3.10 ensures that the equipotential lines end up perpendicular to the passivated backside. Dirichlet boundary conditions are used for the electrodes:

$$\begin{aligned} \Phi(\vec{r}) &= 5000\,V \quad \forall\, \vec{r} \in \partial\Omega_{core} \\ \Phi(\vec{r}) &= 0\,V \quad \forall\, \vec{r} \in \partial\Omega_{segment} \end{aligned} \tag{3.11}$$

with the surface area $\partial\Omega_{core}$ of the core and $\partial\Omega_{segment}$ of the segment electrodes, respectively. The electric potential as calculated by JASS for the S002 detector is pictured in figure 3.4 for a cut at $y = 0$. There are two features that strike the eyes. First, high gradient changes of the potential in front of the core contact can be observed. These are simply due to the short distance to the outer electrodes with just $13\,mm$. There are no areas with a comparable high gradient in the test case and thus in this region a limited precision of the numerical solution can be expected. Additionally, the electric field lines in this region have a strong curvature leading to equally curved trajectories of the charge carriers and consequently to effective segment sizes differing considerably from their physical dimensions (see fig. 3.5). Another observation is the slight warping of the equipotential lines which can be attributed to the impurity distribution and the geometry of the detector. The presence of a space charge pushes the equipotential lines closer to the outer electrodes in a manner that is proportional to the local density. This explains the warping when seen in conjunction with the increasing distance between the core contact and the outside of the crystal in the hexagonal part of the detector. The distance between a given equipotential line and the central electrode decreases with depth, as does the impurity concentration when taken relative to the aforementioned distance.

3.2.3 Mobility of Electrons

The second important ingredient to calculate the signal shape is the mobility of the charge carriers (see 3.1). The fact that the electron's drift velocities within

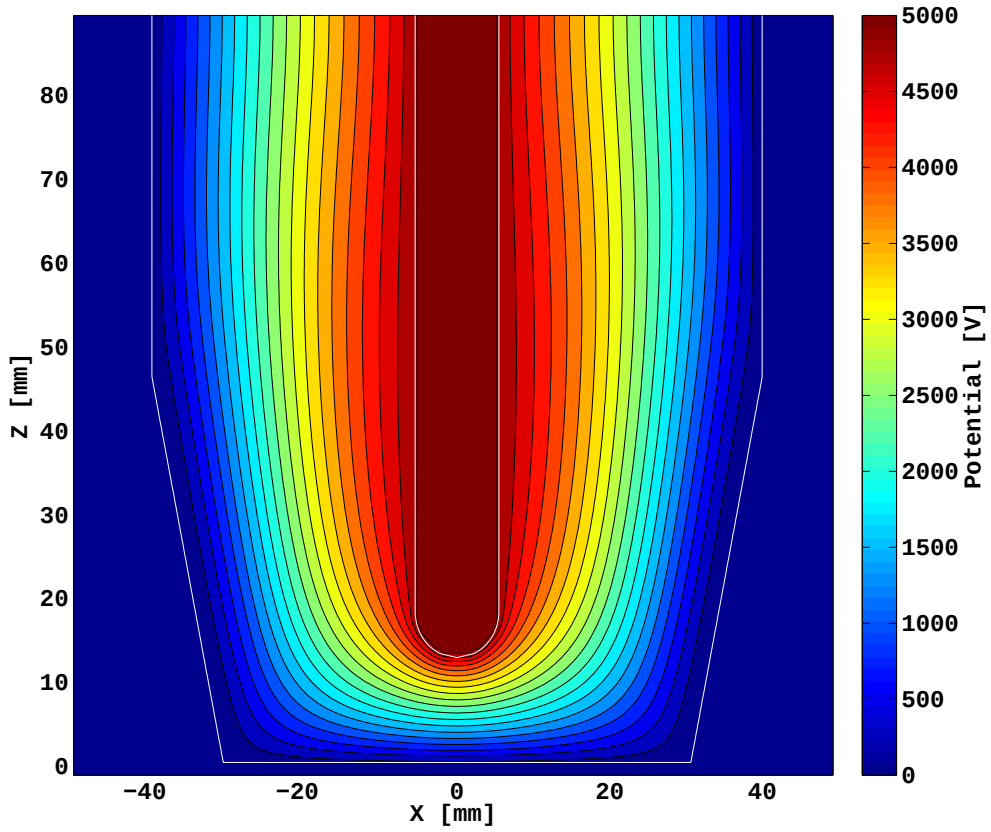

Figure 3.4: Plot of the electric potential inside the S002 AGATA crystal at $y = 0$. The boundaries of the electrodes are marked in white and the black contour lines indicate steps of 250 V. The strong gradient of the potential in front of the core contacts tip is easily noticed. This is a likely source of errors which are possibly larger than those observed in the test case. The apparent warping of the equipotential lines is due to an interplay of the detectors geometry and the model of the impurity distribution.

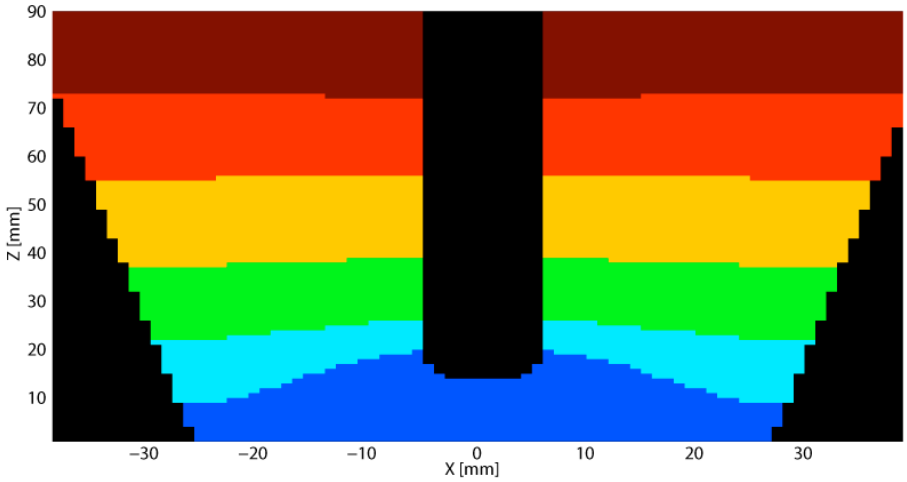

Figure 3.5: The effective segmentation of the yellow AGATA crystal. Due to the curved electric field in the front the charge carriers do not drift horizontally to the nearest electrode but to electrodes further to the front. The effective segment sizes for each row are indicated by different colors with blue showing all locations for which the holes are collected in the first row, cyan for those collected by the second row segments and so forth.

germanium feature an anisotropy has long been established. (Nathan, 1963), for example, found that at $77K$ and low fields, $\sim 100\,V/cm$, the drift velocities of electrons in $\langle 100 \rangle$ direction can be as much as 60% larger than in the $\langle 111 \rangle$ direction. At higher fields of around $10000\,V/cm$ though this anisotropy is reduced to 15%. These results can be understood in terms of an anisotropy of the effective masses and looking at the ϵ-k relation (eqn. 3.12). In germanium the minima of the conduction band are situated on the intersections of the Brillouin zone with the four equivalent $\langle 111 \rangle$ directions. Each of the corresponding eight valleys has a half ellipsoidal shape. A fact that becomes clear when looking at the $\epsilon - k$ relation, written in the principal axis system of one such ellipsoid. It is then given by (Conwell, 1967):

$$\epsilon(\vec{k}) = \frac{\hbar^2 k_x^2}{2m_x} + \frac{\hbar^2 k_y^2}{2m_y} + \frac{\hbar^2 k_z^2}{2m_z} \tag{3.12}$$

with $k_{x,y,z}$ measured from the valley minimum. Considering the y-axis to be the axis of revolution, $k_y \geq 0$ results and the effective masses can be written as $m_y = m_l$ and $m_x = m_z = m_t$. Reported values (Mihailescu et al., 2000) are $m_l = 1.64\,m_0$ and $m_t = 0.0819\,m_0$. This anisotropy of the effective masses leads to the ellipsoidal shape of the valleys and the anisotropy in the mobility. Figure 3.6 shows the ellipsoidal equal energy surface for one valley as given from the above description.

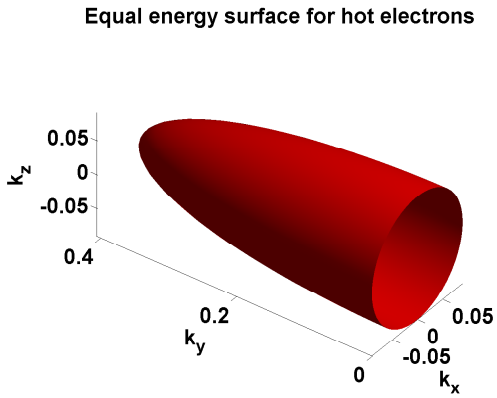

Figure 3.6: The equal energy surface for hot electrons revealing the ellipsoidal shape of the valleys. The y-axis has been aligned with the ⟨111⟩ direction and the boundary of the Brillouin zone is at $k_y = 0$. Comparing equations 3.2 and 3.12 it can be concluded that the ellipsoidal shape is solely due to the difference in effective masses.

To facilitate the analytical model the assumption is made that solely the ⟨111⟩ valleys are populated (Reik & Risken, 1962) and a primitive cell is chosen in which the half ellipsoids sitting on the same axis, but at opposite sides of the Brillouin zone, are joint together (Ashcroft & Mermin, 1976). Transforming the wave vector $\vec{k}$ linearly by $\vec{k}^* = \alpha_i^{1/2}\vec{k}$, with the electron effective mass tensor α_i the ellipsoids, in each of the four remaining valleys become spheres. Using the rotation matrix R_i to align the principal axis of the $i-th$ valley with the y-axis of the lab system the tensor is given by

$$\alpha_i = R_i^T \cdot \begin{pmatrix} m_t^{-1} & 0 & 0 \\ 0 & m_l^{-1} & 0 \\ 0 & 0 & m_t^{-1} \end{pmatrix} \cdot R_i \tag{3.13}$$

To preserve the vector relations the electric field and the drift velocities need to undergo similar transformations. The former translates just as $\vec{k}$, $\overrightarrow{E_i}^* = \alpha_i^{1/2}\vec{E}$, the drift velocity however transforms differently with $\overrightarrow{v_i}^* = \alpha_i^{-1/2}\overrightarrow{v_i}$ (see eqn. 3.3). Equation 3.1 can then be used in $\overrightarrow{k_i}^*$-space as the valleys take on a spherical shape and the drift velocities become isotropic (Conwell, 1967; Reggiani et al., 1985)

$$\overrightarrow{v_i}^* = -\mu^*(E_i^*)\overrightarrow{E_i}^*. \tag{3.14}$$

The mobility μ^* depends only on the amplitude of the effective field strength E^*. From the above equations the total drift velocity $\overrightarrow{v_d}$ in $\vec{k}$-space can be calculated as the weighted average of each valleys drift velocity $\overrightarrow{v_i}$

$$\overrightarrow{v_d}(\vec{E}) = -\sum_{i=1}^{4} n_i \cdot \mu^*(E_i^*) \cdot \alpha_i \overrightarrow{E_i} \tag{3.15}$$

with n_i the relative valley population $\left(\sum_{i=1}^{4} n_i = 1\right)$.

Figure 3.7 shows the distribution of the electron drift times in the coaxial part of a symmetric AGATA detector for two different crystal orientations. All

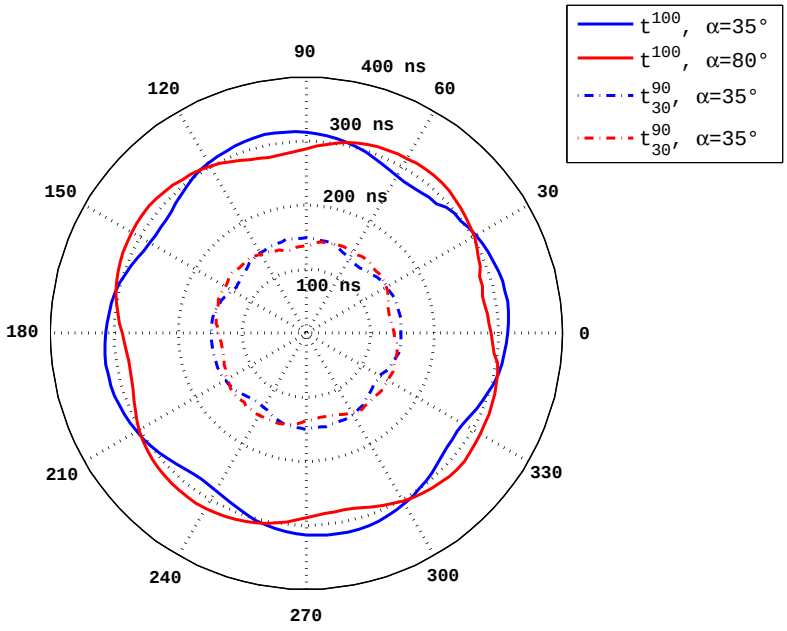

Figure 3.7: The t^{100} (solid) and t^{90}_{30} (dashed) drift times of electrons in the coaxial part of a symmetric AGATA detector for two different orientations of the crystal axis. The angle α is the angle between the x-axis in the lab system and the first $\langle 100 \rangle$ axis. A simple rotation by $\Delta\alpha$ of one distribution makes it coincide with the other. The drift times themselves seem to oscillate around an isotropic distribution.

interactions were located at the boundary of the detector, equivalent to an immediate collection of the holes and only the electrons drifting through the detector. The solid lines depict the time needed for 100% charge collection, or t^{100}, and the dashed lines show the time passed between 30% to 90% charge collection, or t^{90}_{30}. In this specific case t^{100} also corresponds to the electron drift time. For the blue curve the angle α between the first $\langle 100 \rangle$ axis and the x-axis in the lab system is 35° and 80° for the red curve. A rotation by 45°, the difference in the crystal orientation, makes the two distributions coincide. The anisotropy of the distributions is clearly visible for both t^{100} as well as for t^{90}_{30}. The distributions seemingly oscillate around an isotropic form, for the latter the amplitude of the oscillations is naturally smaller.

3.2.4 Mobility of Holes

(Reggiani et al., 1977) first reported the anisotropy of the drift velocity of holes in germanium. They observed a drift velocity v_{d100} in $\langle 100 \rangle$ direction that is as much as 34% larger than in the $\langle 111 \rangle$ direction. Their theoretical model, however, relied on Monte Carlo techniques not feasible for use in a simulation of pulse shapes. A usable model is presented in (Bruyneel et al., 2006a) together with the necessary approximations. The basis of this model will be outlined in the following and the practical details are summarized in appendix B.2.

The maximum energy in the valence band can be found at the center of the Brillouin zone. In this area the band structure is twofold degenerate with a light hole ($0.04\, m_0$) and a heavy hole band ($0.30\, m_0$) (Conwell, 1967). Owing to its larger density of states the heavy-hole band is considerably stronger populated (96%) than the light-hole band. The latter also has a close to parabolic dependence of the energy on the wave-vector and hence only contributes an isotropic drift term to the overall drift velocity. It is therefore justified to neglect the light holes and only consider the heavy holes. This is also backed by experimental results (Reggiani et al., 1977).

In the model the heavy holes are assumed to be trapped in a so called *streaming motion*. The holes are accelerated by the external electric field until their energy is large enough ($0.037\, eV$) for scattering off an optical phonon. Afterward the holes can be found again near the $k = 0$ region and the process starts over again. Given the results from (Pinson & Bray, 1964) and (Alba & Paranjabe, 1964) this is a reasonalble picture of hole movements in germanium. For field strengths in the range of 130-2150 V/cm, the correct order of magnitude for AGATA, it is observed that a *drifted Maxwellian* distribution is in good agreement with the experimentally measured distribution of wave vectors for heavy holes. This distribution takes the form (Conwell, 1967)

$$f(\vec{k};\vec{k_0}) \;=\; a \cdot \exp\left(-\hbar(\vec{k}-\vec{k_0})^2/2mk_bT_h\right) \tag{3.16}$$

with a normalization constant a and the effective mass m of the heavy holes. The mean wave vector is $\vec{k_0}$ and the temperature of the holes is T_h. In the model of streaming motion it is safe to assume $\overrightarrow{k_0}(k_0, \theta_0, \phi_0)$ to be aligned with the electric field. While one might suspect that this rules out any anisotropy because of the symmetric nature of the distribution, it is the energy dependence $\epsilon(\vec{k})$ of heavy holes in germanium that gives rise to the anisotropy (see (Reggiani et al., 1977; Reggiani et al., 1985)):

$$\epsilon(\vec{k}) \;=\; A \cdot \frac{\hbar^2 k^2}{2m_0} \cdot [1 \;-\; q(\theta, \phi)]\,. \tag{3.17}$$

θ and ϕ are the azimuthal and polar angles of $\vec{k}$ with respect to the frame defined by the three $\langle 100 \rangle$ axis and $A = 13.35$ is a germanium-specific constant. The

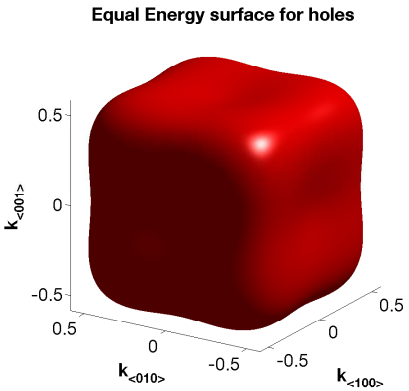

Figure 3.8: Equal energy surfaces for holes in the center of the Brillouin zone as given by eqn. 3.17. Note the dents along the three major axes in accordance with the observation of faster drift times along the $\langle 100 \rangle$ axis as observed by (Reggiani et al., 1977).

function $q(\theta, \phi)$ describes the warping of the equal energy surface as seen in figure 3.8.

$$q(\theta, \phi) \;=\; \left[b^2 + \frac{c^2}{4} \cdot \left(\sin(\theta)^4 \sin(2\phi)^2 + \sin(2\theta)^2 \right) \right]^{1/2} \tag{3.18}$$

The parameters $b = 0.6367$ and $c = 0.9820$ have germanium-specific values. Equations 3.17 and 3.18 have originally been derived for silicon by (Ottaviani et al., 1975).

The drift velocity $\overrightarrow{v_d}$ of holes is then given by averaging over all $\vec{k}$-states with each one weighted according to the distribution function 3.16.

$$\overrightarrow{v_d} \;=\; \frac{\hbar}{a\pi^{3/2}\sqrt{2mk_bT_h}} \int \vec{v}(\vec{k})\, f(\vec{k}; \vec{k_0}) d\vec{k} \tag{3.19}$$

with the velocity $\vec{v}(\vec{k})$ given by equation 3.3. The integrals from equation 3.19 are still too costly to be used in an simulation code and need to be approximated. The approximations are only a practical issue, not related to the physics description of the model, and are presented in appendix B.2. Figure 3.9 shows the t^{100} drift

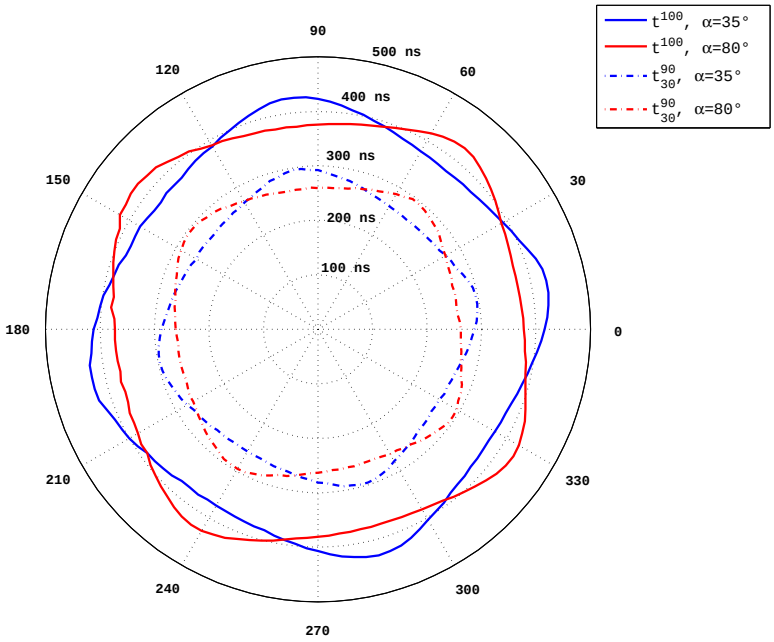

Figure 3.9: The t^{100}(solid) and t^{90}_{30}(dashed) drift times of holes in the coaxial part of a symmetric AGATA detector for two different orientations of the crystal axis. The angle α is again the angle between the x-axis and the first $\langle 100 \rangle$ axis. The effect of the crystal orientation is clearly visible, with a rotation by $\Delta\alpha$ making the two distributions coincide, not only in the case of t^{100} but also t^{90}_{30}. In contrast to figure 3.7, the distributions now look more like a rounded square.

times of the holes in solid lines and for t_{30}^{90} in dashed lines, for interactions located at the core contact in the coaxial part of a symmetric AGATA detector. This is equivalent to the electrons being collected immediately and only the holes drifting through the detector. The angle α is defined in the same manner as in figure 3.7, and is 35° for the blue curve and 80° for the red curve. As is the case with the electrons, the anisotropy rotates along with the crystal orientation and a simple rotation by $\Delta\alpha$ suffices to make both distributions coincide. In stark contrast to the electron drift times the anisotropy is now devoid of any oscillations and looks more like a rounded square or warped circle.

3.3 Calculating the Pulse Shapes

With the trajectories of the charge carriers given from the previous steps, the remaining task is to calculate the signals induced by the charge carriers on each electrode of the AGATA detector along their trajectory. Theoretically, one would have to go through the tedious process of solving equation 3.6 for the electric field with the charge q at $\vec{r}(t)$ and then integrating its normal component over the surface of the electrode in question for every point on the trajectory. This however can be greatly simplified by use of the Shockley-Ramo theorem.

3.3.1 The Shockley-Ramo Theorem

The Shockley-Ramo theorem was independently discovered by (Shockley, 1938) and (Ramo, 1939). Though it was originally derived for vacuum tubes only, it was later shown that it still holds under the presence of a stationary space charge distribution (Jen, 1941; Cavalleri, 1971). A recent review relevant to this thesis can be found in (He, 2001).
The theorem states that, for a set of electrodes $1, \ldots, n$ the charge Q_i induced on electrode i by a moving point charge q at an arbitrary point $\vec{r}$ is given by:

$$Q_i = -q \cdot \psi_i(\vec{r}) \tag{3.20}$$

The so-called weighting potential $\psi_i(\vec{r})$ for electrode i is calculated from the Poisson equation with the boundary conditions:

$$\begin{aligned} \psi(\vec{r}) &= 1\,V \quad \forall\, \vec{r} \in \partial\Omega_i \\ \psi(\vec{r}) &= 0\,V \quad \forall\, \vec{r} \in \partial\Omega_{j\neq i} \end{aligned} \tag{3.21}$$

with the surface area of electrode i given by $\partial\Omega_i$. Additionally, the space charge $\rho(\vec{r})$ is set to zero, hence the induced charge Q_i is independent of the applied electric field and the space charge, just like the weighting potential(see eqn. 3.20). Figure 3.10 shows a 2D-color plot at $y = 0\,mm$ of the weighting Potential for segment A4 of the symmetric prototype. The potential is decaying sharply outside

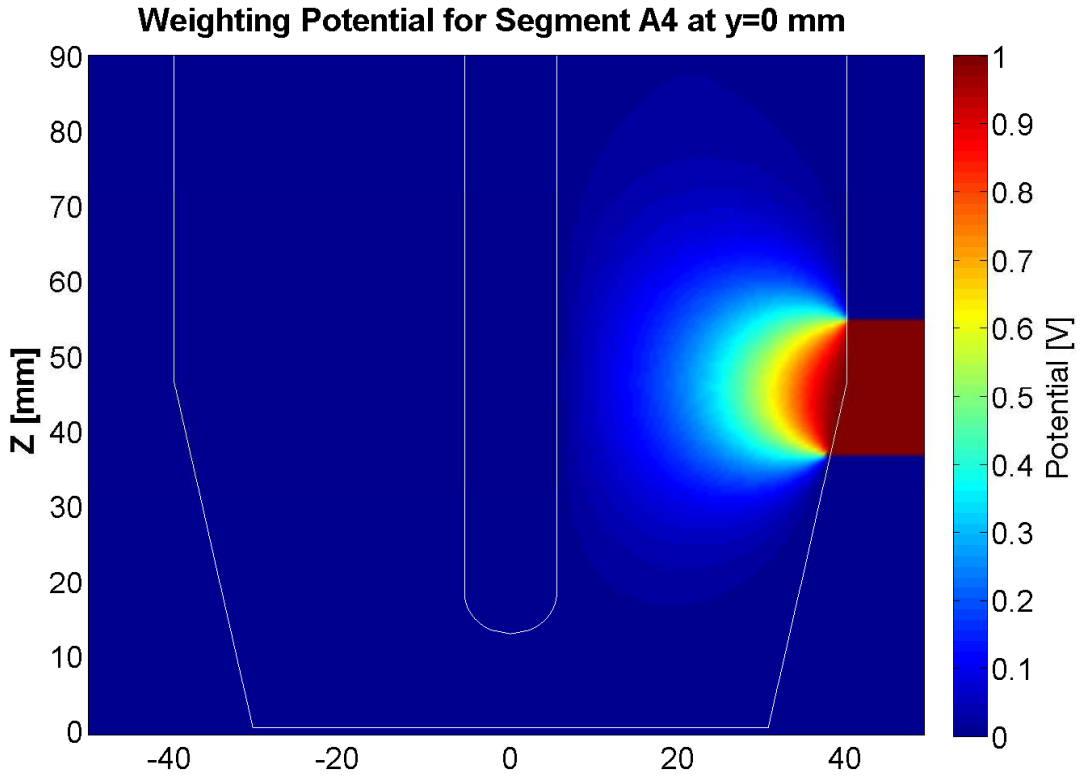

Figure 3.10: The weighting Potential for Segment A4 at $y = 0\,mm$. In order to see the extent of the segment better the outside of the crystal has been marked with unit potential within the spread of the segment. The core contact and all of the outer segment electrodes are indicated in white. A sharp decay of the potential outside the segment boundaries can be observed.

the segment boundaries. To simulate the pulse shapes for AGATA the weighting potentials for all segments and the core electrode have to be calculated (see sec. 3.3.2). The boundary condition for the passivated layer, as given by eqn. 3.10 is taken over unchanged.

3.3.2 Formation of the Pulse Shapes

To fully understand how the pulse shapes are formed only the case of a single interaction needs to be discussed. The interaction of a γ-ray with the detector creates a certain number of electron-hole pairs[3] with the total number of pairs being proportional to the energy deposited by the interaction. Once created the resulting charge clouds of charge $-q$ for the electrons and $+q$ for the holes, start drifting away from the site of the interaction in opposite directions (see left panel of fig. 3.11). The hole cloud will be collected by the segment electrodes and the electron cloud by the central contact, as in any n-type germanium detector. An interaction is said to have taken place within a given segment if that segments electrode is collecting the holes. Along their respective trajectories each type of charge carrier is inducing a charge on the electrodes according to equation 3.20. The overall charge induced at electrode i is then given by the sum for both types of charge carriers and the time dependent charge signal $Q_i(t)$ can hence be written as:

$$Q_i(t) \;=\; q\left[\psi_i(\overrightarrow{r_e}(t)) \;-\; \psi_i(\overrightarrow{r_h}(t))\right]. \tag{3.22}$$

At the end of their trajectory the charge carriers are collected and the position $\overrightarrow{r_{e/h}}$ of the electrons or holes is no longer defined since they immediately recombine with their mirror charges and cause a discontinuous drop in the current signal. The observed charge signals, by contrast show a completely steady behavior (see right panel of fig. 3.11). This can be understood since the charge signals simply are the integral of the current signals. In order for a simulation to reproduce the observed signals correctly the additional assumption has to be made that, once collected, the charge carriers are virtually staying at the collecting electrode, continuing to induce a signal as given by the boundary conditions 3.21. This ensures that the electrodes will record a constant charge signal[4] that is proportional to the total amount of charge having been collected by each electrode.

These are all the ingredients necessary to understand how the different pulse shapes come about. At the time t_0 of the interaction it obviously holds that $\overrightarrow{r_e}(t_0) = \overrightarrow{r_h}(t_0)$ and therefore $Q_i(t_0) = 0$. In the following the contribution of the holes and electrons to the charge signal of segment i is given by the shape of

[3] An interaction always creates as many holes as electrons. If the detector has been damaged by neutrons charge trapping can occur and this balance is no longer valid. The effect, however, is too small to have an influence on the position resolution (Ljungvall & Nyberg, 2005; Descovich et al., 2005)

[4] The effects of the electronics response functions will be applied onto these raw signals and explained in section 3.5

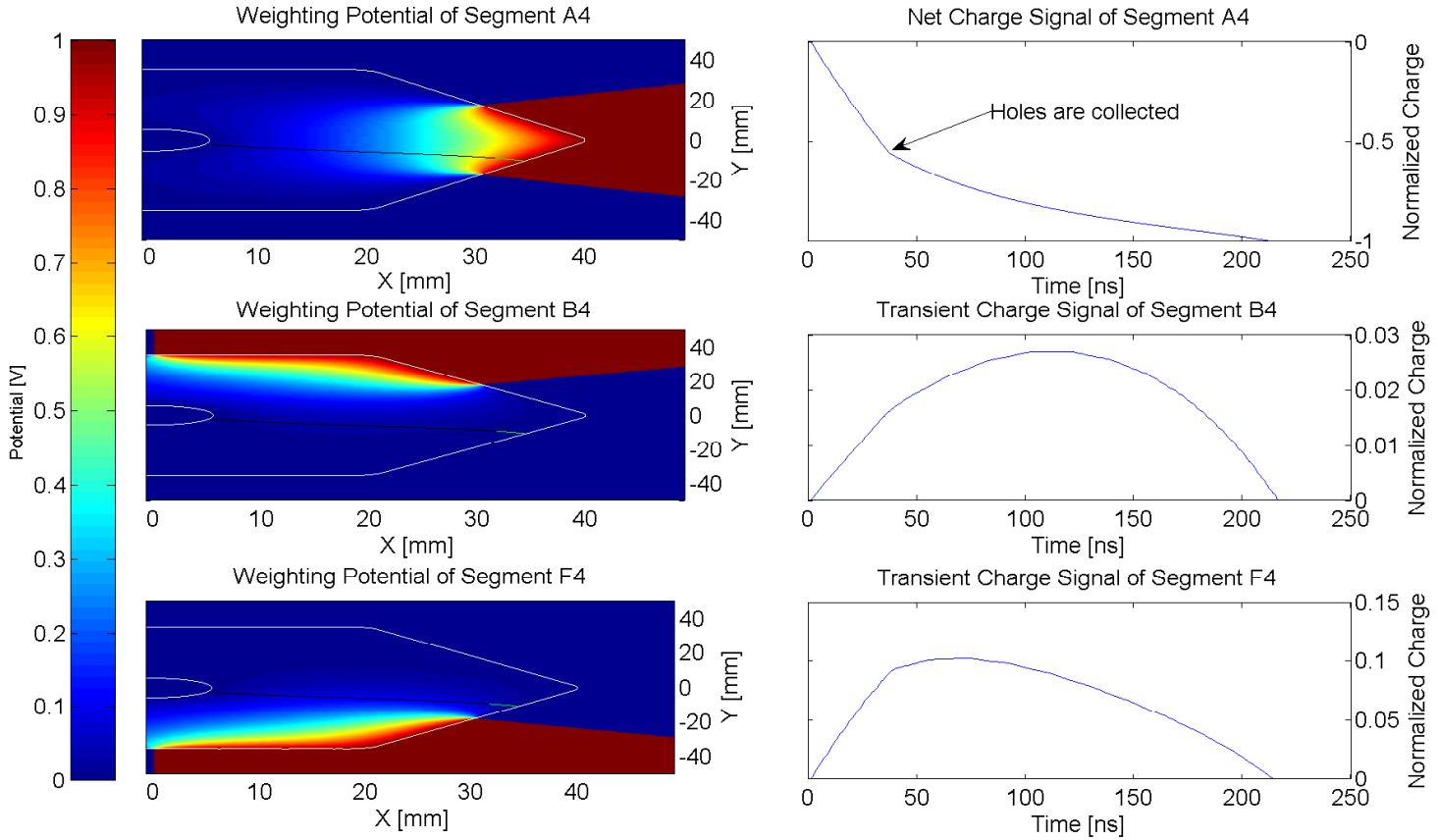

Figure 3.11: Pulse shapes for a sample interaction point. In the left hand panel the trajectories of the electrons, marked in black and of the holes, marked in green are plotted over a 2D plot of the segments weighting potentials at the depth of the interaction. The right hand panel shows the corresponding charge signals as given by eqn. 3.22. The net charge signal has a clearly visible kink at the time when the holes are collected while the electrons are still drifting. With the trajectory running considerably closer to the segment plotted in the last row, the amplitude of the corresponding transient signal is significantly larger than for the other neighboring segment. The boundaries of the detector are indicated in white.

the weighting potential ψ_i along the unique trajectory of the respective charge carrier (see eqn. 3.22). Segments that were not hit will show only *transient charge signals* that return to zero once all charges have been collected. The upper row in figure 3.11 shows the example of a net charge signal for segment A4 of the symmetric prototype detector.

As can be seen in the middle and lower plots of figure 3.11 the amplitude of a transient signal is larger the closer the trajectory runs to the boundary of the respective neighboring segment. The electrodes of the core contact and the hit segment are therefore the only ones recording net charge signals of opposite sign. Once the holes are collected the shape of the signal depends only on the path of the electrons through the weighting potential causing a kink in the recorded signal. Depending on the location the net charge signal can also change curvature if one type of charge carrier is collected. It is this location dependence that forms the basis for the pulse shape analysis to retrieve the interaction location from the recorded pulse shapes (see chap. 4).

3.3.3 Interpolation

Since all potentials needed are only available on fixed grid points with finite spacing, a precise interpolation routine marks a cornerstone of any simulation of pulse shapes. Naturally the accuracy of the interpolation increases with higher interpolation order R as more and more grid points are included (see fig. 3.12 for the 2D case) but only for steady functions. Discontinuities, as they are found at

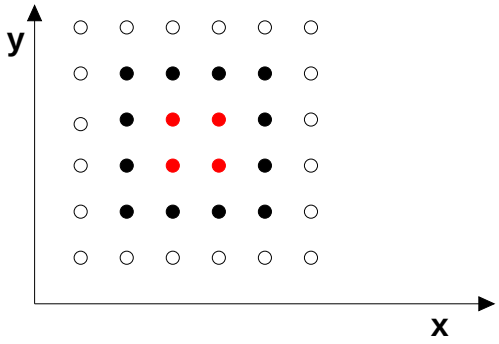

Figure 3.12: For a 0^{th} order interpolation only the innermost red points are used. The black filled circles are added for 1^{st} order and the outermost open circles for 2^{nd} order interpolation.

the segment boundaries, are smoothed increasingly by higher orders. Also a large order would take too long to compute since the simulation needs to interpolate all 37 weighting potentials at every point along the trajectories of the test charges. Hence a compromise between accuracy inside the crystal and at the boundaries as well as computation speed has to be found.

Generally speaking an interpolation calculates a weighted sum of the values given at the used grid points. The weights depend on the distance between the grid point and the point of interpolation and are naturally normalized to unity. (Schönberg, 1946) showed that any interpolation can be written in terms

of a kernel-interpolation in which the distance is weighted by the kernel function $F(\vec{r}, \vec{r_k})$.

$$\tilde{\psi}(\vec{r}) = \sum_{k=1}^{N} F(\vec{r}, \vec{r_k}) \cdot \psi(\vec{r_k}) \tag{3.23}$$

The most simple approach is the trilinear interpolation with a B-Spline of degree 1 as the interpolating kernel. It is only used at 0^{th} order since the linear approximation to the potentials is only justified at the finest grid level.

(Shannon, 1949) showed that the *sinc* function represents the theoretically optimal choice of a kernel in the case of 1-D band-limited signals. This optimality also holds at higher dimensions (see e.g. (Meijering et al., 1999)), but only when using an infinite number of lattice points. In order to be able to use it in a simulation and also to counter the effects of the truncation error, the *sinc* function needs to be multiplied with a windowing function of finite extent. The complete kernel, using a Hamming window is then given by:

$$F(\vec{r}, \vec{r_k}, R) = \prod_{a=x,y,z} \frac{\sin\left(\pi(a - a_k)\right)}{2\pi\,(a - a_k)} \cdot \left(1 + \cos\left(\pi(a - a_k)/(R + 1)\right)\right) \tag{3.24}$$

with the already mentioned interpolation order R. Another possible choice for the kernel is a Gaussian

$$F(\vec{r}, \vec{r_k}) = \frac{1}{\sqrt{2\pi \cdot \sigma^2}} \cdot \exp\left(-\frac{\|\vec{r} - \vec{r_k}\|}{2\,\sigma^2}\right) \tag{3.25}$$

which according to (Schönberg, 1946) falls into the class of smoothing interpolation since then $\tilde{\psi}(\vec{r_k}) \neq \psi(\vec{r_k})$. Yet this kernel is still very attractive for use with equidistant grids. A suitable choice of σ in relation to the grid spacing along with an interpolation order, which includes points within $\pm\,3\,\sigma$ can make the errors of the interpolation negligible (Monaghan, 1985).

Figure 3.13 shows the residuals of the three interpolation methods from the known values of the weighting potential for a true coaxial detector given by eqn. 3.8. The interpolations were conducted along a line inclined 15 degrees with respect to the x-axis. The trilinear method has by far the largest errors and also showed a strong dependence on the orientation within the detector. In fact the only time its output had acceptable errors was for interpolations along one of the axis of the coordinate system. The *sinc*-interpolation with order two fairs considerably better in terms of errors but suffers from substantial ringing. These oscillations would also be visible in the simulated signal and are therefore undesirable. Using the Gaussian kernel of the same order produced the expected smooth curve and also the smallest errors of all the three methods tested. As an added advantage its performance was independent of the orientation within the detector. Going to higher orders has no significant influence on the precision of each kernel.

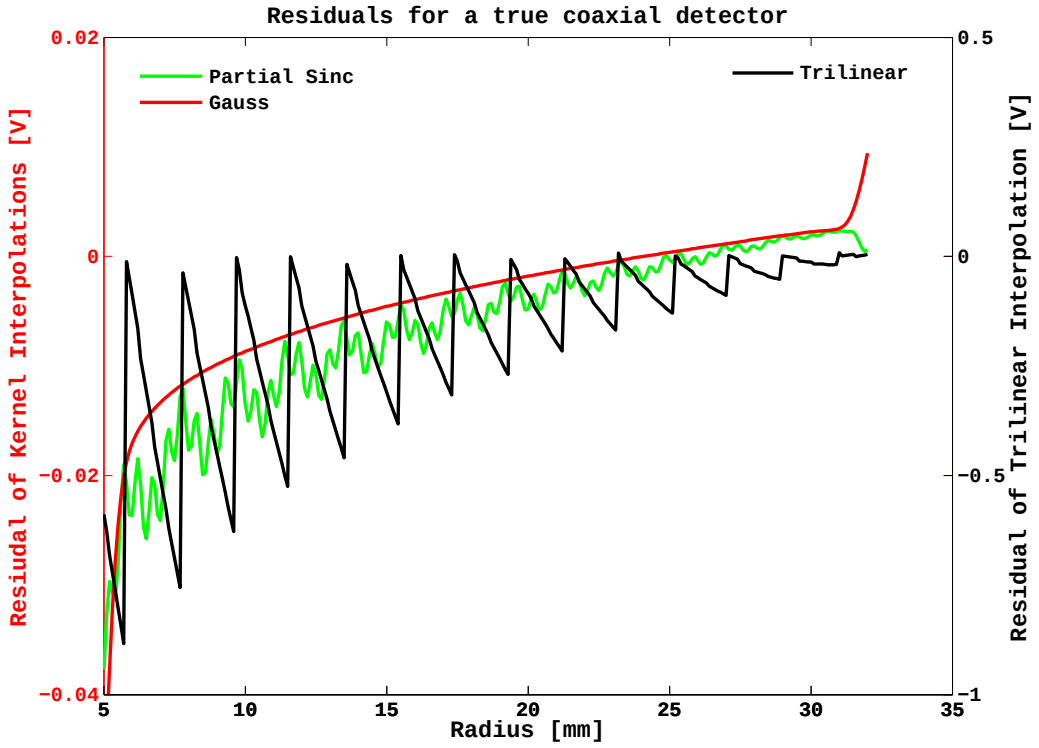

Figure 3.13: Residuals from the interpolation of the core weighting potential of a true coaxial detector as a function of the detector radius. The right abscissa is for the trilinear interpolation, which has by far the largest errors and the left is for the kernel-based methods. The *sinc*-interpolation with order two shows considerable ringing in contrast to the smooth output achievable by using a Gaussian kernel.

Equation 3.22 shows that the interpolated values of the weighting potentials have direct influence on the simulated pulse shape. For example an interpolation method which returns values higher than the actual potential in the strongly varying regions near the respective segments boundaries would lead to transient signals with an absolute amplitude higher than found for any interaction within the segment. Hence the PSA algorithm can find a better agreement with the experimental signal by searching further away from the boundaries, leading to a clustering of the reconstructed positions in the middle of the segments. In the course of this work it was found that this is the case when using the second order Gaussian kernel (see fig. 3.14). An adaptive routine with the interpolation order starting at the default value of two, but which reduces the order to the next smaller level once points from outside the crystal would be included, proves to be better suited to the problem of calculating the signals. Figure 3.14 displays the

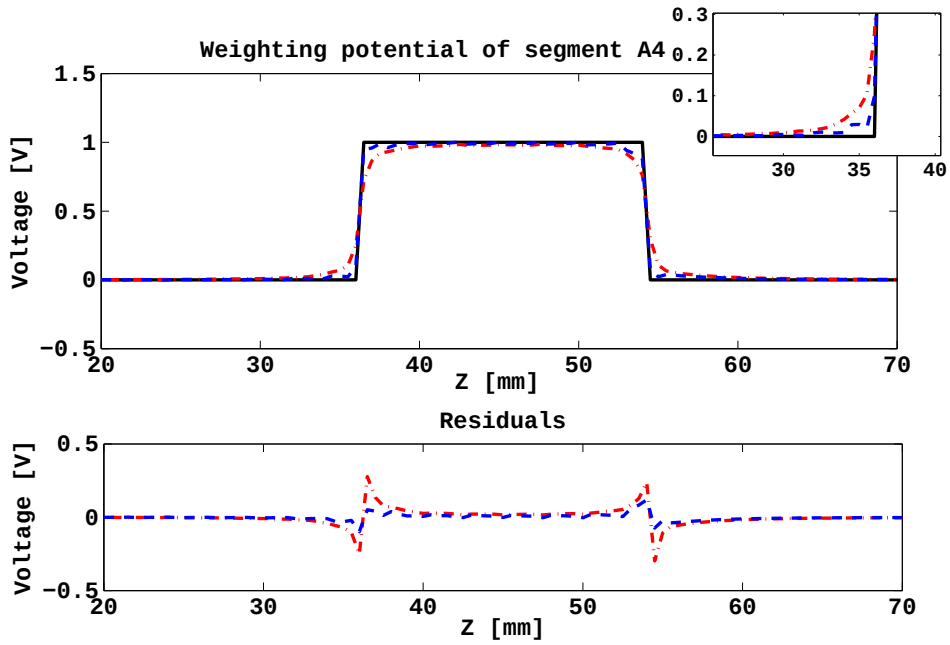

Figure 3.14: The precision of the two Gaussian kernel interpolation methods along the outside of the crystal for the weighting potential of segment A4 (see fig. 3.10). The black line in the main plot shows the theoretical values given by the boundary conditions. The fixed-order method (dash-dotted line) has difficulties reproducing the discontinuities at the segment boundaries. Using the adaptive method (dashed line) reduces the residuals, plotted in the lower panel, considerably. The inset shows a zoomed view of the lower segment boundary.

precision of both of the above methods along the outside of the AGATA crystal for the case of the weighting potential of segment A4 (see fig. 3.10). As demanded by the boundary conditions to the Poisson equation, the correct solution has a discontinuous step from zero to unit potential at the lower segment boundary and then jumps back zero potential at the upper boundary. The fixed-order Gaussian kernel interpolation smooths the discontinuities quite strongly leading to considerably larger residuals, depicted in the lower panel, than with the adaptive method. While there is still some ringing present around the discontinuities for the latter, the steps at the segment boundaries are much better resolved, a fact that is also exemplified in the zoomed view of the lower segment boundary in the inset of the figure.

Besides the test case of the true coaxial detector (see eqn. 3.8) there is an additional way to gauge the accuracy of the interpolation routine. With the segment boundaries having a negligible size the AGATA crystals can safely be considered as completely enclosed by the segment and core electrodes. There are two important consequences to this:

$$\Psi(\vec{r}) = \sum_i \psi_i(\vec{r}) = 1 \tag{3.26}$$

$$Q_{tot}(t) = \sum_i Q_i(t) = 0 \tag{3.27}$$

When looking at the sum of all weighting potentials the volume of the detector is surrounded by electrodes on unit potential. In the absence of any space charge this means that at each point within the detector the weighting potentials of all the segments and the core add up to unity. Equation 3.27 implies that the signal seen by the core contact is equal to the inverse sum of the segment signals and is a direct consequence of equations 3.26 and 3.22. Not surprisingly the first condition does hold on the calculated grid points but it should also hold at off-grid points using only interpolated values for the potentials. For this purpose the two fixed-size kernels and the adaptive-sized kernel were used to interpolate all weighting potentials at 100000 randomly distributed points within the detector. The results in table 3.1 again show that both Gaussian kernels are close to the

Kernel	Mean Sum [V]	Standard Deviation [V]
2^{nd} Order Partial Sinc	0.5404	0.1523
2^{nd} Order Gaussian	0.9984	0.0139
Adaptive Gaussian	1.0007	0.0094

Table 3.1: The sum of all weighting potentials interpolated at off-grid points.

theoretic optimum, while the partial-sinc interpolation is less favorable. Using an adaptive interpolation order yet again trumps the fixed-size kernels with not only the mean sum being closest to unity but also having the smallest standard

deviation of all the methods tested. The ringing that was already apparent in the test case is quite likely also the reason why the partial-sinc interpolation has such a large deviation from the theoretically demanded value of unity for the sum of the weighting potentials. In a last step the same test was repeated with the adaptive interpolation on a $100\,\mu m$ grid. Throughout 97.6% of the detector volume the deviation from equation 3.26 is less than 0.5‰ and the only significant deviations occur in the last $0.5\,mm$ from the detector surface. Consequently, equation 3.27 is fulfilled with deviations in the order of 10^{-8} (see fig. 3.15).

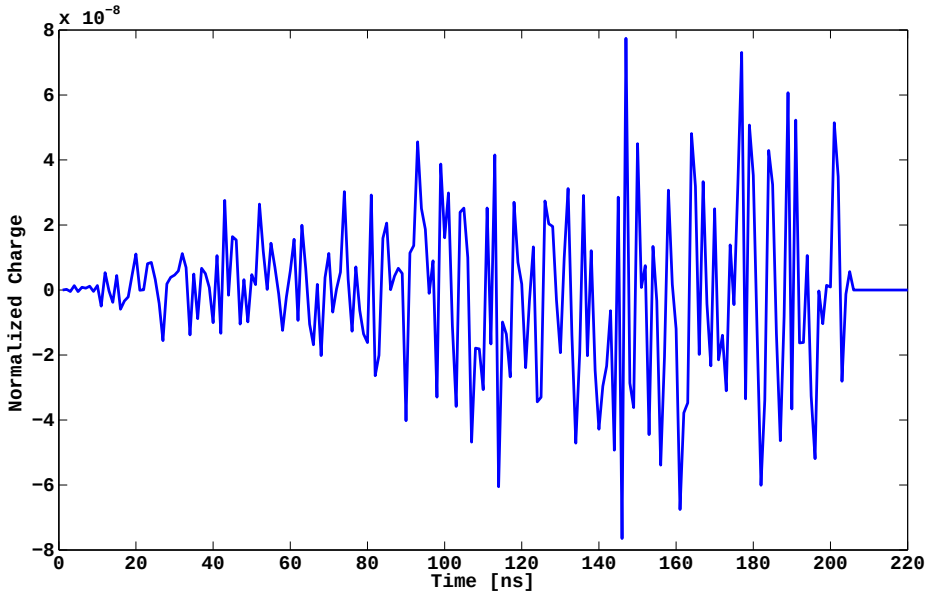

Figure 3.15: Residual between the simulated core signal and the inverse sum of the simulated segment signals.

3.4 Full Pulse Shape Simulation

All of the issues discussed so far have to be combined into a working simulation of AGATA pulse shapes. Before the pulse shape corresponding to an arbitrary point $P(x, y, z)$ can be simulated as shown in figure 3.16, there are some preparatory steps to be done once per crystal. First the Poisson equation is discretized and solved on a 0.5 mm grid with the modeled impurity distribution and the numerical description of the geometry (see eqn. 3.5) to define the detector boundaries. The weighting potentials for all 36 segments and the core are calculated in the same manner but neglecting the space charge (see sec. 3.3.1).

The actual simulation of the pulse shape commences by first checking whether P lies within the active volume of the detector, as given by equations 3.5. If

that is the case the electric field at the initial position is interpolated from the values of the electric potential. The charge carriers positions are then advanced accordingly, using the mobility models described in sections 3.2.3 and 3.2.4 and time steps of $0.1\,ns$ to discretize the equation of motion. These new position are then checked again with the detector boundaries. This is repeated, independently for the electrons and the holes, until the new position is found to be outside the active volume. The small time step ensures that the charge carrier is stopped within $10\,\mu m$ of the actual detector boundary and also prevents the oscillations around the correct path observed with larger time steps. Once both the holes as well as the electrons have reached the collecting electrodes the calculation stops and the trajectory has been fully calculated.

Since the pulse shapes need not be available in the high time precision as the trajectory, due to the $100\,MHz$ sampling of the digitizers (see sec. F.2), it suffices to calculate the signals only for every 10^{th} point on the trajectory, e.g. every $1\,ns$. Starting at P and with the time t set to zero the following steps are repeated for each of the 36 segments and the core individually:

- Interpolate the weighting potential at the charge carriers position.
- Calculate signal at time t using equation 3.22.
- Advance t by $1\,ns$ and update the positions.
- Stop once the holes as well as the electrons have reached their endpoint.

The weighting potential at the endpoint of a trajectory is not interpolated, but the values demanded by the boundary conditions in equations 3.21 are used. In the most common case of different drift times for the electrons and holes, the charge carrier, which has already reached its endpoint is considered to stay at that position conserving its contribution to the charge signal (see 3.3.2).

3.5 Response Functions

The basic approach to AGATA PSA is a direct comparison between simulated and experimental signals (see chap. 4). However, the signal recorded by the digitizers is not just an amplified version of the original signal shape from the detector, as it is simulated, but is altered in two ways. First, like any measuring system the AGATA readout electronics have a unique response function altering the input signal in a defined way. Secondly, although great care has been used in the cabling of the detector capsules the remaining capacitive coupling between any of the segments, or between the core and a segment, still leads to crosstalk effects between the individual signals. Both effects have to be applied to the simulated signals before they can be compared with an experimental trace. In the following these two influences on the signal shape will be discussed in more detail.

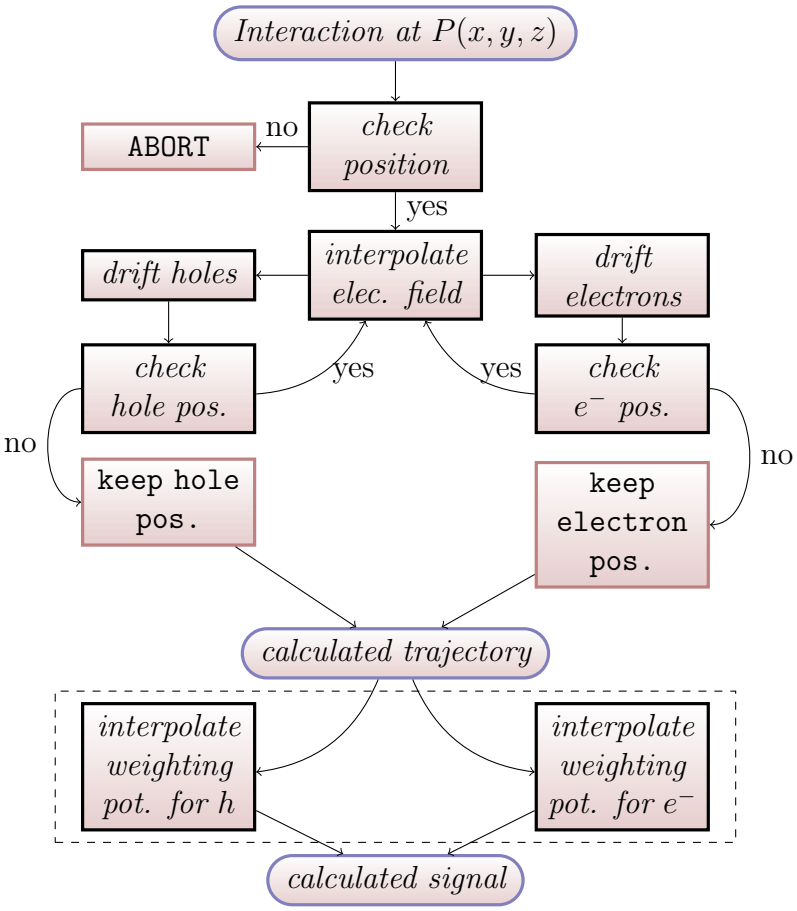

Figure 3.16: The principal work flow of JASS. The first check performed tests whether the point P is within the detectors boundaries. Then the pre-calculated electric potential is interpolated at the given position and the electrons and holes are drifted, independent of one another, according to their mobility models. Once a charge carriers reaches the detector boundary it is stopped and its position kept constant. The calculation of the trajectory is finished if both carriers have reached a boundary. From this the charge signal $Q(t)$ is computed, repeating those parts framed by the dashed rectangle 37 times, once for each of the 36 segments and the core.

3.5.1 Front End Electronics

The influence of a measuring systems response function $H(t)$, given in the time domain, on the recorded output signal $S(t)$ can be described by a convolution of the input signal $I(t)$ with $H(t)$:

$$S(t) = (H * I) = \int_{-\infty}^{\infty} H(u) \cdot I(t-u)\, du. \tag{3.28}$$

Each single stage of the readout electronics has its own response function, determined by its components, resulting in a nested set of convolutions which more often than not cannot be solved analytically. Additionally, determining each single response function is a far from trivial task and not the topic of this thesis. Therefore only the most important effects, in terms of signal shape, will be discussed.

The most simple contribution to the signal shape is the discharging of the capacitance in the charge loop of the preamplifier (see fig. F.1) leading to an exponential decay of the recorded charge signal. The decay time constant of $50\,\mu s$ is given by the values of the resistor and capacitance. This is the only part of the response function which can be inverted analytically and deconvolved, removing its effects on the signal shape. Also the charge loop cannot react instantaneously to an input but has a finite bandwidth. Thus the rise time of the preamplifier, i.e. the time it takes the preamplifier to reach its maximal output for a step function input, is not zero but finite. In the case of the AGATA preamplifiers the rise time can be adjusted within a predefined range and typically is of the order of $30\,ns$.

The last component in the readout chain with a simple response function is the Anti-aliasing filter, applied just before the flash ADCs which digitize the signals. According to the Shannon sampling theorem (Shannon, 1949) the $100\,MHz$ sampling rate of the digitizers suffice to resolve only contributions with frequencies below half the sampling rate. Hence, the anti-aliasing filter acts similar to a low pass filter with a cutoff frequency of $50\,MHz$. Figure 3.17 shows the frequency gain of the output signal in dB for a preamplifier with $30\,ns$ rise time, an anti-aliasing filter with a cut off frequency of $50\,MHz$ and the combined response. The complete response function in the time domain is plotted in figure 3.18(a) and appears to be positively skewed with a non-Gaussian shape to the left of the peak. The effects of the response function on the signal shape are illustrated in figure 3.18(b) and show a delayed start of the convolved signal with respect to the raw detector signal and generally a strong smoothing of the pulse shape. The only discernible effect of the exponential decay is in the non-constant charge signal after all charge has been collected. The analytic deconvolution of the latter effect guarantees a proper normalization of the experimental signals to unit charge.

Experimentally it is possible to determine the complete response function $R(t)$

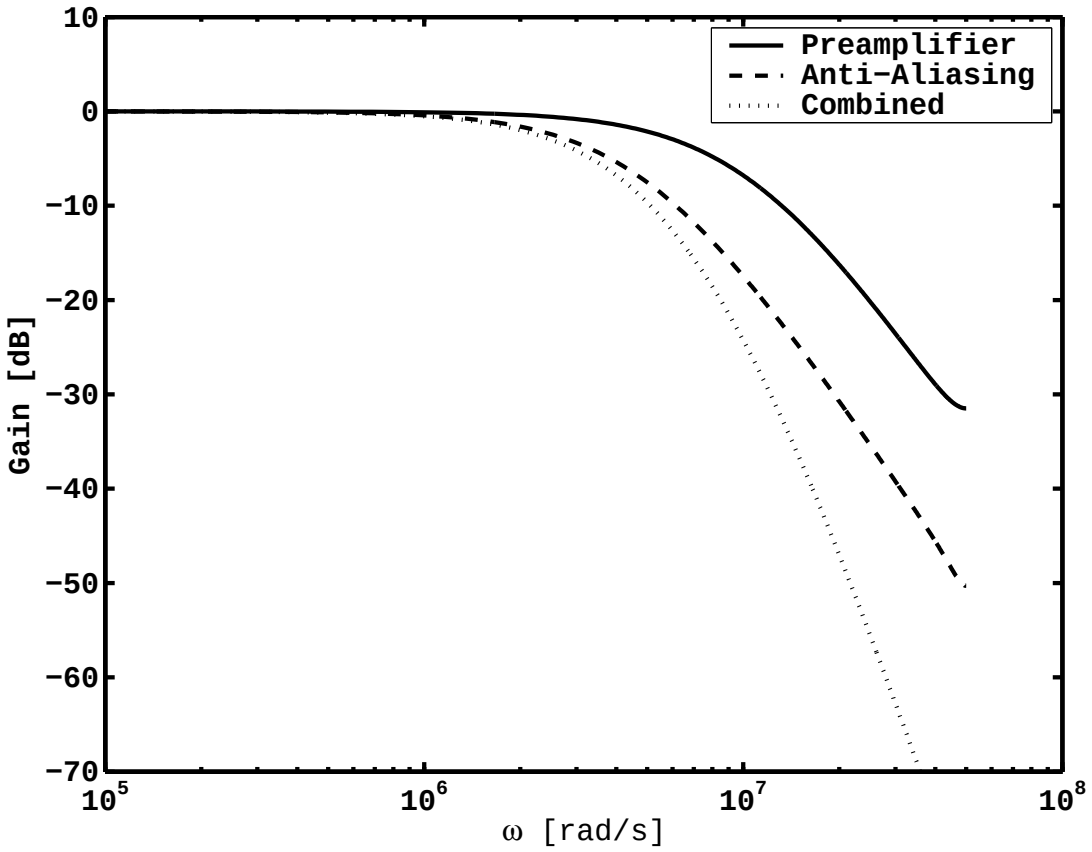

Figure 3.17: The gain-magnitude frequency response of the preamplifier and the anti-aliasing filter. Power gain is shown in decibels and the angular frequency is plotted on a log-scale. The rise time of the preamplifier was $30\,ns$ in this example.

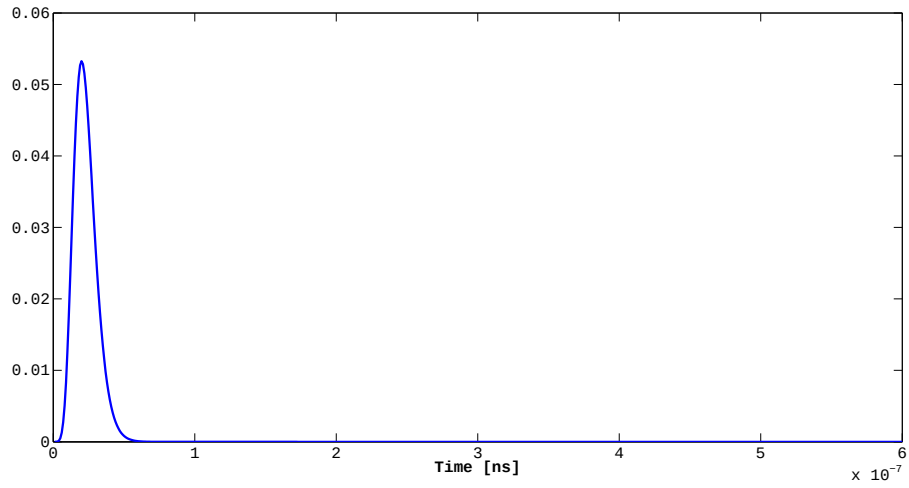

(a) Response function in the time domian.

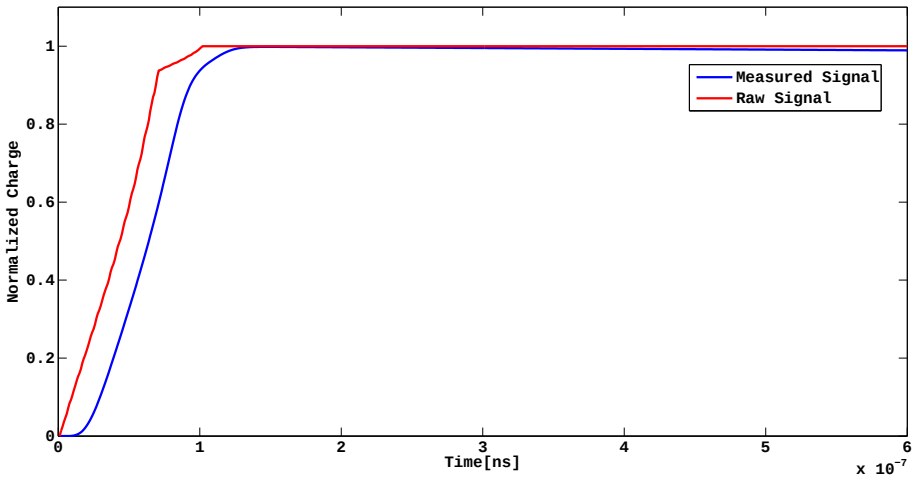

(b) Comparison of raw and convoluted, i.e. measured signal.

Figure 3.18: The plot in (a) shows the response function in the time domain and the effects of the response function on the signal shape are illustrated in (b) Most notably the start of the convolved signal (blue) is delayed with respect to the raw detector signal (red) and the pronounced kink is smoothed rather strongly.

using the core pulser (see sec. F.1) to inject a step function signal $\Theta(t)$. The derivative of the recorded signal $S(t)$ is then equal to $R(t)$ as given by

$$\frac{\partial}{\partial t}S(t) = \frac{\partial}{\partial t}(\Theta(t) * R(t)) = (\frac{\partial \Theta(t)}{\partial t} * R(t)) = (\delta(t) * R(t)) = R(t), \qquad (3.29)$$

with $\delta(t)$ the Dirac delta function. As for the scanning data, the complete response $R(t)$ of the used readout electronics can be approximated by a Gaussian with standard deviation $\sigma = 15\,ns$. This covers all characteristics of $R(t)$, including its finite bandwidth and the frequency limiting of the anti-aliasing filter, except the exponential decay given by the cold part of the preamplifier (Bruyneel, 2007).

3.5.2 Crosstalk

Another signal alteration, inherent to any segmented detector, is the so-called crosstalk due to capacitive coupling between the detectors electrodes. Two types of crosstalk can be discerned. *Proportional crosstalk* is directly proportional to the signal amplitude while *derivative crosstalk* is proportional to the derivative of the signal. The latter contributes only during the rise time of the signal since the derivative is zero anytime else.

Proportional Crosstalk

The origin of the proportional crosstalk lies in the capacitive coupling between the detectors electrodes. The current generated on electrode i will not go in its entity to preamplifier i but parts will be split of by capacitive coupling to electrode j with the amount proportional to the ratio of the electrodes capacities. However, due to the different coupling of the segment preamplifiers to the detector the segment to segment and segment to core crosstalk contributions are at least one order of magnitude smaller than the core to segment crosstalk (Bruyneel et al., 2009). Consequently only the latter effect will be applied to the simulated signals. It can be implemented by simply adding a scaled copy of the core electrodes charge signal onto all segment charge signals. For the AGATA detectors the scaling factor is 0.1% (Bruyneel et al., 2009), in line with the AGATA specifications. Its predominant effect is a shift in the segment signals base line leading to reduction of the energy detected by the segment. Thus the sum of segment energies, which ideally should be equal to the core energy, is reduced around 0.1% per segment fold[5] (see fig. 3.19(b)).

[5]Segment fold or multiplicity denotes the number of segments with a γ-ray interaction, i.e. a net charge signal.

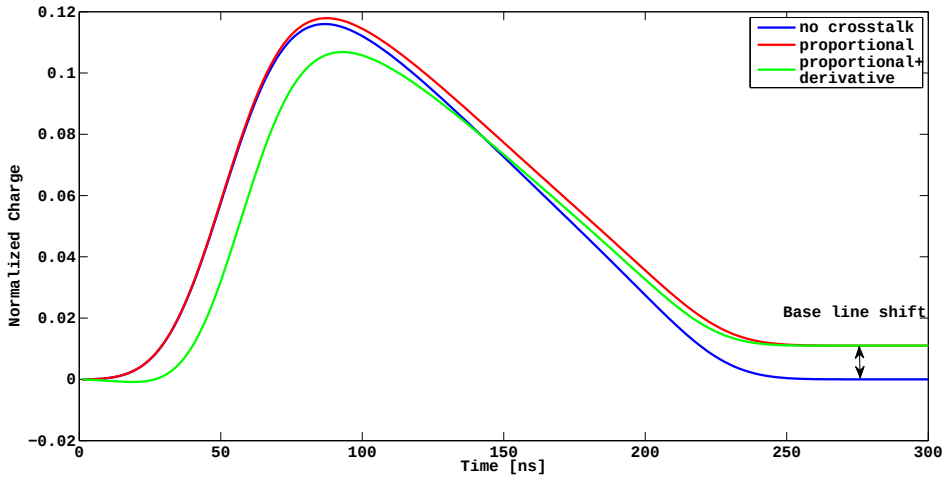

(a) Effects of both crosstalk contributions on a transient signal. The effects have been exaggerated for an enhanced clarity of the figure.

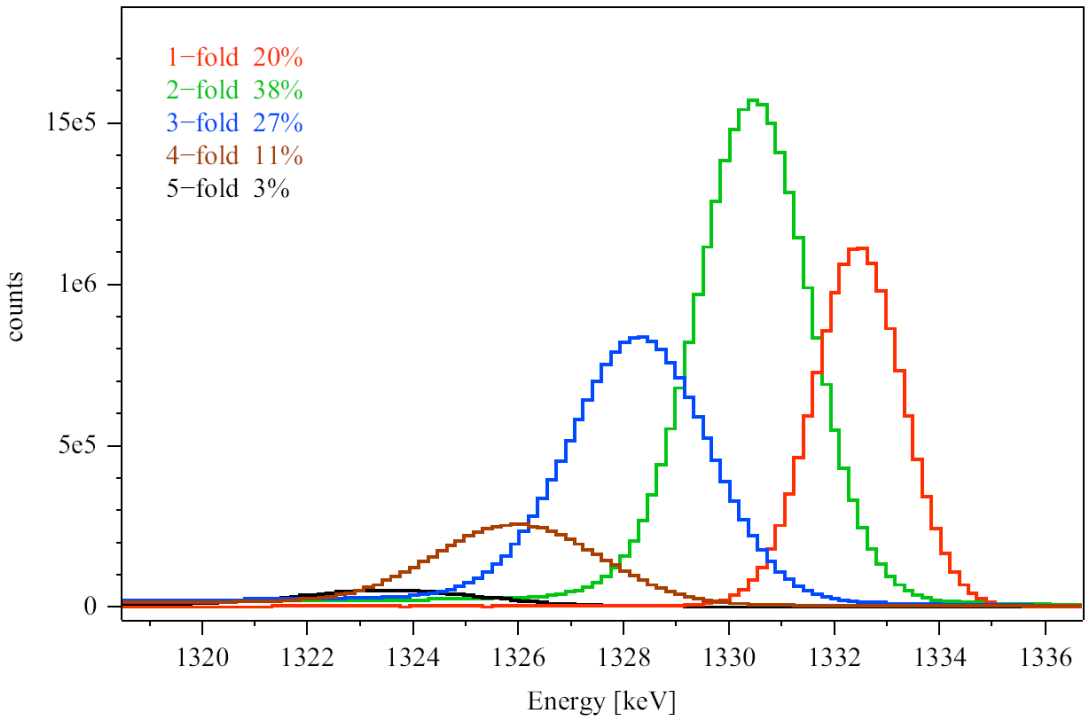

(b) The sum of segment energies as a function of segment fold.

Figure 3.19: Illustration of crosstalk effects on signal shape (a) and energy resolution (b). The proportional core to segment crosstalk(exaggerated by a factor of 10, red, a) leads to a shift of all segment base lines and reduces the energy detected by the segment. The sum of segment energies decreases linearly with increasing segment fold (b) (fig. taken from (Bruyneel et al., 2009)). The signal shape is predominantly influenced by the derivative crosstalk (exaggerated 4 times, green, a) component with a significant change in recorded signal amplitude. The proportional crosstalk by the core affects the signal shape only in the later stages, for instance from t^{90} onward.

Derivative Crosstalk

Derivative crosstalk is proportional to the derivative of the induced net charge signal and contributes to the signal shape only during the rise time of the signal, i.e. the region of interest for PSA (see chap. 4). Only the directly neighboring segments and and segments within the same sector are affected by this type of crosstalk (Dimmock, 2008), which are exactly the segments used by PSA. The shape of the resulting crosstalk signal is similar to that of transient signals, making it rather hard to measure precisely in experimental signals, and has a significant influence on the amplitude of a transient signal (see fig. 3.19(a)). Therefore it would be of great importance to PSA to include the effect but unfortunately there is not yet a measurement of derivative crosstalk for any AGATA crystal since it requires time aligned signals. This was not possible with the electronics used in the scanning of the detector (see sec. 3.6.1) and the effect could not be included in the simulated signals.

3.6 Verification of JASS with experimental data

The verification of the simulated pulse shapes is absolutely essential before simulated traces can be used to perform a pulse shape analysis of experimental data with unknown interaction locations. Any inaccuracies of the simulation would have a direct impact on the accessible position resolution of the PSA and hence on the precision of the tracking algorithms ultimately affecting the Doppler-correction capabilities.

There are two principal ways to achieve a full or partial verification. First of all a collimated source, with a so-called *pencil beam*, can be placed in front of the detector and the reconstructed interaction locations should show the expected exponential distribution with depth. The particular problem with this approach lies in the fact that the majority of events will have multiple γ-ray interactions in the crystal. These have to be decomposed correctly in order for the result to be comparable with the theoretical expectations. These approach will not be taken in this thesis, due to the additional error sources on the PSA side that prevent a proper evaluation of the accuracy of the simulation. The second possibility is to use a coincidence scan setup, where all three coordinates of an interaction are simply given by the setup of the experiment (see sec. 3.6.1) and the vast majority of event will be single γ-ray interactions (see tab. 3.2). If the positions from various scan points are correctly identified by a full search of the simulated dataset the simulation can be considered verified and this is the approach taken in this thesis.

The comparison of the experimental traces with data simulated by JASS was conducted in the following manner. First a signal basis with a grid size of 1 mm was calculated by JASS, using in one case the mobility parameters

reported by (Bruyneel, 2007), this will be called parameters set A in the following. Additionally, the electron mobility parameters from (Mihailescu et al., 2000) in conjunction with the hole mobility parameters for the presented model (see sec. 3.2.4), which were adjusted to the experimental results from (Reggiani et al., 1977) by (Bruyneel et al., 2006a) were used, this will be called parameter set B in the following. For a description of the model parameterization and the respective parameters the reader is referred to appendix B. Next these pulse shapes were folded with the response function as pointed out in section 3.5 and the proportional core-to-segment crosstalk was added. Using these simulated signal bases, an extensive grid search was conducted for each basis, comparing the experimental traces with each pulse shape from the basis and the coordinates of the best fitting trace were recorded. Naturally only basis points within the hit segment were considered and the comparison only used the transients of the segments directly adjacent to the hit segment in addition to the net charge signal. Given the amplitude of transients from segments further away, including these would only have a negligible influence on the overall value of the metric. Since there was no real-time requirement in this setting, the starting time t_0 of the pulse shapes was kept as a fit parameter and only the optimized value of the metric entered the comparison with the other basis points.

3.6.1 Comparison with Scanning Data of S002

The basic idea of the scanning system is to use the AGATA detector together with an ancillary detector, e.g. scintillators, to selectively measure only events in which the γ-ray Compton-scattered by 90°, with the ancillary setup fixing the z position of the interaction within the AGATA detector. The experimental work of the coincidence scan and the setup were done by Matthew R. Dimmock and Laura Nelson, a detailed description of the scanning setup can be found in (Dimmock, 2008). The basic parts for this work are summarized in the following.

A 920 MBq ^{137}Cs source was placed inside a lead block, which had a bore hole with 1 cm diameter located just above the source. This block was fitted onto a motorized x-y-table to allow for a precise positioning of the source and a 1 mm wide collimator was placed in front of the source to constrain the x and y position. The z position is determined by the ancillary detector, either NaI or BGO crystals, which detected a γ-ray in coincidence with AGATA as each detector covers just one collimated slit between adjacent semi-circular sheets of lead placed around the AGATA crystal. The complete setup up is illustrated in figure 3.20. The event selection procedure sorted out all events in which the energies deposited in the AGATA detector and the scintillators did not match those required for a 90° Compton-scattering of a $662\,keV$ γ-ray. Additionally, allowances for the energy resolutions of the detectors were made and only events in which just one AGATA segment recorded an interaction were accepted. Using this setup, shown in figure 3.20, the x and y positions of an interaction are known

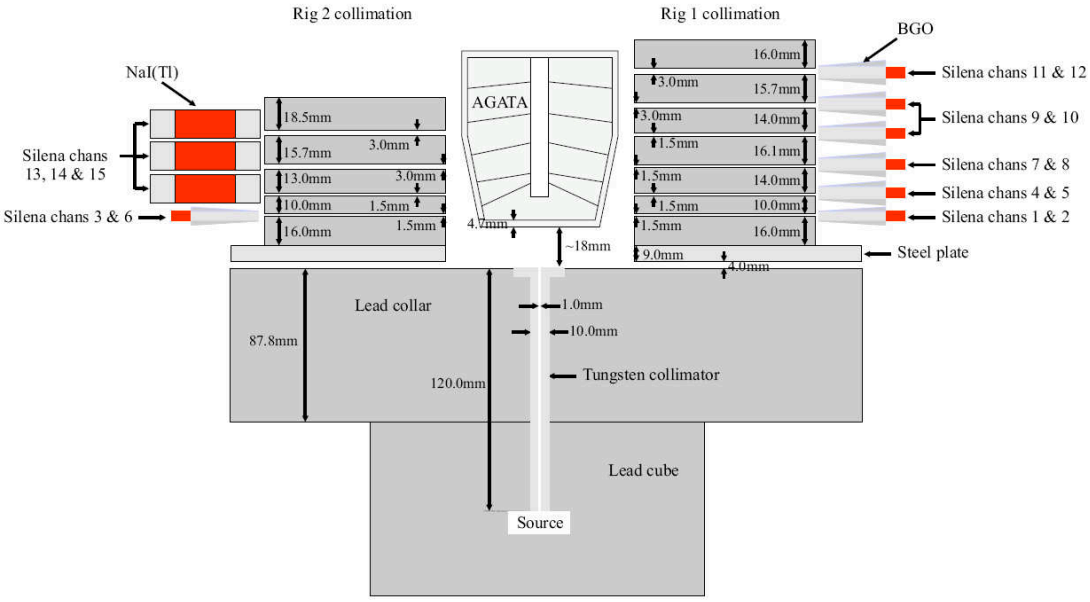

Figure 3.20: Illustration of the setup of the Liverpool scanning system showing the positioning of the various components. The slits forming the collimators for the z-position of the γ-ray interaction have different widths of $1.5\,mm$ and $3.0\,mm$ in order to allow for similar amounts of events to be recorded for each scanned depth. The positions of the slits were chosen in such a way as not to cover two different effective segment rows, indicated by lines in the crystal, with the same collimators. The figure was taken from (Dimmock, 2008).

from the x-y-table and the z position is given by the scintillator, which detected the scattered γ-ray. The pulse shapes from the AGATA detector were read out by GRT4 cards (Lazarus et al., 2004), that were not time aligned, and with a sampling rate of $80\,MHz$. The time alignment of the segment shapes happened later in a post-processing step (for details see (Dimmock, 2008)). It should be noted that a better quality of the data can be expected when using the full AGATA electronics (see sec. 2.2).

The raw data from the scan consisted of non-normalized traces with 250 samples for each segment trace, in need for some preprocessing before a comparison with the simulated data could proceed. The data was already arranged in such a manner that the starting time t_0 of the pulses was always in the vicinity of sample 100. In a first step the known exponential decay from the preamplifier was removed from the traces by analytic deconvolution. Next the baseline of the pulse shapes was adjusted by calculating the average value of the first 80 samples and subsequent subtraction of it. In a last step the traces had to be normalized to the hit segment having unit charge. Therefore all traces were divided by the average of the samples 170 through 250 of the hit segment. Sample 170 is 875 ns away from the typical starting sample 100 and hence has a large enough safety margin to not include parts of the rising pulse since the longest drift times are of the order of 350 ns.

Position uncertainties of the setup

In order to be able to gauge the precision of JASS it is necessary to know the systematic position uncertainties, as given by the setup of the scanning system. For this purpose a GEANT simulation was conducted, using a reduced setup containing only two slits. The first slit was situated at a depth of $31\,mm$ within the detector and had an extent of $1.5\,mm$, while the second one was $3\,mm$ wide and at a depth of $80\,mm$. Additionally it was assumed that the slits are completely covered by two NaI scintillators, affecting only the statistics but not the precision of the setup. Out of the one billion γ's simulated in total, those fulfilling the criterion of a coincident 90° Compton scattering have to be extracted. A $662\,keV$ γ should hence deposit $374\,keV$ in the AGATA crystal and $288\,keV$ in the scintillators. Due to the limited energy resolution of any detector only finite intervals around the correct energies can be used. Even though the intrinsic resolution of AGATA is $1.5\,keV$(FWHM) in the relevant energy regime, the applied interval is $30\,keV$ wide to account for the limited acceptance angle of the geometry. The energy gate for the scintillators had to be chosen rather large with a width of $150\,keV$, because of problems with the data acquisition (Unsworth, 2009). The latter has no significant influence on the results since the energy gate on the AGATA detectors constrains the energy of the outgoing γ such that it is always within the given window, even when the effect of the scintillators' poor energy resolution is included. In addition the energy deposits in the AGATA crystal

have to be constraint to a single segment. After this event selection merely 29000 γ's remain.

Figure 3.21(a) shows a scatterplot of the x and y coordinates of the γ-rays most energetic interaction with AGATA. There is a clear concentration around the source position, indicated by the white cross, but positions outside the area covered by the opening angle of the collimator are observed as well. These correspond to events with multiple γ-interactions and the first interaction not depositing the most energy. As can be seen in figure 3.21(b) a $3\,mm$ wide slit does not constrain the z position of an interaction very well. The distribution is basically uniform over the extent of the slit.

The complete results of this simulation are summarized in table 3.2. The x and y coordinates are precisely constraint by the setup, though the FWHM naturally increases with depth in the detector due to the finite opening angle of the collimator. (Dimmock, 2008) derived similar results, including the uncertainties of the source position, with a FWHM of $1.5\,mm$ at $z = 0$ and $3.0\,mm$ at $z = 90$. The picture looks quite different concerning the depth, or z coordinate, of the interaction. Although the source is located rather close to the outside at a radius of $24\,mm$, and hence close to the collimator, its location is not very well constraint. The positional errors almost double when using the wider collimator of $3\,mm$. Additionally for source position closer to the core, at radii shortly above $5\,mm$, the errors will increase because of the opening angle of the relevant collimator. Also the finite width of the energy intervals do not only allow for

Scanning depth [mm]	$\Delta X\,[mm]$	$\Delta Y\,[mm]$	$\Delta Z\,[mm]$	
31	1.3	1.3	2.2	
80	1.6	1.6	4.2	
Numb. of Inter.	1	2	3	4
Percentage	86%	5.8%	1.8%	5.3%

Table 3.2: The position uncertainties of the scanning setup for the two different tested depth given as FWHM. The precision in x and y is generally quite good and decreases with depth due to the opening angle of the collimator. The z coordinate is by comparison rather poorly constraint by the setup.

scattering angles between 85.5° and 95.5°, but also for multiple interactions to pass the event selection. Therefore only 86% of the events are single interactions opposed to the 100% in the ideal case of solely 90° scattering being allowed. max at 4 phase space.

As the signal shapes vary non-linearly with location (see fig. 4.1) and with a significant number of events featuring multiple γ-interactions within AGATA, an averaging procedure to reduce the influence of noise would not properly reproduce the shape of the mean position of all events. For this reason the decision was taken to use the scanning data event by event instead of one averaged pulse per

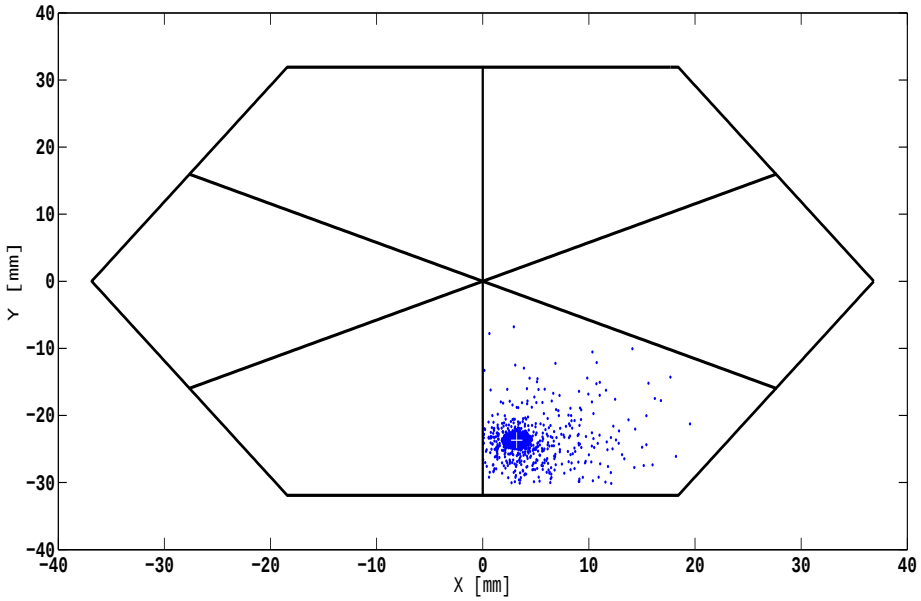

(a) X-Y scatterplot of interaction positions within segment F3, with the source position indicated by the white cross.

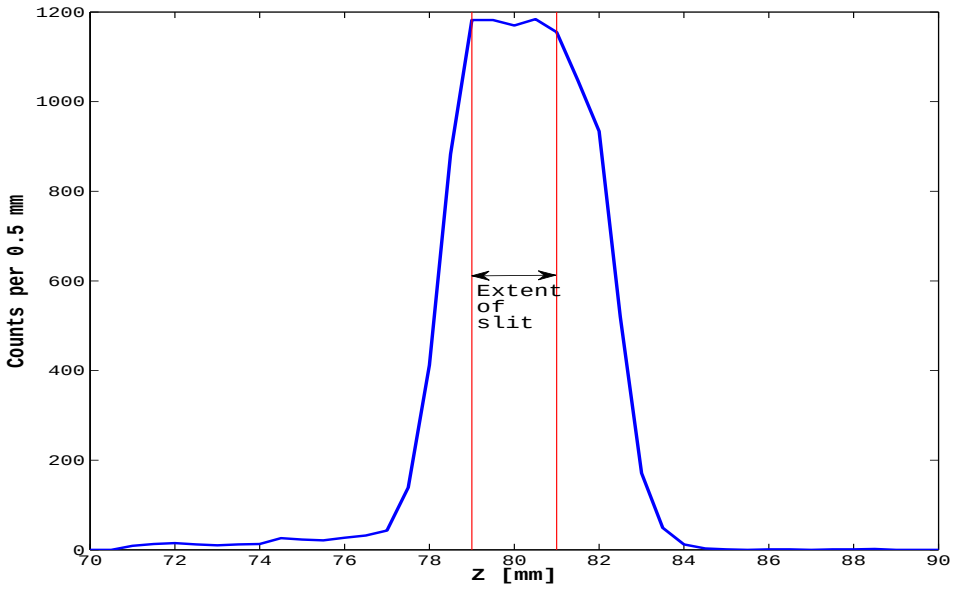

(b) Histogram of z-resolution for the second slit at $z = 80.5\,mm$.

Figure 3.21: The x-y scatterplot of interaction positions shows a clear concentration around the source position, indicated by the white cross. The distribution of the z-coordinates for the second tested depth is almost uniform over the extent of the slit.

scanning position.

Single event data

As was already mentioned the preprocessing of the data consisted of an analytic deconvolution of the exponential decay, given by the preamplifier, and a normalization of the net charge signal to unit charge. Additionally, the scanning positions had to be corrected for a tilt and rotation of the detector (see (Dimmock, 2008)). In order to verify JASS with this data set a basis set of pulse shapes was simulated on a 1 mm grid, using parameter sets A and B and the parameterization of the charge carrier mobility models presented in appendix B. A complete search of all reference signal, including the crosstalk contribution from the core signal (see sec. 3.5.2), in the hit segment was conducted to find the basis signal which best agrees with the experimental signal. The event time t_0 (see fig. 4.3) was a fit parameter and individually optimized for each reference signal. For this purpose each reference signal was subsampled to $12.5\,ns$, i.e. the sampling time of the experimental data, with t_0 being varied in $1\,ns$ steps over a wide enough range to guarantee the inclusion of the correct t_0. Any signal values at sample times without a directly corresponding value in the reference signal, given with $1\,ns$ precision, were interpolated linearly. Only the best χ^2-value from the t_0 fit is used in the comparison with the results of the other reference signals and the grid point with the best overall χ^2 is considered the solution to the search. The uncertainties of the setup (see above) and the non-linearities of the signal shapes prevent a complete assessment of JASS' performance solely based on these spectra. Therefore pulse shapes from a GEANT simulated set of single interactions throughout the detector were calculated, realistic noise (see sec. 4.1) of the correct amplitude was added to the signals and the resulting data set was analyzed in the same manner as the scanning data. Before the position resolutions (dashed red curves in figs. 3.22 through 3.28) were calculated the true interaction locations were smeared by sampling from the position uncertainty distributions, presented in the previous section.

(Bruyneel, 2007) and (Dimmock, 2008) already reported that the scanning depth are offset by $\sim 4\,mm$, thus this offset has been included in the calculated spectra and should in principle lead to a peaking of the resolutions in Z around 0, just like the distributions of the simulated data set. Figures 3.22 through 3.27 show the resolutions for the six different segment rows and figure 3.28 shows the resolution of the complete data set with the blue curves corresponding to the results of the scanning data with parameter set A, the dash-dotted green curves correspond to the results with parameter set B and the dashed red curves belonging to the results with the simulated data set, i.e. the best possible results. Generally the results can be summarized as follows, the distributions of the X, Y and Z coordinates always have a skewness (see app. E.2) around 0 indicating symmetric distributions around the mean. The same is true for the radial coordi-

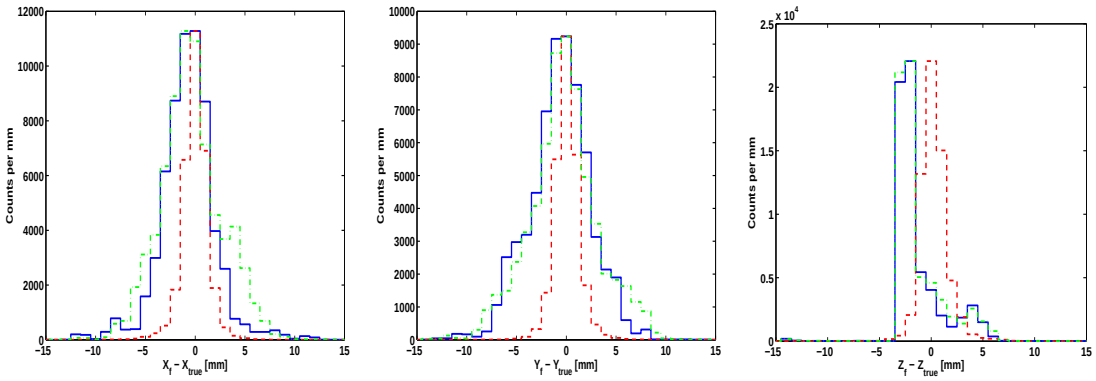

(a) Resolution of X. (b) Resolution of Y. (c) Resolution of Z.

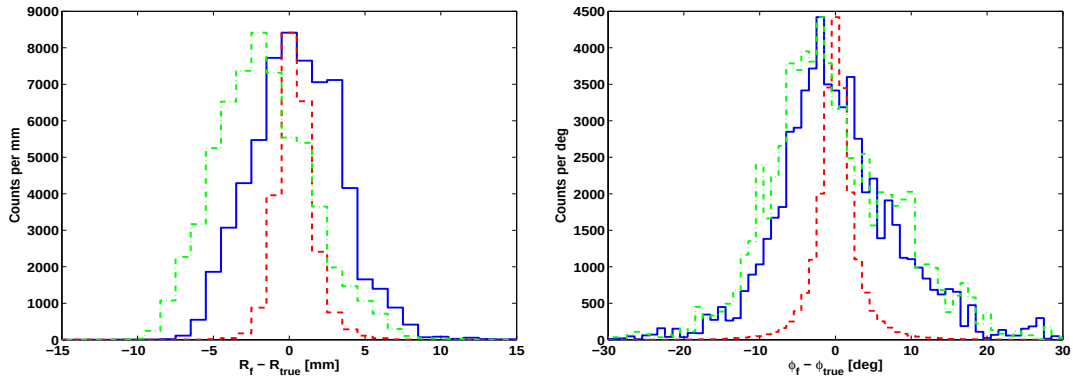

(d) Resolution of R. (e) Resolution of φ.

Figure 3.22: Resolutions of scanning events in segment row 1. The blue curve shows the resolution on the scanning data using parameter set A, the dash-dotted green curve belongs to parameter set B and the dashed red curve shows the resolution on the simulated data.

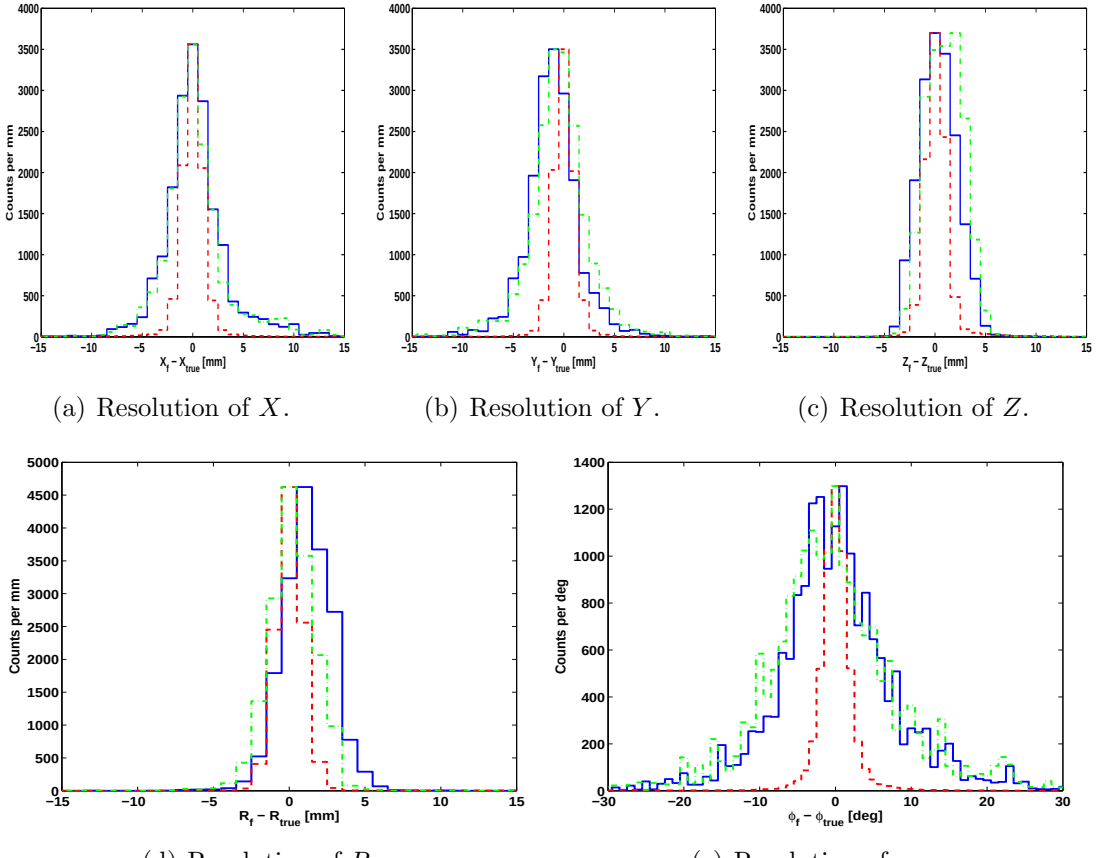

(a) Resolution of X. (b) Resolution of Y. (c) Resolution of Z.

(d) Resolution of R. (e) Resolution of φ.

Figure 3.23: Resolutions of scanning events in segment row 2. The blue curve shows the resolution on the scanning data using parameter set A, the dash-dotted green curve belongs to parameter set B and the dashed red curve shows the resolution on the simulated data.

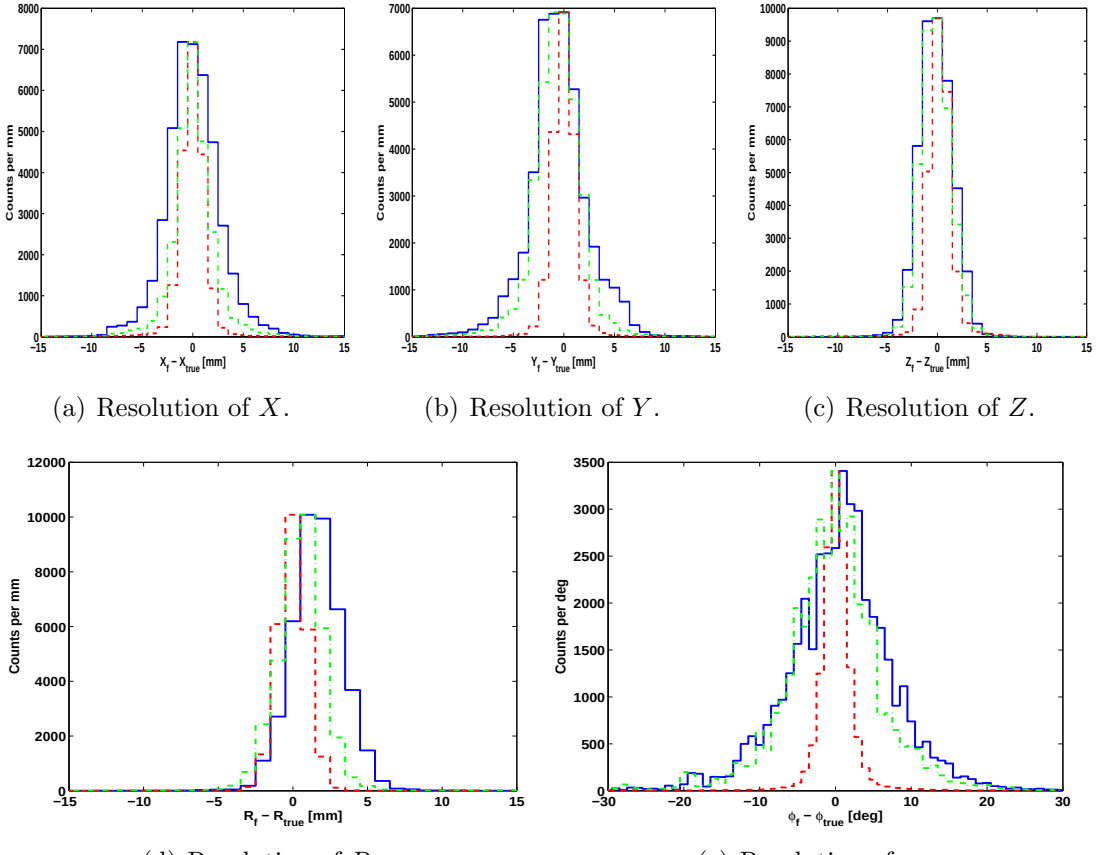

(a) Resolution of X. (b) Resolution of Y. (c) Resolution of Z.

(d) Resolution of R. (e) Resolution of φ.

Figure 3.24: Resolutions of scanning events in segment row 3. The blue curve shows the resolution on the scanning data using parameter set A, the dash-dotted green curve belongs to parameter set B and the dashed red curve shows the resolution on the simulated data.

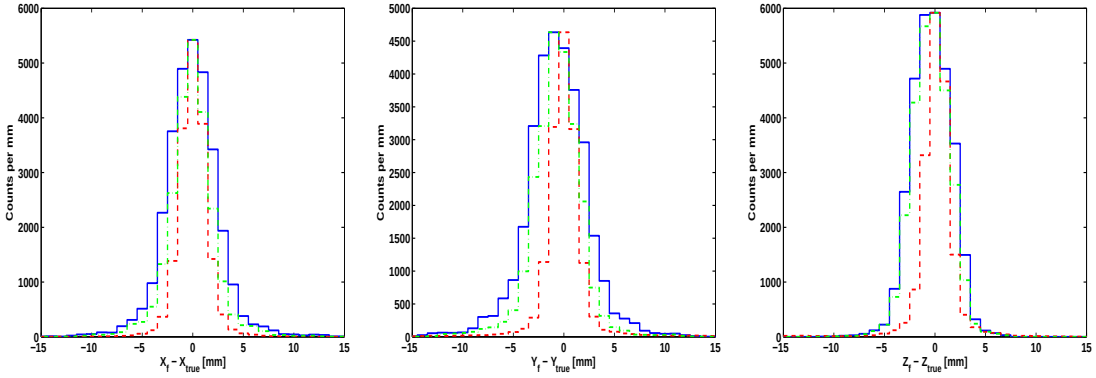

(a) Resolution of X. (b) Resolution of Y. (c) Resolution of Z.

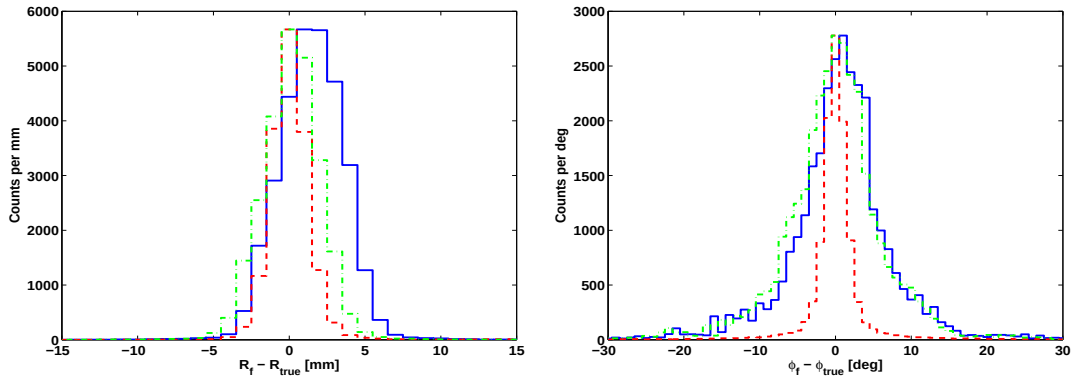

(d) Resolution of R. (e) Resolution of φ.

Figure 3.25: Resolutions of scanning events in segment row 4. The blue curve shows the resolution on the scanning data using parameter set A, the dash-dotted green curve belongs to parameter set B and the dashed red curve shows the resolution on the simulated data.

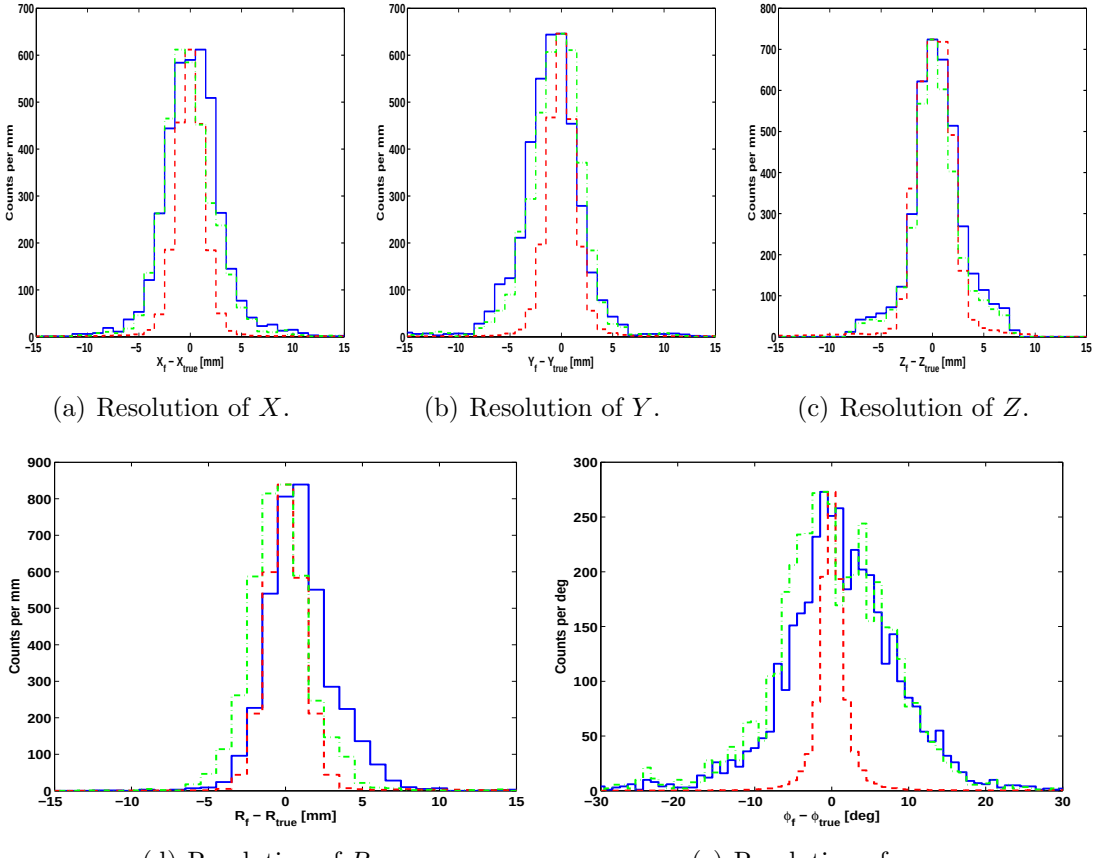

(a) Resolution of X. (b) Resolution of Y. (c) Resolution of Z.

(d) Resolution of R. (e) Resolution of φ.

Figure 3.26: Resolutions of scanning events in segment row 5. The blue curve shows the resolution on the scanning data using parameter set A, the dash-dotted green curve belongs to parameter set B and the dashed red curve shows the resolution on the simulated data.

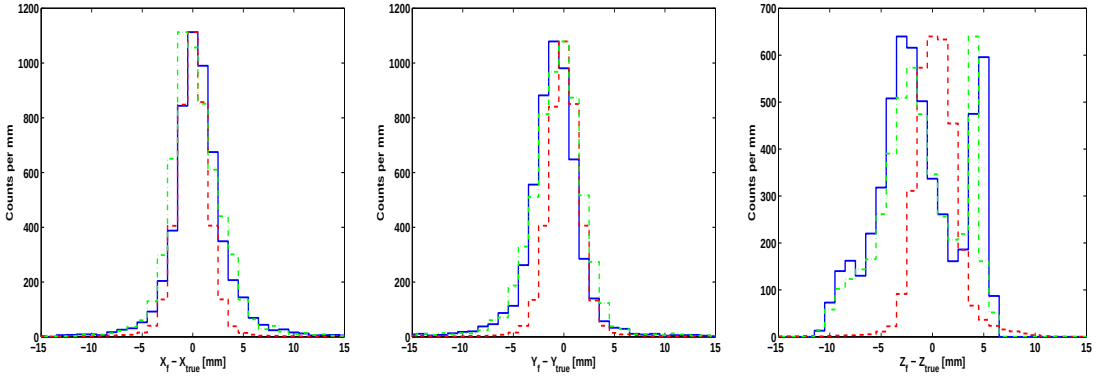

(a) Resolution of X. (b) Resolution of Y. (c) Resolution of Z.

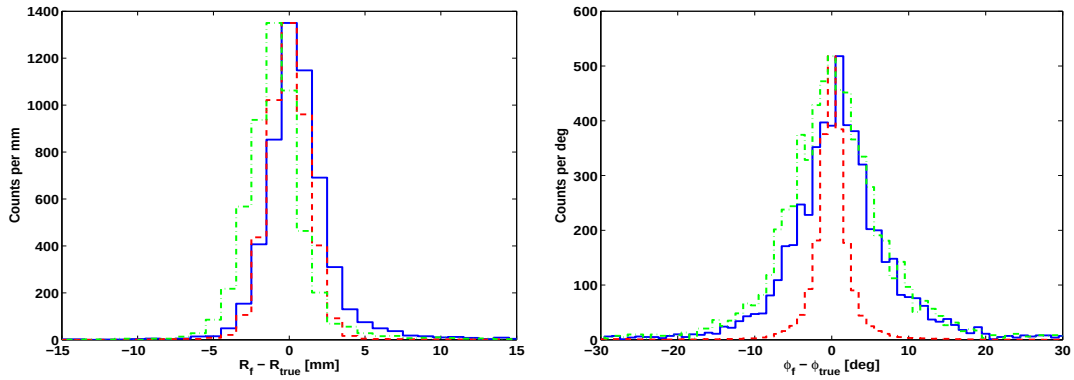

(d) Resolution of R. (e) Resolution of φ.

Figure 3.27: Resolutions of scanning events in segment row 6. The blue curve shows the resolution on the scanning data using parameter set A, the dash-dotted green curve belongs to parameter set B and the dashed red curve shows the resolution on the simulated data.

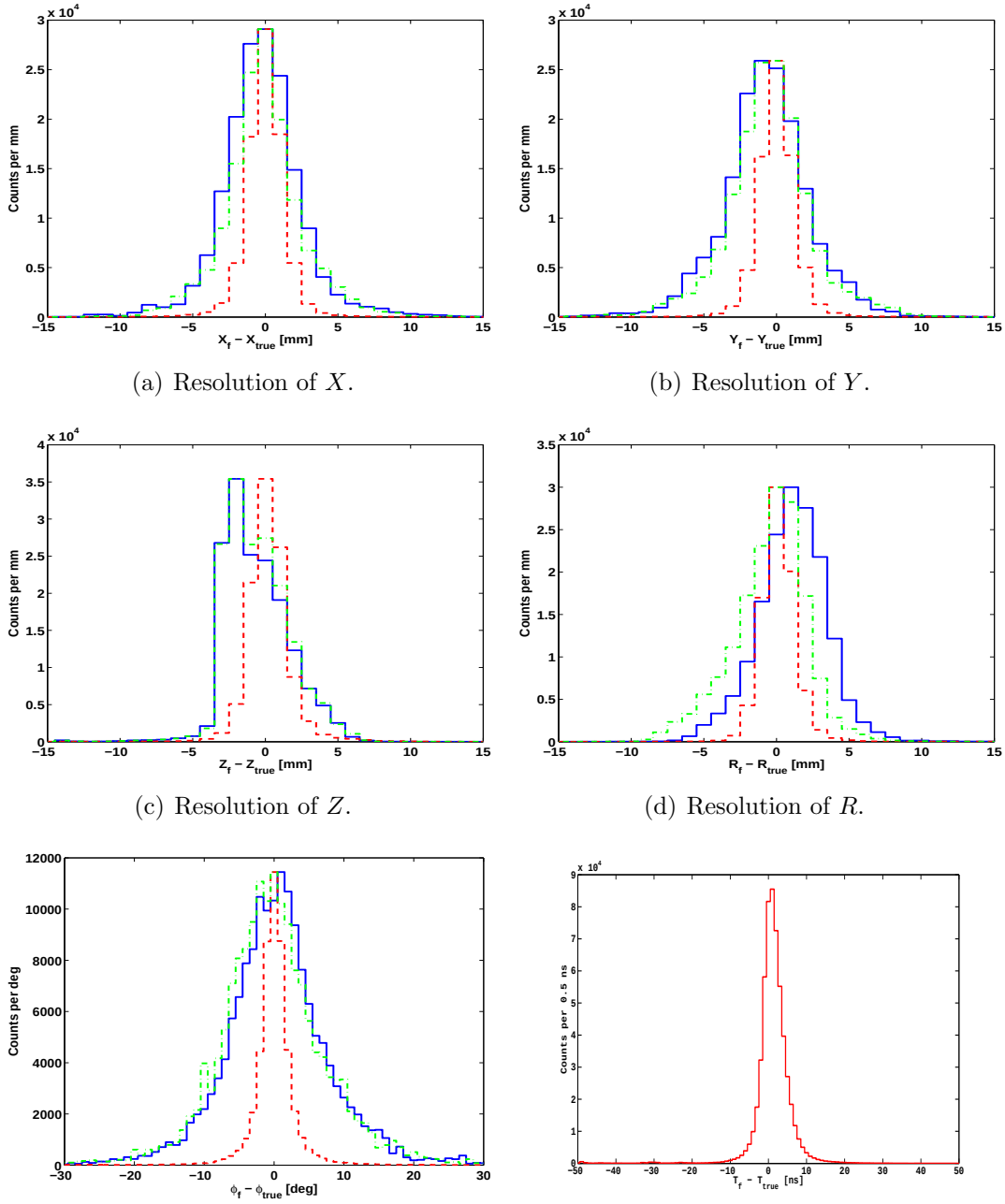

(a) Resolution of X.

(b) Resolution of Y.

(c) Resolution of Z.

(d) Resolution of R.

(e) Resolution of φ.

(f) Timing Resolution of extensive search.

Figure 3.28: Resolutions of all scanning events. The blue curve shows the resolution on the scanning data using parameter set A, the dash-dotted green curve belongs to parameter set B and the dashed red curve shows the resolution on the simulated data. The timing resolution of the simulated data set is plotted in (f) and has a FWHM of 5.4 ns.

nate in the first four segment rows, while the resolution of the angular coordinate is the most skewed distribution. As well, almost all distributions are leptokurtic, i.e. positive excess kurtosis (see app. E.3), indicating *super*-Gaussian distributions[6]. Only the Z resolutions have in some cases a similar excess kurtosis to that of the normal distribution. The actual values of skewness γ_1 and excess kurtosis γ_2 for each of the distributions are given in appendix A. The radial distributions show a systematic offset for both parameter sets (see tab. 3.4) and a possible explanation for this behavior will be given in section 3.7. Additionally, the angular resolution shows the biggest difference with regard to the simulated data set (see also tab. 3.3). The results are also summarized in tables 3.3, giving the

Segment Row	X [mm]	Y [mm]	Z [mm]	R [mm]	φ [°]
1	4.8/4.9/2.4	5.4/5.0/2.5	2.1/2.1/2.6	7.1/7.2/2.5	10.4/13.0/3.7
2	3.9/3.7/2.4	4.4/4.5/2.3	4.6/5.2/2.5	3.9/3.2/2.2	10.7/12.2/3.5
3	5.2/3.1/2.6	4.8/4.7/2.6	4.2/3.7/2.5	3.9/3.2/2.4	10.8/10.4/3.4
4	5.2/3.7/2.9	6.0/4.9/2.8	5.1/4.5/2.7	5.2/4.1/2.8	8.2/8.3/3.1
5	5.6/4.7/3.1	5.2/5.1/3.1	4.4/3.9/4.4	3.9/4.0/2.9	11.8/15.0/3.0
6	4.0/4.6/3.3	4.4/4.8/3.4	5.2/9.2/4.5	3.4/3.4/3.1	7.3/10.1/3.2
All	4.8/3.8/2.6	5.2/4.9/2.6	4.6/4.8/2.7	4.9/4.6/2.5	11.5/11.7/3.4

Table 3.3: Resolutions for single event data, given in FWHM, as function of segment row. The values, from left to right, belong to parameter set A, set B and the simulated data and are given in the same colors as the curves in figures 3.22 through 3.28

FWHM of the position resolutions, 3.4 giving the median 3D distance between the correct and found solutions and 3.5 giving the percentage of events resolved within $\pm 3\,mm$. The values in each table are shown in the same colors as the curves in figures 3.22 through 3.28. Overall parameter set B clearly outperforms set A from segment row 3 onward, especially in terms of the percentage of well resolved events listed in table 3.5.

Looking at the individual results, the Z-resolutions in rows three and four are comparable in terms of well resolved events (see tab. 3.5) and in row 5 the FWHM values are absolutely comparable (see tab. 3.3). However, the results in rows one and six are in need of some further explanation. Segment row one covers the region with the highest gradient of the electric potential (see fig. 3.4) and larger errors of the calculated potential can be expected due to the $0.5\,mm$ grid size. Additionally, the rise times are fastest in the front segments and hence will have the strongest contribution of derivative crosstalk to the actual pulse shape. The corresponding reduction of the amplitude of the upper neighboring segments transient signal causes the search algorithm to find the best matching

[6]These feature a higher and narrower peak but also stronger tails than a normal distribution (see fig. E.1(b)).

Feature	Row 1	Row 2	Row 3	Row 4
Median 3D [mm]	3.9/4.5/1.5	3.4/3.5/1.5	3.3/2.7/1.6	3.5/3.0/1.9
Mean Radial Offset [mm]	0.5/−1.7/0.3	1.2/0.2/0.1	1.6/0.5/0.0	1.5/0.2/0.1
	Row 5	Row 6	All	
Median 3D [mm]	3.8/3.5/2.2	5.7/5.1/4.3	3.6/3.5/1.7	
Mean Radial Offset [mm]	1.0/−0.3/0.1	0.7/−0.7/0.4	1.1/−0.5/0.1	

Table 3.4: The median 3D distance between the correct position and the found solution and radial offset for each segment row. The values, from left to right, belong to parameter set A, set B and the simulated data and are given in the same colors as the curves in figures 3.22 through 3.28

Segment Row	X [mm]	Y [mm]	Z [mm]	R [mm]
1	84.6/72.9/97.4	74.6/71.2/98.1	91.6/91.5/97.7	76.7/63.9/97.2
2	82.5/81.6/97.5	82.4/81.5/98.0	94.2/91.7/97.9	92.9/97.8/99.0
3	84.4/91.5/97.5	80.1/89.2/97.9	97.1/97.9/97.7	86.3/96.9/99.3
4	85.8/89.8/96.6	80.1/87.7/93.7	94.0/94.4/95.3	82.8/94.5/98.1
5	84.0/84.8/96.0	80.4/83.8/95.7	82.9/84.6/94.5	86.0/91.1/97.8
6	84.2/83.8/95.1	84.3/82.8/94.6	49.8/55.0/92.8	90.7/89.2/97.8
All	84.5/82.6/97.1	78.4/80.9/97.1	92.2/92.4/96.8	82.9/83.6/98.1

Table 3.5: Percentage of events resolved within $\pm 3\,mm$ as function of segment row. The values, from left to right, belong to parameter set A, set B and the simulated data and are given in the same colors as the curves in figures 3.22 through 3.28

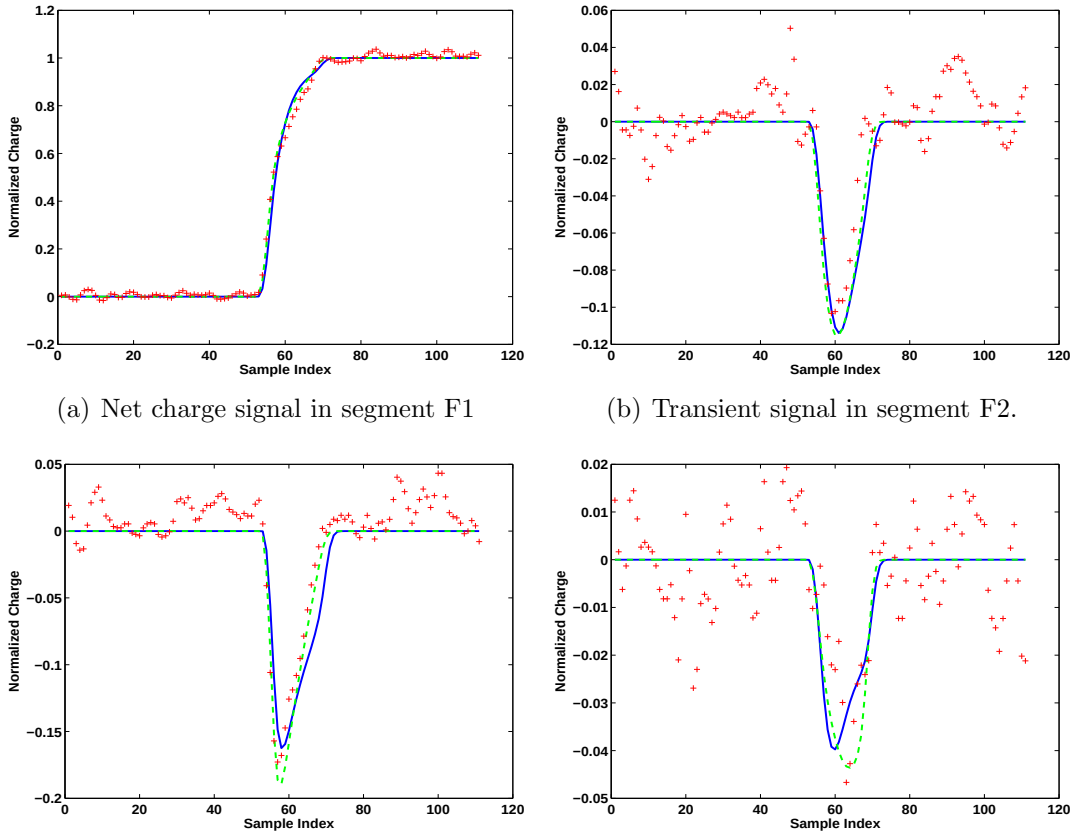

(a) Net charge signal in segment F1

(b) Transient signal in segment F2.

(c) Transient signal in segment A1.

(d) Transient signal in segment E1.

Figure 3.29: Comparison between scanned (red, +) and simulated signals for an interaction in segment F1. As can be seen in (b) the simulated transient signals in segment F2 still have a too large amplitude although their locations are at the absolute front of the detector. The nominal location of the scan point is (x,y,z)=(16.3,-11.7,3.1), the location found with parameter set A (blue, solid) is (11.75,-11,1) and (13.75,-11,2) with parameter set B (green, dashed).

signals to the scanning signals at $z = 3.3\,mm$ at the utmost front of the basis set at $Z = 1\,mm$ (see figs. 3.22(c) and 3.29). Figure 3.29(b) clearly shows the amplitude of the simulated transient signals in the upper neighboring segment is still to large at these locations. Excluding these events changes the FWHM of the Z resolution to $3.6\,mm$ for parameter set A and $3.2\,mm$ for parameter set B. The median 3D distance decreases to $2.5\,mm$ and $2.6\,mm$ respectively, a fact that is easily explained since at a depth of $z = 14.8\,mm$, which is inside the physical boundaries of the second segment row (see fig. 3.5), the number of basis points with a well matching transient signal, which will inevitably have a large amplitude, in the upper neighboring segment is rather low. Concerning the result in row six it should be noted that, due to the crystal being completely coaxial in this area, only the transient signal in the lower neighboring segment carries information on the Z-position of the γ-ray interaction. Conversely, the net charge signal in the first five segment rows also contains information on the Z position due to the tapering of the crystal. The results for parameter sets A and

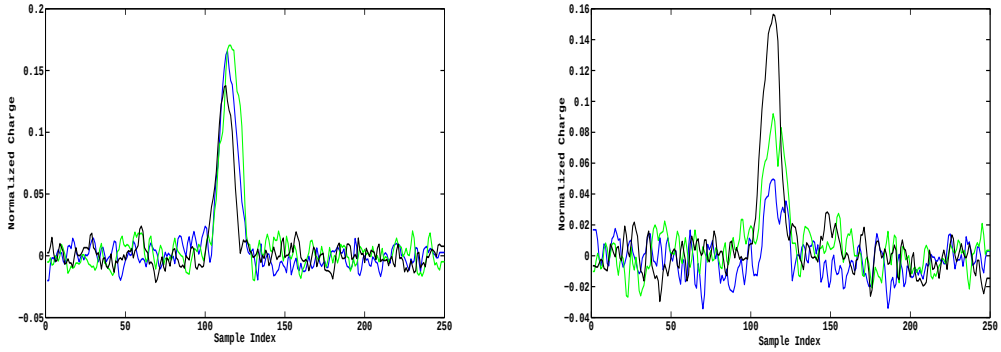

(a) Transient signal in segment B6.

(b) Transient signal in segment A5.

Figure 3.30: Comparison of three scan signals in segment A6 with the same nominal position close to the boundary with segment B6. The great scatter in transient amplitude, especially in (b), is obvious and related to the limited precision of the scanning setup.

B suffer from the limited precision of the scanning setup and subsequent large variation in signal shape, evident in figure 3.30. The amplitude of the transient signal in segment A5 varies by more than a factor of two (see fig. 3.30(b)) causing the found positions to be systematically shifted to lower Z values (black curve), close to the nominal position (green curve) or shifted to larger Z values (blue curve). Judging from the achieved resolutions the nominal green curve seems to be the exception rather than the rule. Parameter set B resolves the radial coordinate far better than set A with more than 90% of well resolved events (see tab. 3.5) and a better FWHM for most segment rows (see tab. 3.3). This hints at a better match with the experimental rise times for set B (see sec. 3.7). The

angular resolution, by contrast, shows the biggest deviations from the optimal values and also between the two parameter sets. The latter is not that surprising since the parameter sets do not only lead to different signal rise times at a given position, but also to different amplitudes of the transient signals (see fig. 3.31). Additionally, the angular resolution suffers the most from the lack of a derivative crosstalk correction since it is solely determined by the transient signals in the left and right neighboring segments. Rather surprisingly the angular resolution for set A is best in row six, while row four produces the best results for set B. The last point to mention concerns the median 3D distance, its limit increases from the front to the back of the crystal, in line with the reduced position sensitivity due to larger segments and the increasing position uncertainties of the setup. This feature is not reproduced by either parameter set although the last segment row also has the largest median distance for both parameter sets. However, the deviation form the limit is smaller than in the front segment rows suggesting that the current scanning setup is not sensitive enough to detect this characteristic. Overall the results are best in the middle of the crystal, rows three and four, with parameter set B performing within the limits set for PSA (see tab. 4.1).

3.7 Discussion

The two main issues to discuss are the precision of the simulated data on one side and the performance of the scanning system on the other side. Regarding the latter, a new data acquisition system for the scanning setup in Liverpool is being installed which will considerably increase the quality of the data. The segment signals will all be time aligned, as with the AGATA DAQ (see sec. 2.2), allowing for a determination of the derivative crosstalk component. This is very important for a precise comparison with the simulated data set. Additionally, the position uncertainties of the setup could be significantly reduced by employing the scanning method from (Crespi et al., 2008). The basic idea of the *Pulse Shape Comparison Scan* (PSCS) is to use a collimated source and illuminate the crystal from two perpendicular position (see fig. 3.32), (a) and (b). The pulse shapes from both data sets are then compared by calculating all χ^2 values between one pulse shape from position (a) and the other pulse shape from position (b). Naturally, the only time a good agreement between both signals can be found is if they belong to the same location within the crystal (see next paragraph). According to the authors a position uncertainty of $\sigma_{x,y,z} < 1\,mm$ can be achieved by selecting a stringent χ^2 threshold and a full detector characterization should take only one week.

Concerning the simulation there are a few things to mention. First of all during the course of this work it was found that, contrary to previous beliefs, the radial distribution of impurities, e.g. either flat or with linear gradient, has no significant influence on the pulse shape given that both distributions have the

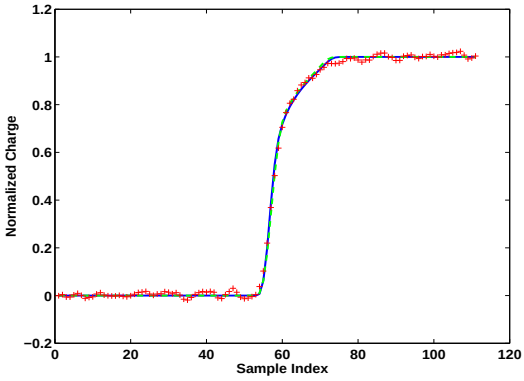

(a) Net charge signal in segment A4

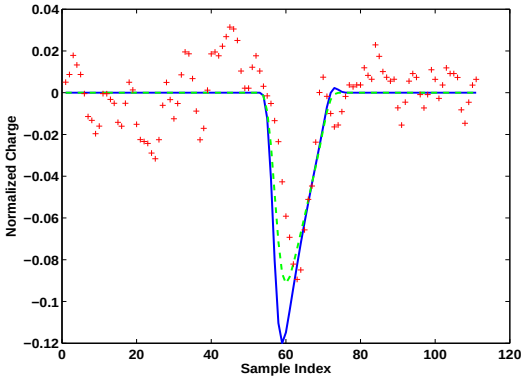

(b) Transient signal in segment A5.

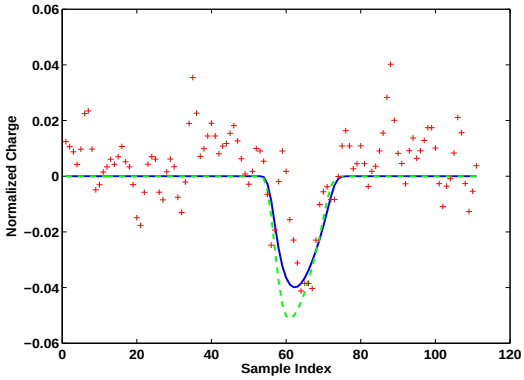

(c) Transient signal in segment A3.

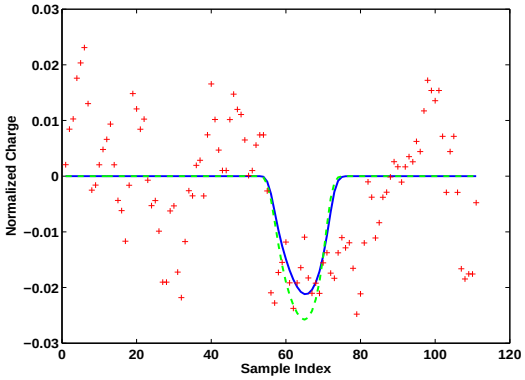

(d) Transient signal in segment B4.

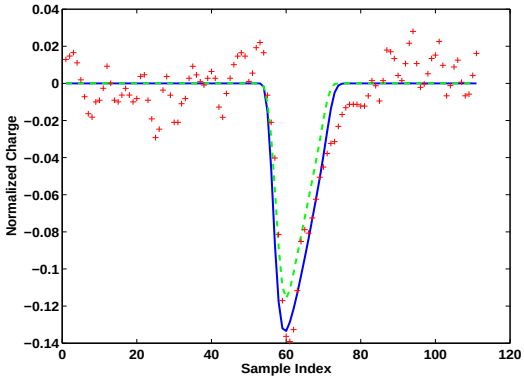

(e) Transient signal in segment F4.

Figure 3.31: Comparison between scanned (red, +) and simulated signals for an interaction in segment A4. The nominal location of the scan point is (x,y,z)=(28.3,-13.6,47.7), the location found with parameter set A (blue, solid) is (29.75,-11,52) and (28.75,-12,49) with parameter set B (green, dashed).

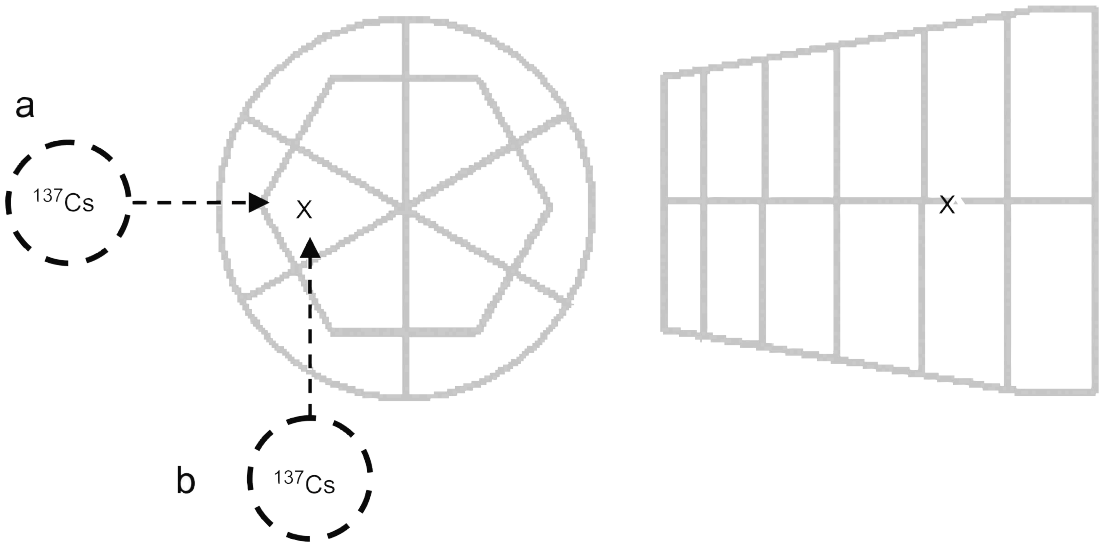

Figure 3.32: Illustration of the PSCS characterization technique. The crystal is illuminated by a collimated source from two perpendicular positions and the recorded pulse shapes will only be similar, producing a low χ^2 value, at the crossing point of the lines defined by the source collimation. This figure was taken from (Crespi et al., 2008).

same average impurity concentration for a given Z-layer. The sum of squares difference (SSD) between pulse shapes calculated with either impurity distribution is two orders of magnitude below the average SSD of 0.07 for pulse shapes located $1\,mm$ apart from each other. However, a determination of the actual impurity distribution is important in its own right since firstly the values given by the manufacturer are too high in order for the detector to be fully depleted at the given voltages, at least according to the theory for true coaxial detectors (Eberth, 2008), and secondly the distributions in Z show a suspiciously perfect linearity for all detectors (see fig. 3.2). The AGATA group at the University of Cologne will measure the detector capacitance, which depends on the depleted volume and hence the impurity distribution, as a function of applied voltage and will try to reconstruct the actual impurity distribution by calculating the electric potential, as described in section 3.2.2, and therewith the detector capacitance. Also, it could be possible to determine whether or not there is an interdependence between mobility parameters and impurity distributions by combining the above measurements with the PSCS characterization method. A second important issue is the performance of the interpolation method and the precision of the Poisson solver (see sec. 3.2.2). The overall performance of the interpolation routine is outstanding with equation 3.26 being fulfilled throughout 97.6% of the detector volume with relative errors smaller than 0.5‰ and the typical deviations of the calculated core signal from the inverse sum of all segment signals (see

eqn. 3.27) are of the order of 10^{-8}. Figure 3.33 shows one of the worst cases

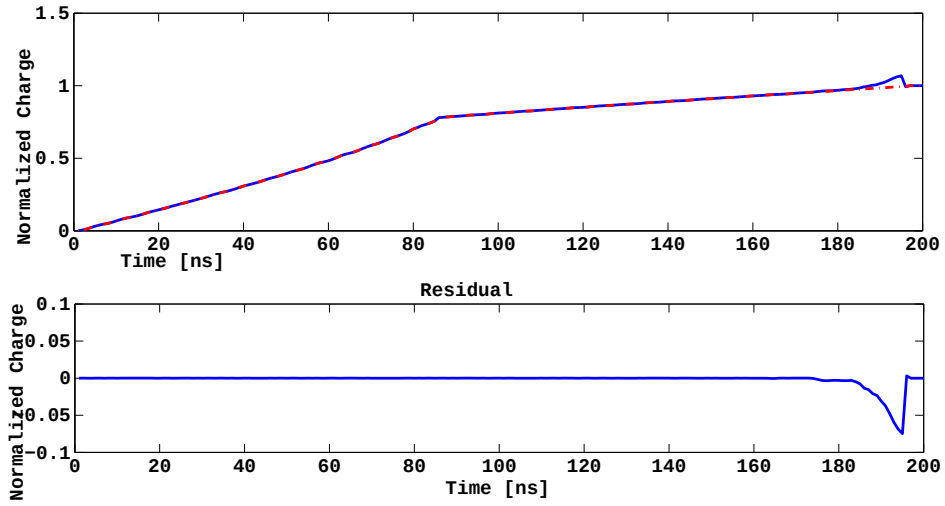

Figure 3.33: Comparison between the inverse sum of the segment signals and the core signal for the worst case. The upper panel shows the sum signal in blue and the core signal in a red dash-dotted line. The lower panel shows the residual, which is only significant at the end where the trajectory of the holes gets close to the segment boundary.

with the sum of segment signals significantly overshooting toward the end. In this exemplary case the trajectory ends at the lower right edge of the hit segment electrode. As the interpolation routine smooths the discontinuous drop from unit charge to zero at the segment boundaries (see fig. 3.14), the weighing potentials of the three neighboring segments are assigned too large values causing the sum of all weighting potentials (see 3.26) to be larger than unity and in turn the segment signal to overshoot the core signal. The first $0.5\,mm$ after the front side electrodes prove to be rather difficult as well, even more so in the center region with the six pointed tips of the electrodes. Since the precision of the calculated electric potential in the area between the core contact and the front side electrodes is also worse than in the rest of the detector an increase in resolution would improve both precisions. The only possibility with the current approach is to selectively reduce the step size in Z direction to 0.25mm and still keep the memory requirements down to manageable amounts. However, this would not improve the interpolation performance near the remaining segment boundaries. The most demanding possibility would be to use an adaptive multigrid solver (see e.g. (Trottenberg et al., 2000),pages 356 ff.), which uses cubes of adaptive size to discretize the problem to solve with the size being chosen according to the de-

sired precision and adapted to the local gradients. Concerning a good agreement between simulated and experimental signals, though, the charge carrier mobility parameters and the derivative crosstalk are the most important components. In absence of the latter, no final conclusion on the examined parameter sets can be drawn, although neither seems to achieve a very good match with the scanned data set throughout the detector. Yet, the systematic deviations of the radial

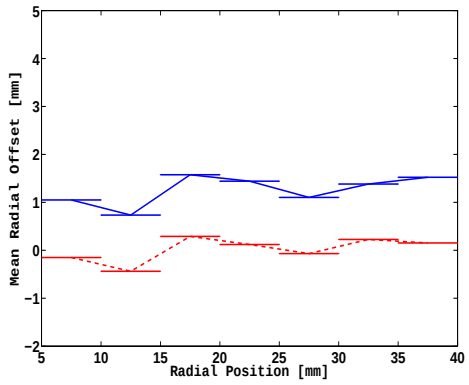

(a) Mean radial offset in segment row 3.

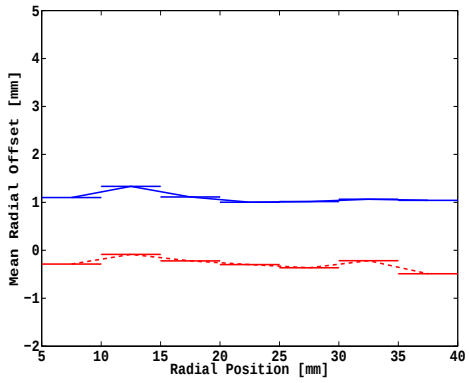

(b) Mean radial offset in segment row 4.

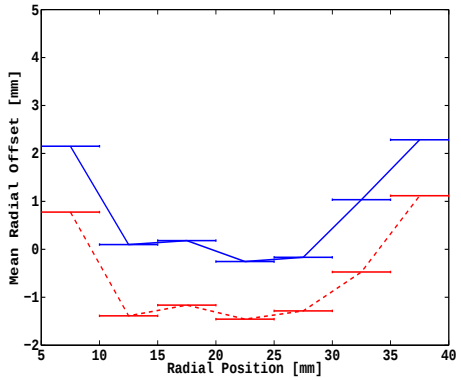

(c) Mean radial offset in segment row 5.

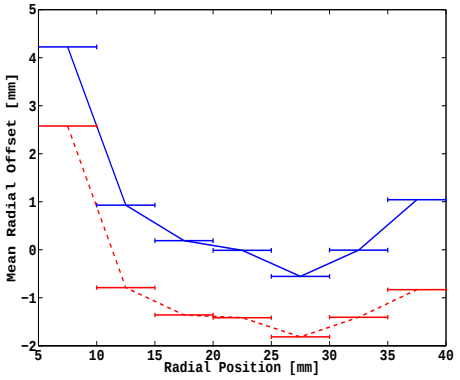

(d) Mean radial offset in segment row 6.

Figure 3.34: This figure shows the mean radial offsets between the found and correct radial position in segment rows 3 through 6 as a function of the correct radial position. The individual values were calculated within intervals of 5 mm, indicated by the horizontal bars with the lines being drawn to guide the eye. The red dashed line corresponds to parameter set B, and the solid blue line to parameter set A. The average absolute displacement with the simulated data set is smaller than $0.4\,mm$.

coordinate (see fig. 3.34), predominantly influenced by the net charge signal and thus not influenced by derivative crosstalk, allow for some conclusions regarding the relation of the true drift velocities and signal rise times to those of the

used parameter sets (see tabs. B.1 and B.2). However, this is only true from segment row three onwards as there is a considerable vertical drift component in the first two segment rows, preventing a clear relation between the drift time and the radial position. Therefore, figure 3.34 shows the mean deviation between the found and correct radial positions as function of the correct radial position in bins of $5\,mm$ width only for segment rows three through six. As can be seen, parameter set B reproduces the drift velocities rather accurately in rows three and four with the offsets being of the order of $0.5\,mm$. Conversely, the radial offsets of parameter set A are always around $1\,mm$ indicating too slow drift velocities. The deviations grow larger in segment rows five and six, yet both follow the same systematic.

This is likely related to the influence of the passivated layer at the back of the crystal. This layer can be up to $7\,mm$ thick and reduces the electric field strength (Eberth & Simpson, 2008). Taking the significant position uncertainties of the scanning setup into account an optimization of the mobility parameters and subsequent optimization of the radial offsets, is only meaningful when using the PSCS method, described above.

Chapter 4

Pulse Shape Analysis

Pulse shape analysis (PSA) is the single most important issue in the AGATA DAQ as it is impossible to reduce the data to manageable amounts without a working PSA (see sec. 2.2). It's goal is to reconstruct in real time and with high precision the position, energy and time of each individual γ-interaction based on the recorded pulse shapes. Previous attempts on data from the MARS detector were successful in achieving a good position resolution of $2-8\,mm$ (FWHM), yet only on a timescale of around $1\,s$ (Kröll & Bazzacco, 2006), too long for the real time DAQ of AGATA. In the following section the requirements of the AGATA PSA, the basic approach taken and the challenges involved will be discussed. Feedforward neural networks, used to determine the event time, will be introduced in section 4.2. The interaction positions will be reconstructed by a particle swarm optimization algorithm, delineated in section 4.3.

4.1 Introduction to AGATA PSA

As was already mentioned the aim of PSA is to determine the number of interactions in a segment or crystal and to reconstruct the positions, time and the deposited energy of each individual γ-ray interaction by analyzing the recorded experimental traces. The real-time frame work of the AGATA DAQ and the requirements of the tracking algorithms demand stringent performance requirements for the PSA algorithm summarized in the following table.

Parameter	Requirement
Position Resolution	$\leq$ 5mm (FWHM)
Energy Resolution	$\sim 3\,keV$
Time Resolution	$< 10\,ns$
Computing Time	$\sim 1\,ms/CPU$

Table 4.1: The performance requirements for the PSA algorithm.

The PSA utilizes the strong dependence of each single pulse shape on the interaction location. Yet the complete information on the interaction location is not stored in a single pulse shape but in the combination of pulse shapes (see fig. 4.1). The transient traces in the neighboring segments to the left and right of the hit segment are most sensitive to the angular position of the interaction while the segments above and below record the most information of all crystal segments on the distance from the front face. The amplitudes of these transient signals depend in a highly non-linear fashion on the distance of the charge carriers trajectory to the neighboring segments. The radial coordinate has the biggest influence on the net charge signal and to a significant extent on the core signal. If one of the charge carriers is collected a discontinuous drop in the current occurs, recorded as a kink in the charge signal (see fig. 3.11). Its position in time gives information on the electron drift time t_d^e and hence the radial position of the interaction. However, the attainable position resolution is not only limited by electronic noise

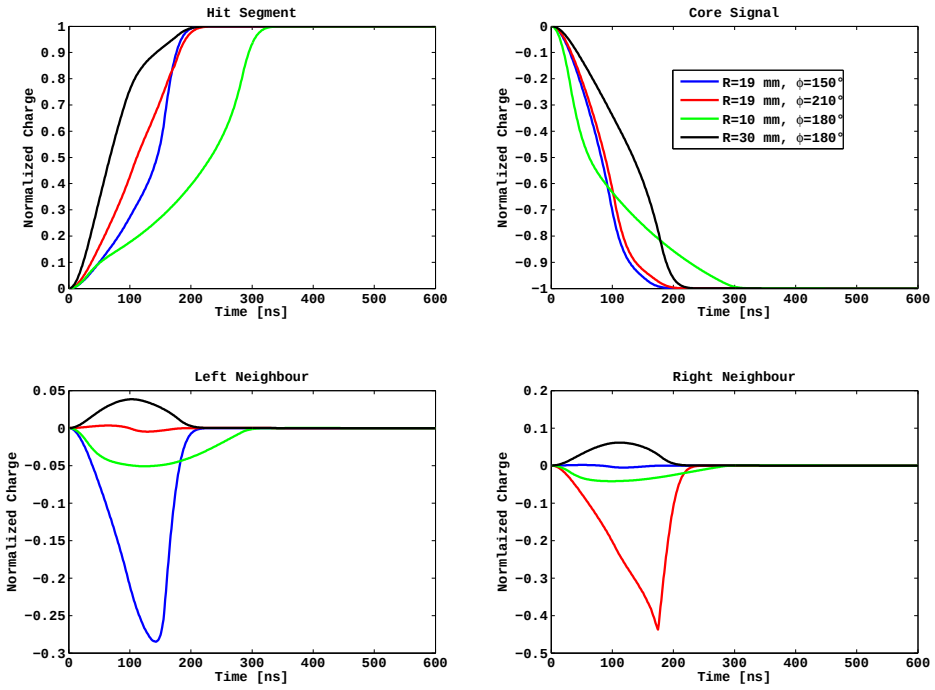

Figure 4.1: The dependence of the pulse shapes on the interaction location. The red and blue shapes differ only in their angular position yet the core signals are almost identical and the net charge signals in the hit segments differ only marginally. The transient signals in the left and right neighbors, shown in the lower panel, by contrast, are easily distinguished. The opposite is observed for the black and green shapes representing two different radial positions.

and the performance of the PSA algorithm but also by the mean free path length of the electron involved in the γ-ray interaction. Precisely speaking, the position reconstructed by the PSA is the location of the electron's interaction with the germanium crystal which can be up to a mm away, dependent on the energy, from the position of the γ- ray interaction. Thus the detector resolution is limited by physics already at an energy deposit of a few MeV in a single γ-ray interaction.

4.1.1 Basic Approach and Challenges

In a simple PSA approach, like the *steepest slope method*, the above mentioned kink in the net charge signal is used to extract the radial position information (Gámir, 1997). As another example the *recursive subtraction algorithm* uses the number of current pulse maxima, coinciding with the position of a kink to retrieve the total number of interactions (Crespi et al., 2007). However, none of these methods allow a full position reconstruction as demanded for by AGATA.

The approach taken for the AGATA PSA is quite different and more global. A pulse shape basis is simulated by JASS on a 3D regular rectangular grid with $1\,mm$ spacing (see fig. 4.2). This means that for each point on the grid a full set of 37 pulse shapes with a $1\,ns$ step and a trace length of 600 ns is generated and stored in the besis. This basis is sorted in ascending order by the hit segment names, i.e. the segments recording the net charge signal. The interaction

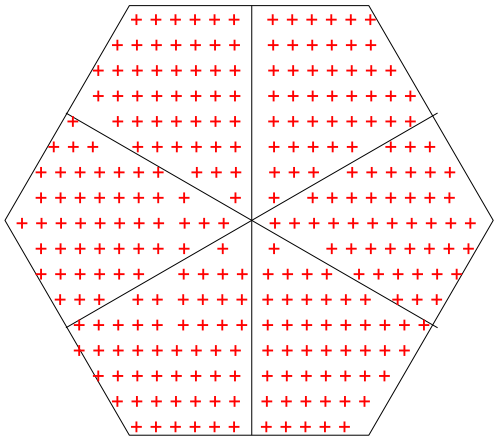

Figure 4.2: A sample grid of interaction locations. For each point in the grid the corresponding pulse shape is calculated. The PSA algorithm then searches only within this basis.

position is reconstructed by comparing the recorded experimental signal directly with the basis signals in the hit segment and identifying the location of the best fitting basis signal with the interaction position. However, a comparison between the signals is only useful within the region of interest containing the position information. Any offset in time would add non-physical components to the fit result (see fig. 4.3), making a precise time alignment compulsory. Since the GTS system (see sec. F.3) ensures that all experimental traces of the individual segments and the core are aligned in time, it suffices to determine the event time, or start time t_0 of the traces relative to the physical interaction of

the γ-ray in the detector material, for just one signal. The core signal has the least dependence on location (see fig. 4.1) and interaction multiplicity and thus is best suited to determine t_0 independent of the position reconstruction. The independent determination of t_0 removes one parameter from the PSA search space and simplifies the remaining task considerably. Additionally, the reduced variability of the core signal facilitates the use of neural networks to determine t_0 (see sec. 5.1).

The description so far concentrated on single interactions only. While there is no principal difficulty preventing the chosen approach to be used for events with multiple interactions in the crystal, the task becomes a lot more challenging. The particular challenge lies in the binomial growth of the search space with interaction multiplicity. Each segment contains between 5000 and 15000 grid points to be searched for agreement with the experimental signal. An extensive search, i.e. comparing the pulse shapes of each single grid point with the experimental signal, of the segments basis takes between 40 and 200 ms in the case of single interactions, just about in the performance requirements (see tab. 4.1). For the

Hit Segments	Number of Interactions				
	1	2	3	4	5
1	5.00E+003- 1.50E+004	1.25E+007- 1.12E+008	1.04E+010- 2.81E+011	2.17E+012- 1.76E+014	9.02E+013- 2.20E+016
2	X	2.50E+007- 2.25E+008	6.25E+010- 1.69E+012	1.56E+014- 1.27E+016	1.30E+017- 3.16E+019
3	X	X	1.25E+011- 3.38E+012	3.12E+014- 2.53E+016	7.81E+017- 1.90E+020
4	X	X	X	6.25E+014- 5.06E+016	1.56E+018- 3.80E+020
5	X	X	X	X	3.13E+018- 7.59E+020

Table 4.2: Number of possible basis point combinations depending on the event type. The lower limit is for segments with 5000 basis points and the upper limit is for 15000 basis points. Impossible combinations, e.g. 1 interaction in 2 segments, are marked by an X and in case there is more than one possibility for a given event type, e.g. four interactions in two segments can either be 3:1 or 2:2 distributed among the segments, the larger number is quoted in the table.

case of two interactions in the same segment the pulse shapes for each interaction have to be added, scaled linearly with energy, and the number of possible combinations of grid points grows to $1.25 \cdot 10^7 - 1.12 \cdot 10^8$, quickly ruling out the extensive search. In addition the energy of each interaction adds in total one more free parameter[1]. Table 4.2 summarizes the size of the search space for

[1]The total energy deposit in a segment is given by the front end electronics (see sec. F.3),

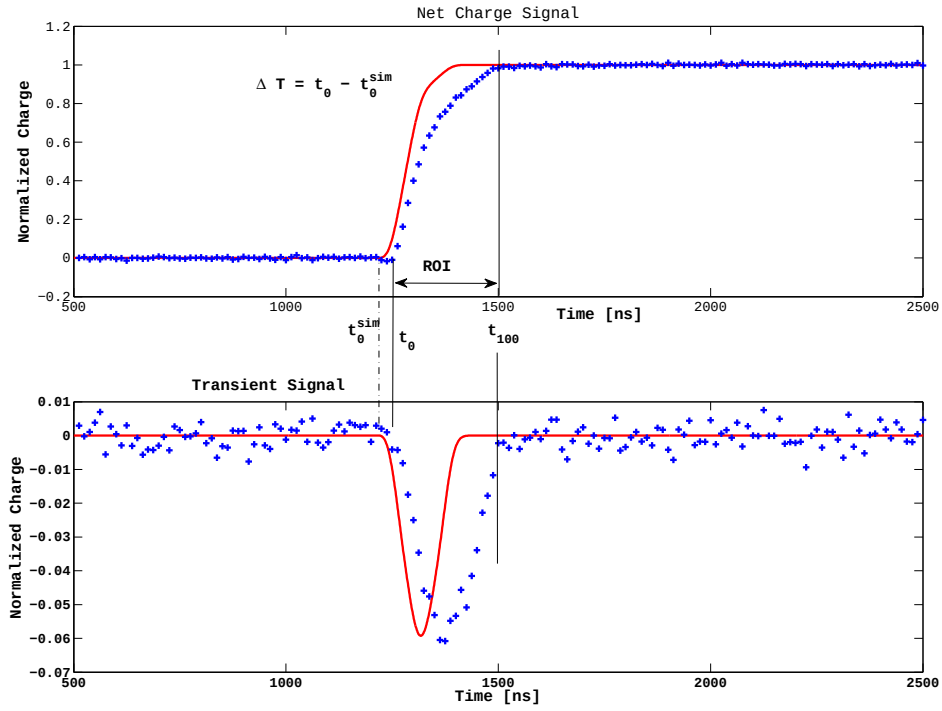

Figure 4.3: Sample comparison between a simulated (red) and experimental signal (blue). Any time shift ΔT between t_0 of the experimental signal and t_0^{sim} of the simulated signal will be the same for every segment signal, the GTS system ensures that all experimental signals are time aligned, and have an adverse effect on the position resolution capabilities. The region of interest (ROI) for PSA, i.e. the rising part of the net charge pulse containing the information on the location, is indicated by two vertical bars.

various multiple interaction events. These numbers exemplify the need for an intelligent search algorithm, like Particle Swarm Optimization (see sec. 4.3), for the position reconstruction. Other approaches like the matrix method (Olariu et al., 2006), which uses a non-negative least squares algorithm to assign energy deposits for all grid points simultaneously followed by a calculation of the energetic barycenters, have so far not been able to meet the requirements in terms of speed for these multiple

4.2 Feedforward Neural Networks

In AGATA PSA a neural network will be used to determine the event time t_0, i.e. the start time of the experimental signal (see fig. 4.3). The much more complicated task of position reconstruction will be performed by the particle swarm optimization (see sec. 4.3). The different types of artificial neural networks (ANN) that exist are almost as diverse as their field of use. Starting out from the simple perceptron developed by (Rosenblatt, 1958) and application to the XOR problem (Minsky & Papert, 1969) newer forms like Radial Basis Function networks (Bors, 2000) have been developed. Spiking Neural Networks (Bothe, 2003) are the latest development and claim to be one step closer to the biological original of a brain. Possible applications range from simple function approximations (Hornik, 1991) over artificial intelligence in computer games to help in controlling fighter jets (NASA, 2006). Feedforward neural networks (FNN) have been shown to be very efficient for problems of pattern recognition (Bishop, 1996), similar to the intended use of a neural network for AGATA. Therefore the following description will cover only FNN and introduce the topology and training methods for these types of ANN.

4.2.1 Topology of a network

The topology of a FNN is relatively simple yet still features massively parallel computations. The basic computational unit is a so called neuron, in reference to the neurons found in a brain. A FNN, however, is only an oversimplified version of a brain in the still limited understanding of a brains inner working. Basically only the idea of having small but independent computational units, the neurons, which are strongly interconnected, is used to form a working computer algorithm. Each neuron in the FNN has an internal state dependent on the received inputs and an activation function, which determines the neurons output. In order to assemble a FNN these neurons are arranged in separate layers. The input stage is counted as the networks first layer passing on its values to the neurons in the next layer. If this layer is already the final layer it is called the output layer giving

so for two interactions only the ratio of energy deposits for the two interactions has to be determined.

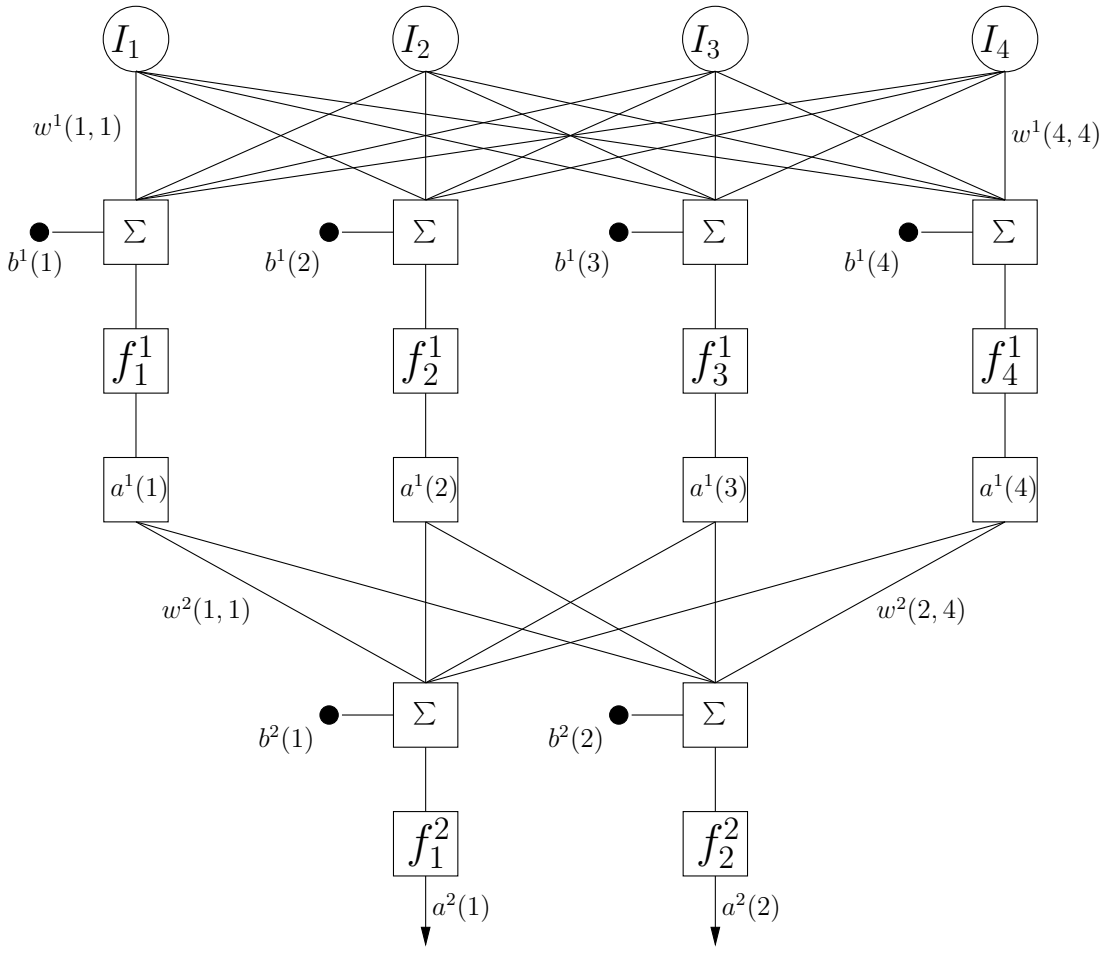

Figure 4.4: Topology of a two-layer feedforward network. The first layer is the input stage passing the values I_i after weighting with the weights $w^k(i,j)$ to the neurons in the hidden layer. Each neuron then adds its own bias $b^1(i)$ to the just calculated weighted sum of the inputs. The neurons output $a^1(i)$ is then computed by applying the activation function f^1 and sent to all connected neurons, but only in forward direction (from top to bottom in the picture). The networks outputs, in this example, are $a^2(1)$ and $a^2(2)$.

the final result of the networks computations. Any layer, located between the input and output layers is called a hidden layer. There is no limit on the number of hidden layers or the number neurons in a specific layer but these numbers define the capabilities of the network (Bishop, 1996). The defining characteristic of a FNN is the fact that there is no backfeeding of a neurons output to neurons situated in layers closer to the input stage or jumping over layers, i.e. neurons in layer m only pass their output to neurons in layer $m+1$. An exemplary setup of a FNN with one hidden layer is shown in figure 4.4.

The inner workings of a FNN are best described adopting the following notation:

- $w^k(i,j)$ weight of input from unit j in layer $k-1$ to unit i in layer k
- $b^k(i)$ bias to unit i in layer k
- $n^k(i)$ the input or internal state of the $i-th$ unit in layer k
- $f^k(n^k(i))$ the activation function of unit i in the $k-th$ layer
- $a^k(i)$ the activation or output of unit i in layer k
- N_k the number of units in layer k

Neuron i in layer k has its own unique set of weighted connections to all the neurons in layer $k-1$, however, the option exists to remove connections with marginal weights since these will only have a negligible influence on the neurons internal state given by:

$$n^k(i) \;=\; \sum_{j=1}^{N_{k-1}} w^k(i,j)a^{k-1}(j) \;+\; b^k(i). \tag{4.1}$$

The output of neuron i will hence be:

$$a^k(i) \;=\; f_i^k(n^k(i)). \tag{4.2}$$

The networks output is calculated by a layer wise application of the two formulas above. In the case of the network depicted in figure 4.4 the output of the two neurons in the output layer can explicitly be written as:

$$a^2(l) \;=\; f_l^2\left(\sum_{i=1}^{4} w^2(l,i)\cdot \underbrace{f_i^1\left(\sum_{j=1}^{4} w^1(i,j)I_j + b^1(i)\right)}_{a^1(i)} + b^2(l)\right) \tag{4.3}$$

with $l = 1$ or $l = 2$ respectively. The weights and biases are the parameters optimized in the training of the network (see sec. 4.2.3).

4.2.2 Activation Functions

The concept of FNN was introduced by (Rosenblatt, 1958)[2] using the Heaviside step function for activating the neurons and featuring no hidden layer. This not only limited the output to binary values but also the general applicability of such a network, e.g. function approximation demands a linear activation function in the output layer ((Hornik, 1991)). The three different activation functions, which are nowadays typically used are the

- Linear function: $a^k(i) = n^k(i)$
- Sigmoid function: $a^k(i) = \left(1 + \exp\left(-n^k(i)\right)\right)^{-1}$
- Hyperbolic tangent: $a^k(i) = \tanh\left(n^k(i)\right)$.

These differ in their range of application. The linear function is the only one which output can access the complete $\mathbb{R}$. Hence the activation function of the output layer for network used in function approximation has to be the linear function. The active region, the input interval for which the functions output is not saturated, of the sigmoid function is larger than for the tanh function (see fig.4.5), which can be advantageous if the inputs are spread over a larger interval. Also the limitation to outputs within $[0, 1]$ makes it the natural choice for approximating probabilities or possibly for the interpolation of weighting potentials (see sec. 3.3). Yet the tanh function is the most common choice, especially for neurons in a hidden layer. First of all the rather small size of its active region, from -1 to 1 allows for sharp decision boundaries, advantageous for pattern recognition. Secondly it allows a neuron to not only exert an excitatory but also an inhibitory influence on other neurons whilst its output range of $[-1, 1]$ is still limited in contrast to the linear function. Lastly is should be mentioned that the role of the bias is to move the zero-crossing point of the activation functions away from the origin.

4.2.3 Training and Validation

No mathematical prescription exists to calculate the weights and biases of a network solely based on its intended use other than in the most simple cases like the XOR-problem. Instead a network has to adapt its parameters in a learning process. There are two main, yet distinctively different learning paradigms for neural networks. In *unsupervised learning* only a set of input data I is given but the target output O of the network is not. The goal of the learning process is to optimize a given cost function $C(I, O)$ which can take on quite complicated forms. Typical tasks treated with unsupervised learning are clustering and estimation of statistical distributions and can generally be classified as estimation problems.

[2]The original name used in the paper was perceptron.

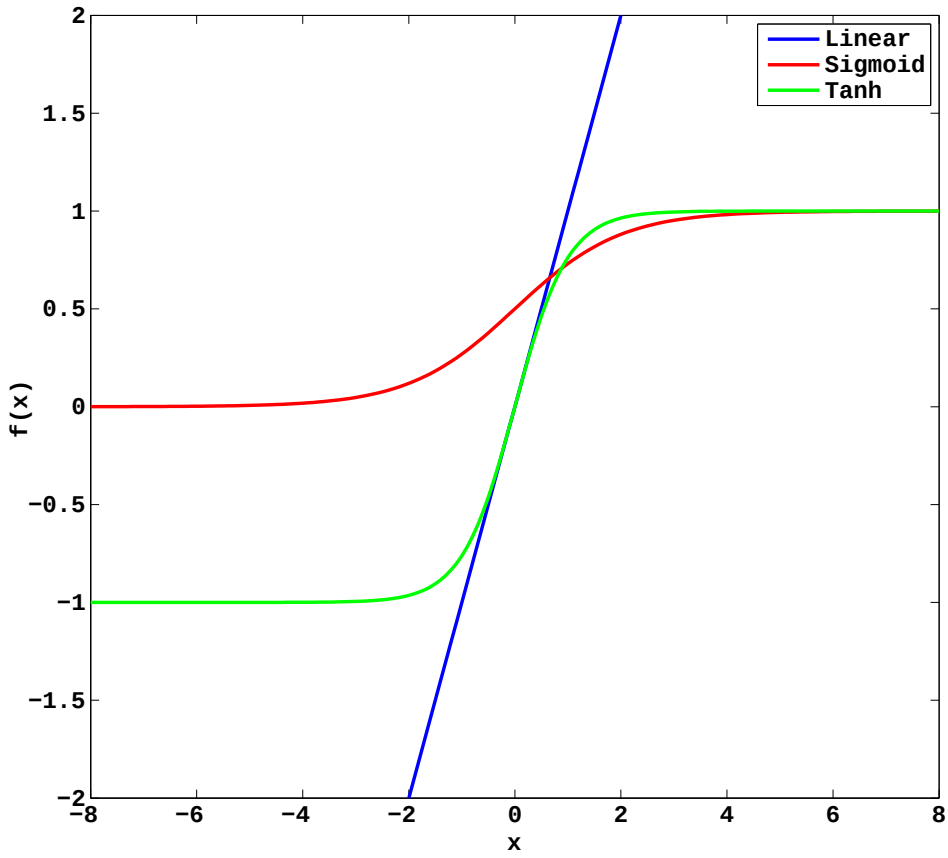

Figure 4.5: The three different activation functions typically used for FNN. Only the linear function can access the complete $\mathbb{R}$ and has an infinite active region, making it ideal to use for function approximation problems. The sigmoid function has a considerably larger active region, e.g. area of non-saturated output, than the tanh function and the smallest slope around the origin.

The neural network used for AGATA (see sec. 5.1) was trained using *supervised learning*. Under this paradigm pairs of input and output data are given and the goal of the training process is to approximate the unknown mapping $I \mapsto O$ with the neural network. During training the networks parameters are adjusted to optimize a cost function of the target output O and the actual output O', e.g. the least squares function $(O - O')^2$. However, not all available data should be used to train the network as otherwise it is more likely that the network will overfit the data and not find a proper generalization. For similar reasons the number of neurons should not be increased infinitely. This is easily understood looking at the example of function approximation where an increase in the number of neurons can be considered equivalent to increasing the order of the approximating polynomial (Bishop, 1996). A boundless increase of the number of neurons will thus lead to the network approximating the data including the noise instead of only the data or in the example of pattern recognition the network will simply memorize the training data as it is. The parts of the data not used for training should be used to validate the performance of the network after the training has finished. The aforementioned problems of pattern recognition and function approximations are characteristic examples for the use of supervised learning. In the following only supervised learning will be explained in more detail as it is the paradigm used for AGATA.

While the training of a network can in principle start out with parameters initialized randomly, (Nguyen & Widrow, 1990) provide a method of initializing the weights that allows to reduce the training time. For reasons of simplicity the method will be outlined for a network with a single input approximating an arbitrary function $g(x)$, with $x \in [-1; 1]$. The network will have one hidden layer with H neurons, each one having a tanh activation function and a single output unit with a linear activation function. Following equation 4.3 the networks output y is:

$$y = \sum_{i=1}^{H} w^2(1,i) \cdot \tanh(w^1(i,1)x + b^1(i)) = \sum_{i=1}^{H} y_i \tag{4.4}$$

The tanh function is almost linear with slope 1 within its active region which is determined by $w^1(i,1)$. Hence the different y_i are piece-wise linear approximations, with approximate slope $w^2(1,i) \cdot w^1(i,1)$, to $g(x)$ which are summed to form the complete approximation. Since the inputs x are from an interval of length 2 each neuron in the hidden layer, i.e. y_i, will be responsible for an interval of length $2/H$ on average whose bounds are

$$-1/w^1(i,1) - b^1(i) < x < 1/w^1(i,1) - b^1(i) \tag{4.5}$$

and is of length $2/w^1(i,1)$. However, $w^1(i,1)$ will not be set to H since it turned out that having a slight overlap between neighboring intervals is preferable and

$w^1(i,1) = 0.7H$ is used. The centers of each interval, given by $-b^1(i)/w^1(i,1)$, should be distributed randomly within the input interval of $[-1;1]$. Consequently, the bias values are initialized with

$$b^1(i) = \text{uniform random value between } -\left|w^1(i,1)\right| \text{ and } \left|w^1(i,1)\right|. \tag{4.6}$$

For the case of multiple inputs the reader is referred to the original publication.

In regular non-linear optimization a direct correspondence between all parameters to be optimized and the gradient of the cost function exists. This is not the case for neural networks since the cost function can only be calculated for the output of the final layer as only the desired outputs are given but no target values for the intermediate stages in the hidden layer(s) exist. Traditional optimization methods can therefore only adapt the parameters of the output layer and do not offer a possibility to propagate the errors to the hidden layers. This dilemma persisted for a long time and prevented the wide spread use of neural networks until the so-called *Back Propagation* algorithm was developed (Rummelhart et al., 1986). The first step consists of calculating the individual sum of squares error V_q for any of the Q input/output pairs

$$V_q = \frac{1}{2}(t_q - a_q^M)^T(t_q - a_q^M) = \frac{1}{2}e_q^T e_q, \tag{4.7}$$

with t_q the target output of the q-th training sample and a_q^M the output of the network with the current set of parameters. Minimizing each individual V_q also minimizes the overall performance metric of the network $\sum_{q=1}^{Q} V_q$ which would be used by traditional techniques. The weights and biases are adapted using an approximate steepest descent algorithm:

$$\Delta w^k(i,j) = -\alpha \frac{\partial V_q}{\partial w^k(i,j)} \tag{4.8}$$

$$\Delta b^k(i) = -\alpha \frac{\partial V_q}{\partial b^k(i)} \tag{4.9}$$

with the learning rate α a customizable parameter. Using equations 4.1 and 4.7 it can be shown that

$$\frac{\partial V_q}{\partial w^k(i,j)} = \frac{\partial V_q}{\partial n^k(i)} \cdot \frac{\partial n^k(i)}{\partial w^k(i,j)} = \delta^k(i) \cdot a^{k-1}(j) \tag{4.10}$$

$$\frac{\partial V_q}{\partial b^k(i)} = \frac{\partial V_q}{\partial n^k(i)} \cdot \frac{\partial n^k(i)}{\partial b^k(i)} = \delta^k(i) \tag{4.11}$$

with

$$\delta^k(i) = \frac{\partial V_q}{\partial n^k(i)} \tag{4.12}$$

the sensitivity of V_q to changes in the net input to unit i in layer k. The sensitivities satisfy the recurrence relation

$$\delta^k = \dot{F}^k(n^k)W^{k+1^T}\delta^{k+1}, \tag{4.13}$$

written for the complete layer k. The weight matrix W^{k+1^T} consists of all weights connecting layers k and $k+1$ and $\dot{F}^k(n^k)$ is a diagonal matrix with the diagonal elements

$$\dot{f}^k(n(i)) = \frac{df^k(n^k(i))}{dn^k(i)}. \tag{4.14}$$

The recurrence relation is initialized at the output layer with

$$\delta^M = -\dot{F}^M(n^M)(t_q - a_q). \tag{4.15}$$

The basic training cycle starts by passing the input data to the network, calculating the errors according to equation 4.7 and a subsequent use of equations 4.15, 4.13, 4.8 and 4.9.

The update of the weights can happen sequentially after each training sample has been presented to the network, this is called online training, or the weights are changed only after the complete training data set has been processed, called batch learning. The most simple approach to the latter is to sum up all the weight changes calculated for each training sample and adapt the weights accordingly, however, higher order methods provide a faster convergence. (Hagan & Menhaj, 1994) adapted the Levenberg-Marquardt (LM) algorithm ((Levenberg, 1944) and (Marquardt, 1963)), an approximate Newton's method, to train neural networks. Even though the latter method was used to train the networks for AGATA, a complete description is beyond the scope of this thesis but the basic idea is summarized here in a few sentences. LM minimizes the complete sum of squares error function over the whole data set instead of the sample wise error like the backpropagation method. The changes to the network's parameters, i.e. $\Delta w^k(i,j)$ and $\Delta b^k(i)$ are calculated by solving a system of linear equations given by the vector of errors for each neuron and the Jacobian matrix, whose elements are computed using the backpropagation equations with a slight change to equation 4.15:

$$\delta^M = -\dot{F}^M(n^M). \tag{4.16}$$

Given there are Q training samples and the network to be trained has O output units and P parameters to be adjusted, the size of the Jacobian matrix is $N \times P$ with $N = O \times Q$. Hence the LM-algorithm cannot be used to train very large networks since it would demand too much computer memory. In this case evolutionary algorithms like a genetic algorithm (Montana & Davis, 1989) or particle swarm optimization (Kennedy & Eberhart, 2001), described in the following section, are most commonly used.

4.3 Particle Swarm Optimization

Particle Swarm Optimization (PSO) was discovered as a byproduct of a simulation of a simplified social model of human behavior (Kennedy & Eberhart, 1995) and comprises a very simple concept to optimize nonlinear functions that is easily implemented and computationally inexpensive. PSO has its roots in evolutionary computation, e.g. genetic algorithms, and simulations of artificial life, in particular bird flocking, fish schooling and swarming theory. In the following section the basic ideas underlying any specific implementation of PSO are introduced, next the original canonical implementation and lastly the *Fully Informed Particle Swarm* (FIPS) are described.

4.3.1 Introduction

There were two key discoveries in the field of social biology which led to the development of PSO. First, simulations of bird flocking revealed that the underlying rules allowing birds to flock synchronously with sudden changes of direction or regrouping are local processes (see e.g. (Reynolds, 1987)). The unpredictable group dynamics of bird flocks are an emergent property of these local processes. The second key hypothesis, fundamental to the development of PSO, was that a social sharing of information can offer an evolutionary advantage. It was first stated by sociobiologist E.O. Wilson: 'In theory at least, individual members of the school can profit from the discoveries and previous experience of all other members of the school in the search for food. [This advantage] can become decisive, outweighing the disadvantages of competition for food items, whenever the resource is unpredictably distributed in patches' ((Wilson, 2000), p. 442). Eberhart and Kennedy used this as a basis for their simulation of human social behavior but a slight modification was inevitable. While fish in a school or birds in a flock cannot hold the same position without colliding, humans can hold the same belief without doing so.

The same is true for particles in PSO. The core component of PSO is a swarm of abstract particles moving throughout the search space of possible solutions to the problem investigated. A particle's position represents a candidate solution, e.g. the interaction location in PSA. Naturally two particles can have the same position, especially when the algorithm is close to convergence. Convergence is achieved through the continuous movement of the particles through the search space. This motion can be characterized as exploration of the search space in the early stages followed by exploitation of the local landscape when close to an optimum. The second main component is the neighborhood of a particle, i.e. the part of the swarm with which the particle exchanges information, given by the topology of the swarm (see fig. 4.6) and is not related to the particle's position in search space. The topology affects the search on a low level defining with whom a particle shares its information. Particles in the same local neighborhood tend

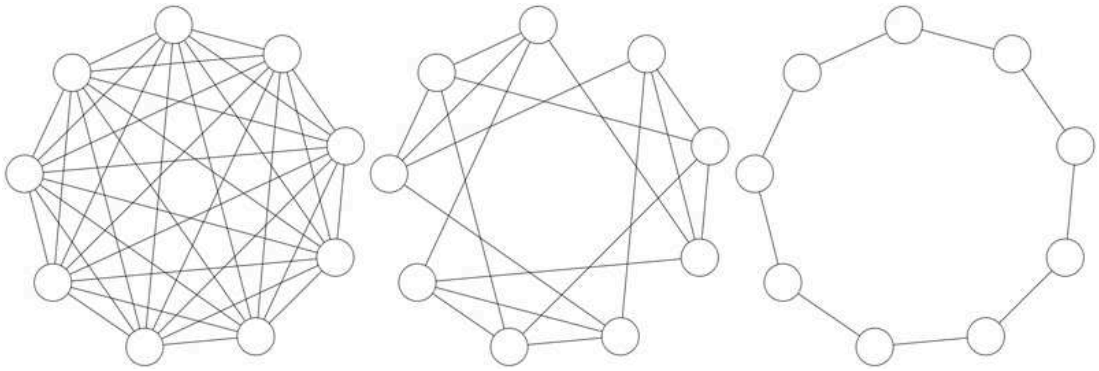

Figure 4.6: Possible topologies for a particle swarm. On the left a fully connected swarm, a.k.a. global neighborhood, is drawn with each particle exchanging information with all other particles in the swarm. Under the von-Neumann topology, shown in the middle, a particle only has 4 neighbors while this number reduces to two for the ring topology on the right. This figure was taken from (Mendes et al., 2004).

to explore the same regions in the search space. The relationships between local neighborhoods, as given by the topology, influence the search at a higher level. These features are common to any PSO implementation, which differ in the way the shared information affects a particles own motion.

4.3.2 Canonical Particle Swarm

The canonical version of the particle swarm optimization (CPSO) was introduced by (Kennedy & Eberhart, 2001) and iteratively searches a region defined by each particle's best previous position $\overrightarrow{P_{ib}^q}$, the best previous position $\overrightarrow{P_{nb}^q}$ found by any of its neighbors, current position $\overrightarrow{X^q}$ and previous velocity $\overrightarrow{v^q}$.

After a random initialization of each particle's position within the search space, the positions are updated iteratively following these equations:

$$\overrightarrow{v^{q+1}} = \chi \cdot \left\{ \overrightarrow{v^q} + r \cdot \varphi_1 (\overrightarrow{P_{ib}^q} - \overrightarrow{X^q}) + r \cdot \varphi_2 (\overrightarrow{P_{nb}^q} - \overrightarrow{X^q}) \right\} \tag{4.17}$$

$$\overrightarrow{X^{q+1}} = \overrightarrow{X^q} + \overrightarrow{v^{q+1}} \tag{4.18}$$

with r drawn uniformly and independently for each coordinate in the search space from $[0; 1]$. Earlier versions did not feature the constriction factor χ, which has to be smaller than 1 to ensure convergence, but a maximal velocity $\overrightarrow{V}_{max}$ heuristically defined to be half the dynamic range of the search space. (Clerc & Kennedy, 2002) give a formula to calculate the appropriate constriction factor for $\varphi_1 + \varphi_2 = \varphi > 4$:

$$\chi = \frac{2\kappa}{\varphi - 2 + \sqrt{\varphi^2 - 4\varphi}} \tag{4.19}$$

with $\kappa = 1.0$ leading to a slow enough convergence to ensure a thorough search of the problem domain. On most occasions φ_1 and φ_2 are chosen to be equal and the recommended value is 2.05 (Kennedy & Eberhart, 2001) which leads to $\chi = 0.7298$. While a maximal particle velocity is not necessary for convergence of the presented approach it can still improve the overall performance of the algorithm.

4.3.3 Fully Informed Particle Swarm

Irrespective of the neighborhood topology, a particle in the CPSO always exchanges information with just one other particle, the best performing particle in the neighborhood. However, this does not necessarily mean that no other particle in the neighborhood can provide viable information. In CPSO the most important source of variation is the difference between $\overrightarrow{P_{ib}^{q}}$ and $\overrightarrow{P_{nb}^{q}}$. The analysis in (Clerc & Kennedy, 2002) showed that more than these two information sources, weighted by $\varphi_{1/2}$, can be utilized since the algorithm is well behaved, in terms of convergence and explosion characteristics, if the constriction factor is calculated with equation 4.19, irrespective of the number of summands in $\varphi = \sum_{i=1}^{N} \varphi_i$. Following this line of thought (Mendes et al., 2004) proposed a change to the update equations 4.18:

$$\overrightarrow{v^{q+1}} = \chi \cdot \left\{ \overrightarrow{v^{q}} + \sum_{n=1}^{N_i} \varphi \cdot r \cdot \left(\overrightarrow{P_i^{q}} - \overrightarrow{X^{q}} \right) \cdot 1/N_i \right\} \tag{4.20}$$

$$\overrightarrow{X^{q+1}} = \overrightarrow{X^{q}} + \overrightarrow{v^{q+1}} \tag{4.21}$$

with N_i the number of neighbors and $\overrightarrow{P_i^{q}}$ the best position found by neighbor i. It is termed *fully informed particle swarm* (FIPS) since a particle uses information from all of its neighbors. Another difference to CPSO is that the particles memory of its past experience is restricted to the velocity term. Although it is possible to include the particle in its own neighborhood and hence include its previous personal best $\overrightarrow{P_{ib}^{q}}$ in the update equations, it was found to be beneficial if $\overrightarrow{P_{ib}^{q}}$ is excluded. The influence of the neighborhood topology on the FIPS performance was found to be profound (Kennedy & Mendes, 2006). However, a difference in the PSA performance could not be observed for any of the three recommended topologies. The performance of the two presented particle swarm implementations on common test functions for evolutionary algorithms was compared in (Mendes et al., 2004) and the latter always outperformed the canonical version. Consequently only the FIPS version is used for AGATA and it's performance for PSA is presented in the next chapter without further discussion of the topology.

Chapter 5

Application of PSA for AGATA

The approach to AGATA PSA taken in this thesis is to first determine the event time t_0 using a neural network (FNN) and then use the FIPS algorithm, presented in section 4.3.3, to reconstruct the individual interaction positions along with their associated energies. A proper evaluation of the performance requires the correct result to be known a priori and can hence only take place using simulated data, which nonetheless has to be as realistic as possible. JASS has already been verified in section 3.6 and shown to faithfully reproduce the original pulse shapes. However, realistic noise still has to be added to the simulated experimental traces.

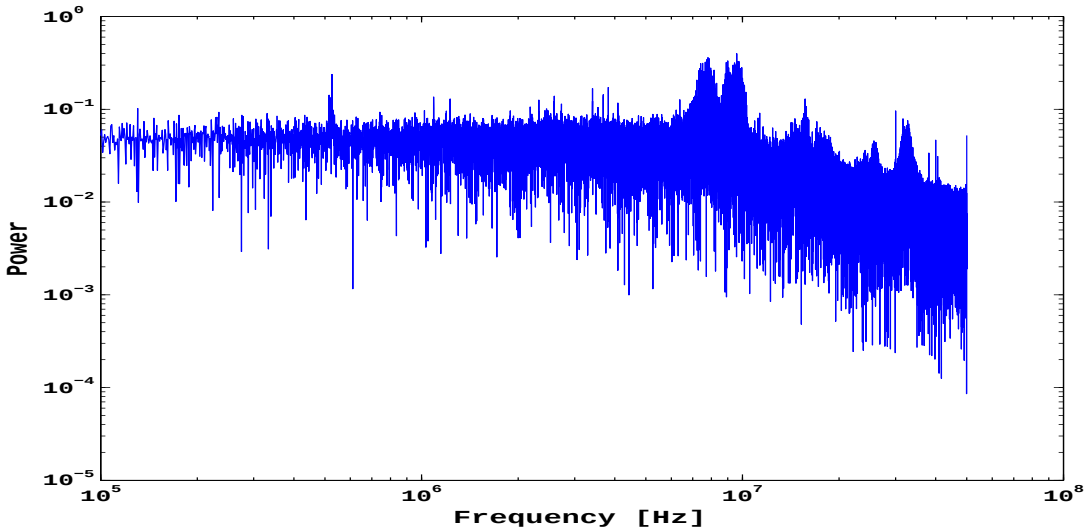

Figure 5.1: Power spectrum of the red crystals noise. The spectrum shows some prominent peaks in contrast to what would be expected if the spectrum were ideally white. The spectrum stops at $50\,MHz$, the cut-off frequency of the anti-aliasing filter (see sec. 3.5.1).

For this purpose $1\,ms$ long traces, i.e. 100000 samples, without any γ interaction in the crystals were recorded. In order to add the noise to the 60 samples of the

simulated signal, correctly scaled with energy, a random starting point within the 100000 samples is chosen and the next 60 samples, wrapping around at the end, are added to the signal. Figure 5.1 shows the power spectrum of the noise for one AGATA crystal ,equipped with the final electronics, featuring some pronounced peaks, a clear sign for a non-white spectrum.

In order to gauge the influence the t_0 resolution has on the attainable position resolution the performance of an extensive grid search, i.e. all points in the PSA basis are tested for agreement with the experimental signal, was examined as a function of normally distributed t_0 resolutions. Additionally, the position resolution is affected by the fact that it is not possible to store the pulse shapes of all 340000 basis points with the full $1\,ns$ precision, as given by JASS, due to constraints on the computer memory to be used by the PSA algorithm. Given

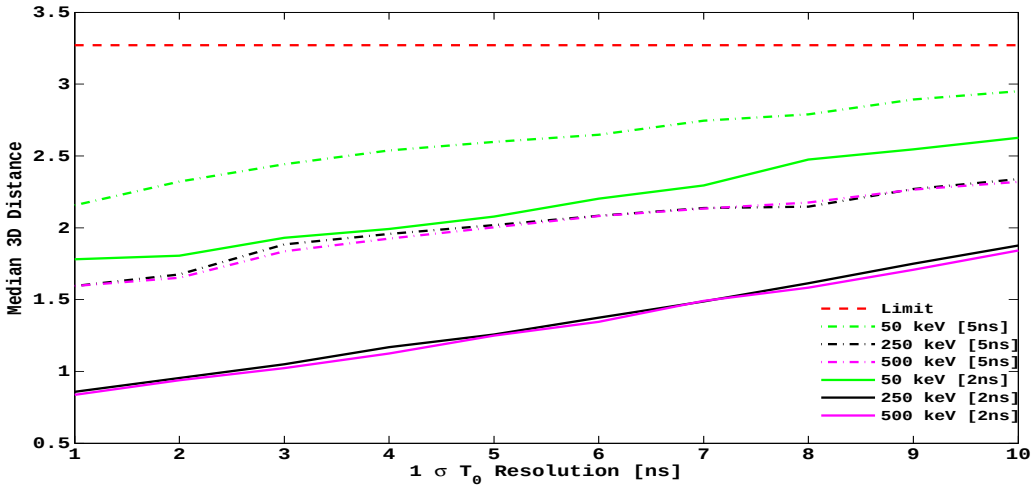

Figure 5.2: Obtainable position resolution as function of t_0 resolution for different γ energies. The dashed red line marks the performance limit corresponding to a normally distributed position resolution of the X, Y and Z coordinates with $5\,mm$ (FWHM), just fulfilling the requirements listed in table 4.1. The extensive grid search is capable of reconstructing the location of a single interaction with the required precision even if the timing resolution is rather poor independent whether the basis points are stored with $2\,ns$ or $5\,ns$ precision.

the ADC'S sampling time of $10\,ns$ and the fact that an interpolation of pulse shapes in time adds an unnecessary computational burden on the performance the only remaining choice is between using a $2\,ns$ or $5\,ns$ sampling of the basis. This can be considered equivalent to adding additional noise onto the experimental signal. The results for events in the front segment ring are summarized in figure 5.2 showing the median 3D distance between the correct and found solutions depending on the timing resolution for both the $2\,ns$ and $5\,ns$ grids. The

extensive grid search is always within the performance requirements listed in table 4.1, marked by the dashed red line in the figure. While this might suggest a precise timing resolution is not of importance it has to be kept in mind that, first of all this investigation was conducted using single interactions only and multiple interaction events will inevitably show a stronger dependence. Secondly the extensive grid search always finds the best fitting basis point, a feature that cannot be guaranteed by FIPS as only a subset of all points will be searched. And lastly, the positive effect a good timing resolution has on the position resolution is reason enough.

The following section will deal with the neural network used to determine t_0, including a description of the data preprocessing, the training and the performance of the network. The position resolution achieved by FIPS, using different neighborhood topologies, on single and multiple interaction events will be shown in section 5.2.

5.1 Determination of t_0 with Neural Networks

The intended task of the FNN is to determine the event time t_0 from the pulse shapes or a subset of the shapes but before the positions are reconstructed by the FIPS algorithm. In this regard it is important to realize that it is possible to present too much information to a neural network and unnecessarily complicating the matter. Thus some effort has to be spent on which trace, or subsets of traces, should be used before starting the training of the FNN. First of all it suffice to determine t_0 for one trace since all traces are time aligned by the GTS (see sec. F.3). Secondly the core signal has the least dependence on interaction location (see fig. 4.1) and multiplicity[1] making it the most suitable trace to be used.

The next point to decide upon is which subset of samples from the core signal is to be presented to the FNN and how to extract these in a reliable manner. Passing the complete trace is deemed unnecessary and unwanted because first of all the variations of the signal shape with location are much more pronounced later in the signal, making it harder for the FNN to find a good generalization of the signal properties, and secondly because the later stages contain less and less information on t_0 (again see fig. 4.1). Since it is rather easy to identify the sample corresponding to t^{10}, i.e. the time until 10% of the total charge have been collected, in an experimental signal this sample lends itself as a starting point of the extraction and time alignment of the traces. However, it was found to be better to extract the samples using the last sample, counting from the end of the trace, above the $2\,\sigma_{noise}$ noise level. In the following these will be called the $2\,\sigma$ and the t^{10} sample. In order to investigate the precision of this rough alignment of the traces, both the t^{10} and the $2\,\sigma$ sample are always at the same position in

[1] In contrast to the core signal the shape of a net charge signal is influenced by transient signals in case of multiple hit segments.

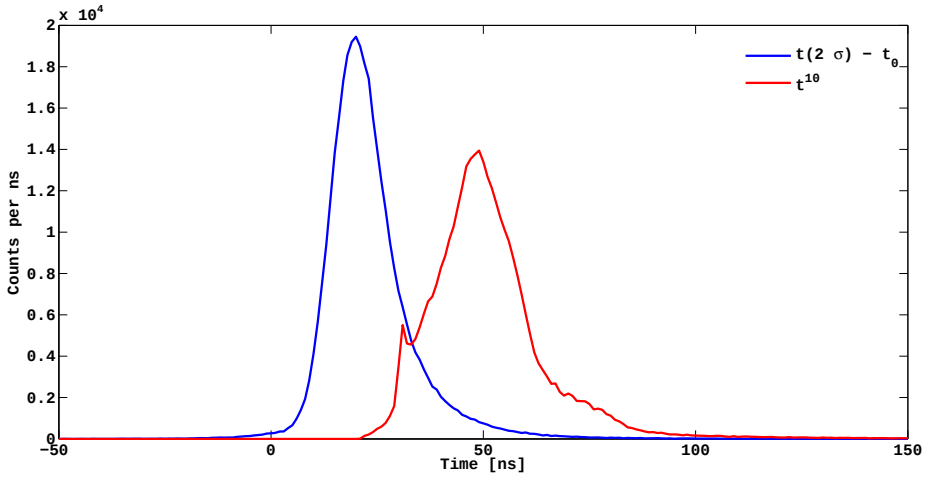

Figure 5.3: Histogram of pulse shape rise times t^{10} (red) and the time between t_0 and the 2σ sample (blue, see text for details). t_0 is within 100 ns of t^{10} or 10 samples in 98.75% of the cases and within 60 ns of the 2σ sample 98.44% of the time. However, the latter has a narrower more pronounced peak.

the input to the FNN, the core traces of the 340000 grid points in the PSA basis set were used. Each trace was assigned an energy E_{core}, uniformly distributed in $[50\,keV, 1500\,keV]$ and a random t_0 before being sampled at $10\,ns$. After adding realistic noise, as described in the previous section, the t^{10} and $2\,\sigma$ samples were identified and the differences to t_0 were taken. The precision of the alignment is related to the width of the peaks in figure 5.3 and the absolute values of the time differences. The chosen $2\,\sigma$ method does not only produce a narrower and more pronounced peak but is also much closer to the actual t_0. The sample extraction starts 6 samples before the $2\,\sigma$ sample, which includes t_0 in 98.44% of the cases, and runs for 20 samples to include t^{10} 99.77% of the time. Additionally it has proved to be advantageous to include σ_{noise}/E_{core} in the input to the FNN.

The topology of the trained network has 21 input units, two hidden layers with 25 and 10 neurons and a single neuron in the output stage, giving a total number of 821 parameters to be optimized. The output of the FNN is limited to the interval $[-1, 1]$ and gives t_0 as percentage of samples with regard to the 20 signal samples in the input. The training data set consisted only of a subset of the samples, normalized to unit energy, used in the comparison of t^{10} and $2\,\sigma$ using 1200 points from each of the six front segments and 500 points each from every other segment. The FNN achieves a resolution of 3.3ns (FWHM) on both the training data and the simulated experimental data, used in the next chapter, featuring any interaction multiplicities. Both distributions can be described as narrowly peaked with positive excess kurtosis (see app. E.3).

The performance of the neural network on experimental signals was tested

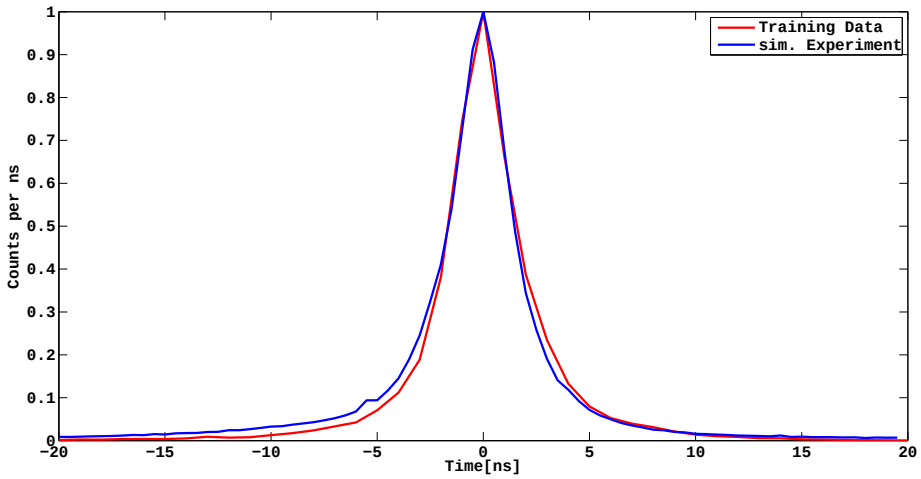

Figure 5.4: Timing resolution of the neural network for simulated data.

using the coincident emission of two γ-rays, at $1.17\,MeV$ and $1.33\,MeV$, by a ^{60}Co source, placed in front of one asymmetric triple cluster. The event selection procedure allowed only events in which exactly two crystals detected a γ-ray to pass. The network has to determine the same t_0 for both hit crystals since the individual traces are time aligned by the GTS (see sec. F.3). Chance coincidences are negligible using gates on the line energies and otherwise are limited to only a few % of all events (Bazzacco, 2009). Figure 5.5(b) shows the result including the line gates for all three possible crystal combinations and figure 5.5(a) shows the performance on all events. The results are summarized in table 5.1 and cannot match the performance on simulated data. All distributions are shifted toward

Combination	RED-BLUE	RED-GREEN	GREEN-BLUE
All data	$22.7\,ns$	$20.4\,ns$	$23.3\,ns$
Lines	$9.0\,ns$	$8.0\,ns$	$9.7\,ns$

Table 5.1: Performance of the trained FNN on experimental data. The resolutions are quoted as FWHM of the distributions shown in figure 5.5.

negative values hinting at a timing mismatch between the crystals.

5.2 Position Reconstruction with FIPS

In the AGATA PSA framework, as in any real time environment predictability plays an important role wherefore a general decision has to be made as to how the stringent time requirements can be enforced. The two options for PSA are to either let the PSA algorithm run for a fixed number of iterations or until a certain

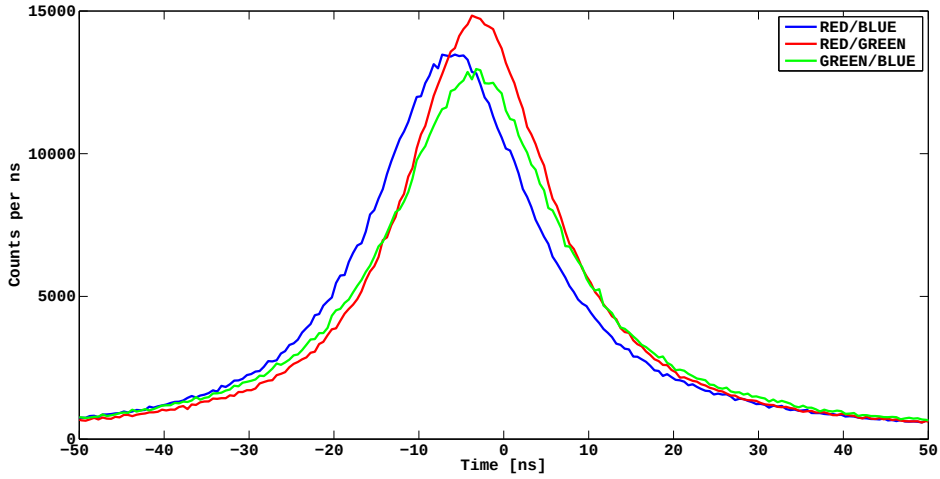

(a) Performance on all data

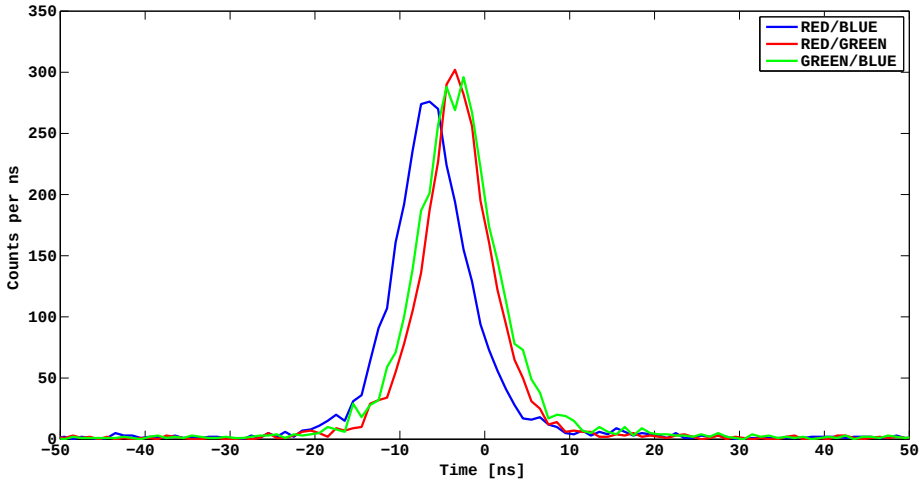

(b) Performance on line gated data

Figure 5.5: All coincident events and line gated events.

goodness of fit, e.g. a χ^2-threshold, is exceeded. There are two problems with the latter approach. First the χ^2-value for a good position resolution in regions of high pulse shape variability, e.g. close to the segment boundaries, is significantly higher than in regions of lower sensitivity, e.g. center of a segment. Setting a χ^2 threshold large enough to accommodate the highly varying regions allows for poor position resolutions in the rest of the segment and it is not possible to generally distinguish the latter from the former simply based on the reconstructed position. Secondly, it fails in terms of predictability as it is not possible to foresee the time taken to reach the threshold value. Hence the FIPS algorithm will run for a fixed number of iterations which will be chosen according to the complexity of the hit pattern. In the following the performance on three different hit patterns, namely single segment hits, multiple hit segments with single interactions and two interactions in one segment, are investigated. The individual results are compared to those of an extensive grid search, in which all relevant reference signals were searched. The event time t_0 was always determined using the neural network approach introduced in section 5.1 since a fit of t_0 will increase the computing times of the extensive search for multiple interactions way beyond reasonable levels and prevent the accumulation of results with at least minimal statistics (see e.g. tab. 5.10). The reference signals with $1\,ns$ precision were used to give an upper limit on the performance since the demands on computing resources prevent such an approach in the experimental environment.

5.2.1 Single Interactions

Obviously, the case of a single γ-ray interaction in a single segment is the easiest possible scenario with the number of relevant reference signals, i.e. the size of the search space, ranging only from 5000 to 12000. The FIPS algorithm was run for just 10 iterations and took on average $0.7\,ms$, comparing favorably to the $40\,ms$ to $200\,ms$ taken by the extensive grid search (XGS). The performance was tested for γ-ray energies of $125\,keV$, $250\,keV$, $500\,keV$ and $1\,MeV$. Above $500\,keV$ the noise predominantly influences the timing resolution and only to a lesser extent the attainable position resolution as the median 3D distance between the correct and found solution of the extensive search only reduces by 0.1mm but the timing resolution is improved by almost 2ns (see tab. 5.2). The lowest tested energy of $125\,keV$ is still considerably above the segment energy threshold of $50\,keV$, that is used in the hardware DAQ. The preamplifier noise level is $4\,keV < 1\sigma < 6\,keV$, depending on the detector. This corresponds to an of $0.08 - 0.12$ for the normalized charge signals at $50\,keV$ and is a factor of two above the average absolute amplitude of the transient charge signals in directly neighboring segments. Hence, only the net charge signal provides limited information on the interaction location and large positional errors have to be expected. At an energy of $125\,keV$ at least some information in the transients is retained and thus presents a reasonable lower limit. The starting positions of the swarm, i.e. the particle positions before

the search starts, were initialized randomly, an initialization in the region with matching t_{10}^{90} rise time had no influence on the results. The results are summarized

Energy	125 keV	250 keV	500 keV	1000 keV
Median 3D (Front)[mm]	3.7/2.6	2.4/1.5	1.9/1.1	1.7/1.0
Median 3D (Back)[mm]	4.0/2.5	2.9/1.4	2.4/1.1	2.2/1.0
Time (FWHM)[ns]	15.6	8.2	4.8	3.1

Table 5.2: The median 3D distance for single hit events at the four tested energies. The results are summarized separately for segments rows $1-3$ (front) and rows $4-6$ (back). In every entry the first quoted number corresponds to the results obtained using the FIPS algorithm and the second to the results with an extensive grid search. The last row gives the resolution of the event time t_0 achieved by the neural net.

in tables 5.2 through 5.5. Due to the considerably varying detector geometry no overall numbers are quoted but these are summarized separately for the front three segment rows as well as the back three rows instead. Figure 5.6 shows a comparison of the individual resolutions at 125 keV and 1 MeV. The resolutions obtained using the FIPS algorithm are plotted in solid blue lines and quoted first in the tables whereas the XGS resolutions are plotted in dashed red lines. The FIPS algorithm performs within the PSA requirements (see tab. 4.1) at energies greater than 125 keV in which case the median 3D distance between the correct and found solution (see tab. 5.2) is slightly above the limit of 3.3 mm. However, the XGS results are also clearly the worst at this low energy and already close to the limit. Test runs with an artificially improved timing resolution suggest this as the root cause. Generally speaking, the results in the first three segment rows are better, due to the smaller search space, and improve with higher energies up to an impressive 1.7 mm median distance at 1 MeV. This trend is also clearly visible in the individual resolutions, depicted in figure 5.6, which show a significant increase in peak height and subsequent decrease of tailing. The radial coordinate is the best resolved individual coordinate. Even at 125 keV the FIPS results are not far off the limiting performance of XGS, especially concerning the percentage of events resolved within $\pm 3\,mm$. At higher energies the only difference between the FIPS and XGS results is in the FWHM but no longer in the aforementioned percentage, which is on par with the best possible results but takes less than 2% of XGS's computing time to achieve.

In contrast to the radial coordinate the angular and Z resolutions are determined by the transient charge signals and seemingly behave antithetic to each other. This behavior is in line with the crystals position sensitivity as exhibited by the XGS results. The overall picture looks similar when comparing the individual FIPS and XGS results. The Z resolutions in the front segments are close or on par with XGS, regarding both the FWHM as well as the percentage of

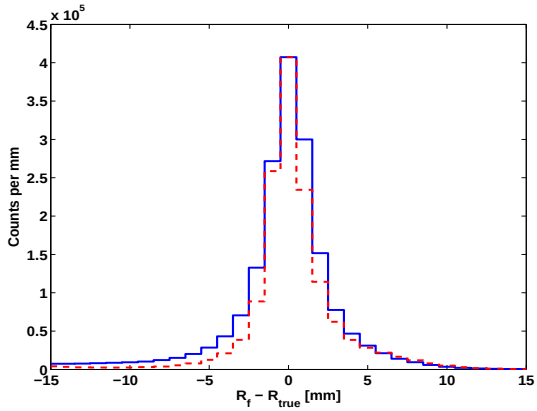

(a) Radial resolution at $E = 125\,keV$.

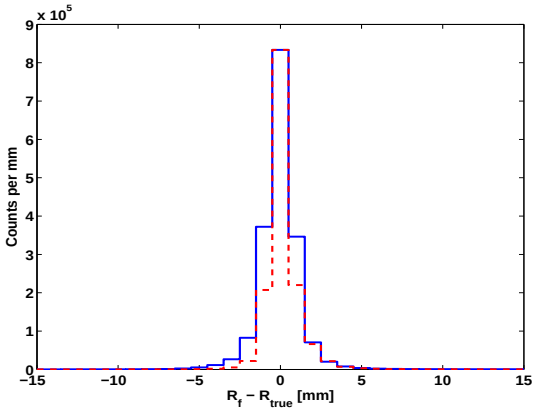

(b) Radial resolution at $E = 1\,MeV$.

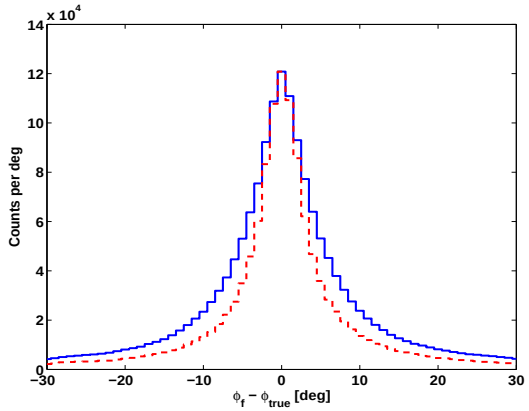

(c) Angular resolution at $E = 125\,keV$.

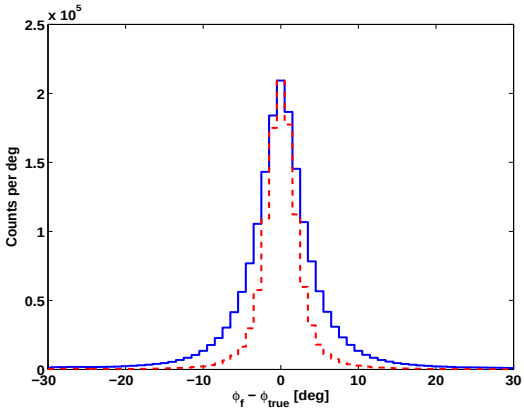

(d) Angular resolution at $E = 1\,MeV$.

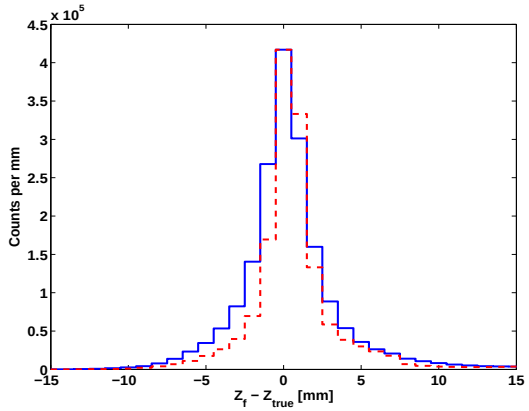

(e) Z resolution at $E = 125\,keV$.

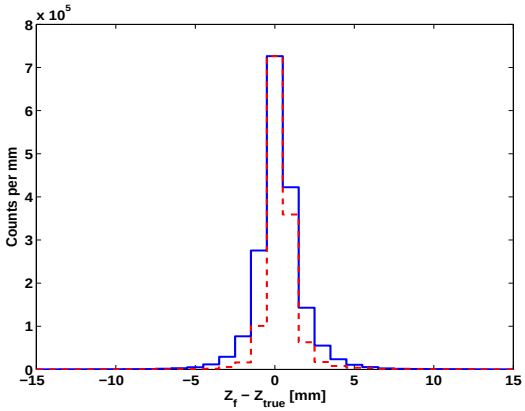

(f) Z resolution at $E = 1\,MeV$.

Figure 5.6: Position resolutions for single hit events in the three front segment rows energies of $125\,keV$ and $1\,MeV$. The results are plotted in solid blue lines for the FIPS algorithm and in dashed red lines for the extensive search.

Energy	125 keV	250 keV	500 keV	1000 keV
Front(FWHM)	3.1/2.6	2.4/1.7	1.9/1.4	1.8/1.3
Front($\pm 3\,mm$)	78.4/82.4	92.2/93.4	96.4/97.2	97.3/98.3
Back(FWHM)	3.0/2.1	2.2/1.4	1.8/1.2	1.6/1.2
Back($\pm 3\,mm$)	89.4/94.8	97.1/98.3	98.0/98.6	98.5/98.6

Table 5.3: Radial Resolutions for single event data (FWHM) and percentage of events resolved within $\pm 3\,mm$ at the four tested energies. The results are summarized separately for segments rows $1-3$ (front) and rows $4-6$ (back). The first quoted number corresponds to the results obtained using the FIPS algorithm and the second to the results with an extensive grid search (XGS).

Energy	125 keV	250 keV	500 keV	1000 keV
Front (FWHM)[°]	8.6/6.1	7.5/5.3	6.7/4.6	6.1/4.2
Back (FWHM)[°]	7.2/4.6	6.7/3.9	6.1/3.6	5.7/3.4

Table 5.4: Angular resolutions for single event data (FWHM) at the four tested energies. The results are summarized separately for segments rows $1-3$ (front) and rows $4-6$ (back). The first quoted number corresponds to the results obtained using the FIPS algorithm and the second to the results with an extensive grid search (XGS).

Energy	125 keV	250 keV	500 keV	1000 keV
Front(FWHM)	3.1/2.5	2.5/2.0	2.2/1.7	2.0/1.6
Front($\pm 3\,mm$)	81.0/84.6	92.0/94.3	95.1/97.2	96.0/98.2
Back(FWHM)	4.4/2.8	3.6/2.2	3.1/2.0	3.0/1.9
Back($\pm 3\,mm$)	76.9/85.1	86.7/95.0	89.2/96.6	89.7/96.9

Table 5.5: Z resolutions for single event data, given in FWHM and percentage of events resolved within $\pm 3\,mm$ at the four tested energies. The results are summarized separately for segments rows $1-3$ (front) and rows $4-6$ (back). The first quoted number corresponds to the results obtained using the FIPS algorithm and the second to the results with an extensive grid search.

well resolved events while in the back segments 90% are never obtained and the FWHM are about $1\,mm$ larger than in the front. The angular resolutions of the FIPS algorithm are better in the back segments, yet the difference to the XGS results is about the same in every category.

5.2.2 Multiple Segment Hits

The task of PSA with multiple hit segments becomes more difficult if more than one segment is hit by a γ-ray. First the size of the search space grows considerably (see tab. 4.2) and secondly because overlapping signals in one segment can be reproduced by a multitude of reference signal combinations, reducing that segments overall information content. Conversely, if none of the segments used for PSA are shared between the hit segments each one can and will be analyzed independently as a single hit event. This leaves two possible general event types to be investigated. In one case directly neighboring segments have been hit, overlapping transient with net charge signals, while in the other case a neighboring segment is shared and only the respective transient signals overlap. In light of the plethora of still possible segment combinations only a few exemplary cases, one of each type in the hexagonal and the coaxial region of the detector, are presented here. Taking the size of the search space into consideration it pays off to initialize the starting positions of the swarm in the region of interest. For this purpose each segments reference signals have been sorted into 20 equally spaced bins according to the t_{10}^{90} rise time of the net charge signal. The starting positions are then chosen randomly from the bins matching the experimental rise time.

Since a search of all reference signal combinations takes at least $600\,s$ per event (segments A1 and C1) which is far from applicable in the experimental setup and furthermore prevents results with high statistics in reasonable time, the extensive search was limited to the reference signals within the appropriate rise time bins. Naturally this leads to a decrease in the obtainable resolutions and in case of segments A1 and C1 with $500\,keV$ γ-ray interactions in each segment to median 3D distances between the correct and found solutions increases from $1.2\,mm$ to $2.2\,mm$ and from $1.1\,mm$ to $2.1\,mm$ respectively. However, the average processing time per event is reduced to $1-2\,s$ which still pales in comparison to the $3-4\,ms$ taken by FIPS. Tables 5.6 and 5.7 summarize the results in terms of the median 3D distance between the correct and found solutions for the tested cases at three different energies and for like and unlike energy split.

The attainable and the obtained resolutions for like energy split strongly depend on the event type and the region within the detector. In the front segments the rise time limited XGS is only within the PSA requirements for hits in non-neighboring segments in which case FIPS performs just slightly worse, $0.1-0.5\,mm$ worse median distance, but still within the requirements. Due to the larger segment size in the back of the crystal the mutual influence on the attainable resolutions for hits in directly neighboring segments is smaller and both

Hit Segments	$E = 250\,keV$	$E = 500\,keV$	$E = 1\,MeV$	CPU Time $[ms]$
A1 C1	2.7/2.4 2.5/2.4	2.6/2.2 2.4/2.1	2.6/2.1 2.4/2.1	3.7/1831
B1 C1	2.6/5.2 3.2/4.4	2.6/5.1 3.1/4.3	2.6/5.0 3.1/4.2	3.0/1811
D4 F4	3.3/2.4 3.6/2.4	3.2/2.2 3.5/2.2	3.2/2.1 3.6/2.1	3.9/1978
E3 E4	3.3/3.6 3.4/3.8	3.3/3.5 3.4/3.5	3.2/3.4 3.4/3.5	4.3/1129
Time [ns]	9.2	6.6	4.9	–

Table 5.6: Median 3D distance between found and correct solution for two hit segments with equal energy. The first number (blue) corresponds to the FIPS results while the second (red) belongs to the XGS results. The timing resolution of the neural net is quoted as FWHM.

Hit Segments	$E = 625\,keV$	$E = 1250\,keV$	$E = 2.5\,MeV$	CPU Time $[ms]$
A1 C1	1.5/1.9 5.1/4.3	1.5/1.7 5.0/3.9	1.5/1.7 5.0/3.8	3.7/1831
B1 C1	1.3/2.6 6.0/8.7	1.3/2.5 6.0/8.5	1.3/2.5 6.0/8.4	3.0/1440
D4 F4	1.7/2.1 7.3/3.8	1.7/2.0 7.2/3.3	1.7/2.0 7.2/3.2	3.9/1978
E3 E4	1.7/2.4 7.2/8.9	1.6/2.3 7.2/8.7	1.6/2.3 7.1/8.6	4.3/993
Time [ns]	6.0	4.5	2.5	–

Table 5.7: Median 3D distance between found and correct solution for two hit segments with unlike energy. The first number (blue) corresponds to the FIPS results while the second (red) belongs to the XGS results. The timing resolution of the neural net is quoted as FWHM and the energies refer to the energy of the higher energetic interaction. The energy deposit of the lower energetic interaction was 20% of the higher energetic one.

XGS and FIPS perform close to or within the limits but with slightly better results for FIPS. The FIPS results do not change if the hits occur in non-neighboring segments but the XGS results improve considerably and are better than FIPS, though at about 500 times the computing time. For an unlike energy split the resolutions of the higher energetic hit are actually exceeding the level of the single event results yet at twice as much iterations. However, the lower energetic interaction is not that well resolved with median distances being about a factor of two larger than the requirements. Only a considerable increase in the number of iterations would lead to resolutions (see tab. 5.8 and discussion below) that are close to the performance requirements (see tab. 4.1). Nonetheless FIPS always outperforms the rise time limited extensive search. The results show that the energy split between the hit segments as well as the event type have a significant influence on the obtained resolutions. Additionally, the extensive search suffers from the restriction to matching rise times whereas the FIPS algorithm is only initialized but not restricted to those rise times. This characteristic is easily explained by the exemplary pulse shapes plotted in figure 5.7. In the case of hits in directly neighboring segments the transient signal of one hit has a significant influence on the shape of the net charge signal of the other hit, especially with such a lopsided energy split as 1/0.2 (see fig. 5.7(b)). If the higher energetic interaction is in close proximity to the segment boundary the transient signal can reach amplitudes equaling or even exceeding that of the net charge signal belonging to the lower energetic interaction. This strong influence of the transient signal on the overall signal shape leads to a wrong determination of the net charge signals t_{10}^{90} rise time, the 10% and 90% level are indicated by black dotted lines in figure 5.7(b), which can be more than $10\,ns$, i.e. two to three bins, off the true value. Subsequently the search either starts (FIPS) or takes place (XGS) in the wrong part of the segment leading to the large median distances in table 5.7. In return the results for the higher energetic interaction improve considerably the more extreme the energy split. The situation is slightly different in the case of non-neighboring segments and only the transient signals overlapping. For a like energy split the obtainable resolutions are considerably better than for directly neighboring segments since the calculated rise times are closer, i.e. correct or one bin off, to the correct value. Yet, the resolutions do not reach the same level as for single interactions of the same energy (see tab. 5.2). The situation changes with an unlike energy split as the higher energetic interaction can now be resolved with comparable resolution while the lower energetic interaction suffers again from a wrongly determined rise time, though to a lesser extent as for directly neighboring segments. Generally it can be observed that the dominant energy also dominates the χ^2-metric and the resulting small gradient of χ^2 with the lower energetic hit reduces the sensitivity and thus the resolution of the lower energetic interaction. A fact that is clearly seen by comparing the FIPS results for different iteration numbers (see tab. 5.8). The resolution of the higher energetic interaction has reached its maximum already after 40 iterations while the resolution of the lower

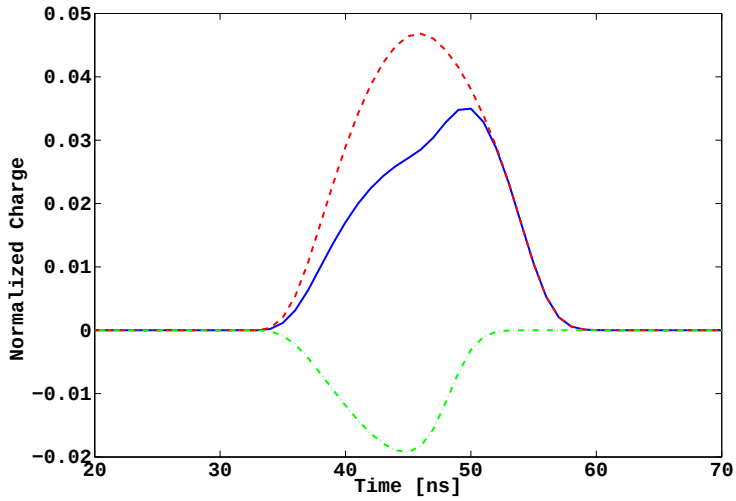

(a) Shared transient signal for two hit segments with unlike energy deposits.

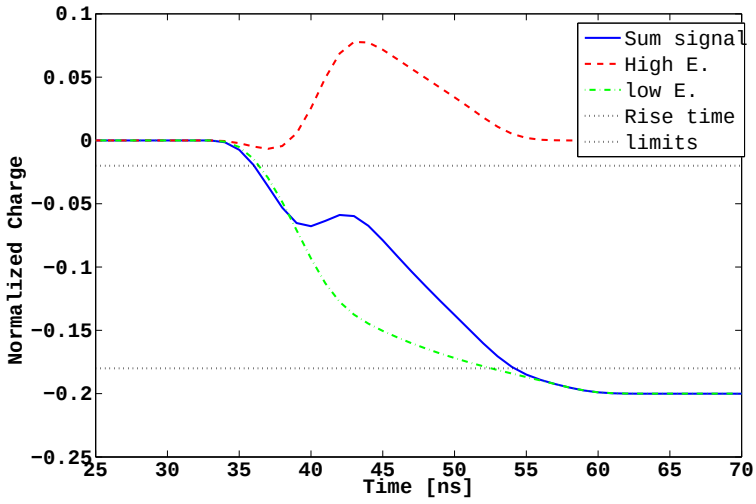

(b) Net charge signal of the lower energetic hit for interactions in two directly neighboring segments.

Figure 5.7: Net charge and transient signals for two hit segments with unlike energy split. The dashed red line corresponds to the signal of the higher energetic interaction, the dash-dotted green line to the lower energetic interaction and the solid blue line to the sum of both signals, i.e. the experimental pulse shape. In both cases the lower energy was 20% of the higher energy. (a)Transient signal in segment E4, interactions in segments D4 and F4 at a distance of 36 mm. (b)Net charge signal in segment E4 with the higher energetic interaction in E3 at distance of 24 mm.

Hit Segments	20 Iter.	40 Iter.	100 Iter.	200 Iter.	XGS
A1	1.5	1.3	1.2	1.2	1.7
C1	5.0	4.0	3.4	3.2	3.8
B1	1.3	1.1	1.1	1.1	2.5
C1	6.0	5.0	4.5	4.3	8.4
CPU Time [ms]	3.9	8.2	14.9	32.9	1800

Table 5.8: Improvement of the median 3D distance between the correct and found solution as function of the number of iterations performed by FIPS. The energy split between the segments was $2500/500\,keV$.

energetic interaction keeps improving though its biggest step is made by going from 20 to 40 iterations. After 200 iterations the median distance only reduces by a further $0.7\,mm$ for hits in directly neighboring segments and by $0.8\,mm$ for shared transient signals.

Max. Energy $[keV]$	A1	B2	C3
500	2.6	3.7	6.1
1000	2.6	3.7	6.0
2000	2.5	3.6	6.0

Table 5.9: FIPS performance for three hit segments. The individual energy deposits were 100%, 60% and 30% of the maximal energy.

The case of three hit segments was tested just for a single combination. The results are summarized in table 5.9 and show the principle feasibility of analyzing these types of events. The two most energetic interactions are always resolved at or within the PSA requirements (see tab. 4.1) while the interaction carrying the least energy is resolved at twice the limit. In the high energy range tested the results are not affected by the different amount of energy deposits. The average computation time was $12.3\,ms$.

5.2.3 Two interactions in one segment

The first and foremost import task concerning this event type is to find objective criteria when to actually search for two hits in the segment. In principle the energy E_1 of the higher energetic interaction can be in the interval $0.5 \cdot E_{seg} \leq E_1 < E_{seg}$, with the lower energy E_2 given by the remainder and E_{seg} the total energy deposit in the segment. In practice, however, there is a lower bound for E_2 that can be resolved. The lowest possible bound for E_2 is $0.1\,E_{seg}$ (Radford, 2005) since then its contribution to the signal shape is simply used to fit the inevitable differences between the reference and experimental signals, due to the grid based approach. Also, the interactions location is no longer restricted but has

only a marginal influence on the overall χ^2-value, even in the ideal noiseless case. Applying the segment energy threshold of $50\,keV$ to E_2 gives $E_{seg} \geq 500\,keV$ as a criterion as to when to search for two interactions. For the same reasons as given in section 5.2.1 a lower limit of $50\,keV$ for E_2 is unrealistic and thus the following minimal energy E_2^{min} will be used:

$$E_2^{min} = \sup\{0.1 * E_{seg}, L\}, \tag{5.1}$$

with L to be determined by the test results. Given the results for single interactions, it was deduced that L can be no less than $125\,keV$. Additionally, it has to be kept in mind that the currently used tracking algorithm packs all individual γ-ray interactions, that lie within $5\,mm$ of one another into a single interaction spot.

Hit Segments	$E = 500\,keV$	$E = 1000\,keV$	$E = 2.5\,MeV$	CPU Time $[ms]$
B1	3.3/1.8 3.5/1.7	3.3/1.4 3.4/1.4	3.2/1.3 3.4/1.3	$5.9/1.4 \cdot 10^6$
A2	3.6/1.7 4.0/1.8	3.5/1.5 3.9/1.5	3.5/1.2 3.9/1.3	$5.4/2.7 \cdot 10^6$
C4	4.3/1.3 4.9/1.2	4.3/1.1 4.9/1.2	4.3/1.0 4.8/1.5	$5.5/1.1 \cdot 10^7$
Time [ns]	6.0	4.5	2.5	–

Table 5.10: Median 3D distance between found and correct solution for two hits in one segment with even energy split. The first number (blue) corresponds to the FIPS results while the second (red) belongs to the XGS results. The timing resolution of the neural net is quoted as FWHM and the energy refers to the total energy deposit in the segment.

The results of the test runs are summarized in tables 5.10 - 5.13 and quote the median 3D distance between the correct and found solutions as obtained by the FIPS algorithm (red, first number) after 20 iterations and an extensive search (XGS, blue, second number). In both cases the energy split for a given combination of reference signals are calculated by a simple fit algorithm minimizing the χ^2-value. Naturally the biggest differences are in terms of computation time as FIPS takes around $5 - 7\,ms$, well within the time constraints, while XGS needs $10^6 - 10^7\,ms$ on a single CPU. Even though the extensive search was run in parallel on 4 CPU's the latter figure still prevents an accumulation of the same statistics for XGS as for FIPS. The tests were run for four different energy splits (first interaction with $50/70/80/90\%E_{seg}$) between the two interactions at three different segment energies ($500/1000/2500\,keV$). It is not surprising to see that the resolution of the first interaction improves with higher energy split and that the resolution of the second interaction improves with higher segment energies

Hit Segments	$E = 500\,keV$	$E = 1000\,keV$	$E = 2.5\,MeV$	CPU Time $[ms]$
B1	2.0/1.4 4.6/2.8	1.9/1.3 4.6/2.4	1.9/1.0 4.5/1.8	$5.6/1.4 \cdot 10^6$
A2	2.1/1.8 5.2/2.9	2.1/1.2 5.1/2.3	2.1/0.9 5.1/1.6	$5.2/2.2 \cdot 10^6$
C4	2.6/1.9 6.4/3.7	2.6/1.3 6.3/2.3	2.6/1.0 6.3/1.8	$5.3/1.1 \cdot 10^7$
Time [ns]	6.0	4.5	2.5	–

Table 5.11: Median 3D distance between found and correct solution for two hits in one segment with energy split 70%/30%. The first number (blue) corresponds to the FIPS results while the second (red) belongs to the XGS results. The timing resolution of the neural net is quoted as FWHM and the energy refers to the total energy deposit in the segment.

Hit Segments	$E = 500\,keV$	$E = 1000\,keV$	$E = 2.5\,MeV$	CPU Time $[ms]$
B1	1.6/1.4 5.8/3.9	1.5/1.2 5.7/3.3	1.5/1.0 5.6/2.5	$5.3/1.4 \cdot 10^6$
A2	1.7/1.3 6.2/4.0	1.6/1.5 6.1/3.7	1.6/0.9 6.0/2.5	$5.5/2.2 \cdot 10^6$
C4	2.0/1.2 7.5/4.3	2.0/1.5 7.5/2.9	1.9/1.0 7.4/3.3	$5.3/1.2 \cdot 10^7$
Time [ns]	6.0	4.5	2.5	–

Table 5.12: Median 3D distance between found and correct solution for two hits in one segment with energy split 80%/20%. The first number (blue) corresponds to the FIPS results while the second (red) belongs to the XGS results. The timing resolution of the neural net is quoted as FWHM and the energy refers to the total energy deposit in the segment.

Hit Segments	$E = 500\,keV$	$E = 1000\,keV$	$E = 2.5\,MeV$	CPU Time $[ms]$
B1	1.2/1.2 8.1/7.4	1.2/1.1 8.0/6.1	1.2/0.9 8.0/5.2	$4.6/1.5 \cdot 10^6$
A2	1.4/1.3 8.1/6.6	1.3/0.9 8.0/5.2	1.3/0.8 8.0/5.0	$6.0/2.2 \cdot 10^6$
C4	1.7/1.3 9.8/7.6	1.6/1.0 9.7/4.2	1.6/1.0 9.7/3.5	$6.7/1.4 \cdot 10^7$
Time [ns]	6.0	4.5	2.5	–

Table 5.13: Median 3D distance between found and correct solution for two hits in one segment with energy split 90%/10%. The first number (blue) corresponds to the FIPS results while the second (red) belongs to the XGS results. The timing resolution of the neural net is quoted as FWHM and the energy refers to the total energy deposit in the segment.

for a given energy split. FIPS is able to resolve the second interaction within or close to the requirements for an even energy split in the front two rows (tested segments B1 and A2) but not in the coaxial part (segment C4). This is easily understood since first of all the size of the search space in segment C4 is an order of magnitude larger (see tab. 4.2) and secondly because of the initialization of FIPS. The first and supposedly higher energetic interaction point is initialized based on the t_{10}^{90} rise time of the experimental signal with the second one chosen randomly from within the segment. In case of an even energy split the determined t_{10}^{90} is most of the times not too close to those of the individual interactions' pulse shape. However, the situation improves the more extreme the energy split becomes. Already at a split of 70/30 FIPS resolves the first interaction well within the requirements (median distance $\leq$ 2.1mm for front segments) and the resolution becomes comparable to XGS in segment B1 with a 90/10 energy split. FIPS resolution of the second interaction suffers first of all from the random initialization and secondly from smaller and smaller gradient of χ^2 with respect to the second interaction, similar to what was observed for multiple hit segments (see sec. 5.2.2). The latter fact is more clearly seen be comparing the improvement in

Energy Split	20 Iter.	40 Iter.	100 Iter.	XGS
50/50	3.2/3.4	2.7/2.8	2.3/2.3	1.3/1.3
80/20	1.5/5.8	1.3/4.7	1.1/4.0	1.0/2.6
CPU Time [ms]	4.6	8.6	19.9	$2.2 \cdot 10^6$

Table 5.14: Improvement of the median 3D distance between the correct and found solution as function of the number of iterations performed by FIPS for two hits in segment B1. The energy deposit in the segment was $2500\,keV$.

resolution with higher iteration numbers for two different energy splits (see tab.

5.14). The resolution of the second interaction improves to very good levels for an even energy split but for a split of 80/20 has only come close to the performance requirements after 100 iterations. Additionally, the first interaction is already close to the XGS results after 20 iterations and on par after 100. However, it still should be emphasized that FIPS achieves these results after a mere $20\,ms$ while XGS takes $2 \cdot 10^6\,ms$.

The last point regards the energy resolution of the individual interactions. In the best possible scenario, a 70%/30% energy split with $E_{seg} = 2.5\,MeV$ in segment B1, the FWHM obtained by XGS is 7.0% and that of FIPS 14.3% corresponding (see fig. 5.8(a)) to $123\,keV$ and 250keV respectively. The spike on the right side of the FIPS spectrum arises when the algorithm used for fitting the energy split between the interactions runs into the 10% limit set for the lower energy. The obtainable energy resolution is typically around 7% and is independent of the error on the lower energetic interaction (see fig. 5.8(b)). FIPS, by comparison, manages $\sim 15\%$ throughout the tested energy range.

5.3 Discussion

The results for t_0 from the neural network show a discrepancy in performance when using real or simulated data. One reason is that the noise samples (see fig. 5.1) were taken after the test data with the ^{60}Co source and also after some modifications to the crystal which reduced the overall noise level. Even more important might be the fact that there were no 3D scanning data for the asymmetric crystals available. From the results of chapter 3 it can reasonably be expected that the simulated data the neural net was trained with is not an exact match of the experimental signals. However, the results using only simulated data show the principal capability of the neural net to determine the event time t_0 with good accuracy. Part of the problems regarding the mismatch between experimental and simulated data could be circumvented by training the neural net with the test data using unsupervised learning techniques. As a prerequisite the correct time alignment of the core signals from both hit crystals (see sec. 5.1) has to be ensured and the signals have to be properly normalized. The obvious choice for the error function $f(\theta)$ to be minimized in the training process is then

$$f(\theta) = \sum_{i=0}^{N} \left(t_0^1 - t_0^2\right)^2 \tag{5.2}$$

with θ the networks parameters, N the number of training data samples and t_0^1 and t_0^2 the event times for crystals 1 and 2 as determined by the neural net.

The first point to mention regarding the PSA results is that the used computer infrastructure is already outdated in terms of performance. Especially the memory bandwidth and the size of the CPU cache play a crucial role in the time

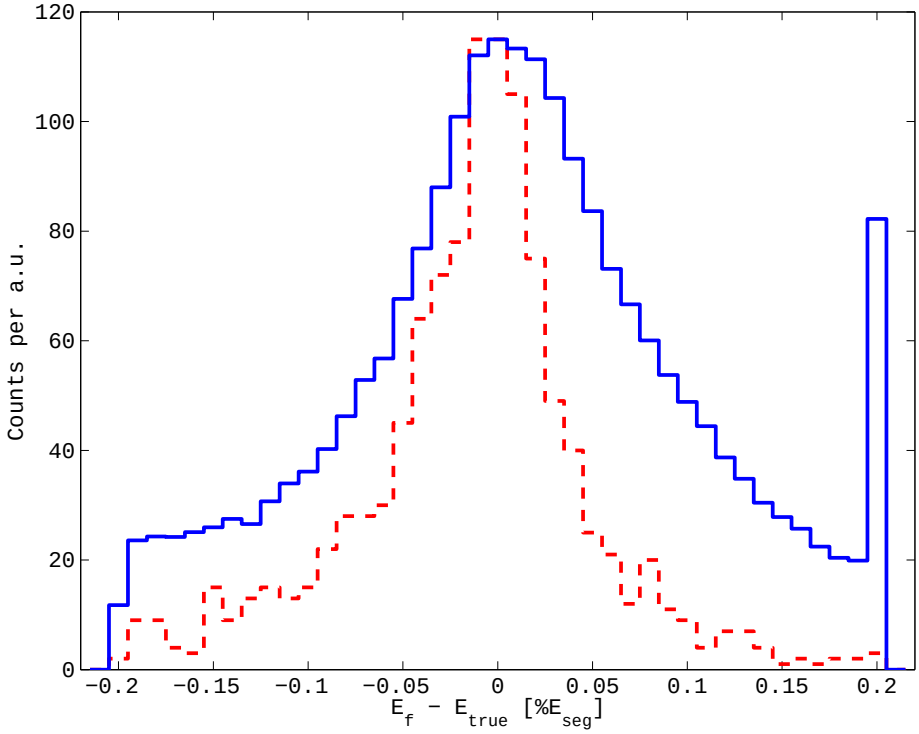

(a) Energy resolution in percent for segment B1 with $E_{seg} = 2.5$MeV.

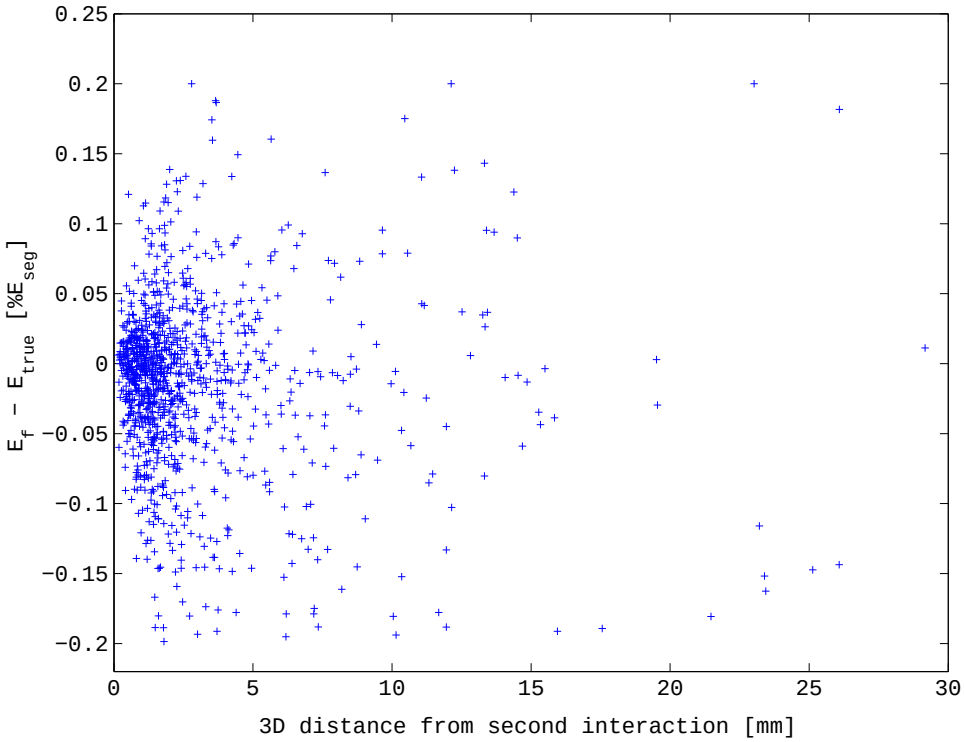

(b) Energy resolution as function of the position resolution of the lower energetic hit.

Figure 5.8: Energy resolution in percent for double interactions in segment B1 with $E_{seg} = 2.5$MeV (a) and its dependence on the position resolution of the lower energetic interaction (b). The energy resolution is given in % of the segment energy with the solid blue line belonging to the FIPS results and the dashed red line to the XGS results. The histogram of the FIPS results has been scaled to peak height of the XGS spectrum due to its vastly larger statistics.

taken for PSA. Given the pace of development it will soon be possible to do PSA for two hit segments in less than $1\,ms$, the stated goal for the final array, without changing the algorithm. Concerning the position resolution, FIPS resolves single interactions within the limits for positional accuracy for energies greater than $125\,keV$ and generally in terms of computing time. Yet, an improvement of the timing resolution (see tab. 5.2) at the low energies will most likely improve the position resolution to within requirements. In the case of multiple hit segments the highest energetic interaction is always resolved within the requirements and will only come close to the limit if the energy split amongst the individual interactions is near even. The opposite is true for the lower energetic hit. Previous tries have shown that a random initialization of FIPS starting positions within the search space is not fruitful and the resolution of the higher energetic interaction clearly profits from the rise time initialization. Hence finding a proper way to initialize the starting positions for the lower energetic interaction, without the problems mentioned in section 5.2.2, should be the next topic to be investigated. However, taking into account that the first γ-ray interaction along the scattering path is likely to deposit the most energy the rather poor resolutions of the lower energetic hit, which do not meet the requirements listed in table 4.1, are not a problem as long as the tracking performance is not affected. The most demanding case of PSA is that of deconvolving two individual γ-ray interactions within a single segment. The results from section 5.2.3 show that the discussed 10% lower limit for E_2, i.e. the energy of the lower energetic interaction, is rather optimistic as XGS resolves the second interaction within the PSA requirements only in segment C4 with $E_2 = 250\,keV$. Based on these results it can be concluded that the search for two interactions in one segment is only feasible for segment energies $E_{seg} \geq 500\,keV$ and rule 5.1 should be rewritten as:

$$E_2^{min} = \sup\{0.2 * E_{seg}, 150\text{keV}\}, \tag{5.3}$$

Regarding FIPS the results can be summarized such that the first interaction location is always resolved within the PSA requirements at a 200000 times higher speed than the extensive search and the resolution of the second location suffers from the random initialization and the comparably small gradient of χ^2 with respect to its location. The next topic to investigate in this regard should be to find a way to initialize the starting positions of FIPS for the second interaction similarly close to the correct location as is done for the first interaction. In light of the energy resolution it should be tested whether the tracking algorithms actually benefits from resolving two hits in the same segment with such a resolution, especially when it comes to separating the interactions of two individual γ-rays hitting the same detector. The probability that the two γ-rays also interact in the same segment is rather low.

Chapter 6

A Simulated Test Experiment

In the previous chapter the position resolution of the chosen PSA approach was tested for certain isolated event types. However, it is the Doppler correction capability of AGATA that is ultimately of interest. While these two issues are related to one another there is no possibility to directly transform a given position resolution into a Doppler-corrected line width. This is especially the case if other experimental factors, e.g. uncertainties in the target or detector position, contributing to the line width are included. Additional factors influencing the quality of the results are additional, non-active material in the path of the γ-ray and the spectral distribution of the measured γ-rays. In order to get an indication of the actual Doppler correction capabilities of AGATA, early on in the development phase, a simple test experiment was conducted using the three symmetric prototype detectors. In the following section the test experiment and the setup are introduced and in section 6.2 the PSA performance is discussed using simulated experimental data for reasons outlined below.

6.1 The Test Experiment and Setup

The test experiment was conducted at the 10 MV Tandem accelerator of IKP in Cologne and featured a (d,p) reaction in inverse kinematics, using a ^{48}Ti beam at an energy of 100 MeV, impinging on a deuterated titanium target. This specific reaction was chosen as it allowed a simple setup for an event-by-event data analysis and a maximization of the excited nucleus' velocity. The AGATA triple cryostat was mounted at 90° to the beam axis and as close as possible to the target (see fig. 6.1(a)) in order to maximize the Doppler-broadening of the observed γ-ray lines. The direction of the scattered nucleus is reconstructed using a double sided silicon strip detector (DSSSD), mounted in forward direction, which detects the emitted proton. As this experiment took place before any component of the AGATA DAQ (see sec. 2.2) was operational the used DAQ system was based on the *Multi Branch System* (Essel & Kurz, 2000), developed

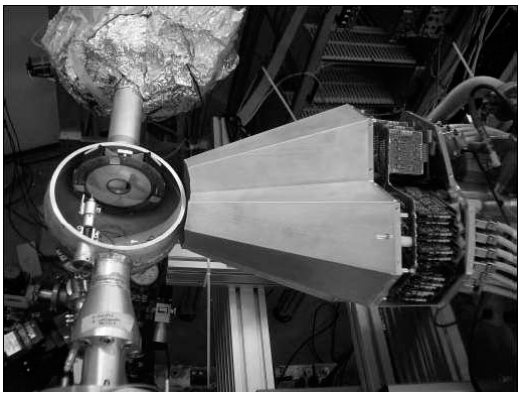

(a) Picture of experimental setup at IKP.

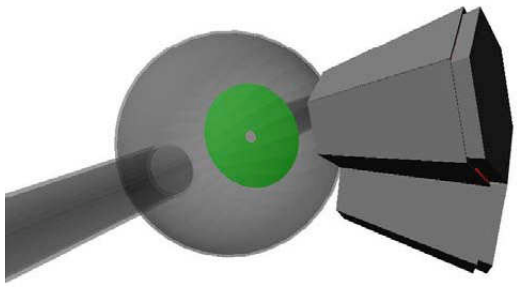

(b) Picture of the experimental setup as used in the GEANT simulation.

Figure 6.1: The setup of the test experiment. (a) The AGATA triple cryostat is on the right and the DSSSD can be seen inside the opened reaction chamber. (b) The triple cryostat is again on the right side of this picture and the DSSSD is represented by a green disc. These figures were taken from (Recchia et al., 2009).

at GSI, and the pulses were digitized using XIA-DGF[1] cards (14 bit). As a consequence the experimental pulse shapes are sampled at $25\,ns$ instead of $10\,ns$ and are also not time aligned. This means that the reference clock for each channel was not distributed using the same cable length but in a daisy chain. So data from different channels could be off by more than one clock cylce ($25\,ns$). Therefore it was decided to use the simulated experimental data, taken from (Recchia et al., 2009), in this thesis in order to get a first impression of AGATAs capabilities. Figure 6.1(b) shows the experimental setup as it has been used in the GEANT simulation of the experiment. Nonetheless, after some extensive post-processing of the experimental data, (Recchia et al., 2009) did analyze the data and report a Doppler corrected line width for the $1382\,keV$ line of $35\,keV$ using just the crystal locations, $14\,keV$ using the segment locations and $4.8\,keV$ using an extensive grid search for PSA.

6.2 Performance of PSA

In order to correlate the Doppler-corrected line width with a certain average position resolution (Recchia et al., 2009) assumed a normally distributed position resolution and simply smeared the interaction points with normally distributed positional errors and took these as the result of the PSA. However, as can be seen from the results in the previous section, either PSA approach delivers results with more strongly peaked resolutions as compared to a normal distribution, i.e.

[1] see `http://www.xia.com/DGF_products.html`

each distribution is leptokurtic. Hence it is not possible to deduce the expected line width from the results of the previous chapter. Therefore the pulse shapes corresponding to each individual interaction location as given by the GEANT simulation were simulated with JASS and later combined into the respective events. A PSA was then conducted for these events using an extensive grid search (XGS) as well as the FIPS algorithm in the same manner as delineated in the previous section. Similarly to (Recchia et al., 2009) the width of the known line at $1382\,keV$ is used to judge the PSA performance. The individual segment and core energies were smeared with the energy resolutions given by straight line fits to the guaranteed resolutions listed in table 2.1. Since no tracking algorithm was used in (Recchia et al., 2009), the same is done in this work and the deconvolved location of the most energetic γ-ray interaction is taken as the first interaction point of the scattering path. Subsequently it is used for Doppler correcting the total energy deposit assigned to the scattering γ-ray. Naturally, all simulated traces were time aligned so only the core signal of the crystal with the highest energy was fed to the neural network determining the event time t_0. This t_0 was not just used by the FIPS algorithm but also by the extensive grid search since it was already shown that fitting t_0 as part of PSA is not possible in a real time environment like the AGATA PSA. Even then, the extensive search takes $27\,ms$ on average for single γ-ray interactions and still does not meet the time limit set in the PSA requirements (see tab. 4.1). Additionally, table 6.1 shows

Event Type	Single Hits	No Overlap	≤ 3 hit segments
Number of Events	197452	218813	332619
Total Percentage	58.6	64.9	98.6

Table 6.1: Statistics of simulated experiment.

that the approach of the extensive search leads to a considerable loss of statistics. Around 41.4% of the data are lost in the standard approach of analyzing only single segment hits and this number is only slightly reduced to 35.1% if those events with multiple hit segments but no overlap in the transient signals are included although at twice the computation time. In practice this loss will be even larger since the relatively long time taken by XGS causes a non-negligible dead time of the DAQ system. By comparison neither event type analyzed by FIPS takes more than $5\,ms$, $2.2\,ms$ on average, and only 1.4% of the data are excluded in the search. Contrary to chapter 5 the reference signals were only given in $5\,ns$ precision bringing the demand on computer memory to the levels foreseen available in the experimental environment[2].

Since the analysis concentrates on the width of the $1382\,keV$ line only events with energy deposits between $1200-1500\,keV$ were simulated and fed to the PSA

[2]3.0 GB of memory were needed for the FIPS approach analyzing up to 3 simultaneously hit segments and could only be run on a $64-bit$ system.

algorithm. Figure 6.2 shows the energy spectrum in this interval. The blue dash-dotted line corresponds to the uncorrected, i.e. Doppler shifted, energy deposits. The dashed green line and the solid red line are obtained after correcting for

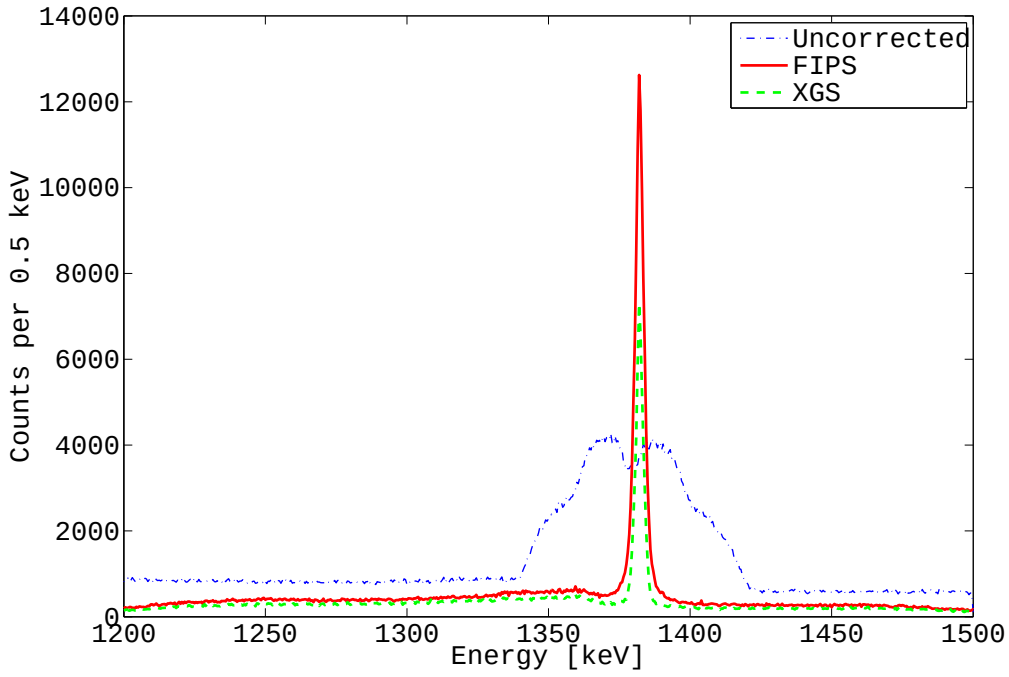

Figure 6.2: Overlay of uncorrected and Doppler-corrected spectra. The energy spectrum in the analyzed interval is shown before Doppler-correction (blue dash-dotted line), Doppler-corrected after PSA with XGS (dashed green line) and Doppler-corrected after PSA with the FIPS algorithm (solid red line).

the Doppler shift using the results of PSA with either XGS or FIPS respectively. Even without a detailed analysis two important conclusions can already be drawn based on these spectra. First, FIPS achieves a position resolution that is at least close to the XGS results, although multiple hit segments are included. This claim is justified by observing that the increase in analyzed events primarily leads to an increase in peak amplitude and only marginally to more events in the background. This gives rise to the second important conclusion that using FIPS will increase the sensitivity of AGATA considerably and hence positively influence the detectability of low intensity transitions.

Besides the two already mentioned cases a PSA with FIPS (FIPS singles) was also performed with the same event selection used by XGS to make a one-to-one comparison of the two approaches. A close inspection of the spectra already reveals that the peaks are not purely Gaussian in shape but do show some tailing (see fig. 6.4). Therefore the model used to fit the spectra in the region of

interest, $1370 - 1395\,keV$, included symmetric exponential tails, i.e. a mixture of a Laplace- and a Gauß-distribution with same peak position μ, plus a linear background:

$$f(x) = N_1 \cdot \exp\left(-0.5(x-\mu)^2/\sigma^2\right) + N_2 \cdot \exp\left(-|x-\mu|/\beta\right) + A \cdot x + B. \quad (6.1)$$

The total peak amplitude is given by $N_1 + N_2$ and the width of the distributions by σ and β respectively. The linear background model has slope A and offset B. The results can be seen in figure 6.3 and the fitted parameter values are summarized in table 6.2. The goodness of fit can be assessed using the R^2 value

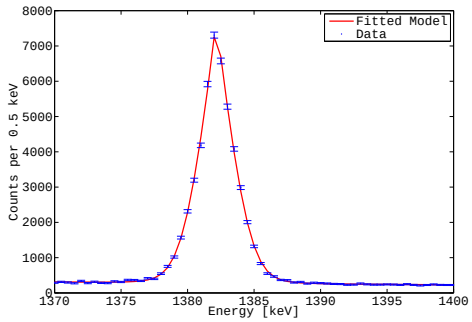

(a) Fit to XGS peak.

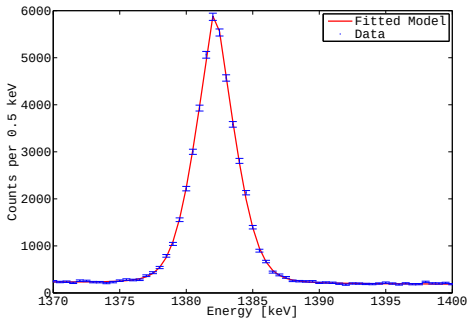

(b) Fit to FIPS single

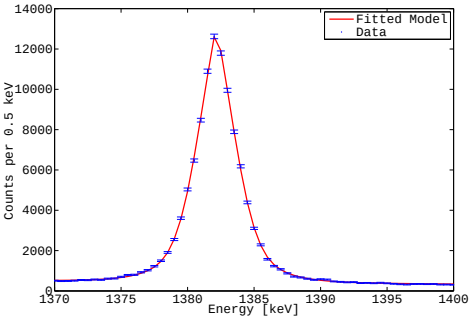

(c) Fit to FIPS all.

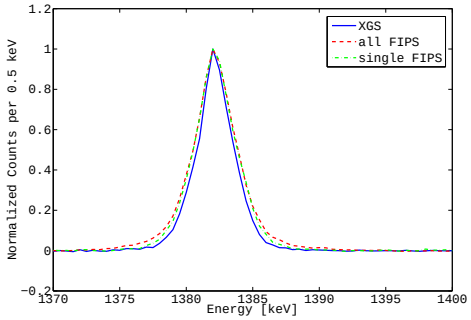

(d) Comparison of background subtracted normalized peaks.

Figure 6.3: Fits of model 6.1 to Doppler-corrected spectra after PSA with (a) XGS, (b) FIPS single segment hits and (c) FIPS with up to three hit segments. The extracted peak spectra were superimposed onto each other after subtraction of the fitted background contributions and subsequent normalization to unit amplitude (d).

$(0 \leq R^2 \leq 1)$ which is a function of the squared residuals and the variance of the data. It is a measure for the correlation between the data and the model with 1 indicating a perfect correlation. The adjusted R^2 values take the degrees of freedom in the same manner into account as is known for χ^2. In case of the fitted

Parameter	XGS	FIPS singles	FIPS all
N_1	3303 ± 514	3065 ± 245	5654 ± 446
N_2	4221 ± 551	2927 ± 297	7091 ± 588
μ	$1382^{+0.2}_{-0.1}$	$1382^{+0.2}_{-0.1}$	$1382^{+0.2}_{-0.1}$
σ	1.57 ± 0.1	1.68 ± 0.07	1.55 ± 0.06
β	$1.2^{+0.2}_{-0.1}$	1.5 ± 0.2	1.96 ± 0.12
A	-2.8 ± 2.3	-1.5 ± 1.5	-5.7 ± 2.8
B	4112 ± 3186	2339 ± 2090	8271 ± 3918
Adj. R^2	0.99	0.99	0.99
FWHM $[mm]$	2.8	3.3	3.4
avg. CPU Time $[ms]$	27	0.8	2.2

Table 6.2: Parameters of the fitted peak model and goodness of fit for the Doppler-corrected peaks. The FWHM is calculated from the background-subtracted spectra. The quoted errors correspond to the 95% confidence level.

model they are close to unity for each fit and indicate a good match with the experimental data. All three approaches reconstruct the correct peak position of $1382\,keV$ with the same small uncertainties. On the other hand the widths of the Laplacian distributions show a sizable difference while the widths of the Gaussian distributions are comparable for each of the three cases. Yet the considerable differences in the contributions of the two distributions to the individual peak shapes make a comparison of their widths in terms of overall peak resolution not meaningful. Therefore the FWHM of each peak was calculated from the spectra after subtraction of the fitted background model. As can be expected XGS produces the narrowest peak with $2.8\,keV$ FWHM but the resolution of FIPS is only $0.5 - 0.6$keV wider. The remarkable result however is that the resolution of FIPS is practically the same independent of whether multiple segment hits are included or not (see fig. 6.3(d)). The only observable differences are the slightly stronger tails for multiple segment hits. Generally speaking the fit results confirm the earlier claim of comparable resolutions not only by the numbers but also because the peak amplitude $(N_1 + N_2)$ increases by the same factor as the number of analyzed events, i.e. 1.7.

6.3 Discussion

An interesting question not yet discussed is whether the PSA algorithms resolve the energetic barycenter of multiple interactions within a segment with the same resolution as for the true single hits analyzed in the previous chapter. Figure 6.4 shows the resolutions of the radial, angular and Z coordinate as well as the distance of the found location from the barycenter for the analyzed simulated

experimental data. The solid blue line always corresponds to the results of the

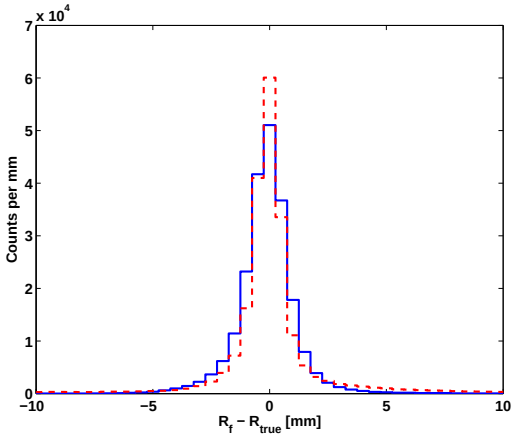

(a) Radial resolution of single segment hits.

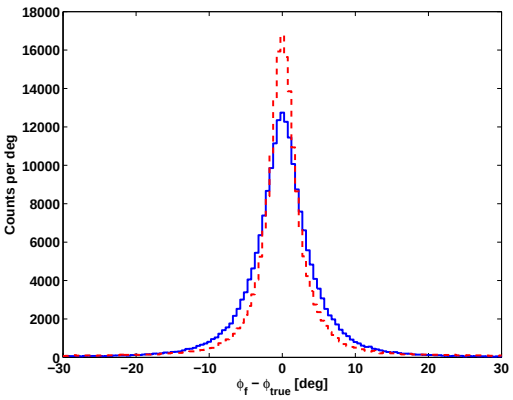

(b) Angular resolution of single segment hits.

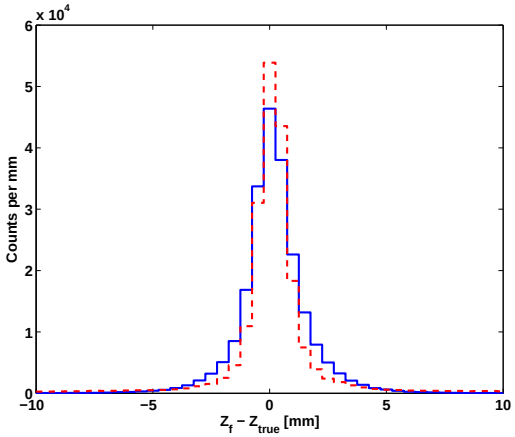

(c) Z resolution of single segment hits.

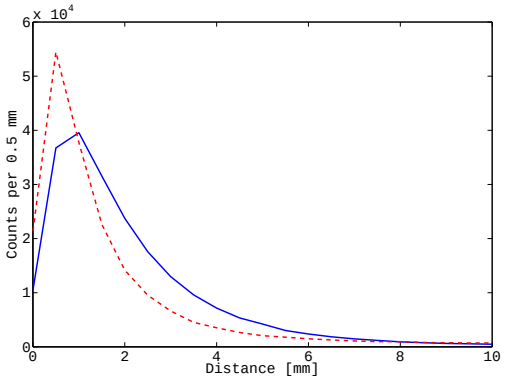

(d) 3D distance from correct location.

Figure 6.4: Position resolution of the energetic barycenter for single segment hits in the simulated experimental data. The solid blue line corresponds to the results of the FIPS algorithm and the dashed red line to the results of XGS.

FIPS algorithm and the dashed red line to the results of XGS. In all cases the resolutions are as if a true single interaction occurred at the energetic barycenter, important to know for the tracking algorithms (compare table 6.3 with tables 5.2-5.5). Interestingly the individual distributions coincide with one another for poorly resolved events, e.g. errors on Z greater than $\pm 5\,mm$ or for distances greater than $8\,mm$. The FIPS algorithm manages to get close to the correct solution rather quickly but does not always end up at that location leading to higher amplitudes around the peaks as opposed to the results with XGS.

As was already briefly mentioned it is possible for FIPS to analyze events up to a segment multiplicity of three and stay within the performance requirements

Algorithm	Radial $[mm]$	Z $[mm]$	Angular $[^\circ]$	Med. 3D distance $[mm]$
XGS	1.3	1.4	4.0	1.4
FIPS	1.7	1.8	6.1	1.8

Table 6.3: Position resolution of XGS and FIPS for single segment hits in the simulated experiment.

set for PSA (see tab. 4.1). The γ-ray interaction with the highest energy deposit, also likely the first interaction used for the Doppler-correction, is practically as well resolved as if it were a single interaction. Thus the energy resolution is not adversely affected compared to single segment hits analyzed with FIPS. This is an important advantage over XGS since the resulting increase in analyzable events as well as the higher speed of FIPS lead to a higher resolving power for AGATA, outweighing the effects of the slightly poorer energy resolution (see eqn. 1.3).

Finally, it can be concluded, that the chosen approach to PSA of determining the event time t_0 with a neural net and subsequent reconstruction of the interactions locations with the FIPS algorithm works well within the performance requirements (see 4.1). The capability of FIPS to accurately resolve the first interaction location independent of the segment multiplicity is crucial to harness the full resolving power offered by AGATA.

Appendix A

Moments of the scanning distributions

In the following tables the higher order moments of the distributions plotted in figures 3.22 through 3.28 are listed. The values, from left to right, belong to parameter set A, set B and the simulated data and are given in the same colors as in the above mentioned figures.

Moment	Row 1	Row 2	Row 3	Row 4
γ_1	$-0.0/0.1/-1.4$	$0.6/0.9/-0.8$	$0.2/0.4/-2.2$	$0.0/-0.0/-0.2$
γ_2	$3.6/0.6/81.0$	$3.5/3.2/58.7$	$4.5/9.3/56.1$	$6.0/9.1/48.5$
	Row 5	Row 6	All	
γ_1	$0.8/1.0/-0.3$	$1.3/1.2/-2.6$	$0.2/0.3/-1.6$	
γ_2	$7.6/9.0/39.8$	$18.2/16.2/44.2$	$5.4/4.5/63.3$	

Table A.1: Moments of X distributions.

Moment	Row 1	Row 2	Row 3	Row 4
γ_1	$-0.2/-0.1/-0.4$	$0.0/-0.3/0.3$	$-0.1/-0.4/0.6$	$-0.1/-0.4/0.4$
γ_2	$0.8/0.6/61.1$	$3.5/3.2/35.4$	$2.5/5.7/28.6$	$3.9/7.0/25.6$
	Row 5	Row 6	All	
γ_1	$-0.2/-0.5/0.4$	$-0.9/-0.9/-0.2$	$-0.2/-0.2/0.1$	
γ_2	$7.5/6.6/35.8$	$14.0/11.6/35.1$	$2.9/3.2/48.5$	

Table A.2: Moments of Y distributions.

Moment	Row 1	Row 2	Row 3	Row 4
γ_1	0.9/1.0/1.0	0.2/0.1/2.5	0.0/0.1/−1.0	−0.1/−0.1/−1.3
γ_2	4.9/4.6/4.2	0.1/−0.2/17.2	0.2/0.6/15.1	0.7/1.2/19.6
	Row 5	Row 6	All	
γ_1	−0.1/−0.1/−1.4	0.0/−0.1/−0.2	0.2/0.2/−0.2	
γ_2	1.0/1.3/11.3	−0.8/−0.7/6.9	2.4/2.6/15.0	

Table A.3: Moments of Z distributions.

Moment	Row 1	Row 2	Row 3	Row 4
γ_1	0.3/0.4/−6.6	0.3/0.3/6.0	0.4/0.2/3.0	0.9/1.3/3.6
γ_2	0.8/0.5/83.6	10.1/12.5/69.9	14.5/21.1/44.9	13.3/21.6/38.8
	Row 5	Row 6	All	
γ_1	2.4/2.7/4.1	4.1/4.2/4.9	0.5/0.1/−0.9	
γ_2	24.3/32.2/37.7	35.2/37.9/54.3	7.8/6.1/74.1	

Table A.4: Moments of R distributions.

Moment	Row 1	Row 2	Row 3	Row 4
γ_1	7.4/7.3/4.7	4.7/5.7/3.6	2.5/3.2/5.3	1.9/2.3/3.2
γ_2	69.7/60.3/80.6	53.4/44.7/87.1	40.5/37.8/95.3	43.2/41.2/88.2
	Row 5	Row 6	All	
γ_1	6.5/6.8/1.5	0.4/6.7/1.4	3.9/4.5/3.8	
γ_2	88.8/64.9/78.9	136.1/107.0/72.6	53.2/47.9/83.7	

Table A.5: Moments of φ distributions.

Appendix B

Details on the mobility models

The description of the physical models for the charge carriers mobilities in sections 3.2.3 and 3.2.4 concentrated on the physics but was lacking a parameterization, usable in a computer simulation, which will be given in the following. The projection of the drift velocities in the direction of the fixed electrical field as well as the velocity component perpendicular to it depend on the orientation of the electrical field with respect to the germanium crystal lattice. The anisotropies on both directions are referred to as *longitudinal* and *transverse* anisotropy. The drift velocities themselves have to be aligned with the crystal symmetry axis - the germanium lattice is symmetric in the $\langle 100 \rangle$, $\langle 110 \rangle$ and $\langle 111 \rangle$ crystallographic directions - as the crystal plus electric field are invariant under a specific rotation if the electric field is oriented along a symmetry axis. Hence this invariance has to be reproduced by the drift velocities and observations of these along symmetry directions give direct information about the longitudinal anisotropy. The longitudinal anisotropy in direction l, as reported in the literature, is reproduced well by the parametrization given by ((Knoll, 1999),p. 423):

$$v_l = \frac{\mu_0 E}{(1 + \left(\frac{E}{E_0}\right)^{\beta})^{\frac{1}{\beta}}} - \mu_n E \tag{B.1}$$

The scalar μ_0 represents the scalar mobility at low fields and is expected to become independent of the crystallographic direction. Table B.1 gives the mobility

	Electron Mobility Parameters				Hole Mobility Parameters			
Direction	μ_0	β	$E_0[\frac{V}{cm}]$	μ_n	μ_0	β	$E_0[\frac{V}{cm}]$	μ_n
$\langle 100 \rangle$	37200	0.805	510	-167	62380	0.727	181	-
$\langle 111 \rangle$	32908	0.774	448	-133	62508	0.757	144	-

Table B.1: Mobility Parameters (μ in $\left[\frac{cm^2}{Vs}\right]$) of parameter set A

parameters for parameter set A as reported by (Bruyneel et al., 2006a) and table

	Electron Mobility Parameters				Hole Mobility Parameters			
Direction	μ_0	β	$E_0[\frac{V}{cm}]$	μ_n	μ_0	β	$E_0[\frac{V}{cm}]$	μ_n
$\langle 100 \rangle$	40180	0.72	493	589	66333	0.744	181	-
$\langle 111 \rangle$	42420	0.87	251	62	107270	0.580	100	-

Table B.2: Mobility Parameters (μ in $\left[\frac{cm^2}{Vs}\right]$) of parameter set B.

B.2 for set B as reported by (Mihailescu et al., 2000; Reggiani et al., 1977). In the following the parameterization of the mobility models for the electrons and holes, as described in sections 3.2.3 and 3.2.4, are presented using equation B.1.

B.1 Parameterization of the electron model

In the case of the electron mobility it is rather straightforward to relate the experimentally accessible parameters, listed in tables B.1 and B.2, to the model described in section 3.2.3. Identifying the effective mobility μ^* in equation 3.15 with the v_{100} drift velocity and utilizing the fact that all four electron valleys are equally populated if the electric field $\vec{E}$ is aligned with the $\langle 100 \rangle$ direction, equation 3.15 can be rearranged and yields the following relation:

$$\mu^*(E) \;=\; \frac{v_{100}(E/\Gamma_0)}{\Gamma_0\, E}. \tag{B.2}$$

The constant $\Gamma_0 = 2.888$ is defined by the mass tensor elements in equation 3.13. The only remaining question now concerns the weights n_i in equation 3.15 for an arbitrarily oriented field. If the field is oriented along the $\langle 111 \rangle$ direction of valley 1 the remaining three valleys are equally populated with an amount of $(1-n_1)/3$ and equation 3.15 an be rearranged to

$$n_1 \;=\; \frac{v_{111}(E) - \Gamma_2^2 \mu^*(\Gamma_2\, E)\cdot E}{\Gamma_1^2 \mu^*(\Gamma_1\, E)\cdot E - \Gamma_2^2 \mu^*(\Gamma_2\, E)\cdot E}. \tag{B.3}$$

The constants $\Gamma_1 = 0.7809$ and $\Gamma_2 = 3.305$ are again given by the mass tensor elements in equation 3.13. The weights n_i can now be calculated with the help of n_1 and the relative field strengths in each of the four valleys obeying the constraint that $\sum_{i=1}^{4} n_i = 1$. Thus the mobility of the electrons is fully specified in any direction using only the mobilities in the $\langle 100 \rangle$ and $\langle 111 \rangle$ directions.

B.2 Parameterization of the hole model

While the numerical evaluation of the three dimensional integral in equation 3.19 is possible, it is too time consuming to be used in a pulse shape simulation. However, the k dependence can be integrated over explicitly and only a 2D integral

has to be approximated. In the following the constant factor $\hbar/\sqrt{2mk_bT_h}$ in equation 3.16 will be absorbed into the definition of k and k_0, which can in turn be interpreted as the solid-state equivalent to the Mach number in fluid dynamics. Rewriting equation 3.19 in Cartesian coordinates gives:

$$\begin{aligned} v_x(\overrightarrow{k_o}) &= \frac{v_{100}(k_o)}{n(k_0)} \int_0^{2\pi} \int_0^{\pi} X(\theta,\varphi) \exp\left[k_0^2(R^2-1)\right] I_3(k_oR)\sin(\theta)d\theta d\varphi \\ v_y(\overrightarrow{k_o}) &= \frac{v_{100}(k_o)}{n(k_0)} \int_0^{2\pi} \int_0^{\pi} Y(\theta,\varphi) \exp\left[k_0^2(R^2-1)\right] I_3(k_oR)\sin(\theta)d\theta d\varphi \\ v_z(\overrightarrow{k_o}) &= \frac{v_{100}(k_o)}{n(k_0)} \int_0^{2\pi} \int_0^{\pi} Z(\theta,\varphi) \exp\left[k_0^2(R^2-1)\right] I_3(k_oR)\sin(\theta)d\theta d\varphi \end{aligned} \quad \text{(B.4)}$$

The normalization constant $n(k_0)$ can be found by identifying $v_x(k_0, \theta = \pi/2, \varphi = 0)$ with the $v_{100}(k_0)$ mobility. The vector $k\,[X(\theta,\varphi), Y(\theta,\varphi), Z(\theta,\varphi)]$ is the gradient $\overrightarrow{\nabla_k}\epsilon(\vec{k})$ (see eqn. 3.3) and R is an abbreviation for the cosine of the angle between $\vec{k}$ and $\overrightarrow{k_0}$:

$$R(\theta,\varphi,\theta_0,\varphi_0) = \frac{\vec{k}}{k}\cdot\frac{\vec{k_0}}{k_0} = \sin(\theta_0)\sin(\theta)cos(\varphi-\varphi_0) + cos(\theta_0)\cos(\theta). \quad \text{(B.5)}$$

The function $I_3(k_oR)$ contains the complete k-dependence of the integration and belongs to a family of integrals given by:

$$I_n(x) = \int_0^{\infty} k^n \exp(-(k-x)^2)dk$$

with the general solution:

$$I_n(x) = \frac{1}{2}\sum_{m=0}^{n}\binom{n}{m}x^{n-m}\left\{\Gamma(\frac{m+1}{2}) + (-1)^m\, sgn(x)\cdot\gamma(\frac{m+1}{2},x^2)\right\} \quad \text{(B.6)}$$

The general solution is obtained by substituting $y = k - x$ and by expanding $(y+x)^n$ in its binomial form and states that the integral can be expanded in term of the complete and incomplete gamma functions, i.e. $\Gamma(x)$ and $\gamma(x)$.

B.2.1 A useful approximation

In order to facilitate the use of the model in a pulse shape simulation (Bruyneel et al., 2006a) developed a fit function for the integrals in equations B.4 and provide a good approximation for $k_0 < 3$. Using the $\overrightarrow{k_o}(k_0,\theta_0,\varphi_0)$ components of the mean wave vector, which is aligned with the electrical field $\overrightarrow{E}(E,\theta_0,\varphi_0)$ (see sec. 3.2.4), the velocities can be expressed as:

$$\begin{aligned} v_r &= v_{100}(E)\left[1-\Lambda(k_0)(\sin(\theta_0)^4\sin(2\varphi_0)^2 + \sin(2\theta_0)^2)\right] \\ v_\theta &= v_{100}(E)\Omega(k_0)\left[2\sin(\theta_0)^3\cos(\theta_0)\sin(2\varphi_0)^2 + \sin(4\theta_0)\right] \\ v_\varphi &= v_{100}(E)\Omega(k_0)\sin(\theta_0)^3\sin(4\varphi_0). \end{aligned} \quad \text{(B.7)}$$

The functions Λ and Ω correspond to the relative difference in radial velocity $\Lambda = (v_{100} - v_{110})/v_{100}$ and the relative tangential velocity $\Omega = v_\varphi(\theta_0 = \pi/2, \varphi_0 = \pi/8)$ and describe the amplitude of the anisotropy. Fitting equations B.7 to the true solution in equations B.4 yielded:

$$\Lambda(k_0) = -0.01322\,k_0 + 0.41145\,k_0^2 - 0.23657\,k_0^3 + 0.04077\,k_0^4 \quad \text{(B.8)}$$

$$\Omega(k_0) = 0.006550\,k_0 - 0.19946\,k_0^2 + 0.09859\,k_0^3 - 0.01559\,k_0^4. \quad \text{(B.9)}$$

The last step to achieve a usable model is to relate the value of the reduced k_0 to the experimentally observed longitudinal anisotropy and thus be able to deduce k_0 from the values listed in table B.1 and equation B.1. (Bruyneel et al., 2006a) assume that k_0 is independent of the field orientation, for fixed electrical field strengths, and thus k_0 is to first order a function of $|E|$ only. Identifying v_r in equation B.7 with v_{111} and evaluating it using the coordinates for the $\langle 111 \rangle$ directions yields the following relation:

$$1.33\,\Lambda(k_0) = \{v_{100} - v_{111}\}/v_{100}, \quad \text{(B.10)}$$

and together with equation B.8 k_0 is now given as a function of $v_{rel} = v_{111}/v_{100}$:

$$k_0(v_{rel}) = 9.2652 - 26.3467\,v_{rel} + 29.6137\,v_{rel}^2 - 12.3689\,v_{rel}^3. \quad \text{(B.11)}$$

Appendix C

Plane Equations and Hesse's Normal Form

The mathematical definition of a plane is quite simple. A plane consists of all points $P(x, y, z) \in \mathbb{R}^3$ that satisfy the following equation:

$$A \cdot x + B \cdot y + C \cdot z + D \; = \; 0. \tag{C.1}$$

The plane equation is written in the so-called component form. A, B and C are the non-normalized components of the plane's normal vector $\overrightarrow{\mathbf{N}}(A, B, C)$. D is zero only if the origin is part of the plane. The direction cosines of $\overrightarrow{\mathbf{N}}$ are:

$$\cos\alpha = \frac{A}{\sqrt{A^2 + B^2 + C^2}}, \cos\beta = \frac{B}{\sqrt{A^2 + B^2 + C^2}}, \cos\gamma = \frac{C}{\sqrt{A^2 + B^2 + C^2}}. \tag{C.2}$$

Multiplying equation C.1 with the normalization factor:

$$\pm\mu \; = \; \frac{1}{\left|\overrightarrow{\mathbf{N}}\right|} \; = \; \frac{1}{\sqrt{A^2 + B^2 + C^2}} \tag{C.3}$$

leads to Hesse's normal form of the plane equation:

$$\cos\alpha \cdot x + \cos\beta \cdot y + \cos\gamma \cdot z - p \; = \; 0, \tag{C.4}$$

with p being the distance of the plane from the origin. The sign of μ has to be chosen opposite to that of D.

On many technical occasions, like the specification of the AGATA crystals (see sec. 3.2.1), a plane is specified by giving three points $P(x_{1-3}, y_{1-3}, z_{1-3})$ that are required to lie on the plane. The plane is thus uniquely defined and the component form is given by:

$$\begin{vmatrix} x - x_1 & y - y_1 & z - z_1 \\ x_2 - x_1 & y_2 - y_1 & z_2 - z_1 \\ x_3 - x_1 & y_3 - y_1 & z_3 - z_1 \end{vmatrix} = 0. \tag{C.5}$$

Appendix D

The finite difference method

The finite difference method is a straightforward approach to solve partial differential equations like the Poisson equation 3.6. The problem is discretized on a regular rectangular grid on which the derivatives are approximated numerically. These approximations will be shown in the next section before the finite difference method will be introduced in the necessary detail. The following description of the approach will be for the 1-D case only. However, as will be shown in section D.2, the generalization to 3-D is straightforward.

D.1 Approximations to derivatives

The general definition of a functions derivative is

$$f'(x) = \lim_{h \to 0} \frac{f(x+h) - f(x)}{h}. \tag{D.1}$$

The difference quotient approaches the functions derivative in the limit of $h = 0$. If h, by contrast, has a finite non-zero value the term finite difference quotient is used and the derivative is approximated only up to a certain precision, which is related to the step size h. There are three commonly used forms for the difference in the nominator:

- **Forward difference:** $\Delta_h [f](x) = f(x+h) - f(x)$
- **Backward difference:** $\nabla_h [f](x) = f(x) - f(x-h)$
- **Central difference:** $\delta_h [f](x) = f(x+h) - f(x-h)$

Naturally, the denominator for the central difference quotient has to be $2h$. In some cases only one of the forms may be applicable due to boundary conditions but their main difference is in the precision given the same step size.

D.1.1 Errors of the approximations

The above approximations can equivalently be deduced by expanding $f(x)$ in a Taylor series to first order and solving for $f'(x)$. According to Taylor's theorem the error of such an approximation is determined by the remainder term $R_n(x+h)$, written in the Lagrange form, ((Bronstein, 2000), p. 434):

$$R_n(x+h) = \frac{f^{(n+1)}(\xi)}{(n+1)!} \cdot h^{n+1}, \text{ with } x < \xi < x+h \tag{D.2}$$

The error of the forward difference is thus:

$$\begin{aligned} f(x+h) &= f(x) + f'(x) \cdot h + \frac{f''(\xi)}{2!} \cdot h^2 \\ \frac{f(x+h)-f(x)}{h} &= f'(x) + \frac{f''(\xi)}{2!} \cdot h \\ \frac{f(x+h)-f(x)}{h} &= f'(x) + O(h). \end{aligned} \tag{D.3}$$

Analogously, the error of the backward difference is $O(h)$. In order to calculate the error of the central difference the Taylor series has to be expanded up to third order twice, once for $f(x+h)$ and once for $f(x-h)$, and subtracted from one another. In this case the second derivatives cancel each other (see eqns. D.4 and D.5) and the remainder term is given by the third derivative leading to errors of order h^2.

D.1.2 Higher order derivatives

The finite difference approximations to higher order derivatives can be derived in similar fashion by expanding $f(x)$ to higher order Taylor series. In the following the central difference approximation to the second derivative of $f(x)$ will be derived as an example. The fourth order Taylor expansions for both $f(x+h)$ and $f(x-h)$ are:

$$f(x+h) = f(x) + f'(x)h + \frac{h^2 f''(x)}{2} + \frac{h^3 f^{(3)}(x)}{6} + \frac{h^4 f^{(4)}(x)}{24} \tag{D.4}$$

$$f(x-h) = f(x) - f'(x)h + \frac{h^2 f''(x)}{2} - \frac{h^3 f^{(3)}(x)}{6} + \frac{h^4 f^{(4)}(x)}{24}. \tag{D.5}$$

Adding both equations eliminates the odd derivatives and solving for $f''(x)$ yields:

$$f''(x) = \frac{f(x+h) - 2f(x) + f(x-h)}{h^2} - \frac{2h^2 f^{(4)}(x)}{24}. \tag{D.6}$$

The remainder term is again of order h^2. In fact, the approximation errors for the higher order derivatives will always be the same as for the first derivatives (see sec. D.1.1).

More generally, the n^{th}-order forward, backward, and central differences are respectively given by:

$$\Delta_h^n[f](x) = \sum_{i=0}^{n}(-1)^i\binom{n}{i}f(x+(n-i)\cdot h) \tag{D.7}$$

$$\nabla_h^n[f](x) = \sum_{i=0}^{n}(-1)^i\binom{n}{i}f(x-i\cdot h) \tag{D.8}$$

$$\delta_h^n[f](x) = \sum_{i=0}^{n}(-1)^i\binom{n}{i}f(x+(n/2-i)\cdot h) \tag{D.9}$$

D.2 Solving Partial Differential Equations

The above presented finite difference approximations can be used to solve partial differential equations. In the following the basic approach undertaken will be explained using the one dimensional Poisson equation:

$$\Phi''(x) = -\frac{\rho(x)}{\varepsilon\varepsilon_0} \quad , x \in [0,1], \tag{D.10}$$

with space charge distribution $\rho(x)$, as an example.

As a first step, equation D.10 is discretized on a regular grid of N points. The i^{th} grid point therefore has the coordinate $x_i = i\cdot h = x_{i-1}+h$ with $h = 1/N$. The values $\Phi(0)$ and $\Phi(1)$ are given by boundary conditions, such as fixed voltages at the electrodes or fixed values for the electric fields. Using equation D.6, the left hand side of equation D.10 is approximated on every grid point:

$$\frac{\Phi(x_{i+1}) - 2\,\Phi(x_i) + \Phi(x_{i-1})}{h^2} = -\frac{\rho(x_i)}{\varepsilon\varepsilon_0}. \tag{D.11}$$

This results in a linear system of $N-2$ equations which has to be solved. The various finite difference methods differ only in the way this system of equations is solved.

The generalization to the three dimensional case is straightforward. Given that $\nabla = \frac{\partial^2}{\partial x^2} + \frac{\partial^2}{\partial y^2} + \frac{\partial^2}{\partial z^2}$, equation 3.6 is approximated using equation D.6 independently for x, y and z. The resulting equation is easily solved for $\Phi(x_i, y_i, z_i)$:

$$\begin{aligned}\frac{\Phi_{x(i+1)} - 2\Phi + \Phi_{x(i-1)}}{h^2} + \frac{\Phi_{y(i+1} - 2\Phi + \Phi_{y(i-1)}}{h^2} + \frac{\Phi_{z(i+1)} - 2\Phi + \Phi_{z(i-1)}}{h^2} &= -\frac{\rho(x_i,y_i,z_i)}{\varepsilon\varepsilon_0} \\ \Phi(x_i,y_i,z_i) &= \frac{\varepsilon\varepsilon_0(\Sigma\Phi_{x(i)} + \Sigma\Phi_{y(i)} + \Sigma\Phi_{z(i)}) + h^2\rho(x_i,y_i,z_i)}{6\cdot\varepsilon\varepsilon_0},\end{aligned} \tag{D.12}$$

with $\Sigma\Phi_{x(i)} = \Phi(x_{i+1},y,z) + \Phi(x_{i-1},y,z)$ and accordingly for y and z.

D.2.1 The Red-Black Gauß-Seidel solver

The Red-Black Gauß-Seidel solver utilizes the fact that $\Phi(x_i, y_i, z_i)$ at even indexes only depends on the values at odd indexes and vice versa (see eqns. D.11 and D.12). Before the iterative solution starts, the grid is split in two parts, one containing the odd indexes and the other only the even indexes. The first step of the algorithm in iteration $j+1$ is to update the odd indexes according to the following equation:

$$\Phi^{j+1}(x_i, y_i, z_i) = \frac{\varepsilon_0\,\varepsilon_r(\Sigma\Phi^{j}_{x(i)} + \Sigma\Phi^{j}_{y(i)} + \Sigma\Phi^{j}_{z(i)}) + \rho_{x_i,y_i,z_i}\,h^2}{6\,\varepsilon_0\,\varepsilon_r}. \tag{D.13}$$

Since the odd indexes have thus already been updated their values can be used to update the even indexes. The correspondingly modified iteration directive for the even indexes is:

$$\Phi^{j+1}(x_i, y_i, z_i) = \frac{\varepsilon_0\,\varepsilon_r(\Sigma\Phi^{j+1}_{x(i)} + \Sigma\Phi^{j+1}_{y(i)} + \Sigma\Phi^{j+1}_{z(i)}) + \rho_{x_i,y_i,z_i}\,h^2}{6\,\varepsilon_0\,\varepsilon_r}. \tag{D.14}$$

This approach has the advantage that, first of all only one copy of the grid has to be kept in computer memory and secondly it converges faster than the standard Gauß-Seidel algorithm. The solver has converged once the changes from one iteration to the next are below a given threshold for every grid point.

Appendix E

Moments of Distributions

The moments of a random variable X are characteristic parameters used in descriptive statistics. For instance, a distribution function $f(x)$ can be completely expressed in terms of all its moments. The mean, variance, skewness and kurtosis, i.e. bulging or curvature, of a distribution are all related to the distributions moments. The k^{th} moment about the mean or central moment is given by

$$\mu_k \;=\; E\left[(X - E(X))^k\right] \;=\; \int_{-\infty}^{\infty} (x-\mu)^k \, f(x)\, dx \text{ with } k \in \mathbb{N}. \tag{E.1}$$

Standardized moments are central moments normalized with respect to the standard deviation σ and the k^{th} standardized moment is thus given by $\frac{\mu_k}{\sigma^k}$. There are distributions for which not all or no moment exists. An example for the latter is the Cauchy distribution since its mean is undefined.

E.1 Mean and Variance

The mean μ of a real-valued distribution function $f(x)$ is calculated by the integral

$$\mu \;=\; E(X) \;=\; \int_{-\infty}^{\infty} x\, f(x)\, dx. \tag{E.2}$$

and is equal to the first moment around the origin or the expectation value $E(X)$. Naturally the first central moment is zero.

The variance $Var(X)$ is a measure of the dispersion or variability of a distribution. It is independent of the location of the mean, equal to square of the standard deviation σ and the second central moment of $f(x)$:

$$\mu_2 \;=\; Var(x) \;=\; E\left[(X - E(X))^2\right] \;=\; \int_{-\infty}^{\infty} (x-\mu)^2 \, f(x)\, dx. \tag{E.3}$$

Obviously the second standardized moment is always 1. Measurement errors are typically stated in terms of σ.

E.2 Skewness

Skewness, the third standardized moment, is written as γ_1 and defined as

$$\gamma_1 = \frac{\mu_3}{\sigma^3}. \tag{E.4}$$

It is a measure of the lopsidedness or asymmetry of a distribution. In skewed distributions the mean is farther out in the tail than the median. Symmetric distributions like the normal distribution have a skewness of zero and the mean and median are the same. Left leaning distributions (blue curve in fig. E.1(a)) have a negative skewness and right leaning (red curve in fig. E.1(a)) a positive skewness.

E.3 Kurtosis

The kurtosis is the fourth standardized moment about the mean, given by $\frac{\mu_4}{\sigma^4}$, and is a measure of the *peakedness* of a distribution. However, often it is more convenient to compare distributions in terms of the excess kurtosis γ_2:

$$\gamma_2 = \frac{\mu_4}{\sigma^4} - 3, \tag{E.5}$$

which is zero for the normal distribution. Leptokurtic distributions, i.e. positive γ_2, like the Laplace distribution ($\gamma_2 = 3$) exhibit a narrower peak around the mean but stronger tails than the normal distribution meaning that more of the variance is due to infrequent extreme deviations, as opposed to frequent modestly-sized deviations. Platykurtic distributions, i.e. negative γ_2, like the uniform distribution ($\gamma_2 = -1.2$) have a broader peak around the mean than the normal distribution and weaker tails. Distributions with an excess kurtosis of zero are called mesokurtic. Leptokurtic distributions have the highest probability for values close to the mean, while platykurtic have the lowest. Figure E.1(b) shows one example each for the three cases, all distributions have unit variance and are normalized to unit integral.

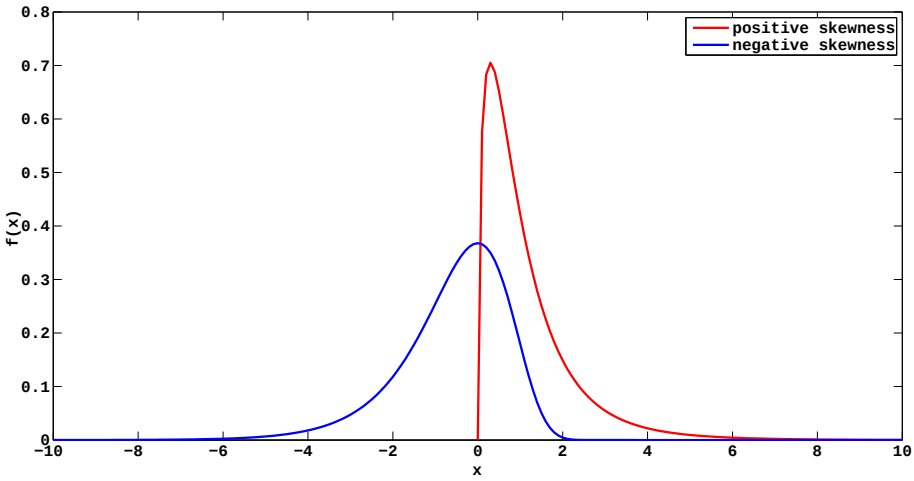

(a) Illustration of Skewness.

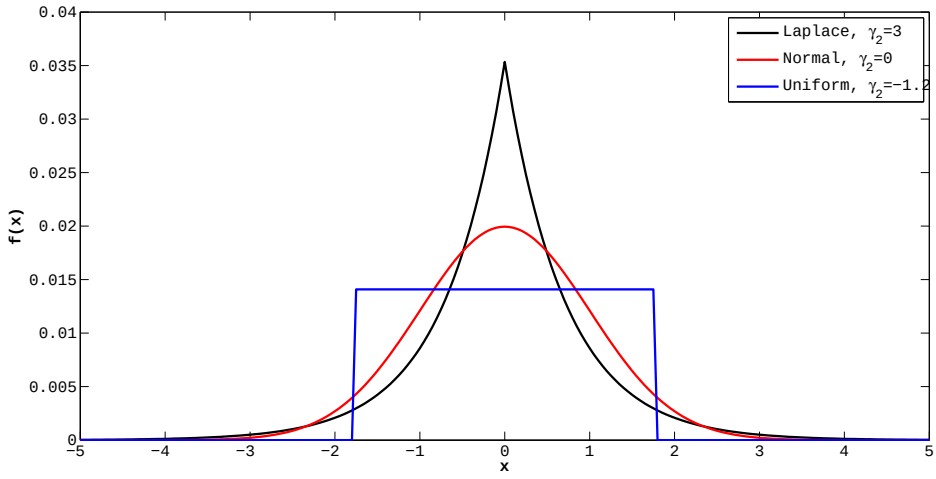

(b) Illustration of Kurtosis.

Figure E.1: Illustration of Skewness and Kurtosis. (a) Negatively skewed (blue curve) distributions have an increased probability for values below the mean, i.e. strong tailing to the left. The opposite is the case for positively skewed distributions like the red curve. (b) Comparison of the Laplace (black), normal (red) and uniform (blue) distributions in terms of excess kurtosis γ_2. The Laplace distribution has the highest and narrowest peak around the mean, i.e. the highest probability, while no peak is present for the uniform distribution. All distributions have zero mean,unit variance and been normalized to unit integral.

Appendix F

Electronic DAQ Components

In the following the electronic components of the AGATA DAQ chain, shortly mentioned in section 2.2, are introduced in a bit more detail.

F.1 The AGATA Charge-sensitive Preamplifiers

The signals from the AGATA segments and the core contact are readout simultaneously through charge-sensitive preamplifiers. The preamplifiers consist of a cold part, located in close proximity to the detector electrodes and operated near the temperature of the detector, and a warm part operated at room temperature. The cold part features a low-noise Field Effect Transistor (FET), model BF862, and a specifically designed shielding arrangement in order to minimize inter-channel crosstalk. The warm part consist of a charge-sensitive amplifier, a pole-zero stage, a differential output buffer, and a fast-reset circuitry (see fig. F.1).

Two versions of segment preamplifiers were developed at the University of Milano and at GANIL, differing in two key aspects. The latter was constructed using FR4 laminates and has a fixed bandwidth of $8\,MHz$ while the former uses alumina substrates and has an adjustable bandwidth between $8\,MHz$ and $12\,MHz$. Yet no disparity in performance could be observed and hence both versions will be installed in equal numbers at the AGATA demonstrator. The achieved energy resolutions are $1.15\,keV$ (FWHM) at $122\,keV$ and $2.15\,keV$ at $1.3\,MeV$. The initial version of the core preamplifier, developed in Cologne, only had a single amplification channel, while the newly developed version has two channels, operated simultaneously („dual gain“) to optimize the energy-range. The first channel covers energies up to $5\,MeV$, for an optimal energy resolution at lower energies, while the upper limit of the second channel is $20\,MeV$. The energy resolution of the core preamplifier is $1.1\,keV$ (FWHM) at $122\,keV$ and $2.19\,keV$ (FWHM) at $1.3\,MeV$, comparable to the resolution of a segment preamplifier. Additionally a custom programmable high-precision pulser is included on the

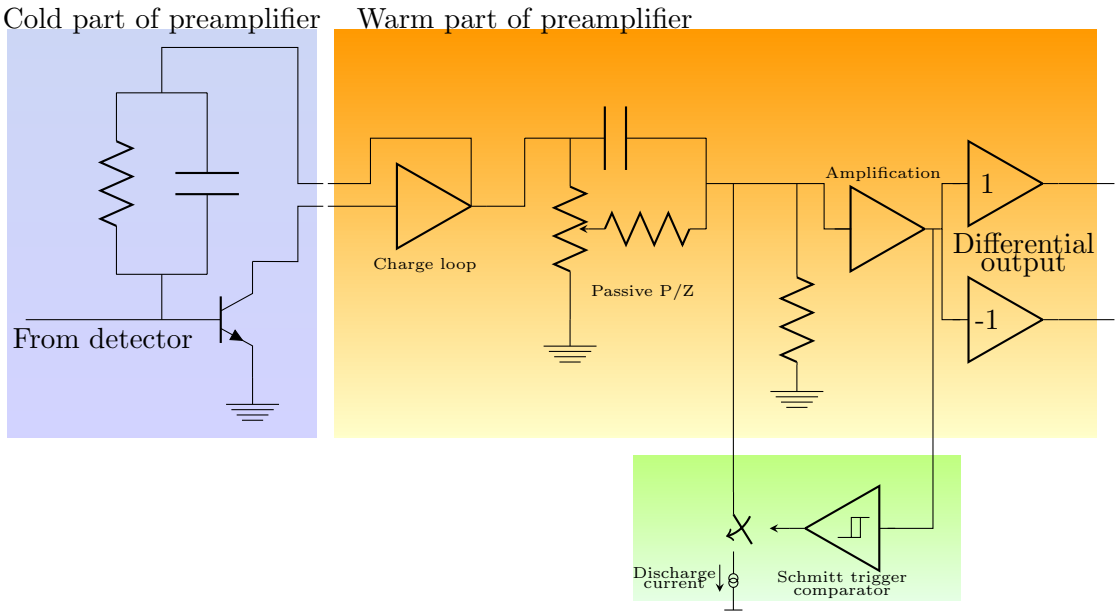

Figure F.1: Simplified schematic diagram of the AGATA preamplifiers (the pulser is not shown). The cold part (blue rectangle) integrates the detector currents and is spatially separated from the warm part (orange rectangle). The pole-zero stage cancels any overshoot in the integrated charge signal and the differential output consists of the original signal and an inverted copy of it. In order to discharge the capacitor of the pole-zero (P/Z) stage the Schmitt trigger in the de-saturation circuitry (green rectangle) continuously compares the preamplifier output signal against an adjustable threshold and turns on a current sink if the threshold is exceeded. The sink is turned off again once the zero voltage floor is reached.

core preamplifier boards, which can be used to inject calibration pulses to the core electrode itself as well as to all segment electrodes through the detector bulk capacitance. The energy resolution of the spectral line provided by the pulser is $1.005\,keV$ (FWHM).

The core contact has a considerably higher event rate than a single segment electrode, about 36 times as high in a first approximation, and is thus the component most sensitive to pile up and subsequent saturation of the ADC. In order to limit the resulting system dead-time to acceptable levels a fast-reset circuitry, working on the first channel of the core preamplifier, was included in the design. Additionally it is also an essential component in implementing the *Time over Threshold* method. (Zocca et al., 2007) showed that the time needed to reset the signal back to the zero level baseline, i.e. the time over threshold, is proportional to the deposited energy and derived the corresponding mathematical relation. The signal in the first channel is redirected into a charge drain if it is in excess of 10 MeV, overlapping with the second channels range and hence allowing for a calibration of ToT. The obtainable energy resolution depends on the overall event rate and the baseline level before the saturating event. Testing ToT in the energy range between 3 MeV and 50 MeV produced resolutions below 0.4% (FWHM) for all events and an astounding 0.21% for the $8.99\,MeV$ line of Ni.

F.2 The AGATA Digitizers

The digitizers bridge the gap between the analog world of the preamplifiers and the digital realm of the preprocessing and subsequent PSA. One digitizer unit includes all parts necessary to digitize the output of one detector with 38 channels. It is setup no further than $10\,m$ away from the associated detector, so that the risk of induced noise can be minimized. Due to the rather large power consumption of 400 W for the complete unit, a special housing was constructed in order to provide water cooling for the equipment. Figure F.2 shows the electronics board of the digitizer without the housing.

The differential output from a preamplifier is sent through a driver, including an anti-aliasing filter ensuring a band-limited signal in the sense of (Shannon, 1949), before it is sampled by a Flash ADC at 100 MHz with 14 bit resolution. The *effective number of bits* is 12.30 on average. One unit has 38 Flash ADCs, 36 for the segments and two for the two different output channels of the core preamplifier. A Virtex2Pro Field Programmable Gate Array (FPGA) performs a synchronization of the individual pulses and transmits them afterwards to the pre-processing units at 2 GBit/sec via optical links. Finally the ToT method, explained above, is implemented on the FPGA to provide a possibility to measure energies beyond the $20\,MeV$ limit of the second channel of the core preamplifier.

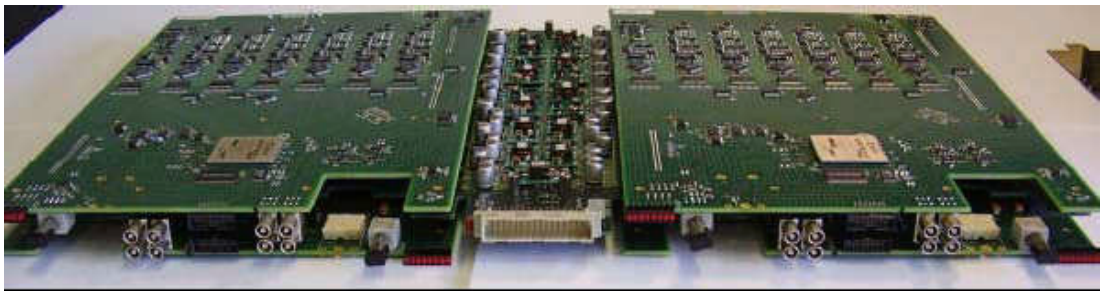

Figure F.2: The electronics board of one AGATA digitizer, without the housing. In the back part the sampling ADC's, one for each of the 38 channels, are visible. The FPGA's used for synchronizing the channels and formatting the data for the optical links are in the front of this picture. The figure was taken from (Simpson et al., 2008).

F.3 Front End Electronics

The digitizers continuously sample the signals from the detectors, sending a data stream of $6.19\,GB/s$ per detector to the front-end electronics. This number is given by the $100\,MHz$ sampling rate and the 14 bit precision of the ADC's times the 38 channels read from each detector. It is therefore a continuous load and independent of an experiments event rate. The main task of the electronics is to extract the useful data, which can be calculated on a per-channel basis out of this incoming data stream. These are the energy deposition through MWD, the event time and a leading edge trigger on the core. The latter ensures that only those parts of the incoming traces are kept which include an actual pulse shape belonging to an interaction in a crystal. For an event rate of $10\,kHz$ in one crystal the data rate is thus reduced to $74\,MB/s/detector$.

The Global Trigger and Synchronization Hardware System (GTS) is in charge of synchronizing the data acquisition for the complete array. It issues a global clock signal to all digitizers, ensuring that all samples are aligned in time and hands out global time stamps and event numbers to the data coming from the various detectors. The latter part allows the event builder (see sec. F.5) to merge corresponding data packets. The bottom side of a GTS mezzanine is shown in figure F.3. The two plugs connecting the card to the ATCA carrier are situated on the left side of the picture.

Additionally, the possibility exists to use the GTS global trigger mechanism to reduce the data rate going out of the front-end electronics by pre-selecting data based on criteria like multiplicity of hit crystals or coincidence with ancillary detectors. The default operating mode, however, is triggerless, sending all processed data to the PSA stage and using the GTS trigger only as a start signal for the extraction of the signals out of the incoming data.

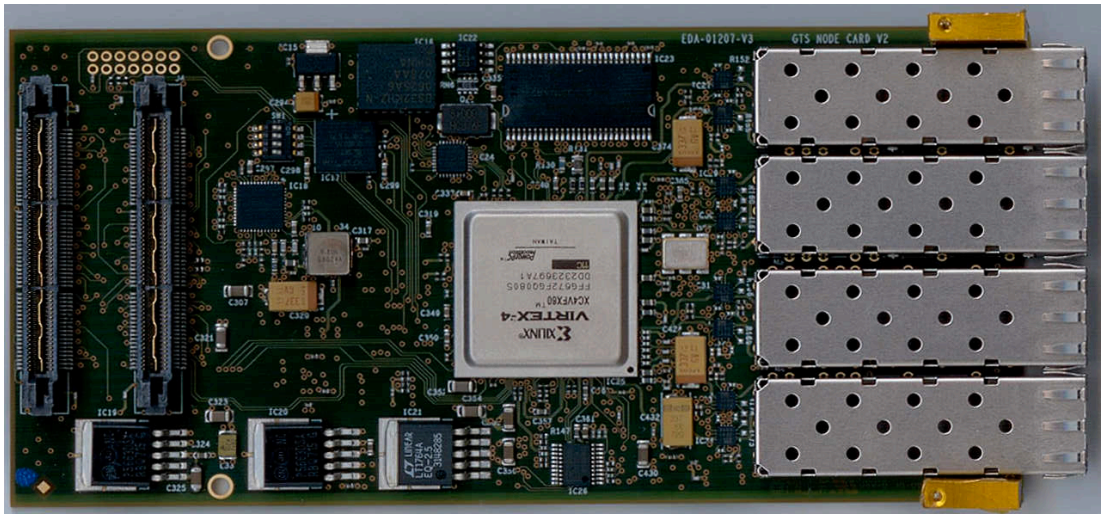

Figure F.3: The bottom side of the GTS mezzanine card. On the left side the two plugs connecting the card to the ATCA carrier card can be seen.

In light of the high data rate it was decided to use ATCA[1] crates for the electronics. A mezzanine based approach was chosen for the separate tasks with

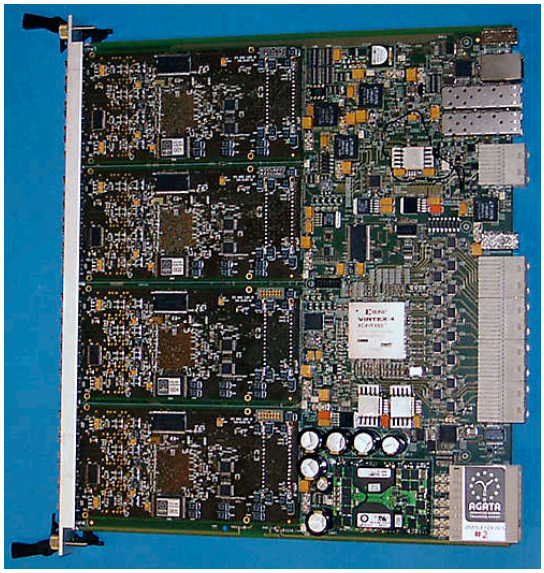

Figure F.4: An ATCA carrier card with all four mezzanines mounted on the left side. The right side connects to the back plane of the ATCA crate.

one mezzanine card each for the core, the segments and the GTS. Up to four mezzanines can be plugged into one ATCA carrier card (see fig. F.4). It takes two of these carriers to handle all the data from a single crystal, since one segment mezzanine can only handle the data from six segments.

[1]The *Advanced Telecommunications Computing Architecture* is an electronics standard developed for high-data rate telecommunication applications.

F.4 Pulse Shape Analysis

The highly challenging task of pulse shape analysis (PSA) is to disentangle the individual γ-ray interactions within one crystal and to determine the position, the time and the energy deposition of each individual interaction by analyzing the recorded experimental pulse shape. The output of the PSA consists only of the above parameters and the associated errors, allowing for the largest reduction in data rate in the whole DAQ chain. Since PSA and the related issue of pulse shape simulation are the topic of this thesis only issues relevant for the DAQ will be covered in the following. The working principle of PSA, along with the used algorithms will be described in detail in chapter 4 and the reasons why a reliable simulation is a prerequisite for a successful PSA will be given in chapter 3.

The PSA and the necessary preprocessing, outlined below, will run exclusively on a dedicated server farm, with one multi-processor server per crystal. However this number could change in the future, if the need arises. An important matter to note is that the PSA will be run independently for each crystal, although a scattering from one crystal to another is a likely process. But the pulse shapes are independent for each crystal since intra-detector crosstalk has been shown to be nonexistent (Wiens, 2008). Before the traces are fed to the PSA algorithm for the position reconstruction, some more preprocessing must be performed. First the baseline must be adjusted to zero and the exponential decay originating from the preamplifier response functions is removed by analytic deconvolution. Before the traces can be normalized to unit charge in the last step, a crosstalk correction, depending on the number of hit segments, is applied.

F.5 Event Building and Merging

Each reconstructed interaction location and energy deposit keeps the timestamp and event number issued by the GTS and attached to the pulse shapes. Based on this information the event builder packs all corresponding events together and transmits them to the tracking algorithm. At this stage the data from AGATA can optionally be merged with time correlated data from an ancillary detector, e.g. a CD-Detector in an experiment with Coulomb excitation. Depending on the experiment the ancillary detector may provide useful data for the tracking algorithm in order to facilitate the determination of the emission direction of the γ-ray, important for a precise Doppler correction.

List of Figures

List of Tables

References

Alba, E.D., & Paranjabe, V.V. 1964. Energy distribution of holes in electric fields. Phys. Lett., **11**, 12–13.

Ashcroft, N.W., & Mermin, N.D. 1976. Solid State Physics. Brooks Cole.

Bazzacco, Dino. 2009. private communications.

Bishop, Christopher M. 1996. Neural Networks for Pattern Recognition. Oxford University Press, USA.

Bors, Adrian G. 2000. Introduction to the Radial Basis Function Networks. http://axiom.anu.edu.au/ daa/courses/GSAC6017/rbf.pdf.

Boston, A.J., Boston, H.C., Cresswell, J.R., Dimmock, M.R., Nelson, L., Nolan, P.J., Rigby, S., Lazarus, I., Simpson, J., Medina, P., Santos, C., & Parisel, C. 2007. Gamma-ray tracking: Characterisation of the AGATA symmetric prototype detectors. Nucl. Instr. and Meth. B, **261**(1-2), 1098 – 1102. Proceedings of the Nineteenth International Conference on The Application of Accelerators in Research and Industry.

Bothe, Sander. 2003. Spiking Neural Networks. Ph.D. thesis, Unversiteit Leiden.

Bronstein, I.N. 2000. Taschenbuch der Mathematik. Thun, Frankfurt am Main, Germany: Verlag Harri Deutsch.

Bruyneel, Bart. 2007. Automated optimization of detector simulation to fit S002 scan data. `http://agata.lnl.infn.it/AgataWeek2007/talks/Characterization\%20and\%20PSA/BruyneelAGATA_2007_talk2.pdf`.

Bruyneel, Bart, Reiter, Peter, & Paskovici, Georghe. 2006a. Characterization of large volume HPGe detectors. Part I: Electron and hole mobility parameterization. Nucl. Instr. and Meth. A, **569**, 764–773.

Bruyneel, Bart, Reiter, Peter, & Paskovici, Georghe. 2006b. Characterization of large volume HPGe detectors. Part II: Experimental results. Nucl. Instr. and Meth. A, **569**, 774–789.

Bruyneel, Bart, Reiter, Peter, Wiens, Andreas, Eberth, Jrgen, Hess, Herbert, Pascovici, Gheorghe, Warr, Nigel, & Weisshaar, Dirk. 2009. Crosstalk properties of 36-fold segmented symmetric hexagonal HPGe detectors. Nuclear Instruments and Methods in Physics Research Section A: Accelerators, Spectrometers, Detectors and Associated Equipment, **599**(2-3), 196 – 208.

Cavalleri, G. 1971. Extension of Ramo's theorem as applied to induced charge in semiconductor devices. Nucl. Instr. and Meth. A, **92**, 137.

Clerc, M., & Kennedy, J. 2002. The particle swarm - explosion, stability, and convergence in a multidimensional complex space. Evolutionary Computation, IEEE Transactions on, **6**(1), 58–73.

Conwell, Esther M. 1967. High Field Transport in Semiconductors. Vol. 9 of Solid State Physics. Academic Press.

Crespi, F.C.L., Camera, F., Wieland, O., Benzoni, G., Brambilla, S., Million, B., & Montanari, D. 2007. A pulse shape analysis algorithm for HPGe detectors. Nucl. Instr. and Meth. A, **570**, 459–466.

Crespi, F.C.L., Camera, F., Million, B., Sassi, M., Wieland, O., & Bracco, A. 2008. A novel technique for the characterization of a HPGe detector response based on pulse shape comparison. Nuclear Instruments and Methods in Physics Research Section A: Accelerators, Spectrometers, Detectors and Associated Equipment, **593**(3), 440 – 447.

Deleplanque, M. A., Lee, I. Y., Vetter, K., Schmid, G. J., Stephens, F. S., Clark, R. M., Diamond, R. M., Fallon, P., & Macchiavelli, A. O. 1999. GRETA: utilizing new concepts in γ-ray detection. Nucl. Instr. and Meth. A, **430**(2-3), 292 – 310.

Deleplanque, M.A., & Diamond, R.M. (eds.). 1987. Gammasphere proposal. Tech. rept. LBNL-5202.

Descovich, M., Lee, I. Y., Luke, P.N., Clark, R.M., Cromaz, M., Deleplanque, M.A., Diamond, R.M., Fallon, P., Macchiavelli, A.O., Rodriguez-Vieitez, E., Stephens, F.S., & Ward, D. 2005. Effects of neutron damage on the performance of large-volume segmented germanium detectors. Nucl. Instr. and Meth. A, **545**, 199–209.

Dimmock, Matthew R. 2008. Characterisation of AGATA symmetric prototype detectors. Ph.D. thesis, University of Liverpool.

Duchêne, G., Beck, F. A., Twin, P. J., de France, G., Curien, D., Han, L., Beausang, C. W., Bentley, M. A., Nolan, P. J., & Simpson, J. 1999. The Clover: a new generation of composite Ge detectors. Nucl. Instr. and Meth. A, **432**(1), 90 – 110.

Eberth, J., & Simpson, J. 2008. From Ge(Li) detectors to gamma-ray tracking arrays-50 years of gamma spectroscopy with germanium detectors. Prog. Part. Nucl. Phys., **60**(2), 283 – 337.

Eberth, J., Brentano, P. Von, Teichert, W., Thomas, H.G., Werth, A.V.D., Lieder, R.M., Jger, H., Kmmerling, H., Kutchin, D., Maier, K.H., Berst, M., Gutknecht, D., & Henck, R. 1992. Development of a composite Ge detector for EUROBALL. Prog. Part. Nucl. Phys., **28**, 495 – 504.

Eberth, J., Thomas, H.G., Brentano, P.v., Lieder, R.M., Jger, H.M., Kmmerfing, H., Berst, M., Gutknecht, D., & Henck, R. 1996. Encapsulated Ge detectors: Development and first tests. Nucl. Instr. and Meth. A, **369**(1), 135 – 140.

Eberth, J., Pascovici, G., Thomas, H. G., Warr, N., Weisshaar, D., Habs, D., Reiter, P., Thirolf, P., Schwalm, D., Gund, C., Scheit, H., Lauer, M., Duppen, P. Van, Franchoo, S., Huyse, M., Lieder, R. M., Gast, W., Gerl, J., & Lieb, K. P. 2001. MINIBALL A Ge detector array for radioactive ion beam facilities. Prog. Part. Nucl. Phys., **46**(1), 389 – 398.

Eberth, Jürgen. 2008. private communications.

Essel, H.G., & Kurz, N. 2000. The general purpose data acquisition system MBS. Nuclear Science, IEEE Transactions on, **47**(2), 337–339.

Fallon, P., Rodriguez-Vieitez, E., Bazin, D., Campbell, C. M., Cook, J. M., Clark, R. M., Dinca, D-C., Gade, A., Glasmacher, T., Lee, I-Y., Macchiavelli, A. O., Mueller, W. F., Prussin, S. G., Wiedeking, M., & Yoneda, K. 2006. Transition to the Island of Inversion: Study of Excited States in $^{28-30}Ne$. J. Phys.: Conf. Ser., **49**, 165–169.

Gadea, A, Marginean, N, Corradi, L, Lenzi, S M, Ur, C A, Farnea, E, de Angelis, G, Fioretto, E, Napoli, D R, Stefanini, A M, Szilner, S, Axiotis, M, Behera, B R, Latina, A, Rusu, C, Zhimin, W, Bazzacco, D, Beghini, S, Lunardi, S, Montagnoli, G, Menegazzo, R, Scarlassara, F, Vedova, F Della, Nespolo, M, Bracco, A, Camera, F, Leoni, S, Million, B, Pignanelli, M, Pollarolo, G, Trotta, M, Bizzeti, P G, Bizzeti-Sona, A M, Curien, D, Medina, P, Chambit, M, Chapman, R, Liang, X, Freeman, S J, Smith, A, Varley, B J, Pucknell, V, & Lemmon, R. 2005. The CLARA-PRISMA setup installed at LNL: first results. Journal of Physics G: Nuclear and Particle Physics, **31**(10), S1443–S1448.

Gámir, L.P. 1997. A new method for the determination of the entry position of γ-rays in HPGe detectors by current pulse analysis. Ph.D. thesis, Max-Planck-Institut f¨ur Kernphysik, Heidelberg.

Georgiev, A., Gast, W., & Lieder, R.M. 1994. An analog-to-digital conversion based on a moving window deconvolution. Nuclear Science, IEEE Transactions on, **41**(4), 1116–1124.

Gerl, J., & Korten, W. 2001. AGATA technical proposal. Tech. rept. AGATA, http://agata.pd.infn.it/Agata-proposal.pdf.

Grave, X., Canedo, R., Clavelin, J.-F., Du, S., & Legay, E. 2005. NARVAL a modular distributed data acquisition system with Ada 95 and RTAI. Real Time Conference, 2005. 14th IEEE-NPSS, June, 5 pp.–.

Habs, D., Rudolph, D., Thirolf, P., Fischbeck, C., Gund, Ch., Schwalm, D., Eberth, J., Grosse, E., Prade, H., Emling, H., Gerl, J., Lieder, R. M., Duppen, P. Van, Rossi-Alvarez, C., & Pignanelli, M. 1997. Physics with Ge-Miniball-arrays. Prog. Part. Nucl. Phys., **38**, 111 – 126. 4 pi High Resolution Gamma Ray Spectroscopy and Nuclear Structure.

Hagan, Martin T., & Menhaj, Mohammad B. 1994. Training Feedforward Networks with the Marquardt Algorithm. IEEE Trans. Neural Networks, **5**, 989–993.

He, Z. 2001. Review of the Shockley-Ramo theorem and its application to semiconductor gamma-ray detectors. Nucl. Instr. and Meth. A, **463**, 250–267.

Hornik, Kurt. 1991. Approximation capabilities of multilayer feedforward networks. Neural Netw., **4**(2), 251–257.

Jen, C.K. 1941. On the Induced Current and Energy Balance in Electronics. Proc. IRE, 345.

Johnson, A., Ryde, H., & Hjorth, S. A. 1972. Nuclear moment of inertia at high rotational frequencies. Nucl. Phys. A, **179**(3), 753 – 768.

Kennedy, J., & Eberhart, R. 1995 (Nov/Dec). Particle swarm optimization. vol. 4.

Kennedy, James, & Eberhart, Russel C. 2001. Swarm Intelligence. San Diego, USA: Morgan Kaufmann Publishers.

Kennedy, James, & Mendes, Rui. 2006. Neighborhood topologies in fully informed and best-of-neighborhood particle swarms. IEEE Trans. on Systems, Man, and Cybernetics, Part C: Applications and Reviews, **36**, 515–519.

Khoo, T. L., Carpenter, M. P., Lauritsen, T., Ackermann, D., Ahmad, I., Blumenthal, D. J., Fischer, S. M., Janssens, R. V. F., Nisius, D., Moore, E. F., Lopez-Martens, A., Døssing, T., Krücken, R., Asztalos, S. J., Becker, J. A., Bernstein, L., Clark, R. M., Deleplanque, M. A., Diamond, R. M., Fallon,

P., Farris, L. P., Hannachi, F., Henry, E. A., Korichi, A., Lee, I. Y., Macchiavelli, A. O., & Stephens, F. S. 1996. Excitation Energies and Spins of a Superdeformed Band in $194Hg$ from One-Step Discrete Decays to the Yrast Line. Phys. Rev. Lett., **76**(10), 1583–1586.

Knoll, Glenn F. 1999. Radiation Detection and Measurement. 3rd edn. Wiley & Sons.

Korten, W., & Lunardi, S. 2003. Achievements with the EUROBALL spectrometer 1997-2003. Tech. rept. LNL.

Kröll, Th., & Bazzacco, D. 2001. Simulation and analysis of pulse shapes from highly segmented HPGe detectors for the γ-ray tracking array MARS. Nucl. Instr. and Meth. A, **463**(1-2), 227 – 249.

Kröll, Thorsten, & Bazzacco, Dino. 2006. A genetic algorithm for the decomposition of multiple hit events in the γ-ray tracking detector MARS. Nucl. Instr. and Meth. A, **565**(2), 691 – 703.

Lazarus, I.H., Appelbe, D.E., Boston, A.J., Coleman-Smith, P.J., Cresswell, J.R., Descovich, M., Gros, S.A.A., Lauer, M., Norman, J., Pearson, C.J., Pucknell, V.F.E., Sampson, J.A., Turk, G., & Valiente-Dobon, J.J. 2004. The GRT4 VME pulse processing card for segmented germanium detectors. IEEE Transactions on Nuclear Science, **51**(4), 1353– 1357.

Levenberg, Kenneth. 1944. A Method for the Solution of Certain Non-Linear Problems in Least Squares. The Quarterly of Applied Mathematics, **2**, 164–168.

Ljungvall, Joa, & Nyberg, Johann. 2005. A study of fast neutron interactions in high-purity germanium detectors. Nucl. Instr. and Meth. A, **546**, 553–573.

Lopez-Martens, A., Hauschild, K., Korichi, A., Roccaz, J., & Thibaud, J-P. 2004. γ-ray tracking algorithms: a comparison. Nucl. Instr. and Meth. A, **533**(3), 454 – 466.

Maierbeck, P., Gernhuser, R., Krcken, R., Krll, T., Alvarez-Pol, H., Aksouh, F., Aumann, T., Behr, K., Benjamim, E.A., Benlliure, J., Bildstein, V., Bhmer, M., Boretzky, K., Borge, M.J.G., Brnle, A., Brger, A., Caamao, M., Casarejos, E., Chatillon, A., Chulkov, L.V., Cortina-Gil, D., Enders, J., Eppinger, K., Faestermann, T., Friese, J., Fabbietti, L., Gascn, M., Geissel, H., Gerl, J., Gorska, M., Hansen, P.G., Jonson, B., Kanungo, R., Kiselev, O., Kojouharov, I., Klimkiewicz, A., Kurtukian, T., Kurz, N., Larsson, K., Bleis, T. Le, Mahata, K., Maier, L., Nilsson, T., Nociforo, C., Nyman, G., Pascual-Izarra, C., Perea, A., Perez, D., Prochazka, A., Rodriguez-Tajes, C., Rossi, D., Schaffner, H., Schrieder, G., Schwertel, S., Simon, H., Sitar, B.,

Stanoiu, M., Smmerer, K., Tengblad, O., Weick, H., Winkler, S., Brown, B.A., Otsuka, T., Tostevin, J., & Rae, W.D.M. 2009. Structure of ^{55}Ti from relativistic one-neutron knockout. Physics Letters B, **675**(1), 22 – 27.

Marquardt, Donald. 1963. An Algorithm for Least-Squares Estimation of Nonlinear Parameters. SIAM Journal on Applied Mathematics, **11**, 431–441.

Medina, P., Santos, C., & Villaume, D. 2004. A simple method for the characterization of HPGe detectors. Instrumentation and Measurement Technology Conference, 2004. IMTC 04. Proceedings of the 21st IEEE, **3**(May), 1828–1832 Vol.3.

Medina, Patrice. 2006. private communications.

Meijering, Erik H. W., Niessen, Wiro J., Pluim, Josien P. W., & Viergever, Max A. 1999. Quantitative Comparison of Sinc-Approximating Kernels for Medical Image Interpolation. **1679 of Lecture Notes in Computer Science**.

Mendes, Rui, Kennedy, James, & Neves, José. 2004. The Fully Informed Particle Swarm: Simpler, Maybe Better. IEEE Trans. on Evolutionary Computation, **8**, 204–210.

Mihailescu, L. 2000. Principles and methods for γ-ray tracking with large volume germanium detectors. Ph.D. thesis, Universität Bonn.

Mihailescu, L., Gast, Werner, Lieder, R. M., Brands, H., & Jäger, H. 2000. The influence of anisotropic electron drift velocity on the signal shapes of closed-end HPGe detectors. Nucl. Instr. and Meth. A, **447**, 350–360.

Minsky, M.L., & Papert, S. A. 1969. Perceptrons: An Introduction to Computational Geometry. MIT Press.

Monaghan, J.J. 1985. Particle Methods for Hydrodynamics. Computer Physics Reports, **3**, 71–124.

Montana, David J., & Davis, Lawrence. 1989. Training Feedforward Neural Networks Using Genetic Algorithms. Pages 762–767 of: IJCAI.

NASA. 2006. Intelligent Flight Control System. http://www.nasa.gov/centers/dryden/news/FactSheets/FS-076-DFRC.html.

Nathan, Marshall I. 1963. Anisotropy of the Conductivity of n-Type Germanium at High Electric Fields. Phys. Rev., **130**(6), 2201–2204.

Nguyen, Derrick, & Widrow, Bernard. 1990. Improving the Learning Speed of 2-Layer Neural Networks by Choosing Initial Values of the Adaptive Weights. Pages 21–26 of: Proceedings of the International Joint Conference on Neural Networks, vol. 3. IEEE.

Olariu, A., Desesquelles, P., Diarra, Ch., Medina, P., Parisel, C., & Collaboration, C.S.Obot.A. 2006. Pulse shape analysis for the location of the γ-interactions in AGATA. Nuclear Science, IEEE Transactions on, **53**(3), 1028–1031.

Ottaviani, G., Reggiani, L., Canali, C., Nava, F., & Quaranta, A. Alberigi. 1975. Hole drift velocity in silicon. Phys. Rev. B, **12**, 3318.

Pinson, W.E., & Bray, R. 1964. Experimental determination of the energy distribution functions and analysis of the energy-loss mechanisms of hot carriers in p-type germanium. Phys. Rev., **136**, 1449–1466.

Radford, David C. 2005. private communications.

Ramo, S. 1939. Currents induced by electron motion. Proc. IRE 27, 584.

Recchia, F., Bazzacco, D., Farnea, E., Gadea, A., Venturelli, R., Beck, T., Bednarczyk, P., Buerger, A., Dewald, A., Dimmock, M., Duchne, G., Eberth, J., Faul, T., Gerl, J., Gernhaeuser, R., Hauschild, K., Holler, A., Jones, P., Korten, W., Krll, Th., Krcken, R., Kurz, N., Ljungvall, J., Lunardi, S., Maierbeck, P., Mengoni, D., Nyberg, J., Nelson, L., Pascovici, G., Reiter, P., Schaffner, H., Schlarb, M., Steinhardt, T., Thelen, O., Ur, C.A., Dobon, J.J. Valiente, & Weihaar, D. 2009. Position resolution of the prototype AGATA triple-cluster detector from an in-beam experiment. Nucl. Instr. and Meth. A, **604**(3), 555 – 562.

Reggiani, L., Canali, C., Nava, F., & Ottaviani, G. 1977. Hole drift velocity in germanium. Phys. Rev. B, **16**, 2781–2791.

Reggiani, L., Canali, C., Nava, F., Pozhela, Y.K., Asche, M., Komiyama, S., Kurosawa, T., Masumi, T., Hess, K., Iafrate, G.J., & Constant, E. 1985. Hot-Electron Transport in Semiconductors. Vol. 58 of Topics in Applied Physics. Springer-Verlag.

Reik, H. G., & Risken, H. 1962. Drift Velocity and Anisotropy of Hot Electrons in n Germanium. Phys. Rev., **126**(5), 1737–1746.

Reynolds, Craig W. 1987. Flocks, Herds, and Schools: A Distributed Behavioral Model. Computer Graphics, **21**(4), 25–34.

Rosenblatt, Frank. 1958. The Perceptron: A Probabilistic Model for Information Storage and Organization in the Brain. Psychological Review, **65**, 386–408.

Rummelhart, D.E., Hinton, G.E., & Williams, R.J. 1986. Learning internal representations by error propagation. Vol. 1. The M.I.T. Press. Pages 318–362.

Sasaki, W., & Shibuya, M. 1956. Experimental evidence of the anisotropy of hot electrons in n-type germanium. J. Phys. Soc. Jpn., **11**, 1202–1203.

Schmid, G. J., Deleplanque, M. A., Lee, I. Y., Stephens, F. S., Vetter, K., Clark, R. M., Diamond, R. M., Fallon, P., Macchiavelli, A. O., & MacLeod, R. W. 1999. A γ-ray tracking algorithm for the GRETA spectrometer. Nucl. Instr. and Meth. A, **430**(1), 69 – 83.

Schmid, G.J., Lee, I.Y., Deleplanque, M.A., Hendriks, P., Stephens, F.S., Vetter, K., Asztalos, S.J., Clark, R.M., Diamond, R.M., Fallon, P., Kruecken, R., Macchiavelli, A.O., & MacLeod, R.W. 1997. Gamma-ray cluster identification in a spherical shell of highly segmented germanium detectors. Nuclear Science, IEEE Transactions on, **44**(3), 975–978.

Schönberg, Isaac J. 1946. Contributions to the problem of approximation of equidistant data by analytic functions, Part A: On the problem of smoothing or graduation, a first class of analytic approximation formulas. Quart. Appl. Math., **4**, 45–99.

Shannon, Claude E. 1949. Communication in the presence of noise. Proceedings of the Institute of Radio Engineers, **37**(1), 10–21.

Shockley, W. 1938. Currents on Conductors Induced by a Moving Point Charge. J. Appl. Phys., **9**, 635–636.

Simpson, J., Korten, W., & Nyberg, J. 2008. AGATA Technical Design Report. Tech. rept. AGATA.

Trottenberg, U., Oosterlee., C.W., & Schuller, A. 2000. Multigrid. Academic Press.

Unsworth, Carl. 2009. private communications.

van der Marel, J., & Cederwall, B. 1999. Backtracking as a way to reconstruct Compton scattered γ-rays. Nucl. Instr. and Meth. A, **437**(2-3), 538 – 551.

Vetter, K., Kuhn, A., Lee, I. Y., Clark, R. M., Cromaz, M., Deleplanque, M. A., Diamond, R. M., Fallon, P., Lane, G. J., Macchiavelli, A. O., Maier, M. R., Stephens, F. S., Svensson, C. E., & Yaver, H. 2000a. Performance of the GRETA prototype detectors. Nucl. Instr. and Meth. A, **452**(1-2), 105 – 114.

Vetter, K., Kuhn, A., Deleplanque, M. A., Lee, I. Y., Stephens, F. S., Schmid, G. J., Beckedahl, D., Blair, J. J., Clark, R. M., Cromaz, M., Diamond, R. M., Fallon, P., Lane, G. J., Kammeraad, J. E., Macchiavelli, A. O., & Svensson, C. E. 2000b. Three-dimensional position sensitivity in two-dimensionally segmented HP-Ge detectors. Nucl. Instr. and Meth. A, **452**(1-2), 223 – 238.

Wiens, Andreas. 2008. CAT of AGATA detectors & The AGATA triple cluster detector. `http://www.agata.org/aw7/presentations`.

Wilson, Edward O. 2000. Sociobiology: The New Synthesis. Harvard University Press.

Zocca, F., Pullia, A., Boiano, C., & Bassini, R. 2007. A Smart Reset Circuit for Low-Noise Preamplifiers of X- ? Ray Sensor Signals. IEEE Trans. Nucl. Sci., **54**(1), 197–201.

Danksagung

Als erstes möchte ich Prof. Dr. Reiner Krücken für die Möglichkeit zu einer sehr interessanten Doktorarbeit und die immer vorhandene herzliche Unterstützung danken. Roman Gernhäuser verdient besonderen Dank nicht nur für die intensive Betreuung sondern auch für anregende Diskussionen und entsprechende Denkanstöße.

Eine so Computer-lastige Arbeit wie diese erfordert natürlich einen reibungslosen Betrieb der Rechenfarm. Ohne die fleißige Arbeit der Admins, insbesondere Ludwig Maier, wäre dies schlicht unmöglich. Im Anschluss bedanke ich mich gleich noch bei meinen Kollegen die sehr verständnisvoll waren wenn die Farm mal wieder komplett von mir belegt war. Ralf, Sigrid (Danke für die Zeitungen!), Michael und Wolfgang danke ich für die angenehmen Mittagspausen und Gespräche, auch wenn die Bayern am Tag zuvor mal wieder schlecht gespielt hatten. Die angenehme Arbeitsatmosphäre bei uns im Büro weiß ich sehr zu schätzen. Des weiteren danke ich den Mitgliedern der AGATA Kollaboration für ihren Beitrag zum Gelingen dieser Arbeit. Ich möchte mich noch bei Freunden und Verwandtschaft für das Verständnis bedanken wenn ich mal keine Zeit hatte.

Natürlich verdient auch meine Familie gebührend Dank. Konni, Dennis und Melissa, ihr ward sehr geduldig mit mir und habt es immer wieder geschafft mir die Ablenkung und Erholung zu bieten, die bisweilen ziemlich notwendig war. Konni, ich kann dir nicht genügend dafür danken wie positiv du mein Leben verändert hast und wirst. Schließlich gebührt meinen Eltern ein großes Dankeschön. Ihr habt mir nicht nur das Studium und die Doktorarbeit ermöglicht sondern mich auch immer nach besten Kräften unterstützt.